Order number: 4612

THESIS

submitted to
UNIVERSITÉ BORDEAUX 1
ÉCOLE DOCTORALE DES SCIENCES PHYSIQUES ET DE L'INGÉNIEUR
and
UNIVERSIDAD POLITÉCNICA DE MADRID
E. T. S. DE INGENIEROS AERONÁUTICOS

by **CARLOS YÁÑEZ VICO**

for the degree of

DOCTOR
in ASTROPHYSICS, PLASMAS AND CORPUSCLES at Université Bordeaux 1
and
in AEROSPACE ENGINEERING at Universidad Politécnica de Madrid

---

HYDRODYNAMIC STABILITY THEORY OF DOUBLE ABLATION FRONT STRUCTURES IN INERTIAL CONFINEMENT FUSION

Defended on November 19, 2012 at Talence (France)

Board of examiners:

Mr **BETTI** Riccardo	Professor, University of Rocherster	Reviewer
Mr **BOUQUET** Serge	Professor, CEA/INSTN	Reviewer
Mr **SANZ RECIO** Francisco Javier	Professor, Polytechnical University of Madrid	Supervisor
Mr **TIKHONCHUK** Vladimir	Professor, University of Bordeaux	Supervisor
Ms **OLAZABAL-LOUME** Marina	Research engineer, CEA	Supervisor
Mr **PELAEZ ALVAREZ** Jesus	Professor, Polytechnical University of Madrid	Examiner
Mr **KELLAY** Hamid	Professor, University of Bordeaux	Examiner

¡Intelijencia, dame
el nombre exacto, y tuyo
y suyo, y mío, de las cosas!

Juan Ramón Jiménez

Dedicated to my lovin’ wife Cécile and my lil’ Lou-Andréa,
am the eternal witness of your beauty

CURRICULUM VITAE

The author was born in Madrid, Spain on June 22, 1984. He attended the School of Aeronautics in the Polytechnical University of Madrid from 2002 to 2008, and received a degree in Aeronautical Engineering in 2008. He completed the graduate studies with a Diploma Thesis defended in 2008 at the Institute for Hydromechanics of Karlsruhe Institute of Technology, where he conducted a research in the field of stability theory in stratified turbulent shear flows under the supervision of Dr. Manuel García-Villaba. After a first experience working as aeronautical engineer in the helicopter industry, he came to the University of Bordeaux in the fall 2009 as a graduate student at CELIA laboratory. He received a three-year funding from the CEA/Aquitaine Region to carry out doctorate studies under an international joint supervision between the University of Bordeaux and Polytechnical University of Madrid. He pursued his research in the hydrodynamic instabilities in inertial confinement fusion under the directions of Professor Javier Sanz and Professor Vladimir Tikhonchuk.

PUBLICATIONS RELATED TO THIS THESIS

Some results from this PhD research work have given rise to the following publications:

1. C. Yañez, J. Sanz, M. Olazabal-Loumé and L. F. Ibañez. *Linear stability analysis of double ablation fronts in direct-drive inertial confinement fusion.* Phys. Plasmas 18, 052701 (2011) doi ;
2. C. Yañez, J. Sanz and M. Olazabal-Loumé. *Self-consistent numerical dispersion relation of the ablative Rayleigh-Taylor instability of double ablation fronts in inertial confinement fusion.* Phys. Plasmas 19, 062705 (2012) doi
3. C. Yañez, J. Sanz, M. Olazabal-Loumé and L. F. Ibañez. *Modeling hydrodynamic instabilities of double ablation fronts in inertial confinement fusion.* EPJ Web of Conference (submitted)

and have been partially presented in the following conferences:

1. EPS 2010, 37th Conference on Plasma Physics (Dublin, 2010),
2. 4th Forum ILP: Lasers and Plasmas (Praz-sur-Arly, 2011),
3. EPS 2011, 38th Conference on Plasma Physics (Strassbourg, 2011), and
4. IFSA 2011, 7th International Conference on Inertial Fusion Sciences and Applications (Bordeaux, 2011);
5. EPS 2012, 39th Conference on Plasma Physics (Stockholm, 2012)

and in the following graduate summer schools:

1. Erasmus Intensive Programme: Applications of Electronics in Plasma Physics (Crete, 2010), and
2. High Energy Density Physics Summer School (San Diego, 2011).

ACKNOWLEDGMENTS

This PhD thesis has been an amazing three-year trip with people in every station that I would like to thank now.

The itch for research does not come alone but someone should introduce you to this awesome world. In my case, I have to go back some years in time to find that person in my German experience in the Karlsruhe Institute of Technology. There, Manuel Garcia-Villalba showed me the path to research. Going back to Spain, I went to the industry. In the farewell he told me: “I bet you’ll come back. I did”. He was right.

I came back and I began this PhD thesis. Beginnings are usually hard, plenty of changes, especially when they are abroad. I would like to thank those persons who make first steps in Cheeseland easier for me. In a professional frame, much was the help that Virginie Saavedra gave to me. In a personal frame, I will never forget the warm welcome of Maurice, Edith and Corinne. From the very first day, I was already part of the family. I continued with happiness the son-in-law tradition.

I would like to express my deep gratitude to Javier Sanz. Javier has transmitted to me the passion for research, the shrewdness to look for the fundamentals, to decompose inaccessible problems in complex but pure ones, to non-stopping search elegant and analytic insights. He loves science and physics. And now, me too.

I would also like to thank my French supervisors, Vladimir and Marina, who have always been there for all my questions, who have always been patient to explain me the tricky points of fusion physics.

I continue to list (sorry if I forget anyone) all the persons in CELIA lab that has contributed to make this three years nicer; the permanents Jerome, Jean-Luc, Xavier, Edouard, Guillaume, Gerard, Philippe, Loic, Rachel..., the PhD students Jessy, Céline, Marion, Candice, Cyril, François, Benjamin, Mickael, Remi, Alexandra..., my office mates Igor, Marie and Thibault and the secretaries Céline, Fabienne and Emmanuelle, always ready to help me with any paper stuff.

I sincerely thank all the members of the Applied Physics department of the School of Aeronautics in Madrid for their kind welcome to my stays there and the fruitful coffee break discussions. A special thanks to the secretary Maricarmen that has helped me so much with the administration stuff.

I would also like to thank the reviewers, Riccardo Betti and Serge Bouquet, for their time dedicated to careful reading this manuscript and all their valuable comments and suggestions that have definitely improved the text.

Friends are always there, sharing all the moments, joyful and sorrowful ones. Thank you, Gerardo. Thank you, David. We will continue redoing the world.

In all my life steps, there are always some constant references of love and affection, of hard-working and peaceful enjoyment. They come from my mom, dad and sister. Simply, thank you. I am what I am because of you.

And last but not least (not at all), some words to my sweetheart, my beloved wife. You know you are the core of my life. Thanks for supporting me and staying at my side... And there is a new arrival while preparing this text, my new born daughter Lou-Andréa. What to say about her? You are now the sun of our days (and the storm of our nights!).

ABSTRACT

The Rayleigh-Taylor instability is a major issue in inertial confinement fusion capable to prevent appropriate target implosions [20]. In the direct-drive approach, the energy deposited by directed laser irradiation ablates off the external shell of the capsule (ablator) into a low-density expanding plasma. This induces a high pressure around the ablating target surface (ablation region) that accelerates the capsule radially inwards. This situation, a low density fluid pushing and accelerating a higher density one, is the standard situation for the development of the Rayleigh-Taylor instability, and therefore a potential source of target compression degradation.

Actual target capsule designs comprise a core of thermonuclear fuel (mixture deuterium and tritium), which is enclosed by a thin layer that behaves as ablator. The choice of the ablator material that provides the best performances to achieve succesful implosions has been the object of intense reasearch in recent years. First experiences were performed using hydrogenic ablators, i.e., cryogenic deuterium and tritium with a thin plastic overcoat. The use of hydrogenic ablators is motivated by their relatively low density that permits them to achieve high ablation velocities with low in-flight aspect ratio and, therefore, exhibit good hydrodynamic stability [25, 35]. However, direct-drive cryogenic implosion experiments on the OMEGA laser facility have shown that this type of ablators presents a low threshold for the two-plasmon decay instability leading to elevated levels of hot electron preheat for ignition-relevant laser intensities [38, 30]. This excessive preheat is another source of compression degradation and implies not achieving the onset of ignition requirements on high total area densities and high hot spot temperatures. If hydrogenic ablators (low-Z material) are excluded as viable ablators, other concepts of target design need to be explored. One of these alternative target designs involves the use of moderate-Z ablators such as SiO_2 or doped plastic. Recently, the performance of this concept was tested on direct-drive implosion experiments on OMEGA [40]. In that study, the use of glass ablators (SiO_2) suggested a mitigation of target preheat for ignition-relevant laser intensities. Thus, moderate-Z materials are less affected by the TPD instability, and hence they are a potential candidate for ICF target ablators. Furthermore, experiments carried out in GEKKO XII laser facility indicated that the use of brominated plastic foils significantly reduces the growth of the RT instability

compared to an undoped plastic targets [11, 12]. This improvement in the hydrodynamic stability properties seems to be explained by the increasing importance of radiative energy transport in the ablated moderate-Z material.

For moderate-Z materials, the hydrodynamic structure of the ablation region formed by the irradiation of high intensity laser beams differs from that of low-Z materials (hydrogenic ablators). In particular, the role played by the radiative energy flux becomes non-negligible for increasing atomic number material and ended up forming a second ablation front. This structure of two separated ablation fronts, called double ablation (DA) front, was confirmed in the simulations carried out by Fujioka et al. [12]. A qualitative measure of the relative importance of radiative and material energy transport is given by the dimensionless Boltzmann number $\mathrm{Bo} = 5Pv/(8\sigma T^4)$, where σ is the Stefan–Boltzmann constant. A one-dimensional hydrodynamic radiation theory [34], in agreement with simulations [10], showed that below a critical value, Bo^*, of the Boltzmann number evaluated at the peak density ($y = y_a$), a second minimum of the density gradient scale length appears in the ablation region. This indicates the formation of a second ablation front at $y = y_e$, around the same place where radiation and matter temperatures are equal. Moreover, as the Boltzmann number decreases below Bo^*, a plateau in density/temperature develops between the two fronts. In this configuration, the energy flux in the region is practically radiation dominated. Thus, the first/inner ablation front is also called radiation ablation (RA) front. Around the second ablation front, a transition layer develops where radiative energy flux changes its sign. This ablation front is always driven by the electronic heat flux. However, the developed transition layer is as well a very strong emitter of radiation. Thus, second/outer ablation front is also called electronic-radiative ablation (ERA) front. Beyond the ERA front, almost all the incoming electron heat flux is outwardly radiated.

A linear stability theory of DA fronts is developed for direct-drive inertial confinement fusion targets. Two models are proposed. First, a sharp boundary model where the thin front approximation is assumed for both ablation fronts. The information about the corona region that permits to close the sharp boundary model is obtained from a prior self-consistent analysis of the ERA front. Numerical results are presented as well as an analytical approach for the radiation dominated regime of very steep double ablation front structure. Second, a self-consistent numerical method where the finite length of the ablation fronts is considered. Accurate hydrodynamic profiles are taken into account in the theoretical model by means of a fitting parame-

ters method using one-dimensional simulation results. Numerical dispersion relation is compared to the analytical sharp boundary model showing an excellent agreement for the radiation dominated regime, and the stabilization due to smooth profiles. 2D simulations are presented to validate the linear stability theory.

RÉSUMÉ

Le contrôle de l'instabilité de Rayleigh-Taylor ablative est crucial pour la fusion par confinement inertiel (FCI) puisque son développement peut compromettre l'implosion et la correcte compression de la cible [20]. En attaque directe, l'énergie déposée par les nombreux faisceaux laser provoque l'ablation de la couche externe de la cible (ablateur). En réaction au phénomène d'ablation, une très haute pression apparait autour de cette surface, ce qui conduit finalement à l'accélération de la cible vers l'intérieur. On se trouve alors en présence d'un fluide de basse densité (le plasma ablaté) qui pousse et accélère le fluide plus dense (l'ablateur comprimé). C'est une des situations typiques qui favorisent le développement de l'instabilité de Rayleigh-Taylor et, en conséquence, une source potentielle de dégradation de la compression de la cible.

Les cibles de FCI sont constituées d'un noyau de combustible thermonucléaire (mélange de deutérium et tritium) enfermé par une fine couche, l'ablateur. Le choix du matériau pour l'ablateur a fait l'objet d'une intense recherche ces dernières années. Les premières expériences furent réalisées avec des matériaux hydrogénoïdes (glace de deutérium et tritium, numéro atomique bas) et une fine couche de plastique. L'utilisation de ce type de matériaux est favorisée pour sa densité relativement basse qui leur permet d'atteindre de hautes vitesses d'ablation et un rapport d'aspect en vol peu élevé qui leur confère de bonnes propriétés de stabilité hydrodynamique [25, 35]. Cependant, des expériences sur l'installation laser OMEGA (Rochester, USA) ont démontré que ce type de matériaux présente un seuil suffisamment bas pour l'apparition de l'instabilité *two-plasmon decay* (TPD) avec des intensités laser significatives pour l'ignition et, par conséquent, la génération d'électrons suprathermiques qui provoquent un préchauffage excessif de la cible [38, 30]. Ce préchauffage excessif empêche d'atteindre les conditions requises de température et de densité au centre de la cible pour l'ignition. D'autres concepts de design de cible sont alors considérés comme, par exemple, l'utilisation d'ablateurs de nombre atomique modéré tels que la silice ou le plastique dopé. Récemment, les performances de ce type d'ablateurs alternatifs ont été testées lors d'expériences réalisées sur l'installation OMEGA [40]. Cette étude suggère que l'utilisation de la silice réduit le préchauffage de la cible et, en même temps, ouvre la possibilité d'utiliser des matériaux de nombre atomique modéré pour la fusion par confinement inertiel. De plus,

des expériences réalisées sur l'installation laser GEKKO XII (Osaka, Japon) indiquent que l'utilisation de plastique brominé comme ablateur réduit la croissance de l'instabilité de Rayleigh-Taylor ablative par rapport à des cibles avec des ablateurs de plastique sans dopant [11, 12]. Cette amélioration de la stabilité hydrodynamique est, en principe, expliquée par le rôle important qui joue le transfert d'énergie radiative dans la région d'ablation lors de l'utilisation d'un matériau de nombre atomique modéré.

Pour des matériaux de nombre atomique modéré, la structure hydrodynamique de la région d'ablation est différente de celle qu'on peut trouver avec des matériaux de nombre atomique bas (matériaux hydrogénoïdes). En effet, l'importance du flux d'énergie radiative n'est pas négligeable et la compétition entre celui-ci et le transfert thermique électronique fait apparaitre une structure avec deux fronts d'ablation, nommée « structure à double front d'ablation ». Cette structure fut confirmée par les simulations réalisées dans Fujioka et al. [12]. Une mesure qualitative de l'importance du transfert d'énergie radiative est donnée par le nombre adimensionné de Boltzmann $\mathrm{Bo} = 5Pv/(8\sigma T^4)$, où σ est la constante de Stefan-Boltzmann. En effet, une théorie d'hydrodynamique radiative [34] démontre qu'en dessous d'une certaine valeur critique du nombre de Boltzmann, Bo^*, évalué au maximum de densité, un deuxième minimum de la longueur du gradient de densité apparait dans la région d'ablation. Ce fait indique la formation d'un deuxième front d'ablation, autour du point où la température de la matière et la température radiative sont égales. De plus, si on diminue le nombre de Boltzmann en dessous de la valeur critique, une région de densité/température constante apparait entre les deux fronts (appelée le « plateau »). Dans cette configuration, le flux d'énergie dans le plateau est pratiquement dominé par le flux radiatif. Pour cette raison, ce premier front est nommé front d'ablation radiatif (RA). Autour du deuxième front d'ablation, une couche de transition se développe où le flux d'énergie radiative change brusquement de signe. Bien que ce soit le flux de chaleur électronique qui fournit l'énergie pour maintenir ce front d'ablation, la couche de transition est quand même un puissant émetteur de photons. Pour cela, ce deuxième front est nommé front d'ablation électronique-radiatif (ERA). Au-delà du front ERA presque tout le flux de chaleur électronique est propagé vers l'extérieur.

Cette thèse développe pour la première fois, dans le contexte de la fusion par confinement inertiel, une théorie linéaire de stabilité pour des structures à double front d'ablation. Deux modèles sont alors proposés. D'abord, un modèle de discontinuité où l'approximation de front mince est considérée

pour les deux fronts d'ablation. L'information concernant la région au-delà du deuxième front (la couronne) qui permet de fermer le modèle de discontinuité est donné par une analyse auto-consistant du front ERA. Des résultats numériques sont présentés ainsi qu'une solution analytique dans le régime radiatif où l'approximation du front mince est valable. D'autre part, une méthode numérique auto-consistant est présentée où l'épaisseur finie des fronts d'ablation est prise en compte, ce qui permet d'agrandir la liste de choix des ablateurs à analyser et le domaine d'intensité laser. Des profils plus réalistes de densité/température sont considérés dans le modèle théorique à travers une méthode d'ajustement de paramètres avec les résultats de simulations numériques. La relation de dispersion provenant de l'analyse numérique est comparée avec celle obtenue avec la méthode de discontinuité. Un excellent accord est observé dans le régime radiatif, ainsi que pour la stabilisation due aux profils d'épaisseur finie. Des simulations bidimensionnelles sont présentées afin de valider cette théorie de stabilité linéaire.

RESUMEN

La inestabilidad de Rayleigh-Taylor es crucial para la fusión por confinamiento inercial al ser capaz de impedir adecuadas implosiones del blanco [20]. En ataque directo, la energía suministrada por la irradiación directa del láser provoca la ablación de la capa externa del blanco generando así un plasma en expansión de baja densidad. Este hecho induce la aparición de una alta presión alrededor de esa superficie que acelera el blanco violentamente hacia el interior. Se llega, entonces, a una situación en la que un fluido de baja densidad empuja y acelera otro de alta densidad. Ésta es una situación típica para el desarrollo de la inestabilidad de Rayleigh-Taylor, y, por consiguiente, una fuente potencial de degradación de la compresión del blanco.

Diseños de blanco recientes incluyen un núcleo de combustible termonuclear (mezcla de deuterio y tritio) encerrado por una delgada capa, la capa ablativa. La elección del material para la capa ablativa ha sido objeto de intensa investigación en los últimos años. Las primeras pruebas fueron realizadas con materiales hidrogenoides (hielo de deuterio y tritio) y una fina capa de plástico. El uso de material hidrogenoide viene propiciado por su relativa baja densidad que les permiten alcanzar altas velocidades de ablación con una baja relación de aspecto en vuelo, y por ello, presentan una buena estabilidad hidrodinámica [25, 35]. Sin embargo, experimentos en la instalación láser OMEGA han demostrado que este tipo de materiales presenta un bajo umbral para la inestabilidad *two-plasmon decay* (TPD), lo que conlleva un precalentamiento elevado del blanco por electrones supra-térmicos [38, 30]. Este excesivo precalentamiento impide alcanzar el conjunto de requisitos de densidad y temperatura en el centro del blanco necesarios para la ignición del mismo. Por tanto, otros conceptos de diseño se han planteado en los que no se recurre al uso de materiales hidrogenoides (de bajo número atómico). Uno de estos diseños alternativos incluye el uso de materiales de número atómico moderado como el sílice (SiO_2) y plástico dopado. Recientemente, las prestaciones de este diseño han sido probadas en experimentos realizados en OMEGA [40]. En ese estudio, el uso de capas ablativas de vidrio (SiO_2) sugiere la mitigación del precalentamiento del blanco y, por tanto, abren la posibilidad de utilizar materiales de número atómico moderado para la fusión por confinamiento inercial. Además, experimentos realizados en la instalación láser GEKKO XII indicaron que el uso de plástico brominado como capa externa

del blanco reduce el crecimiento de la inestabilidad de Rayleigh-Taylor en comparación con blancos provistos de una capa ablativa de plástico sin dopar [11, 12]. Esta mejora en la estabilidad hidrodinámica parece explicarse por la creciente importancia del trasporte de energía radiativa en la región de ablación cuando se utiliza un material de número atómico moderado.

Para materiales de número atómico moderado, la estructura hidrodinámica de la región de ablación difiere de aquella que se encuentra para materiales de bajo número atómico (materiales hidrogenoides). En concreto, la importancia del flujo de energía radiativa no es despreciable y éste acaba formando un segundo frente de ablación. Esta estructura de dos frentes de ablación separados, llamada doble frente de ablación, fue confirmada en la simulaciones llevadas a cabo en 2004 por Fujioka et al. [11, 12]. Una medida cualitativa de la importancia del transporte de energía radiativa viene dado por el numero de Boltzmann $\mathrm{Bo} = 5Pv/(8\sigma T^4)$, donde σ es la constante de Stefan-Boltzmann. Una teoría de hidrodinámica radiativa aparecida en 2009 [34] muestra que por debajo de un valor crítico del número de Boltzmann, Bo^*, evaluado en el pico de densidad ($y = y_a$), un segundo mínimo en la longitud del gradiente de densidad aparece en la región de ablación. Este hecho indica la formación de un segundo frente de ablación en $y = y_e$, alrededor del punto donde la temperatura de la materia y la radiación son iguales. Además, al disminuir el número del Boltzmann por debajo del crítico, una región de densidad/temperatura constante aparece entre los dos frentes (región *plateau*). En esta configuración, el flujo de energía en el plateau está prácticamente dominado por la radiación. Por ello, este primer frente de ablación se llama frente de ablación radiativo (RA). Alrededor del segundo frente de ablación una capa de transición aparece donde el flujo de energía radiativa cambia bruscamente de signo. Aunque el flujo de calor electrónico es el que aporta la energía para mantener este frente de ablación, la capa de transición es también un potente emisor de radiación. Por ello, este segundo frente de ablación se llama frente electrónico-radiativo (ERA). Más allá del frente ERA casi todo el flujo de calor electrónico es radiado hacia el exterior.

En esta tesis se desarrolla, por primera vez, una teoría lineal de estabilidad para estructuras de doble frente de ablación aplicada a la fusión por confinamiento inercial. Dos modelos son propuestos. Primero, un modelo de discontinuidad en el que se asume la aproximación de frente delgado para ambos frentes de ablación. La información sobre la región de la corona que permite cerrar el modelo de discontinuidad es proporcionada por un análisis auto-consistente del frente ERA. Resultados numéricos son presenta-

dos al igual que una solución analítica en el régimen radiativo en el que la aproximación de frente delgado es válida. Y segundo, un método numérico auto-consistente en el que se tiene en cuenta el espesor finito de los frentes de ablación, ampliando, así, los posibles materiales a analizar para la capa ablativa y el rango de intensidades láser. Se consideran perfiles hidrodinámicos realistas en el modelo teórico a través de un método de ajuste de parámetros usando para ello los resultados de simulaciones unidimensionales. La relación de dispersión numérica se compara con la proporcionada por el modelo de discontinuidad mostrando un acuerdo excelente para el régimen radiativo, y la estabilización debida a perfiles suaves. Simulaciones en dos dimensiones se presentan para validar la teoría de estabilidad lineal.

CONTENTS

LIST OF FIGURES

LIST OF TABLES

ACRONYMS

D	deuterium
DA	double ablation
DL	Darrieus-Landau
EA	electron-conduction ablation
EM	electromagnetic
EPW	Electron plasma wave
ERA	electronic-radiative ablation
HXR	hard x-ray
IAW	Ion acoustic wave
ICF	inertial confinement fusion

IFAR	in-flight aspect ratio
LTE	local thermodynamic equilibrium
MCF	magnetic confinement fusion
NIF	National Ignition Facility
ODE	ordinary differential equation
PDI	Parametric decay instability
RA	radiative ablation
RT	Rayleigh-Taylor
RTL	radiative transition layer
SBS	Stimulated Brillouin Scattering
SRS	Stimulated Raman Scattering
T	tritium
TPD	Two-plasmon decay
WKB	Wentzel-Kramers-Brillouin

Part I

INTRODUCTION

This opening part of the thesis deals with the essential concepts that permit to tackle the core of the present research, the stability analysis of double ablation fronts. A brief overview of inertial confinement fusion (ICF) is given as well as an introduction to the Rayleigh Taylor instability and the several stabilization mechanisms that the ablation process provides. Next, a complete state-of-the-art is presented, enumerating and commenting the most relevant analytical and numerical studies of the ablative Rayleigh-Taylor instability since the first approaches to the problem in the early 1970's until nowadays. The emergence of double ablation front structures during the target implosion is due to the use of high laser intensities and moderate-Z ablators that enhance the importance of radiative transport flux in the ablation region. The choice of this type of ablators in ICF targets is discussed, and its relation to some damaging effects of laser-plasma interactions are explained through recent experiments on the OMEGA laser facility. Finally, the one-dimensional theory of double ablation front is presented. The study of the hydrodynamic profiles of double ablation fronts is a fundamental preliminary task before analyzing its stability.

... like some sweet gravity
H - Maynard James Keenan

1

SCOPE AND CONTEXT: THE INERTIAL CONFINEMET FUSION.

1.1 SCOPE OF THIS THESIS

This thesis is devoted to a hydrodynamic stability analysis of a fluid structure, which is of special interest in the inertial confinement fusion (ICF) domain. Our attention is focused on studying the linear phase of the acceleration-driven *ablative* Rayleigh-Taylor (RT) instability that may occur during the implosion of the ICF target.

The classical RT instability takes place when a light fluid pushes a heavy fluid accelerating it. This situation is unstable and any perturbation in the interface separating both fluids will grow indefinitely and break the interface up.

In ICF context, the ablation of the external surface of the target entails an *alive* interface, through which a continuous flux of mass from the heavy to the light fluid crosses. Although this fact improves the stability performance of the target, there may still appear non-uniformities in its surface that will grow subject to the ablative RT instability. This unstable growth can lead to the rupture of the shell filled with the thermonuclear fuel, making unattainable the compression requirements for the target ignition. Therefore, ablative RT instability is a major constraint that shall be understood and overcome to be able to achieve the final purpose of ICF, large-scale energy production.

1.2 WHY FUSION ENERGY

Our society needs an increasing energy supply whose covering is not assured by conventional energy sources. A cheap-petrol based economy is at risk by the continuous (since 2005) petrol barrel price rises and the envisaged reinforced controls (and consequent price increases) and even closures of actual fission thermonuclear power plants after Fukushima accident in 2011. These risks are permanent. The crisis that already happened in the past (petrol crisis in the 70s and Chernobyl accident in 1986) already

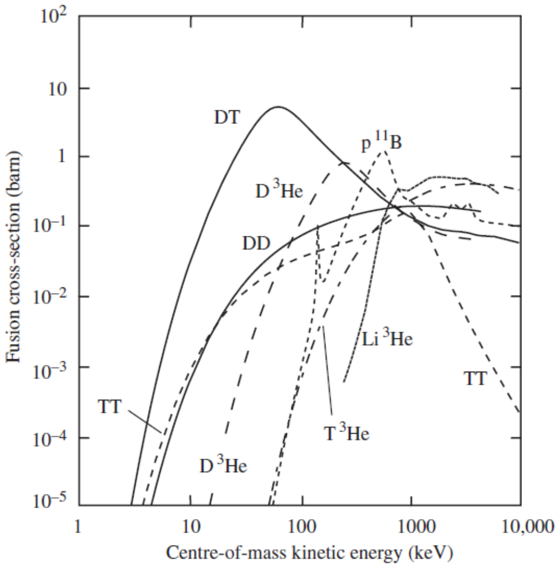

Figure 1: Fusion cross sections versus centre-of-mass energy for reactions of interest to controlled fusion energy. Figure taken from the reference [1]

alerted the governments and encouraged the research in new energy sources. A lot of effort has been (is) made in the development of *green energies* (mainly hydraulic, biomass, geothermal, wind and photovoltaics) but at the present, although they cover around 20% of global final energy consumption, it is still controversial that they could completely replace conventional sources. Another line of civil research started over 40 years ago and it is the context of this work: fusion energy. It consists in the fusion reaction of two light elements that roughly gives a heavier element and releases energy. In general and because of the higher probability the reaction to occur, measured by their fusion cross section σ (see figure 1), the fuel used is a mixture of hydrogen isotopes, deuterium (D) and tritium (T), that produces the following four exothermic reactions:

$$D + T \rightarrow^{4} He + n + 17{,}6\,\mathrm{MeV}, \tag{1}$$

$$D + D \rightarrow^{3} He + m + 3{,}3\,MeV \;\; or \;\; T + p + 4{,}0\,\mathrm{MeV} \tag{2}$$

$$D +^{3} He \rightarrow^{4} He + p + 18{,}3\,\mathrm{MeV} \tag{3}$$

Arriving to the conditions necessary to trigger these reactions requires a huge amount of power. It can be estimated with the *Lawson criterion* [19], which holds that the ignition will take place if the fuel satisfies $p\,\tau_e > f\,(T)$, where p is the pressure, τ_e is the confinement time and $f(T)$ is some function depending on the temperature. This function has a minimum f_{min} for around $T = 15\,\text{keV}$ that gives the minimum value of $p\,\tau_e$ for ignition to occur, $(p\,\tau_e)_{min} = 8{,}3\,\text{atm}\cdot\text{s}$. The immediate problem that arises is how to confine a fuel in plasma state at this so high temperature since no material can support it without melting. Two approaches to controlled fusion were, then, envisaged to fulfill these criteria. One was to maintain the fuel at a pressure of some atm. during a time of the order of the second confined by some magnetic trap. This leads to the domain of magnetic confinement fusion (MCF). The other option consists in a pulse approach where the fuel is brought to extreme conditions of pressure (Gatm), density and temperature in a very short time of the order of less than one tenths of nsec. Fuel is confined by its own inertia forces, and therefore, this technique is called inertial confinement fusion (ICF).

At first glance, fusion is a very promising way of producing energy since we can enumerate the following advantages over other energy sources:

- the abundance of the fuel (deuterium and tritium),
- the absence of waste material with a long radioactive decay time,
- it does not depend on the season or weather conditions.

Nevertheless, it remains an energy of the future which still needs a huge effort in technological development and science research. Indeed, on the way to a commercial ICF reactor there are still open crucial questions such as the scheme to get the fuel ignition or the later achievement of a high repetion rate that makes the fusion reactor economically profitable. An optimistic roadmap will take decades of years of research before we can use this energy source.

1.3 ICF BASICS

The concept of ICF is to burn few miligrams of thermonuclear fuel highly compressed (more than 1000x liquid density) in a very short time interval (∼100 ps) while the fuel is kept confined by the inertia forces. The requirement on density can be achieved by the implosion of a spherical shell by high-power supply usually delivered by laser beams. In the direct-drive approach the laser beams directly irradiate the target surface heating it up. That leads to the ablation of the outer surface of the shell and generates, by momentum conservation, the necessary pressure to drive a violent implosion. Ideally the

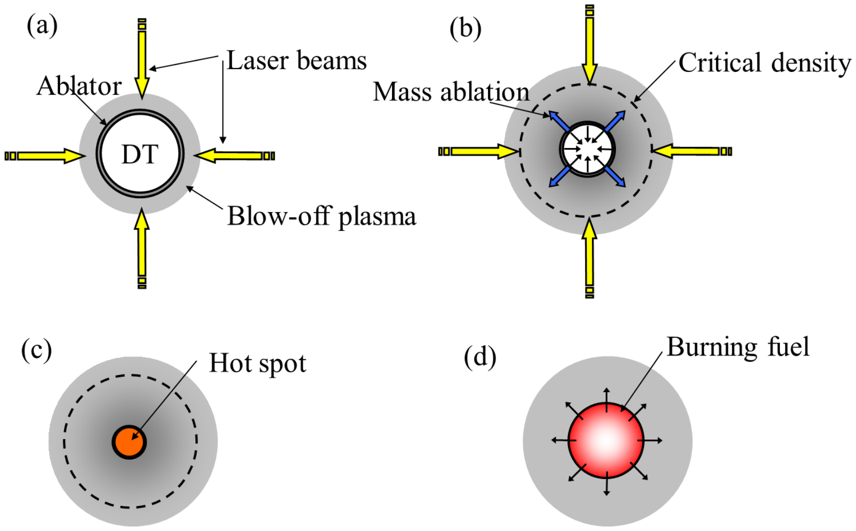

Figure 2: Four main stages of a classical direct-drive ICF scheme

implosion should be symmetric to get at the end of compression a point in the centre of the pellet (hot spot) with the required density and temperature to trigger the ignition of the fuel. Thus, schematically, the target goes through four main stages in the direct-drive approach of ICF (see figure 2) that can be enumerated as follows:

(a) irradiation,
(b) implosion driven by ablated material,
(c) hot spot ignition and
(d) burning and explosion.

In this thesis, we will focus on a physical process that occurs during the implosion phase, which is the unstable growth of perturbations at the shell external surface. At the begininng of the target implosion, this surface is not perfectly spherical but already has a certain level of distortion mainly due to inhomogenities of the laser irradiation or inherent fabrication defects. During the target implosion phase, the compressed material is continuously ablated off the shell[1] into a low-density expanding plasma (the corona). Notice that the external surface of the shell is not an interface between two separated fluids but an *alive* interface that is crossed by the ablated material, it will be called hereafter *ablation front*. In the ablation front frame of reference, the blowoff plasma (light fluid) accelerates the compressed material (heavy fluid) radially inwards. This is the standard situation for the development

---

[1] The mass shell loss is characterized by the mass ablation rate, $\dot{m}$

of the Rayleigh-Taylor (RT) instability, that is to say, the unstable growth of initial distortions. This instability can prevent the achievement of appropiate implosions by considerably distorting and even breaking the target shell up. A deep understanding of this instability is mandatory for a succesful high-energy-gain target design for inertial confinement fusion [20].

1.4 CLASSICAL RAYLEIGH-TAYLOR INSTABILITY

The Rayleigh-Taylor instability is a fingering instability of an interface between two fluids of different densities, which occurs when the light fluid is pushing the heavy fluid [44, 29]. A simple possible description of the instability is as follows [36]. Imagine a box which is divided horizontally by a flat and rigid foil into two equal subboxes. The upper subbox is filled with water and the bottom subbox with air. At a given time, we take the separating foil away and see how the system develops. Obviously, the air will rise and the water will fall inversing their positions, but this will not happen because of lack of support from the air to the water. The pressure of the air is sufficient to hold the water in the upper part of the box provided that air-water interface is kept completely flat. Nevertheless, we will never have this interface of perfect flatness; no matter how carefully we have removed the foil, there will be some deviation from planarity by some small amount. Those portions of the fluid which lie higher than the average experience more pressure than is needed for their support. They begin to rise, pushing aside water as they do so. A neighboring portion of the fluid, where the surface hangs a little lower than average, will require more than average pressure for its support. It begins to fall. The air cannot supply the variations in pressure form place to place necessary to prevent the interface irregularities from growing. The initial perturbations therefore increase in amplitude, exponentially with time at the beginning. The water which is moving downward concentrates in spikes. The air moves upward through the water in bubbles. The water falls to the bottom. The configuration of the system air-water resulting from the instability process has a lower potential energy than initially. The Rayleigh-Taylor instability is then a process by which fluids seek to reduce their combined potential energy.

This instability was first described in 1883 by Lord Rayleigh [29] who studied the stability of fluids at rest with density increasing upwards In 1950, G. I. Taylor [44] generalized Rayleigh's results recognizing the essential ingredient of the instability, that the acceleration producing instability must be directed from the lighter fluid towards the denser. It is relevant in many physical domains as astrophysics (supernovae collapse), oceanography and meteorology and also in technological applications as the subject of this thesis, inertial confinement fusion.

1.4.1 *Phenomenology of the RT instability.*

The phenomenology associated with the evolution of a RT unstable interface is rather complex. Sharp [36] gave a helpful description organizing the instability development into a number of stages as follows:

A. *Stage 1.* If the initial perturbations in the interface or velocity field are sufficiently small, the early stages in the development of the instability can be analyzed using the linearized form of the fluid mechanics equations. The result is that small amplitude perturbations of wavelength λ grow exponentially in time. Linear theory begins to fail when the amplitude of the inital perturbation grows to a size of order 0.1λ to 0.4λ.

B. *Stage 2.* During the second stage, while the amplitude of the perturbation grows nonlinearly to a size of order λ, the development is strongly influenced by three-dimensional effects and the value of the Atwood number $A_T = (\rho_H - \rho_L) / (\rho_H + \rho_L)$, where ρ_H and ρ_L are the density of the heavy fluid and light fluid, respectively. If $A_T \lesssim 1$, the light fluid moves into the heavy fluid in the form of round topped bubbles with circular cross sections. The heavy fluid will form spikes and walls or curtains between the bubbles, so that a horizontal section would show a honeycomb pattern. If $A_T \gtrsim 0$, one will instead find a pattern more like two sets of interpenetrating bubbles.

C. *Stage 3.* The next stage is characterized by the development of structures on the spikes and interactions among the bubbles. The Kelvin-Helmholtz instability[2] along the side of the spike can lead to a mushroom shape, increasing the effect of drag forces on the spike. Also, bubble amalgam can develop, a process in which large bubbles absorb smaller ones, with the result that large bubbles grow bigger and move faster.

D. *Stage 4.* In the final stage, we encounter a series of complicated behaviours like the breakup of the spike that leads to a regime of turbulent or chaotic mixing of the two fluids.

---

[2] The Kelvin-Helmholtz instability occurs at the shear layer between two fluids with oppositely directed velocities.

1.4.2 *Linear growth of the RT instability*

In this thesis we are interested in the first stage of the RT instability development, where the growth of perturbations can be analyzed by means of a linear theory. In this paragraph, as an illustrative example, we examine the simplest flow configuration subjected to RT instability in its linear phase.

Let us take two infinitely extended inviscid fluids separated horizontally by a plane interface of negligible width located at the origin of coordinates. The fluids are considered initally at rest with zero velocity, with the upper fluid being the heavier ($\rho_H > \rho_L$). The fluids support a constant acceleration field, g, in the vertical direction normal to the interface, acting downwards. At a given time (e. g. $t = 0$), the interface is slightly perturbed with a sinusoidal perturbation of semi-amplitude ξ. The study consists in determining how these perturbations grow in time, so, actually, we will solve an *Initial Value Problem*.

1.4.2.1 *Unperturbed problem: the equilibrium state*

The unperturbed problem is steady and only depends on the direction of the gravity field. The resolution of this problem defines the pressure profiles (p) in the fluids. The governing equation is the momentum conservation in the vertical y-axis that reads

$$0 = -\nabla p + \rho \vec{g} \Rightarrow \frac{dp}{dy} = \begin{cases} -\rho_L g & \text{for } y < 0, \\ -\rho_H g & \text{for } y > 0. \end{cases} \tag{4}$$

1.4.2.2 *Perturbed problem: the stability analysis*

Any hydrodynamic quantity (density, velocity, pressure...) is expanded into a steady component issued from the equilibrium state and a small perturbation in the form $\psi = \psi_0(y) + \psi_1(x, y, t)$ where $|\psi_1| \ll |\psi_0|$ and the subscripts 0 and 1 refer to the unperturbed and perturbed state, respectively. Note that two-dimensional disturbances are assumed. The evolution equations for the perturbations are obtained by introducing the expanded hydrodynamic quantities into the mass and momentum conservation equations, and substracting the equations of the equilibrium state. The resulting equations are non-linear in the perturbation. In order to study the first stage of the RT instability development, we use a linearized form of the hydrodynamic equations, neglecting terms of order two and greater in the perturbation. For simplicity, we suppose the fluid to be irrotational and incompressible. The irrotational condition implies that the curl of the perturbed velocity is zero, $\bigtriangledown \times v_1 = 0$, so that it can be derived from a potential function ϕ_1 in the way $v_1 = \bigtriangledown \phi_1$. The incompressibility condition of the fluid means $\rho_1 = 0$. Under these assumptions, the continuity equation in each region is reduced to the laplacian of the velocity potential,

$$\bigtriangledown^2 \phi_1 = 0, \tag{5}$$

and the momentum equation reads

$$\rho_0 \frac{dv_1}{dt} = - \bigtriangledown p_1. \tag{6}$$

Because the coordinate x is homogeneous and the system is linear, it is possible to work in wavenumber space and consider the behaviour of a single Fourier component. The equations for the single Fourier component are found by taking the Fourier transform in the horizontal (x) direction

$$\Psi_{1k}(k, y, t) = \mathcal{F}(\psi_1) = \int_{-\infty}^{\infty} \psi_1(x, y, t) e^{-ikx} dx, \tag{7}$$

where k is the wavenumber of perturbation. If we want to analyze the evolution of perturbations for *long times*, we can apply the Laplace transform

$$\Psi_1(k, y, \sigma) = \mathcal{L}(\Psi_{1k}) = \int_0^{\infty} \Psi_{1k}(k, y, t) e^{-\sigma t} dt, \tag{8}$$

where σ is the Laplace variable. The notation used in this section names the physical quantity with a lower-case letter, its Fourier transform with a capital letter with a subscript k and the Laplace transform with a capital letter. It is useful to recall the properties of the derivative for the Fourier-Laplace transform

$$\begin{gathered} \mathcal{F}(d\psi_1/dx) = ik\Psi_{1k}, \\ \mathcal{L}(d\Psi_{1k}/dt) = \sigma\Psi_1 - \Psi_{1k}(k, y, 0). \end{gathered} \tag{9}$$

The Laplace and Fourier transforms take the resolution of problem to the $k - \sigma$ phase space. In this phase space, equations (5) and (6) read

$$(D^2 - k^2)\Phi_1 = 0, \tag{10}$$

$$\rho_0 \left(\sigma V_x - V_{xk}(k, y, 0)\right) = -ikP_1, \tag{11}$$

where $D \equiv d/dy$ and $V_x = ik\Phi_1$. Note that we can recover the physical space by applying the inversion of the Laplace and Fourier transforms. The choice of $k \in \mathbb{R}$ and $\sigma \in \mathbb{C}$ is known as the *temporal problem* where the spectral structure of the wavelike perturbation is unchanged and the amplitude of wave grows or decays as time progresses.

The solution of the above equations in each region reads

$$\Phi_1 = C_1 e^{ky} + C_2 e^{-ky}, \tag{12}$$

$$P_1 = \rho_0 \left(\sigma \Phi_1 - (ik)^{-1} V_{xk}(k, y, 0) \right), \tag{13}$$

where the constants C_1 and C_2 are determined with boundary conditions.

1.4.2.3 *Boundary conditions*

The Rayleigh-Taylor instabililty is assumed to be localized in the interface between two fluids. This implies the first set of boundary conditions that state that at any moment the perturbation cannot blow up away from the interface, that is to say, the perturbed quantities shall be bounded in the limits $y \to \pm\infty$. We can particularize the velocity potential for each region

$$\begin{array}{lll} \text{Region L)} & y < 0 & \Phi_1 = A e^{ky}, \\ \text{Region H)} & y > 0 & \Phi_1 = B e^{-ky}, \end{array} \tag{14}$$

where the unbounded modes for $y \to \pm\infty$ have been removed ($C_{1H} = C_{2L} = 0$).

Other boundary conditions concern the interface between two fluids. In particular, the vertical velocity and the pressure shall be continuous at $y = 0 + \xi(x, t)$, where ξ is the semi-amplitude of the surface disturbance and $|\partial_x \xi| \ll 1$. We will denote with the superscript "-" a point situated just below the interface surface, and with the superscript "+" a point just above it. With this notation, the boundary conditions at the interface or *matching conditions* read

- Velocity continuity

$$\partial_t \xi = \partial_y \phi_1^- = \partial_y \phi_1^+, \tag{15}$$

- Pressure continuity

$$\begin{aligned} & p_1(0^+ + \xi) = p_1(0^- + \xi) \\ & \Rightarrow p_1(0^+) + \xi \left(\partial_y p_0\right)_{y=0^+} = p_1(0^-) + \xi \left(\partial_y p_0\right)_{y=0^-}. \end{aligned} \tag{16}$$

1.4.2.4 *Dispersion relation*

The non-homogeneous system of equations (15)-(16) can be solved, after applying Fourier-Laplace transform, for the unknowns A, B and $\Xi \equiv \mathcal{L}\left(\mathcal{F}\left(\xi\right)\right)$. This leads to

$$\Xi = D_R^{-1}\left(\sigma\Xi_k(k,0) + \frac{i}{(1+r_D)}\left(V_{xk}(k,0^+,0) - r_D V_{xk}(k,0^-,0)\right)\right), \tag{17}$$

$$A = k^{-1}\left(\sigma\Xi - \Xi_k(k,0)\right), \quad B = -A, \tag{18}$$

where $D_R \equiv \sigma^2 - A_T k g$ and $r_D = \rho_L/\rho_H$. The inverse Laplace transform of (17)-(18) gives us the time evolution of each Fourier component. In order to calculate it, we turn to its definition that reads

$$\Psi_k(y,t) = \frac{1}{2\pi i}\lim_{R\to\infty}\int_{c-iR}^{c+iR}\Psi\exp\left(\sigma t\right)d\sigma. \tag{19}$$

It is a complex integral (in the σ-plane) with a path of integration along a vertical line (Re(σ)$=c$), so that c is bigger than the real part of σ corresponding to the singularities of the integrand (see figure 3). We integrate equation (19) for the Fourier-Laplace transform of the semi-amplitude of the perturbation (Ξ) by using the theory of residues. This theory states that

$$\lim_{R\to\infty}\int_{c-iR}^{c+iR}\Psi\exp\left(\sigma t\right)d\sigma = 2\pi i\text{Res}\left(\Psi\exp\left(\sigma t\right)\right), \tag{20}$$

where Res () refers to the residue of the function in its singularities. In this case there are two single poles $\sigma = \pm\sqrt{A_T k g}$, given by $D_R = 0$. The existence of *single poles only* indicates that the time response of each Fourier component to an initial excitation exhibits exponential growth, $\exp\left(\gamma t\right)$, where γ is the value of σ at the pole. The Fourier component $\Psi_k(y,t)$, for $t > 0$, reads

$$\Psi_k(y,t) = F_k(0)\exp\left(\sqrt{A_T k g}t\right) + G_k\left(0\right)\exp\left(-\sqrt{A_T k g}t\right), \tag{21}$$

where

$$F_k(0) = \frac{1}{2}\left(\Xi_k(k,0) + \frac{i}{\sqrt{A_T k g}(1+r_D)}\left(V_{xk}(k,0^+,0) - r_D V_{xk}(k,0^-,0)\right)\right), \tag{22}$$

$$G_k\left(0\right) = \frac{1}{2}\left(\Xi_k(k,0) - \frac{i}{\sqrt{A_T k g}(1+r_D)}\left(V_{xk}(k,0^+,0) - r_D V_{xk}(k,0^-,0)\right)\right). \tag{23}$$

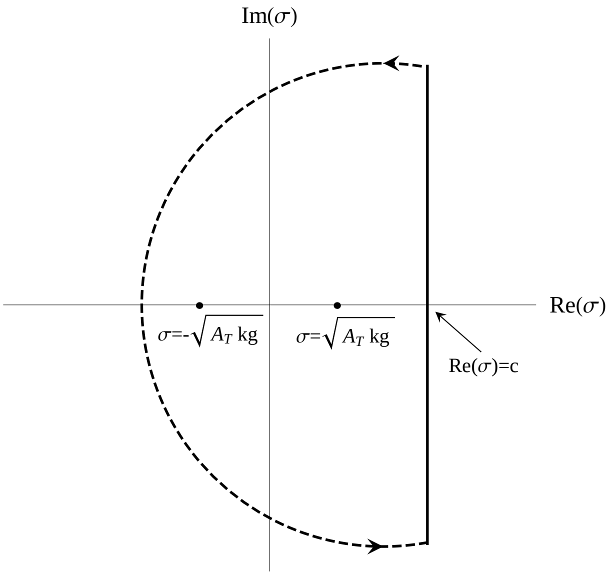

Figure 3: Integration path for calculating the inverse Laplace transform.

This can be an arduous calculation for more complex configurations. For simplicity, assuming that the singularities of the Fourier-Laplace transform are only single poles, we will solve an equivalent problem by directly considering a wavelike disturbance of the form $\psi_1(x,y,t) = \psi_1(y)\exp(ikx)\exp(\gamma t)$ for each perturbed quantity. Thus, we arrive from the matching conditions (15)-(16) to the following homogeneous system of linear equations with three unknowns, two coming from the velocity potential (A and B) and the semi-amplitude of the perturbed interface, ξ.

$$\begin{pmatrix} -k & 0 & \gamma \\ 1 & 1 & 0 \\ -\gamma\rho_L & \gamma\rho_H & (\rho_H-\rho_L)\,g \end{pmatrix} \begin{pmatrix} A \\ B \\ \xi \end{pmatrix} = 0 \tag{24}$$

The homogeneous system of linear equations (24) has a solution different from the trivial one ($A = B = \xi = 0$) if the determinant is zero, i. e., if

$$\begin{vmatrix} -k & 0 & \gamma \\ 1 & 1 & 0 \\ -\gamma\rho_L & \gamma\rho_H & (\rho_H-\rho_L)\,g \end{vmatrix} = 0. \tag{25}$$

Then, the system has *infinitely many solutions*, that is to say, we can find a solution for any value of the semi-amplitude of the perturbation provided that we are in the linear regime, $\xi \ll 2\pi/k$. Equation (25) imposes a relation between the growth rate of perturbation and its wavenumber that reads

$$\gamma = \pm\sqrt{A_T k g}, \tag{26}$$

where A_T is the Atwood number, $A_T = (\rho_H - \rho_L)/(\rho_H + \rho_L)$. This relation (that is equivalent to $D_R = 0$) will be called *dispersion relation* and it defines the growth rate (units of the inverse of time) of a perturbation for a given wavelength (units of the inverse of length) and a given equilibrium state. In this case the equilibrium state is defined with the Atwood number and the value of the vertical acceleration. There are two roots of the growth rate, one negative which is quickly damped with time and one positive which is the unstable one.

The dispersion relation for the RT instability states that if the equilibrium state is infinitesimally disturbed by a perturbation of wavelength $\lambda = 2\pi/k$ and initial semi-amplitude ξ_i, this perturbation will exponentially grow in time in the form $\xi(t) = \xi_i \exp\left(\sqrt{A_T k g} t\right)$ until non-linear effects intervene. Any small perturbation no matter its shape will be unstable since it can described by linearity as a sum of sinusoidal single-mode perturbations, $\xi(x,t) = \sum_{k=0}^{\infty} (\xi_k)_i \exp(ikx) \exp\left(\sqrt{A_T k g t}\right)$ which are all unstable in time.

1.4.2.5 *Note on the mathematical method*

In the preceding paragraphs we have seen how, instead of studying an Initial Value problem, it is solved an eigenvalue problem (where the eigenvalue is the complex growth rate γ) that leads to a dispersion relation and, therefore, defines the behaviour of the solution for long times. This is a general method for linear problems that is applied in plasma physics and other domains. In spite of the simplicity for solving the linear phase of the RT instability of an inviscid fluid, the method has some caveats and it is worth considering it in more detail.

Let $\psi(x,y,t)$ be a physical magnitude that obeys an evolution equation $P(y) \cdot \psi(x,y,t) = 0$, where $P(y)$ is a linear operator that depends on the variable y and acts over the variables x, y and t. The problem is reduced to find $f(x,y,t)$ that fulfills the initial condition $f(x,y,0) = \varphi(x,y)$ and verifies certain physical boundary conditions. We take the Fourier transform for the spatial coordinates (except y) and the Laplace transform for the temporal coordinate. Then, when computing the inverse Laplace transform, we obtain in general for each Fourier component an expression as follows

$$\Psi_k(y,t) \propto \int_{c-i\infty}^{c+i\infty} \frac{h(y)\cdot\varphi_k(y)}{D_R(\sigma,k)} \exp\left(\sigma t\right) d\sigma. \tag{27}$$

The solution of the inverse transform may not be easy to compute. However, in simple cases, the behaviour for long times is determined by the poles of the integrand. Also, by the roots of the following equation

$$D_R(\sigma,k) = 0, \tag{28}$$

that is called dispersion relation. If γ is the $\sigma-$value of a simple root of the dispersion relation, then, according to the Laplace transform theory, $\Psi_k(y,t) \propto \exp(\gamma t)$. Nevertheless, the inverse Laplace transform may be much more complex to compute, especially if *branch points*[3] exist, that can lead, for example, to solutions of the form $t^{-1/2}\exp(\gamma t)$. In other words, even if an Initial Value problem can be reduced to a system of differential equations with coefficients that do not depend on time, the solution not always has an exponential form $\exp(\gamma t)$. This fact is rigorously treated in the work by Ott and Russell [26] where the authors study a diffuse-boundary RT instability. It is shown there that, for density profiles decreasing monotonically with y, the RT instability exhibits essentially different behavior above and below a certain critical wavenumber, k_{crit}. For $k > k_{crit}$ the growth of the response to an initial perturbation is slower than exponential (solutions associated to branch points), and for $k < k_{crit}$ an unstable eigenmode (analogous to that in the sharp boundary case) exists, and purely exponential growth occurs.

The method consists then, in simple cases, not to solve an Intial Value problem but the eigenvalue problem of computing the solutions of the equation $D_R(\sigma,k) = 0$. Sometimes it is not possible to find $D_R(\sigma,k)$ in an eigenvalue problem (for example, there are more unbounded modes that one can remove). The solution is apparently the trivial solution, but this is wrong. In these cases, we have to return to the Initial Value problem, whose resolution would lead to temporal solutions that are not purely exponential in time. In contrast, when there is compatibility in the number of modes, we look for physical solutions, bounded in the spatial domain, by solving the equation $D_R(\sigma,k) = 0$ in a certain region of the complex plane σ.

---

[3] A branch point of a multi-valued function is a point such that the function is discontinuous when going around an arbitrarily small circuit around this point.

1.5 MECHANISMS OF ABLATIVE STABILIZATION

We have just seen that the classical RT instability affects all the possible perturbation wavelengths, being the unstable growth faster for smaller wavelengths. Nevertheless, in inertial confinement fusion, we do not find the surface interface separating two fluids as it is assumed above in the frame of the classical RT instability, but, instead, an ablation front which is continuously crossed by mass ejection (the ablation process). The effect of this flux of ablated mass is stabilizing, and it can damp and even suppress the unstable growth for certain wavelengths. Although this stabilization makes the ablative RT instability not so dramatic as in the classical case, it can still be dangerous and lead to the target shell breakup. In this paragraph, we try to give a qualitative overview of the different stabilization mechanisms that are found due to the ablation process in the target surface.

- Restoring force. The dynamic pressure effect

This is the dominant ablative stabilization mechanism in steep ablation fronts (for instance in DT fronts) and it is due to a reaction in the dynamic pressure[4] that tends to equilibrate the gravity force (see figure 4). It is also known as the *rocket effect*. In a corrugated ablation front all fluid elements on the front stay at the same temperature (the front is an isotherm), but the temperature gradient as well as the energy flux behind the front depend on the position. In this way, a fluid element on the crest (toward the hot region) and a fluid element on the valley of the perturbation (toward the cold region) are at the same temperature but the temperature gradient is different, in particular, it will increase on the crests. There is a variation of the local temperature gradient. This fact produces an enhancement of the dynamic pressure due to the increase of the fluid velocity behind the front. Analogously, in the valleys we find a decrease of the dynamic pressure. We can see the rocket effect as an "overpressure" generated on the peaks of the perturbation and an "underpressure" on the valleys that tends to relax the disturbance. This mechanism leads then to a self-regulating restoring force that can inhibit the instability. The nature of the ablation driving energy flux will determine if the stabilization is effective for long or short perturbation wavelengths. The rocket effect usually yield to the suppression of the instability for short wavelengths.

- Fire polishing effect

---

[4] The dynamic pressure Q is defined as $Q = P + \rho V_a^2$, where P is the static pressure and V_a the ablation velocity.

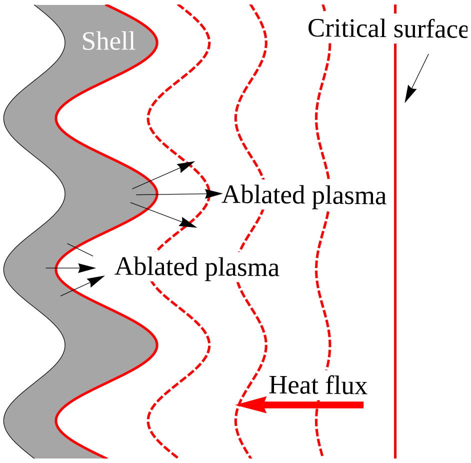

Figure 4: Schematic of the rocket effect. Red lines (solid and dashed ones) are isotherms.

The fire polishing effect is the physical removal of the perturbation through ablation. The RT instability is localized within the ablation front, i.e., in the density jump, but this unstable region is continuously being ablated off the shell and the ablation front moves inwards to regions of the shell that are less perturbed. We can roughly see the quantitative effect of this stabilization as follows (see figure 5). Let us consider an inviscid and incompressible fluid representing the shell. The perturbed velocity inside the shell will be proportional to $v_1 \propto \exp{(ky)} \exp(\gamma_{cl} t)$, where the origin of coordinates is taken at the ablation front at the initial time and a classical growth rate is assumed, $\gamma_{cl} = \sqrt{A_T k g}$. The ablation front moves inwards with a velocity called *ablation velocity* (V_a). If we fix the frame of reference to the moving ablation front, the coordinate transformation will read $y' = y + V_a t$, where y' is the spatial coordinate in the new frame of reference. Then, the perturbed velocity takes the form $v_1 \propto \exp{(k (y' - V_a t))} \exp(\gamma_{cl} t) = \exp{(ky')} \exp((\gamma_{cl} - kV_a)\, t)$. The fire polishing effect represents a reduction in the unstable growth rate, and the dispersion relation taking into account only this stabilization effect is approximately

$$\gamma = \sqrt{A_T k g} - kV_a. \tag{29}$$

- Vorticity convection effect

The ablation process across a corrugated front involves vorticity convection through the light ablated plasma. This vorticity has also a stabilizing effect.

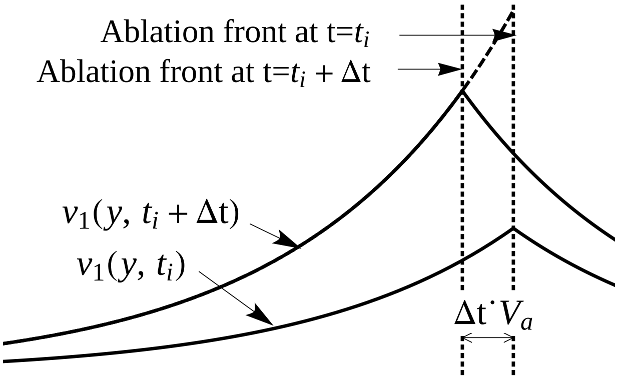

Figure 5: Schematic of the fire polishing effect. Diagram of the perturbed velocity at two different time steps.

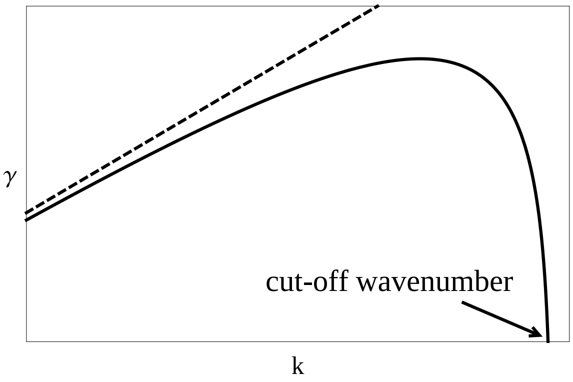

Figure 6: Dispersion relation for the ablative RT instability (solid line) and the classical RT instability (dashed line). It is a logarithmic plot.

These three effects usually affect the disturbance evolution for short wavelengths, yielding the suppression of instability beyond a characteristic wavenumber which is called a *cut-off wavenumber* (see figure 6). A perturbation with a wavenumber larger than the cut-off wavenumber will be completely damped due to the different mechanisms of ablative stabilization.

2

STATE OF THE ART: THE LINEAR ABLATIVE RAYLEIGH-TAYLOR INSTABILITY

THE study of the linear phase of the ablative RT instability in the context of inertial fusion started over 35 years ago. It is difficult to summarize all the related research papers on this field. Nevertheless, in this section a global overview will be given and some fundamental papers that has contributed to the understanding of this physical processes will be outlined.

2.1 FIRST APPROACHES TO THE TOPIC (1974-1993)

1974 can be considered the starting year of research about the ablative RT instability in ICF. This year several papers were published that reveal two fundamental ways of attempting the hydrodynamic analysis of this instability.

First, we can mention some *numerical self-consistent analysis* (Shiau et al. [37], Henderson et al. [15], Brueckner et al. [7]). The study of the flow stability with a self-consistent model resolves any hydrodynamic quantity into a zero-order component and a small perturbation (first-order component), both of them governed by the same basic equations. We start by analyzing the zero-order variables, that will be used later on as the background flow. Next, through linearization of the basic equations, we obtain a new self-consistent set of equations for the spectral components of the perturbations. The zero-order quantities appear as coefficients in these perturbed equations. The resolution of this set of equations leads, finally, to the linear growth rate of the ablative RT instability. The three papers mentioned above attempt the resolution through an *initial-value-problem* approach, that is to say, solving the temporal problem of the perturbations. They conclude that ablative flow stabilizes the RT instability, but the stabilization mechanisms stay unclear.

Second, Bodner published a *sharp boundary model* [5] this year. Sharp boundary models have been a line of intense research. They are based on the assumption of the ablation surface as a zero-thickness interface and homogeneous flow at both sides of it. Problem is not mathematically closed by imposing only conservation laws across the ablation surface, but some additional information in the way of a closing assumption may be introduced. The selection of the closing equation defines the physical validity of the model. This lack of information mainly concerns the outer region of the flow, the near-corona region. In this paper, Bodner introduced the concepts of possible stabilization mechanisms affecting the ablative RT instability: convective flux and fire polishing effect. The latter was presented as follow, "as the Rayleigh Taylor instability grows, the peaks will be closer than the valleys to the laser deposition surface. The temperature gradients will thus be larger and the ablation faster at the peaks". An approximate expression was suggested for the convective stabilization, $\gamma = \sqrt{kg} - kv_0'$, where v_0' is the velocity of the heavier fluid in the background state. Bodner stated that the size of the stabilization depends on details of the thermal conductivity near the ablation surface, but without providing any scaling law about this phenomenon. The closure equation that Bodner assumed in this paper is a definition of the perturbation semi-amplitude ξ as $\tilde{p}'(\xi) + \rho_0' g \xi = \beta p_0'(0)\, \xi / L$ where L is a scale length, the tilde quantities are perturbed ones and the prime denotes the heavier fluid. This model lies then on the unknown constant β, that Bodner says depending on the unspecified details in the energy transport. Together with the RT type unstable roots, Bodner found another one, $\gamma = g/v_0'' - kv_0''$ where double prime denotes the lighter fluid. The physical mechanisms behind this mode was unknown.

During the next years, the choice of the closing assumption was a major point of controversy. In 1978, Baker continued the study by Bodner by suggesting improvements on the closing assumption [2]. He found that Bodner's model failed actually in the closing assumption. This assumption leads to a pressure imbalance at the boundary, that is the origin of the unknown unstable root reported by Bodner. In his words "we conclude this mode should not be seen at physical circumstances, for such a pressure imbalance would be quickly removed by sound waves". Sharp boundary models continued to be a source of reasearch in the 1980's. Outstanding papers are those by Manheimer and Colombant [23] in 1984 and Kull and Anisimov [18] in 1986.

A step forward in the numerical resolution of the stability problem was given by Takabe et al. [42, 43] in the mid 1980's. Takabe developed a mathematical method for self-consistent analysis of localized unstable modes, reducing the linearized equations into a five-coupled first-order differential equations system. The linearized fluid equations are solved as an *eigenvalue problem* instead of as an inital-value problem. The eigenvalue is the linear growth rate of the perturbation, γ. The first paper [42] deals with the explanation of the method used in the stability analysis. The background flow considered there is the stationary solution of the governing hydrodynamic equations (one-fluid one-temperature model) in spherical geometry. The five eigenmodes arising from the linearized perturbed system correpond to one convective mode, two thermal conduction modes and two surface modes. Takabe performed in the second paper [43] a systematic study of the relation dispersion varying two parameters,

- the dimensionless acceleration G, and
- the density rate $R_\rho = \frac{\rho_a}{\rho_s} = \frac{\text{density at ablation front}}{\textit{density at sonic point}}$,

in order to find a suitable fitting of the dispersion relation curves, $\gamma = \gamma(k, G, R_\rho)$ in its dimensionless form. He arrived to an expression, that takes his name (the *Takabe formula*), in the following dimensional form:

$$\gamma = \alpha\sqrt{kg} - \beta k v_a, \tag{30}$$

where v_a is the flow velocity across the ablation front in the frame moving with the ablation front, and α and β are two dimensionless parameters, $\alpha = 0.9G^{-0.02}$ and $\beta = 3.1G^{-0.2}\left(R_\rho/50\right)^{0.075}$. The dependence of α and β on G and R_ρ is very weak, therefore, they can be taken as constant, and the Takabe formula is reduced to its simplest form $\gamma = 0.9\sqrt{kg} - 3.1kv_a$. This result essentially indicates the enhancement of the stabilizing flow effect by a factor 3 compared to the results by Bodner [5]. This expression was found to agree quite well with the availabe two-dimensional simulations in the classical transport regime.

In 1989, Kull [17] published a numerical self-consistent model with the aim of covering a broader range of cases . The difference with Takabe's work lied in the underlying steady-state assumptions. Actually, Kull model is incompressible and based on a steady ablation front only, while the compressible Takabe model assumes steady-state conditions up to the sonic point region. Kull arrived to a one-parameter family of dimensionless growth curves of the form

$$\gamma = \gamma\left(k, \Gamma\right), \tag{31}$$

where $\Gamma = g\frac{\chi_1}{v_1^3}$, g is the slab acceleration, χ_1 the local value of the thermal diffusivity and v_1 the ablation velocity. In Kull words, "the compressible steady-flow conditions are much more restrictive and are actually found limited to a narrow parameter range $\Gamma \approx 0.1 - 0.2$. Within the incompressible approximation steady ablation fronts can exist for arbitrary Γ and one can therefore extend previous results both toward the convective ($\Gamma \ll 1$) and the diffusive ($\Gamma \gg 1$) regime."

2.2 THE FIRST ANALYTICAL SELF-CONSISTENT THEORIES (1994)

At that time, although much effort was spent in the preceding two decades, there was no clear understanding of the linear phase of the ablative RT instability in plasmas yet. Several issues were still conjectures, such as the stabilization mechanisms (the convective stabilization and fire-polishing effect had been proposed). A quantitative description of the ablative RT instability was only given by the Takabe formula, that is no more than a numerical fitting of prior experimental results and numerical simulations. Answers will come from the theory. In particular, two studies are published this year (1994) that provide for the first time the scaling laws and the stabilization mechanism. They are analytical models based on a self-consistent background flow (all the previous analytical works were based on the sharp boundary model). These models share several assumptions such as isobaric steady state around the ablation front and planar geometry. In order to be able to reach analytical solutions, steady state and perturbed eigenvalue problem are divided in different regions with characteristic scaling laws and, therefore, asymptotic techniques (for example Wentzel-Kramers-Brillouin (WKB) approximation) are used to consistently match the solutions of each region. Three regions are usually identified associated to a different variable scale length of the eigenfunction: the overdense region, the ablation front and the blow-off region.

The first paper that was published that year is by Bychkov et al. [8]. The set of linearized perturbed equations are solved, using the WKB aproximation, for two asymptotic limits, $K \ll 1$ and $K \gg 1$ where $K = k\Delta_2$ and Δ_2 is the total thickness of the ablation region. The second limit (short wavelength perturbations) is of interest since an estimate of the cut-off wavenumber is obtained. For a wide region of values of the acceleration, this cut-off wavenumber (k_{co}) is determined by the formula

$$k_{co} u_1^2 / g = (k_{co}\Delta_1)^{2/5} \frac{1 - (k_{co}\Delta_1)^{2/5}}{1 + (k_{co}\Delta_1)^{2/5}} \approx 0.13, \tag{32}$$

where $\Delta_1 = \Theta_1^{5/2} \Delta_2$ is the length scale of thermal conduction in the cold layers of the target. Analytical results from both asymptotic limits are used to derive approximate values of the coefficients of the Takabe formula (30), being $\beta = 2.5 - 3.2$ and α the square root of the Atwood number.

The second analytical self-consistent model was published by Sanz [31]. This model takes into account a finite characteristic Mach number of the flow velocity at the maximum density ρ_a, $M_a = v_a/\sqrt{p_a/\rho_a}$, that is assumed to be a small parameter, and a general power law dependence of the thermal conductivity ($\kappa \sim T^{\nu}$). The latter can roughly describe transport energy mechanisms, such as optically thick radiation, other than electronic heat conduction ($\nu = 5/2$). This model considers, on the one hand, the inner structure of a thin transition layer (ablation surface), and, on the other hand, performs in a rigorous way an asymptotic matching to both sides of it, that is to say, to a cold and adiabatically compressed zone and to a hot plasma corona where the flow reaches sonic conditions. This asymptotic matching requires the prior development of the perturbed flow variables in a power expansion with respect to two assumed small parameters: $\delta \equiv (kL)^{1/\nu}$ and $\epsilon \equiv M_a\,(kL)^{1/2\nu}$, where k is the perturbation wavenumber and L is the characteristic length of the heat conduction energy transfer. Retaining the dominant order of expansion, a dispersion relation is obtained in the following form

$$\gamma \approx \sqrt{kg\left[1 - \frac{(\rho_{av}/\rho_a)\,kd}{(kL)^{1/\nu}}\left(q_1 + \frac{q_3}{(kL)^{1/\nu}}\right)\right]} - kv_a\,(1 + f_1 + q_2)\,/2, \qquad (33)$$

where ρ_{av} is the slab average density, and the functions f_i and q_i, which depend on the coefficient ν, are the different orders of power expansion of the perturbed flux of mass and momemtum in the connection region between the hot corona and the ablation layer. Usually the factor $(1 + f_1 + q_2)\,/2$ takes a value of 2, that indicates a less stabilizing effect that the term $\beta = 3.1$ in the Takabe formula.

Among the different physical contributions to the stabilization mechanisms, two are pointed out in this work, which are:

- first, the *fire polishing effect*, the crest of the rippled ablation surface coming into the corona is evaporating more quickly than the valley, and
- second, the dominant one, which is due to heat conduction that causes "the momentum flux to increase on the crests of the rippled ablation front and decrease in the valley, damping the growth of the unstable ablation front and being able to stop it". This is the first time that the *overpressure mechanism* is proposed as a stabilization mechanism for ablation fronts.

2.3 THE BETTI AND GONCHAROV THEORY (1995/96)

Between 1995 and 1996 a series of papers by Betti and Goncharov [3, 4, 13, 14] are published describing another self-consistent analytic stability theory, which is commonly used as the reference of this field. The steady state considered here is a subsonic ablation flow, characterized by two dimensionless parameters: the Froude number $Fr = V_a^2/gL_0$ and the power index for thermal conduction ν $(\kappa \sim T^\nu)$, where L_0 is the characteristic thickness of the ablation front. The stability problem is reduced to a single fifth-order differential equation which is solved in regions of different scale lengths for the perturbation, and, then, the solutions are asymptotically matched at the boundaries of each region. This procedure leads to a unique value of the growth rate. The fifth-order differential equation can only be solved using asymtotic techniques in the limits of large or small Froude numbers (Fr $\gg 1$ or Fr $\ll 1$).

In the small acceleration regime (Fr $\gg$ 1), an approximate solution was found in the limit of long wavelength modes $(\epsilon \equiv kL_0 \ll 1)$. The presence of the small parameter makes the problem solvable by the boundary layer theory. The dispersion relation formula is written in the following form

$$\gamma = \sqrt{A_T kg - A_T^2 k^2 V_a V_{bo}} - (1 + A_T)\, kV_a, \tag{34}$$

where

$$A_T \equiv \frac{1-(\rho_{bo}/\rho_a)}{1+(\rho_{bo}/\rho_a)}, \quad V_{bo} = V_a \frac{\rho_a}{\rho_{bo}}, \quad \frac{\rho_{bo}}{\rho_a} = \mu_0\,(kL_0)^{1/\nu},$$
$$\mu_0 = \frac{(2/\nu)^{1/\nu}}{\Gamma(1+1/\nu)} + \frac{0.12}{\nu^2},$$

$\Gamma(x)$ is the gamma function and the subscript *bo* refers to a variable of the blow-off material at the distance $\sim \lambda$ from the ablation front. This formula reproduces the results by Sanz [31]. The authors claimed that in this regime the main stabilizing effects are ablation and blow-off convection.

In the large acceleration regime (Fr $\ll$ 1), the analytic theory becomes more complicated and can be carried out only in the limit for long- $(\epsilon \ll 1)$ and short-wavelength $(\epsilon \gg 1)$ modes, where the boundary-layer theory and the WKB approximation are used, respectively. In this regime, perturbations are mitigated by

(1) *ablative convection* that reduces the instability drive from $\gamma = \gamma^{drive} \sim \sqrt{kg}$ to $\gamma = \gamma^{drive} - c_2 kV_a$ $(c_2 \sim 1)$ leading to a cutoff wavenumber that scales as $k_c L_0 \sim \mathrm{Fr}^{-1/3}$,

(2) *thermal smoothing* that lowers the drive to $\gamma^{drive} \sim g/V_a \left(k^2 L_0^2\right)$ for $kL_0 \gg \mathrm{Fr}^{-1/4}$ and finite density gradient that reduces the instability drive to $\gamma^{drive} \sim \sqrt{g/L_0}$ for $1 \ll kL_0 \ll \mathrm{Fr}^{-1/4}$. This additional stabilizing mechanism is important only at short wavelengths, where the large perturbed heat flux reduces the amplitude of the temperature and density perturbations.

In line with the growth rate formulas obtained for the different asymptotic limits of the Froude number and the perturbation wavelength, they built up a fitting expression for arbitrary Froude number that reproduces the analytic results in those limits.

In the paper that ended the series by Betti and Goncharov [28], one of the limitation of these analytic models was pointed out. In their words: “Even though the analytic theory yields satisfactory results for DT, CH and Be targets, it might not be adequate for other materials such as chlorinated plastic. The hydrodynamic profiles of plastic targets with high-Z dopants are not well reproduced by the single temperature model and the dispersion relation formula cannot be applied to determine the RT growth rate”. This statement is, in fact, one of the motivations of this thesis.

2.4 FURTHER REASEARCH (1997-2007)

In this paragraph, we will focus our attention on four papers published recently that contribute in the understanding of the linear phase of the ablative RT instability in accelerated targets. First of them (reference [27]) is a sharp boundary model that manages to overcome the difficulties of the first attempts concerning the supplementary boundary condition. The sharp boundary model is a helpful tool to understand the physics underlying the ablative RT instability, despite a lack of precision in the description of the physical mechanisms (that can only be reached with the asymptotic analysis). The three other papers provide a new vision about the origin of the stabilization mechanisms. Two of them (references [9, 24]) point to the transverse thermal diffusion as source of stabilization, and the other one (reference [33]) claims that the vorticity generated at the ablation front is in the origin of the stabilization mechanism by overpressure.

In 1997 Piriz et al. [27] presented a sharp boundary model with the aim of overcoming the difficulties arising in previous attempts. As we have seen, the weak point of the sharp boundary models is the need of additional information besides the conservation relations across the ablation surface. To overcome the difficulty of the lack of the boundary conditions, it had been assumed one or another supplementary boundary condition without any justification of it. This fact usually lead these models to fail in reproducing numerical results. A breakthrough for sharp boundary model was given by two major considerations [27]. First, the recognition of the ablation front to be an isotherm, which is actually a correct boundary condition of the problem; and, second, an adequate introduction of the characteristic length of the energy deposition mechanism driving the ablation. The latter means that the relation dispersion formula is derived in terms of an unkown parameter, the density jump across the front $r_D = \rho_2/\rho_1$, where subscripts 1 and 2 refer to the light and heavy fluid respectively. The determination of r_D can be done by means of either a simple corona model or 1D simulations, that is to say, we provide the information concerning the structure of the near-corona region *a posteriori*, in contrast to what has been done in the preceding attempts of sharp boundary model where this information is assumed *a priori*. The dispersion relation formula in terms of the density jump reads as follows

$$\gamma = \sqrt{\left(\frac{2kv_2}{1+r_D}\right)^2 - kg\left(\frac{kv_2^2}{gr_D} - A_T\right)} - \frac{2kv_2}{1+r_D}, \tag{35}$$

where $A_T = (1-r_D) \,/\, (1+r_D)$. This expression agrees with the Kull numerical results [17] by assuming the following corona model

$$r_D = \left(\frac{2kL_0}{\nu}\right)^{1/\nu}, \quad L_0 = \frac{3\kappa_{D2}}{5\rho_2 v_2}, \tag{36}$$

where κ_{D2} is the thermal conductivity at the heavy fluid, and it also reproduces the analytical results by Sanz [31] and Goncharov et al. [13] for $\mathrm{Fr} > 1$. This choice of density jump is consistent with a required characteristic length of the order of $1/k$.

Clavin and Masse [9] published in 2004 a work where they compared the instabilities of ablation fronts with flames. The main contribution of this work is to include the critical surface (region where the laser energy is absorbed) in the model and its numerical resolution. The solution of the flame instability, that is to say, the Darrieus-Landau (DL) instability is recovered in the small acceleration regime, $\mathrm{Fr} \gg 1$ ($g \simeq 0$) for perturbation wavelengths of the order of the distance between the laser absorption region and the ablation front. The authors, using a simple analytical model, resolve the stability problem of a thermal wave relaxation, claiming that this result demonstrates that the physical origin of part of the generic damping term ($\gamma = -kV_a$) in ablation fronts is due to the thermal relaxation (transverse heat conduction). In line with this work, Sanz et al. [33] presented in 2006 an analytical self-consistent model that analyzes the ablation front stability in a large domain of conditions, ranging from long wavelengths, of the order of the distance between the critical surface and the ablation front, to short wavelengths. An expresion for the dispersion relation, matching the known results for short [8, 31, 32, 13, 3, 4] and long [8] wavelength modes, was obtained for bridging the gap between these two limits. At leading order the dispersion relation formula has the following form

$$\gamma = \sqrt{kg - (T_c/T_a)\, q_0\,(\kappa)\, k^2 V_a^2\,(\kappa)^{-1/\nu}} - (1 + \tanh(\kappa))\, kV_a, \qquad (37)$$

where subscripts a and c refer to the ablation front and critical surface, respectively, q_0 is the first order momemtum flux which is computed numerically and $\kappa = kd_c/\nu$ where d_c/ν is the total thickness. A novelty of this work is the interpretation of the vorticity as the source of the overpressure that generates the stabilization of the RT instability. At leading order, the dominant stabilization effect appears in the second term inside the square root of equation (37), that is related to the dynamical pressure at the ablation front, q_0. Pressure fluctuations are playing then a stabilizing role (as it was proposed in reference [31]). The origin of these fluctuations in pressure comes from the density variation just down-stream to the ablation front, that generates vorticity by the baroclinic effect. Pressure and vorticity being linked together at the ablation front, the authors claim that stabilization may be viewed through the vorticity as well.

Masse [24] presented in 2007 a sharp boundary model highlighting the importance of transverse thermal diffusion. In a similar way that in reference [27] but introducing a coefficient $D \equiv \kappa_x/\kappa_y$, the ratio between transverse and longitudinal thermal conductivities, Masse arrives to a dispersion relation formula for a large Froude number that reads as follows

$$\gamma^2 + 2\left(\sqrt{D} - 1\right) kV_a\gamma + r_D\left(2\sqrt{D} - 1\right) k^2V_a^2 - kg = 0. \qquad (38)$$

Note that in the case of isotropic conduction ($D = 1$), this formula reproduces the results by Sanz [31]. By analyzing the above dispersion relation formula, the author claims that the transverse diffusion has a pronounced stabilizing role. In addition, the author demonstrates that the physical origin of the rocket effect is an increase of the dynamical pressure due to the transverse thermal conduction, which is in accordance with all the physical interpretations of the main stabilizing effect for $\mathrm{Fr} > 1$. In order to exploit the advantages of the anisotropic thermal diffusion, a target design was proposed using a laminated ablator made of successive layers of different diffusive properties.

3

TARGET DESIGN: THE CHOICE OF THE ABLATOR MATERIAL

For direct-drive target designs two major effects can prevent the correct assembly of the fuel:

- Preheat of the fuel, generated by suprathermal electrons produced by instabilities in the laser-plasma interaction, and
- Hydrodynamic instabilities of the imploding shell (the object of this thesis).

In the next paragraphs we will see how the ablator material can influence the extent of these effects. The ablator material is then an important parameter that may be taken into account for successful target designs.

3.1 HYDRODYNAMIC INSTABILITIES

3.1.1 *In-flight aspect ratio criteria*

An important hydrodynamic parameter determining target perfomance is the aspect ratio (A) that measures the ratio between the average pellet radius (R_1) and the shell thickness (Δ). A large aspect ratio refers to a thin shell compared to the pellet radius. The aspect ratio varies in time due to the compression of the shell, the ablated material and the convergence effects (see figure 7). The maximum aspect ratio is obtained when the first shock arrives at the rear surface of the shell (shock break-out). At that moment the shell is compressed around 4 times with respect to the initial value, and begins to implode. This maximum aspect ratio is usually known as in-flight aspect ratio (IFAR), and its expression read

$$A_{\text{max}} \equiv \text{IFAR} = \frac{R_1}{\Delta_{sb}}, \tag{39}$$

where Δ_{sb} is the shell thickness at the shock break-out and R_1 the shell radius.

The IFAR can be related to the Rayleigh-Taylor instability growth, and it is commonly used to assess the stability properties of ICF implosions [51]. The

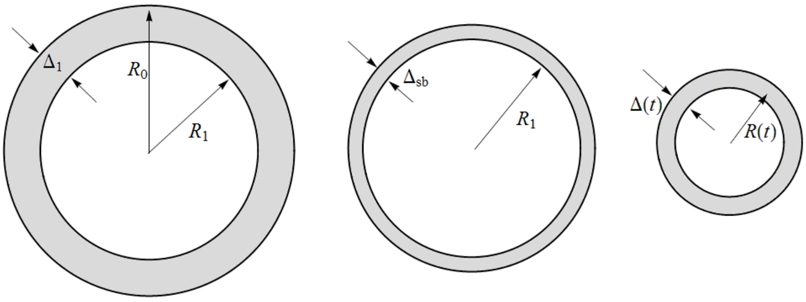

Figure 7: Schematic of the capsule evolution with time. At the left, the capsule at the initial time; in the center, the capsule at the shock break-out moment; and at the right, the capsule during the implosion. The shell is represented in grey colour.

growth rate of the RT instability for a typical direct-drive DT capsule can be approximated by the Takabe formula $\gamma = 0.9\sqrt{kg}–3.1kV_a$ [43], where k is the mode wave number, g is the acceleration and V_a is the ablation velocity. According to the hydrodynamic scaling relations given by Zhou and Betti [51], the linear growth rate formula can be rewritten in the following form

$$\gamma t = 1.33\sqrt{\mu\left(k\Delta_{sb}\right)\mathrm{IFAR}}–5.4\mu\left(k\Delta_{sb}\right)\mathrm{IFAR}\left(V_a/V_i\right) \tag{40}$$

where $\mu = D/R$ is the ratio between the distance D travelled by the shell during the acceleration phase and the target radius R, V_i the implosion velocity, and the subscript sb denotes shock break-out values. In the term $(k\Delta_{sb})$ we introduce the wavenumber k of the modes that can cause the shell break-up. In order to scale the most damaging modes, we use the following reasoning. We consider that the front shell surface is pertubed in a sinusoidal form of amplitude ξ_f. This fact induces a distorsion in the rear surface of amplitude $\xi_r = \xi_f \exp(-k\Delta)$. Depending on the order of magnitude of $k\Delta$, we have different scenarios (see figure 8) :

- $k\Delta \ll 1$: In this case the rear surface is as distorted as the front surface. Both surface distorsions are in phase, and the shell behaves as a surface of zero thickness. There is no risk of shell break-up in the linear phase of the hydrodynamic instability.

- $k\Delta \gg 1$: The distorsion of the front surface is completely damped across the shell, and the rear surface is not concerned with the first stages of linear development of the Rayleigh-Taylor instability on the front surface. This kind of modes are not suspected of breaking the shell up.

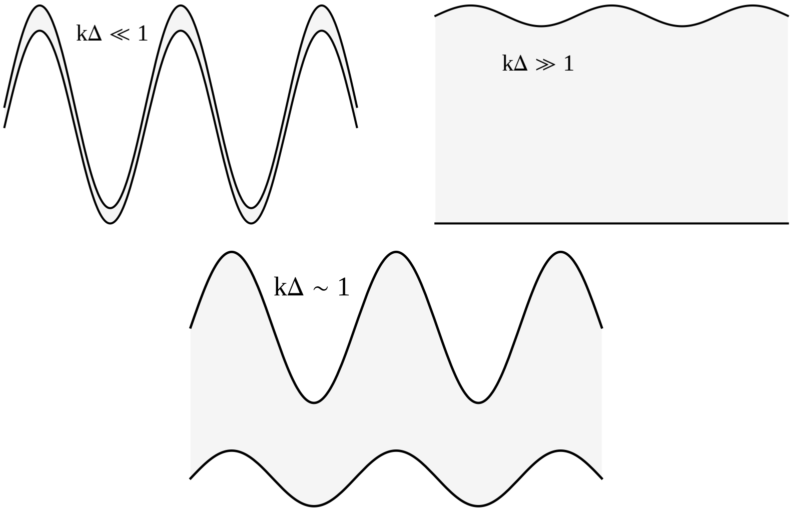

Figure 8: Schematic of different scenarios of shell distorsion. Upper figures correspond to cases where the shell does not break, and bottom figure correspond to a case where the integrity of the shell can be at danger.

- $k\Delta \sim 1$: This is the most damaging scenario. The rear surface gets distorted induced by the Rayleigh-Taylor unstable growth on the front surface, but with an amplitude around $1/e$ times smaller. This leads to different compression rates across the shell, and this strain can yield the shell break-up. We assume $k\Delta = 1$ as the most damaging case. We can rearrange this expression to obtain an estimate of the most damaging mode as a function of the parameter IFAR:

$$k\Delta = kR\left(\Delta/R\right) = \ell\,\mathrm{IFAR}^{-1} = 1 \Longrightarrow \ell_{most\,dangerous} = \mathrm{IFAR}. \qquad (41)$$

Equation (40) indicates that for the most dangerous modes ($k\Delta = 1$) and typical values of the velocity ratio $V_a/V_i \sim \mathcal{O}\left(10^{-2}\right)$, lower IFAR shells are less sensitive to the hydrodynamic instability growth during the implosion. However, there is an opposite effect of the IFAR that does not let us reduce its value with the only consideration of preventing shell break-up. Actually, if we keep the laser intensity parameters unchanged (imagine that we have reached the maximum perfomance of our laser device), the implosion velocity is proportional to the IFAR[1]. This means, *grosso modo*, that for the same amount of energy released to the target, the largest velocity is reached in the target of thinner shell (the lighter one). If we increase the thickness of the

---

[1] Let us consider an imploding thin shell at the shock break-out. Its mass is $m \sim \rho\Delta_{sb}R_1^2$. The shell kinetic energy is equal to the work done on the shell, $mV_i^2 \sim P_aR_1^3$. We can write then the implosion velocity in terms of the IFAR as follows, $V_i^2 \sim \mathrm{IFAR}\,P_a/\rho$.

shell (lower IFAR), it becomes heavier and, consequently, it is more difficult to accelerate. Then, the requirement of obtaining an ignition relevant implosion velocity imposes a minimum on the IFAR.

3.1.2 *Hydrogenic ablators*

High-gain target designs for direct-drive ICF are constrained by achieving opposite objectives as minimizing the RT unstable growth of the most dangerous modes (with low IFAR) and obtaining, at the same time, an ignition relevant implosion velocity (with a high IFAR). The baseline direct-drive designs for National Ignition Facility (NIF) at the beginning of 2000's [25] employed a solid (cryogenic) DT-shell target (hundred of microns layer) with a thin polymer ablator (a plastic layer of a few microns thickness required to fabricate the cryogenic shell) surrounding the DT-ice shell. Often the cryogenic DT is solidified around a plastic foam matrix forming a wetted foam layer [$CH(DT)_6$ or $CH(DT)_4$]. Wetted foam targets consist of a pure DT ice layer enclosed by a wetted foam layer inside a thin CH overcoat. Since the thin CH overcoat is quickly ablated off in the early stages of the driving laser pulse, the main ablator is hydrogenic, even in wetted foam targets, and the DT ice plays both roles of ablator and thermonuclear fuel. The choice of hydrogenic ablators (mainly DT-ice) is motivated by their relatively low density that enables to achieve high implosion velocities with low IFAR, and therefore exhibit good hydrodynamic stability. Two-dimensional simulations have demonstrated the favorable hydrodynamic stability properties of hydrogenic ablators [35].

The choice of a non-hydrogenic ablator is suspected of worsening the hydrodynamic stability of the shell. Arguments appeal to the impossibility of achieving high implosion velocities unless the shells are thinner (because they are heavier). Thus, we would have a configuration of a high IFAR shell that, according to equation (40), exhibits poor hydrodynamic stability properties. However, we present in the next paragraph some experiments performed by Fujioka et al. [11] that refute this postulate indicating that the use of brominated plastic foils significantly improves the hydrodynamic stability properties by reducing the growth of RT instability. This work opened a new axis of research focused on the use of moderate-Z materials (like Si, SiO2, CH, or CD doped with moderate-Z elements) as ablators in direct-drive ICF.

3.1.3 *Experiments with non-hydrodgenic ablators (Fujioka et al. [11, 12])*

Fujioka et al. presented in 2004 some simulation and direct-drive experimental results comparing the RT unstable behaviour of two different planar targets: one plastic target (CH) without dopants and one plastic target doped with moderate-Z elements (brominated plastic, CHBr). They found a reduction of the density of the ablation front and an increase of the mass ablation rate in the CHBr target compared to the CH one, that lead to the improvement of the hydrodynamic stability properties. This behaviour seems to be explained by the increasing importance of radiative energy transport in the ablated moderate-Z material.

Numerical simulations show the development of a double ablation front structure in the brominated plastic case (see figure 9). It was selected a 25 μm-thick CHBr target (in particular $C_{50}H_{47}Br_3$) with an initial density of 1.26 g/cm^3 (1.06 g/cm^3 for the CH target). The flat-top laser pulse of intensity $I_L = 1.0 \times 10^{14}$ W/cm^2 irradiates the target during 2.5 ns. According to Fujioka et al. [12], the development of the double ablation front structure in directly laser driven plasma is the following. The absorption of the laser energy around the critical density point generates thermal electrons that heat up the target surface and drive the primary ablation front (or electron-conduction ablation (EA) front). In the high-temperature corona plasma, the atoms of the dopant (in this case, bromine atoms) emit strong radiation that is locally reabsorbed inside the target, driving, in this way, the secondary ablation front (or radiative ablation (RA) front). Figure 9 (panel (a)) shows that in the region between both fronts (plateau region) the electron and radiation temperatures are nearly equal. It was found this behaviour along the simulation time. This feature indicates that radiation and matter are almost in equilibrium inside the plateau layer, result that will be used in the development of a one-dimensional radiation hydrodynamic theory. Moreover, as shown in figure 9, the peak density of the plasma in the CHBr target is lower that for the plasma in the CH target. It was attributed to the preheating caused by the high energy component of the self-emitted radiation. This feature is an indication of the role played by the radiation in the improvement of hydrodynamic stability, in particular, with the reduction of the Atwood number of the ablation region.

Fujioka et al. also performed single-mode 2D simulations (figure 10). They used a planar foil of the same thickness as in the 1D simulations, and keep the laser parameter unchanged. There, the configuration of the double-ablation

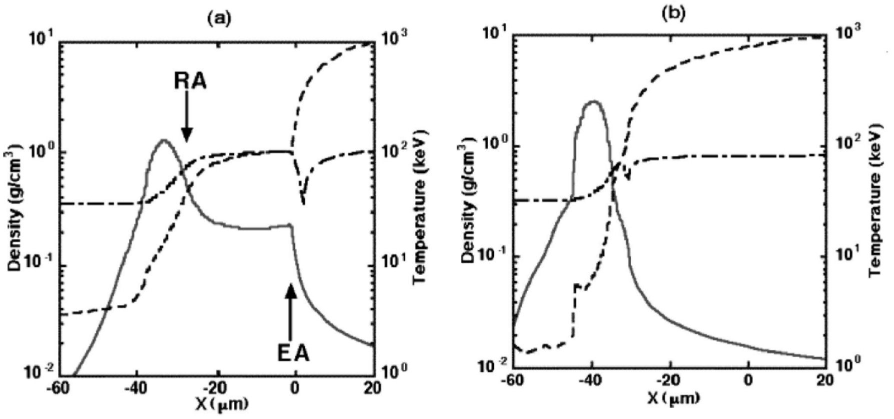

Figure 9: 1D simulated profiles of mass density (solid), electron temperature (dashed), and radiation brightness temperature (dashed-and-dotted) in CHBr (a) and CH (b) targets at 1.2 ns after the onset of the main laser pulse. The origin of space is set to be the initial position of the target rear surface. RA and EA in (a) indicate the radiation-driven ablation surface and the electrondriven ablation surface, respectively. Figure taken from Fujioka et al. [12].

structure with the density plateau region was observed again as in one-dimensional calculations. It is remarkable to notice that, for the perturbation wavelength considered (80 μm), the perturbation predominantly grows at the RA surface, while EA surface remains without any substantial deformation. Moreover, the deformation of the ablation surface of the CH target is much larger than that for the CHBr target. Then, they apply the Betti and Goncharov linear theory [28] to estimate the parameters determining the linear RT growth rate from the hydro-profiles calculated by 1D simulation in the interval from 1.5 to 2.0 ns. Since it is not possible to apply it directly to the CHBr target case because of the double-ablation structure, they considered the RA front as the only unstable one and restricted the evaluation procedure to the region covering the RA front and the plateau layer. In table 1, we can see that the ablation velocity for the CHBr target is three times larger that that for the CH target, and, as well, the characteristic thickness of the ablation front is more than two times longer in the CHBr target case. These two effects, jointly with the decrease in the Atwood number discussed just above, explain a significant suppression in the RT instabilitly observed in the doped plastic.

In order to verify the simulation results, experiments were performed at the GEKKO XII laser facility with two kinds of brominated plastic target, CHBr-

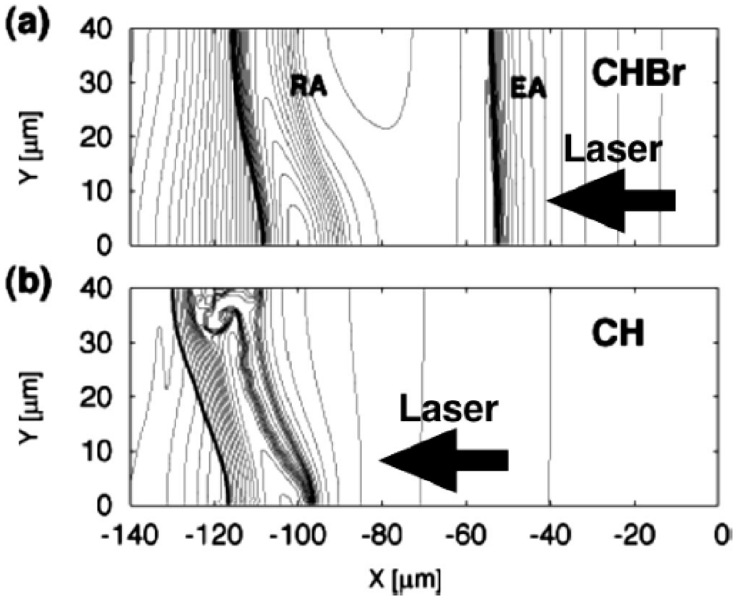

Figure 10: 2D simulated density contours of CHBr (a) and CH (b) targets at 1.9 ns after the onset of the main laser pulse. The contour lines are drawn at isodensities of 40 levels increasing logarithmically from 10^{-2} to 10^{-1} g/cm^3. Figure taken from Fujioka et al. [12].

	V_a(μm/ns)	L_0(μm)	g (μm/ns^2)	ν
CH	0.92	0.42	50	0.67
CHBr	3.0	0.99	45	0.93

Table 1: Parameters determining linear RT growth rate. Data taken from Fujioka et al. [12].

3 and CHBr-4. Their compositions and initial densities were $C_{50}H_{41.5}Br_{3.3}$ and 1.35 g/cm^3 for CHBr-3, and $C_{50}H_{45.8}Br_{4.2}$ and 1.45 g/cm^3 for CHBr-4, respectively. They first tested the one-dimensional radiation-dydrodynamic simulation code comparing its results with experimental measurements:

- *Target trajectory measurements*. The target was a 26 μm thick foil of CHBr-4 that was irradiated by a laser pulse of intensity 5.0×10^{12} W/cm^2 for the foot pulse and 1.1×10^{14} W/cm^2 for the main pulse. The results indicated that the code reproduces the experimental measurements well.
- *Density profile measurements*. It was used the same CHBr-4 target. The intensities of the foot and main laser pulses were 0.5×10^{12} W/cm^2 and 0.9×10^{14} W/cm^2, respectively. It was observed experimentally for

	target thickness (μm)	perturbation wavelength (μm)	perturbation amplitude (μm)	foot intensity pulse (10^{12} W/cm^2)	main intensity pulse (10^{14} W/cm^2)
CHBr-3	18	25	0.3	1.0	1.5
CH	25	20	0.2	1.0	1.5
CHBr-3	22	47	0.3	0.7	0.7
CH	25	50	0.2	0.7	0.7

Table 2: Targets and laser configurations used in RT instability measurements. Data taken from Fujioka et al. [12].

the first time a double ablation front structure formed inside a laser-driven CHBr target. Some differences were found between the density profile measurements and the simulation results. They concerned the length of the plateau layer and the peak densities. These differences were attributed to the opacity model, and the necessity of improving it for reproducing the full characteristics of the density profile in a CHBr target.

For the Rayleigh-Taylor instability measurements, they used temporally resolved x-ray shadowgraphs of the target. They measured areal-density perturbations, defining the growth factor as the areal density perturbation divided by its inital value. CHBr-3 and CH targets were used with different foil and laser configuration as shown in table 2. In figures 11 (a) and 11 (b), we can see that the variation in the contrast in the radiograph is significantly suprressed in the CHBr target, showing a smooth pattern different from the modulated one present in the CH target. The temporal evolution of the growth factors of the area-density perturbations (see figures 11 (c), (d), (e) and (f)) shows that:

- for the 20 μm perturbation wavelength case, no signficant growth is observed in the CHBr target within the experimental resolution, while the growth rate of the perturbation in the CH target is 2.6 ± 0.3 ns^{-1}, and
- for the 50 μm perturbation wavelength case, the growth rate of the CHBr target is 1.2 ± 05 ns^{-1}, less than the growth rate in the CH target ($\gamma = 1.7 \pm 0.5$ ns^{-1}).

These experimental results confirm the mitigation in the Rayleigh-Taylor instability using moderate-Z ablators (CHBr) compared to the CH ablators. The large ablation velocity and the long density scale length due to the radiation drive seem to be the reasons of the stabilization.

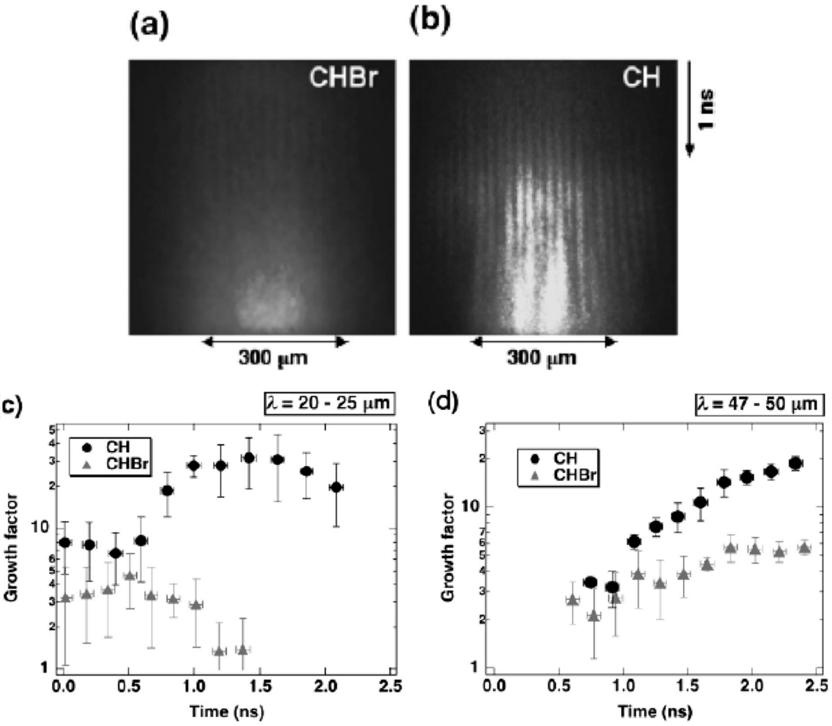

Figure 11: Face-on x-ray radiographs of laser dirven corrugated CHBr (a) and CH (b) targets for 20 μm- wavelength perturbation. The temporal evolution of the areal-density perturbation in CHBr (triangle) and CH (circle) targets for 20 μm-wavelength perturbation (c) and 50 μm (d).

3.2 LASER-PLASMA INTERACTION

Corona region is rich in physical processes related to the laser-plasma interaction. Indeed, absorption of the laser beams involves collective modes of interaction with the plasma. Some of them have an unstable growth, with a negative effect in the inertial fusion process that should be minimized as possible. Our concern is restricted to the two-plasmon decay instability, that, as we will see hereafter, can condition the choice the ablator material.

3.2.1 *Basics*

A characteristic feature of a plasma is its ability to support waves. In the simple case with no imposed magnetic fields, these plasma waves are mainly charge density fluctuations. Using a two-fluids model (that consider the plasma made of two species: electrons and ions), one can distinguish two different plasma waves, a high and a low frequency ones, that are associated with the motion of one of the species:

- Electron plasma wave (EPW) is the high frequency one. The dispersion relation for this oscillation is $\omega^2 = \omega_{pe}^2 + 3k^2 v_e^2$, where ω_{pe} is the electron plasma frequency and v_e is the electron thermal velocity. The term proportional to the wavenumber is usually negligeable, so, in a first approximation we can take $\omega^2 \simeq \omega_{pe}^2$.
- Ion acoustic wave (IAW) is the low frequency one. The dispersion relation for this oscillation is $\omega = \pm k v_s$, where $v_s = \sqrt{(ZT_e + 3T_i)/M}$ is the ion-sound velocity (equivalent to the sound speed in gases), and $\omega \ll \omega_{pe}$.

One of the fundamental processes in the interaction of intense electromagnetic waves (laser) with fully ionized plasmas (corona region) is the parametric excitation of two new waves (parametric instabilities). Laser may excite plasma waves or other electromagnetic (EM) waves. In all cases we have three-wave interaction (the laser pumping two other waves), where the phase matching conditions

$$\omega_0 = \omega_1 + \omega_2,\ \vec{k}_0 = \vec{k}_1 + \vec{k}_2 \tag{42}$$

are satisfied. Note that $(\omega_0, \vec{k}_0)$ correspond to the incident laser, and $(\omega_1, \vec{k}_1)$ and $(\omega_2, \vec{k}_2)$ to the excited modes. The various modes of parametric instabilities that can develop depends on the nature of the excited modes:

- Stimulated Raman Scattering (SRS). It involves scattering of the laser photon by an electron plasma wave. SRS may occur in subcritical plasma with a density $n < n_{cr}/4$.
- Stimulated Brillouin Scattering (SBS). It involves scattering of the laser photon by an ion-accoustic wave. SBS may occur in the whole volume of the underdense plasma ($n < n_{cr}$).
- Parametric decay instability (PDI). The laser photon decay into two plasma waves: one ion-accoustic wave running inwards like the laser photon, and one electron-plasma wave that runs outwards in opposite direction. PDI is an absorption process, which may occur in a region close to the critical surface ($n \simeq n_{cr}$).

- Two-plasmon decay (TPD) instability. The laser photon decay into two electron-plasma waves. Since both EPW have approximately a frequency ω_{pe} , this instability occurs at a density $n \simeq n_{cr}/4$. Direction of propagation of both EPW is simmetrical at 45° to both $\vec{k}_0$ and $\vec{v_{os}}$, where $\vec{v_{os}}$ is the oscillatory velocity of an electron in the large amplitude light wave.

Parametric instabilities have negative effects in inertial fusion. Interaction between laser and plasma may lead to scatter light and also to the appearance of populations of high energy (suprathermal) electrons. In this way, SRS and SBS reduce the efficiency of the laser energy coupling to the fusion target because part of the laser energy delivered does not arrive to the dense part of the target. This would impose the need of higher power laser devices, which are technologically challenging. Laser light scattering also implies an asymmetric deposition of the laser energy, and, consequently, an asymmetric target implosion. This can result in target surface nonuniformities, the seed for the subsequent development of hydrodynamic instabilities.

Regarding hot electron populations, they are produced when part of the laser energy is converted into energy carried by an EPW. These suprathermal electrons are generated by plasma waves due to the interaction with electrons moving with the wave at its phase velocity. Electrons may get trapped in the high-amplitude plasma waves, excited by the parametric instabilities, and are then accelerated to high energies. These long mean free path, hot electrons can penetrate into the target and preheat the shell, increasing the shell entropy[2]. Therefore, this shell preheat can be an obstacle to obtain high compression (i.e., high areal density ρR) in target implosions. Indeed, as shown in [51] the total target areal density goes like

$$\rho R \left(mg/cm^2 \right) \approx 2600 \left[E_L \left(MJ \right) \right]^{1/3} \alpha^{-0.6}, \qquad (43)$$

where E_L is the laser energy. Thus, achieving high compression requires keeping the shell entropy (adiabat) low, that implies, among others, reducing the possible shell preheat.

3.2.2 *Experiments about target preheat by suprathermal electrons produced by TPD instability*

A series of experiments have been carried out on OMEGA Laser Facility to demonstrate that high compression can be achieved in laser-driven implo-

---

[2] The entropy is definied through the adiabat $\alpha = \left[P \left(Mb \right) \right] / 2.2 \left[\rho \left(g/cm^3 \right) \right]^{5/3}$

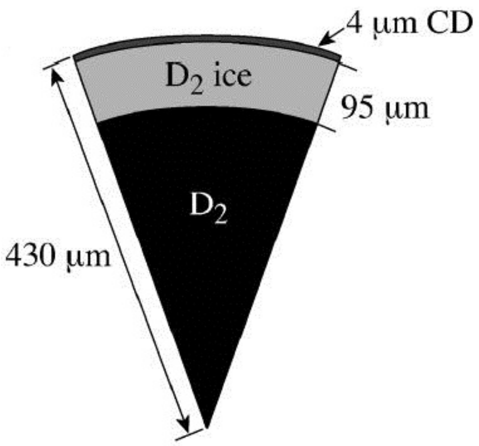

Figure 12: A typical cryogenic target. Figure taken from Sangster et al. [30].

sions. During these experimental campaigns, the role of hot-electron preheating has been studied. Main results are the following:

1. *Shell preheating by hot electrons produced by TPD instability in the coronal plasma is correlated with a significant increase in the shell adiabat* [39]. Direct-drive implosions of $\sim 860\,\mu$m initial-diameter target with shell consisting of a $\sim 95\,\mu$m thick inner D_2 ice layer and an outer $\sim 4\,\mu$m thick plastic CD layer were carried out using the 351 nm, 60-beam OMEGA Laser System. The targets were imploded with shaped, high-compression pulses in the range of intensities from $\sim 3 \times 10^{14}$ to $\sim 1 \times 10^{15}\,\mathrm{W/cm^2}$. The hard x-ray (HXR) signals (with photon energies of >40 keV) generated by hot electrons from the TPD instability were measured by the HXR detector. It was seen that the areal density decreases significantly for peak laser intensities above $\sim 3 \times 10^{14}\,\mathrm{W/cm^2}$. This degradation correlates with the increase of the HXR signal. Moreover, the highest compresssion in low-adiabat implosions was achieved at the lowest intensities, when the HXR signals and associated hot-electron preheating were low. These considerations and the intensity scaling of the HXR signal suggested that the areal-density degradation at high intensities is due to the hot-electron preheating generated by TPD instability.

2. *Plastic (CH) ablators reduce preheat levels compared to D_2 ablators* [30]. In the previous work, it was seen that the highest compression with areal densities of $\sim 140\,mg/cm^2$ was achieved at a low peak laser intensity of $\sim 3 \times 10^{14}\,\mathrm{W/cm^2}$, where the TPD hot-electron X-ray generation was small. However, with such a low intensity, ignition relevant implosion

velocities ($\sim 3.5\times10^7 cm/s$) cannot be achieved. The order of magnitude of implosion velocity can be wrritten as

$$V_{imp}^2 \sim \frac{P_a}{\rho} IFAR \sim I_L^{2/3} IFAR. \tag{44}$$

It is possible then to increase implosion velocities in two ways. On one hand, we can increase the in-fligth aspect ratio. This is not an advisable solution, since a thinner shell will be exposed to a possible break up due to hydrodynamic instabilities during the implosion phase. On the other hand, with a robust target design, we find an upper limit in the implosion velocity given by laser-plasma instabilities. Indeed, if we try to increase laser intensity, we will strengthen laser-plasma instabilities, yielding elevated preheating rates (high adiabat α), and, hence, degradating ρR. In Sangster et al. [30], implosion experiments were carried out using on OMEGA using two different concepts of target designs: $\sim 4\,\mu$m thick CD cryogenic D_2 and thick-CH-shell (typically $20-26\,\mu m$) gas-filled, room-temperature (see figure 12). The hot-electron preheat is inferred by measuring the bremsstrahlung radiation ($\sim 20-150$ keV x-rays) produced as the suprathermal electrons transit the fuel. It was obserbed that the x-ray production threshold for the CD shells is lower than for the plastic (CH) shells. For instance, the threshold for the warm CH shell is situated around 5×10^{14} W/cm^2, so, significantly reducing target preheat at that laser intensity compared to CD shells implosions. The explanation given in [30] states that "the intensity-threshold difference follows from the high laser absorption in CH (relative to D_2) due to the higher ion charge Z. The enhanced absorption increases the coronal temperature and lowers the laser intensity at the quarter-critical density surface".

3. *The use of glass (SiO_2) ablators significantly reduces hot-electron preheat at ignition relevant peak intensities of $\sim 1\times10^{15}$* W/cm^2 [40]. Spherical $20\,\mu$m thick glass shells with $\sim 860\,\mu$m initial diameter, filled with D_2 gas, were imploded on the 351 nm, 60 beam Omega Laser Facility. The targets were driven by two shaped pulses at peak intensities of $\sim 5\times10^{14}$ and $\sim 1\times10^{15}$ W/cm^2 (see figure 13). The aim of these experiments was to measure target performance with glass ablators and to compare them with those from plastic implosions. It was obserbed a reduction on the preheat in SiO_2 ablators more than one order of magnitude compared to CH ablators at ignition-relevant laser intensity $\sim 1\times10^{15}$ W/cm^2. In addition, increased fast electrons scattering in high-Z ablators reduced

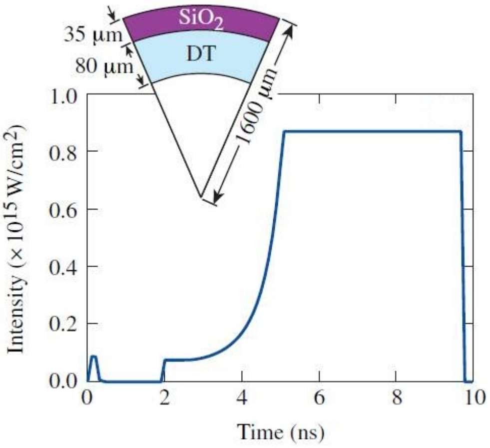

Figure 13: A typical glass ablator target taken from Smalyuk et al. [40]. The target is driven by a 10-ns pulse with a total laser enregy of 1.5 MJ and a peak intensity of $\sim 8.7 \times 10^{15}$ W/cm^2.

the number of hot electrons reaching and preheating the inner shell compared to low-Z ablators [3]. There was no hard x-ray signal detected in low-energy glass implosion, indicating a higher intensity-threshold for the TPD instability in the case of glass ablators. These results widen the potential candidates for ablator materials in direct-drive target design, including moderate-Z ablators for their benefits in target preheat reduction.

---

[3] The role of scattering of fast electrons created by TPD instability is studied in Yaakobi et al. [47]. There, results of experiments on Omega Laser Facility with a 1-mm-diam solid Cu sphere and a 1-mm-diam solid CH sphere, both coated with a 15 μm layer of CH, are compared with Monte Carlo code simulations. Among several aspects to the transport of fast electrons (slowing down, scattering, divergence or angular distribution at the point of generation), it is shown that the reduction in fast-electron penetration is mainly due to scattering for a high-Z dopant in a ICF target. Scattering, that is mainly due to collisions with the atomic nucleus, is proportional to $N_a Z^2$, where N_a is the atomic density. Experiments show a reduction, by a factor of ~ 2, in fast-electron energy depositon (preheat) in Cu compared to CH.

4

RADIATION HYDRODYNAMIC THEORY OF DOUBLE ABLATION FRONT

The development of a double ablation front structure during the capsule implosion is directly related to the importance of radiation effects inside the ablation layer. A necessary condition for such development requires that the radiation flux becomes comparable with the material energy flux. A dimensionless number measures the relative weight of the contribution of the radiation in the overall problem. It is the *Boltzmann number*, which can be defined as the ratio between the material energy flux and the radiation energy flux. In our case, it takes the form

$$\mathrm{Bo} = \frac{\frac{5}{2} P_a \,\mathrm{v}}{4\sigma T^4}, \tag{45}$$

where σ is the Stefan-Boltzmann constant. In this way, for a Boltzmann number not very large, the radiation will affect hydrodynamics and the equations describing the hydrodynamic equilibrium profiles shall contain the radiation contribution. In 2009, such a theory was presented by Sanz et al. [34]. This one-dimensional radiation hydrodynamic theory assumes a subsonic and steady ablation region resulting from an incoming heat flow, an ablated mass flow, and a uniform pressure P_a. This description is appropriate inside a layer in the vicinity of the maximum density gradient, where the isobaric approximation is valid. The general energy equation can be written as

$$\nabla \cdot (\rho \vec{\mathrm{v}} \epsilon + P_a \vec{\mathrm{v}}) = -\nabla \cdot \left(\vec{Q}_e + \vec{S}_r \right). \tag{46}$$

Three energy contributions are considered. In the left-hand side of equation (46), we find the enthalpy energy flux, which comprises the convection of the internal energy $\rho\epsilon$ and the work done by the pressure forces per unit area per unit time. If we introduce the equation of state of an ideal gas

$$\rho\epsilon = \frac{P_a}{\gamma - 1}, \tag{47}$$

	$Z=1$	$Z=2$	$Z=4$	$Z=16$	$Z=\infty$
δ_t	0.2252	0.3563	0.5133	0.7907	1.000
ϵ	0.4189	0.4100	0.4007	0.3959	0.4000

Table 3: Values of transport coefficients (taken from Ref. [41])

where γ is the ratio of specific heats, we can rearrange the enthalpy term yielding $(5/2)\,P_a\vec{v}$ when we assume $\gamma = 5/3$. Two terms in the right-hand side of equation (46) correspond to the electron thermal conduction ($\vec{Q}_e$) and the radiation energy flux ($\vec{S}_r$). A detail description of them is given in the following paragraphs.

4.1 ELECTRON THERMAL CONDUCTION

Part of the laser energy absorbed in plasma around the critical density is conducted towards the ablation layer with the electron heat flow. The heat flow vector in a statistically isotropic fluid is given by the Fourier law

$$\vec{Q}_e = -\kappa\,\nabla T_e, \tag{48}$$

where κ is the coefficient of thermal conductivity. The sign minus refers to the heat flow passing from the hot regions to the cold ones. The thermal conductivity of a material generally varies with the temperature. In 1953 Spitzer and Härm [41] treated the problem of transport phenomena in a completely ionized gas with a wide variety of mean ionic charges. They obtained a solution of the complete diffusion equation considering the effect of electron-electron and electron-ion collisions. They computed the coefficients of electrical and thermal conductivity. The latter, in the presence of a small temperature gradient ∇T, reads

$$\kappa = 20\left(\frac{2}{\pi}\right)^{3/2}\epsilon\delta_t\frac{k_B\left(k_B T_e\right)^{5/2}}{m_e^{1/2}e^4 Z\,\ln\Lambda}, \tag{49}$$

where k_B is the Boltzmann constant, m_e is the electron mass, Z is the mean ionic charge, $\ln\Lambda$ is the Couloumb logarithm and the factors ϵ and δ_t depend on the charge Z of the ions, and are tabulated in Table 3. An approximation valid to a few percent is $\epsilon\delta_t \simeq 0.095\,(Z+0.24)\,/\,(1+0.24Z)$. Thus, the electron thermal conduction can be rewritten as $\vec{Q}_e = -\bar{\kappa}\,T_e^{5/2}\nabla T_e$, where $\bar{\kappa}$ is a factor that basically depends on the nuclear charge of the ions.

4.2 RADIATIVE TRANSFER

In the following paragraphs, a simple overview of radiation, its transport and its effects on matter is given. A full description of radiation is rather complicated: the radiation can fill the space, vary in time, and propagate in any direction at any frequency. Additionally, there are several interaction mechanisms between radiation and matter. An accurate representation of the radiation is out of the scope of this thesis. Instead, we look for a simple model that captures the most relevant physics leading to the appearance of a double ablation front structure and that, at the same time, provides tractable expressions that enable to carry out the stability analysis.

4.2.1 *Basic quantities*

The basic quantity of a classical radiation field is the spectral radiation intensity, $I_\nu(\vec{x}, t, \vec{\Omega}, \nu)$, which is the radiation energy transported per unit area (dA), per unit time (dt), per unit solid angle ($d\Omega$), per unit frequency ($d\nu$). A complete description of radiation would have to describe the variations in I_ν as a function of all these variables. We can see the spectral radiation intensity as the analog of the distribution function in the Boltzmann transport equation. The rest of quantities are derived from the spectral radiation intensity. Amongst them, we can define the first moments as the spectral radiation energy density (U_ν) and energy flux ($\vec{S}_r$):

$$U_\nu(\vec{x}, t, \nu) = \frac{1}{c}\int_{4\pi} I_\nu(\vec{x}, t, \vec{\Omega}, \nu)d\Omega = \frac{4\pi}{c}J_\nu, \tag{50}$$

$$\vec{S}_\nu(\vec{x}, t, \nu) = \int_{4\pi} I_\nu(\vec{x}, t, \vec{\Omega}, \nu)\,\vec{n}\,d\Omega, \tag{51}$$

where J_ν is a useful quantity known as the mean spectral intensity, and $\vec{n}$ is a unit vector in the direction of propagation for any value of Ω. It is possible to define further moments of the radiation distribution function (e.g. the second moment would correspond to the spectral radiation pressure tensor). However, within this work the crucial quantity is the radiation energy flux. We can see in the energy equation (46) presented at the beginning of this chapter that the only radiative term retained corresponds to the radiation energy flux and that the terms related to the energy density and pressure of radiation are neglected.

All the quantities defined above are *spectral* quantities, that is to say, quantities depending on the radiation frequency. We can integrate it over the frequency to obtain the *total* quantity. For instance, the radiation intensity is defined as follows

$$I_r(\vec{x}, t, \vec{\Omega}) = \int_0^\infty I_\nu(\vec{x}, t, \vec{\Omega}, \nu) d\nu. \tag{52}$$

4.2.1.1 *Thermal equilibrium radiation*

Black-body (or thermal equilibrium) radiation is found within an infinite medium in thermodynamic equilibrium at a constant temperature. Thermal equilibrium radiation is characterized by the fact that the amount of radiation energy emitted by the medium in a given frequency is equal to the amount of radiation energy absorbed by the medium at that frequency. Thermal equilibrium radiation is isotropic, that is to say, independent of the direction of propagation. Its total energy density is only function of the temperature of the medium. The spectral thermal radiation intensity distribution, $B_\nu(\nu, T)$, follows the Planck's law

$$B_\nu(\nu, T) = \frac{2h\nu^3}{c^2} \frac{1}{\exp(h\nu/(k_B T)) - 1}, \tag{53}$$

where h is the Planck's constant. Integrating over the frequency, one finds the total thermal radiation intensity, $B(T)$,

$$B(T) = \sigma T^4/\pi. \tag{54}$$

The planckian radiation energy density reads

$$U_P(T) = \frac{4\pi}{c} B(T) = \frac{4\sigma}{c} T^4. \tag{55}$$

4.2.1.2 *Interaction of radiation and matter*

The interaction between radiation and matter involves a photon-particle energy exchange. In general, this results in transition of an electron into a different energy level (bound-bound, bound-free, and free-free transitions) and an emission, absorption or scattering of photons. A detail description should account for every distinct interaction of radiation and matter. However, for the purpose of this work, it suffices to consider the net total emission and absorption of radiation (scattering will be neglected). We can define such contributions in the following way.

- The spectral emissivity, $\eta_\nu(\vec{x}, t, \vec{\Omega}, \nu)$, is the radiation intensity emitted per unit area, per unit time, per unit solid angle and per unit frequency. The integral of this term over all frequencies and solid angles gives the power loss rate of the matter due to radiation.

- The spectral absorption opacity, $\kappa_\nu(\vec{x}, t, \vec{\Omega}, \nu)$, with units of the inverse of length. The energy absorbed by the matter (heating) per unit volume per unit time is given by the integral $\int_{4\pi}\int_0^\infty \kappa_\nu I_\nu d\nu d\Omega$.

4.2.2 *The radiation transfer equation*

The classical equation of radiation transfer is

$$\left[\frac{1}{c}\frac{\partial}{\partial t} + \vec{\Omega}\cdot\nabla\right] I_\nu(\vec{x}, t, \vec{\Omega}, \nu) = \eta_\nu(\vec{x}, t, \vec{\Omega}, \nu) - \kappa_\nu(\vec{x}, t, \vec{\Omega}, \nu) I_\nu(\vec{x}, t, \vec{\Omega}, \nu). \tag{56}$$

This equation describes the change in radiation intensity (left hand side) due to sources and losses of radiation (right hand side). Next, we will consider that the plasma is in a local thermodynamic equilibrium (LTE). This assumption implies an equilibrium between the plasma constituents, including the radiation, that is to say the photon and electron mean free paths are very small compared to the gradient scale length of the temperature and any variations in time are slow compared to the time required for a radiation and matter equilibrium distribution to be established. Under LTE, emission and absorption of radiation are in equilibrium and the Kirchoff's law applies

$$\eta_\nu(\vec{x}, t, \nu) = \kappa_\nu(\vec{x}, t, \nu) B_\nu(T, \nu). \tag{57}$$

Under other circumstances than LTE, the radiation emitted by electrons is accurately described by the Kirchoff's law (57). This is the case of a high-energy-density system where collisions are assumed rapid enough that the distribution of electrons is Maxwellian. It is a necessary and sufficient condition that the electron distribution is a Maxwell distribution for the Kirchoff's law (57) to describe the radiation emission.

Hereafter we will assume a quasi-steady limit in the radiation transfer equation (56), i.e., the time derivative will be neglected. This is justified by the fact that motion of the radiation is effectively instantaneous in comparison with that of the matter. Thus, the radiation transfer equation can be written as

$$\vec{\Omega}\cdot\nabla I_\nu = \kappa_\nu (B_\nu - I_\nu). \tag{58}$$

Integrating over all frequencies and solid angles, we obtain

$$\nabla \cdot \vec{S}_r = 4\pi \int_0^\infty \kappa_\nu (B_\nu - I_\nu) d\nu = c\kappa \left(U_P - U_r\right), \tag{59}$$

which relates the overall absorption of radiation to changes in the radiation flux. This equation can be seen as an expression of the law conservation of radiation energy. It is worth noting that this equation describes a nonequilibrium radiation field. It involves a nonlinear average of the opacity coefficient. Unfortunately, evaluating κ requires the prior solution of the radiation transport problem. So, for a practical application, assuming that plasma is not too far from the equilibrium, the average κ is approximated to the Plank mean opacity,

$$\kappa \simeq K_P \equiv \frac{1}{B(T)} \int_0^\infty \kappa_\nu B_\nu d\nu. \tag{60}$$

Two-temperature diffusion grey approximation

The radiation energy conservation equation in a quasi-steady case (59) introduces a new unknown in the radiative hydrodynamic problem (46), which is the radiation energy density. Therefore, a second equation relating the radiation energy flux and density is necessary to complete the system of equations. This relation can be obtained assuming the diffusion approximation that implies that the flux $\vec{S}_r$ is proportional to the gradient of the energy density in the form

$$\vec{S}_r = -\frac{c}{3K_R} \nabla U_r, \tag{61}$$

where K_R is the Rosseland mean opacity, another spectral-average opacity defined as

$$\frac{1}{K_R} \equiv \left(\frac{\partial B}{\partial T}\right)^{-1} \int_0^\infty \frac{1}{\kappa_\nu} \frac{\partial B_\nu}{\partial T} d\nu. \tag{62}$$

Thus, the radiation model used within this thesis considers that the radiation transport is diffusive but that the radiation and the matter are not in equilibrium. It is called two-temperature model since a “temperature” is assigned to the radiation (T_r) by defining $U_r = 4\sigma T_r^4 / c$. Equations (59) and (61) can be rewritten in the form

$$\nabla \cdot \vec{S}_r \simeq 4\sigma K_P \left(T^4 - T_r^4\right), \tag{63}$$

$$\vec{S}_r = -\frac{16\sigma T_r^3}{3K_R} \nabla T_r = -\kappa_R \nabla T_r, \tag{64}$$

where κ_R represents a Rosseland conductivity. It is important to note that both mean opacities are material functions depending on matter temperature and density. Explicit formulas can be found for fully ionized plasmas, where only free-free transitions are considered. The expressions given by Zeldovich [50] read

$$K_P^{ff} = 0.43(Z^3/A^2)\rho^2 T^{-7/2}\mathrm{cm}^{-1}, \tag{65}$$

$$K_R^{ff} = 0.014(Z^3/A^2)\rho^2 T^{-7/2}\mathrm{cm}^{-1}, \tag{66}$$

where Z is the nuclear charge, A the mass number and ρ and T are taken in the units of $\mathrm{g/cm^3}$ and keV, respectively. In order to reproduce the more relevant physical features of opacities in real materials, we will model both opacities by means of a piecewise continuous simple power law (isobaric plasma is assumed inside the ablation layer) defined by the analytical expression

$$K_P = \frac{l_R}{l_P} K_R = \begin{cases} l_P^{-1}(T_a/T)^{q_1}, & T < T_t, \\ l_P^{-1}(T_a/T_t)^{q_1}(T_t/T)^{q_2}, & T \geq T_t, \end{cases} \tag{67}$$

where l_P and l_R are the Planck and Rosseland photon mean free paths, respectively at the peak density ρ_a and temperature T_a. T_t is some characteristic transition opacity temperature for the material and $0 < q_1 < q_2$ (see figure14). In the stability analysis, the value $q_2 = 11/2$ will be used, assuming in this way an isobaric and fully ionized plasma in the near-corona region. The motivation for this opacity model is provided by the simulations performed with the code CHIC. In Fig. 14, the isobaric Rosseland and Planck mean opacities for plastic CH are plotted. Notice the change of behaviour in the CH opacities for roughly $T_t \approx 100$ eV. This change of behaviour of the opacities is related to the transition to a deeper electron shell, that is to say, around the temperature $T = T_t$ the outer electron shell of the ablator molecules (or atoms) is completely ionized and electrons from a deeper shell begin to be pulled out.

4.3 SYSTEM OF EQUATIONS AND BOUNDARY CONDITIONS

In the preceding paragraphs, the different terms of radiation hydrodynamic system of equations have been described. In planar geometry, the one-dimensional system of equations along the spatial coordinate y reads

$$\frac{d}{dy}\left(\frac{5}{2}P_a v - \bar{\kappa} T^{5/2}\frac{dT}{dy} + S_r\right) = 0, \tag{68}$$

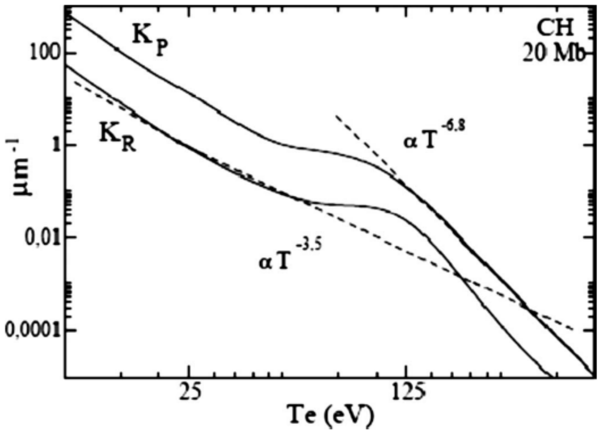

Figure 14: CH isobaric Rosseland and Planck meanopacities (μm^{-1}) vs electron temperature T (eV). Figure taken from Sanz et al. [34]

$$\frac{dS_r}{dy} = 4\sigma K_P \left(T^4 - T_r^4\right), \tag{69}$$

$$\frac{dT_r^4}{dy} = -\frac{3K_R}{4\sigma} S_r. \tag{70}$$

The boundary conditions required to close the system of equations (68)-(70) are the following:

- At the peak density ($y \to -\infty$)

$$\begin{aligned} &T\left(-\infty\right) = T_r\left(-\infty\right) = T_a, \\ &S_r\left(-\infty\right) = 0, \end{aligned} \tag{71}$$

that indicates the equilibrium between radiation and matter.

- At the far away plasma region ($y \to +\infty$)

$$S_r\left(\infty\right) = cU_r/2, \tag{72}$$

that assumes that the radiation energy flux is given by a beamlike relation. We consider that the plasma is expanding outward to the vacuum, and, moreover, that in the limit $y \to \infty$ there is an interface plasma-vacuum. This problem was treated by Zeldovich[50] in the following terms. Let us assume that the radiation emerging from the surface of

> a body into a hemispherical volume, in the direction of vacuum, has an isotropic angular distribution. The intensity in the complementary hemisphere is zero, that is, no photons arrive from the vacuum side. Then at the vacuum interface we have $S_\nu = \frac{cU_\nu}{2}$, where the flux is in the direction of the outward normal to the surface.

The dimensionless problem is set out by normalizing the flow variables by their values at the peak density. Let the normalized variables be

$$\theta = \frac{T}{T_a},\ \theta_r = \frac{T_r}{T_a},\ \phi = \frac{S_r}{\frac{5}{2}P_a v_a}. \tag{73}$$

The system of equations (68)-(70) can be rewritten in the form

$$L_{Sp}\theta^{5/2}\frac{d\theta}{dy} = \theta + \phi - 1, \tag{74}$$

$$l_P Bo\frac{d\phi}{dy} = \delta_t\left(\theta^4 - \theta_r^4\right), \tag{75}$$

$$l_R Bo^{-1}\frac{d\theta_r^4}{dy} = -3\delta_t\phi, \tag{76}$$

where

$$\delta_t = \begin{cases} \theta^{-q_1}, & \theta < \theta_t, \\ {\theta_t}^{-q_1+q_2}\theta^{-q_2}, & \theta \geq \theta_t, \end{cases} \tag{77}$$

and

$$L_{Sp} = \frac{\kappa_a T_a}{\frac{5}{2}P_a v_a} \tag{78}$$

is the characteristic length for the electronic thermal diffusion. The boundary conditions in solving the system of equations are then

$$\theta\left(-\infty\right) = \theta_r\left(-\infty\right) = 1,\ \phi\left(-\infty\right) = 0, \tag{79}$$

$$\phi\left(\infty\right)/\theta_r^4\left(\infty\right) = Bo^{-1}/2 \tag{80}$$

4.4 FEATURES OF THE ABLATION REGION

Some results of the theory by Sanz et al. [34] are summarized below.

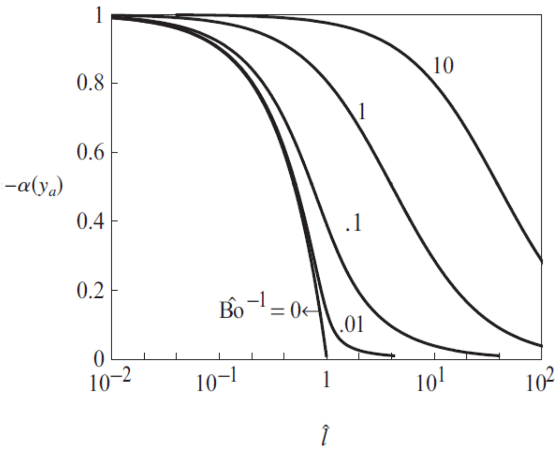

Figure 15: Fraction of radiative energy flux at the peak density ($\alpha(y_a)$) vs $\hat{l}$ (approximately the ratio of electron thermal diffuxion length to photon mean free path) for several values of the reduced Boltzmann number, $\hat{\mathrm{Bo}} = \mathrm{Bo}\sqrt{3l_P/l_R}$. Figure taken from Sanz et al. [34]

A. The character of the energy diffusively transported at the first front, $y = y_a$ closer to the peak density, only depends on the ratio of lengths $\hat{l} \equiv \sqrt{3}L_{sp}/\sqrt{l_P l_R}$ and the Boltzmann number Bo. Both dimensionless parameters are calculated at the peak density. A measure of the importance of radiative energy flux can be defined locally by means of the ratio $\alpha(y) \equiv S_r/\left(|S_r| + |q_e|\right)$. At the peak density, the radiation dominated regime is then described by $\alpha(y_a) \simeq -1$, and the other limit of dominant electronic heat flux is described by $\alpha(y_a) \simeq 0$. Figure 15 shows the fraction of radiative energy flux at the peak density, $\alpha(y_a)$, depending on $\hat{l}$ and Bo.

B. Below a critical value, Bo*, of the Boltzmann number (evaluated at the peak density), a second minimum of the density gradient scale length ($|d \log \rho/dy|^{-1}$) appears in the ablation region. This indicates the formation of a second ablation front located at $y = y_e$, around the same place where T_r and T are equal. The energy flux is found to be practically radiation dominated ($\alpha(y_a) \simeq -1$) through all the region $y_a < y < y_e$. This explains why in numerical simulations except D and DT the region between y_a and y_e is dominated by radiation and the electron heat flux does not play any role even in materials such as beryllium or CH plastic.

C. Decreasing the Boltzmann number below Bo*, a plateau in density/temperature develops between the two fronts. In this region, radiation and matter are almost in equilibrium and the radiation energy flux is $S_r \sim -\left(\sigma T^3/K_R\right) dT/dy < 0$. The thickness of this plateau region widens as the Boltzmann number decreases. Around the second ablation front a transition layer (TL) develops where S_r changes its sign.

D. Very steep electronic-radiative ablation (ERA) front can develop. The condition for its development is

$$\beta_t \equiv \frac{16}{25} \frac{\left(\sigma T_t^4 K_{Pt}\right)\left(\kappa_t T_t\right)}{\left(P_t v_t\right)^2} > 1, \tag{81}$$

where the subscripts t refer to the conditions at the ERA front (roughly around the same place where T_r and T are equal). The larger the Planck emission (equal to $\sigma T_t^4 K_{Pt}$), the steeper the ERA fronts. The role of radiation at the ERA front is essential. Although the second front is always driven by electronic heat flux, it develops a transition layer that is a very strong emitter of radiation, radiative transition layer (RTL). The fraction $\alpha(y)$ changes very abruptly through the RTL, from the value -1 to nearly 1/2, remaining almost constant beyond the ERA front. At the exit of the RTL, S_r^+ $\left(\sim \sigma T_r^4\right)$ is much larger than $|S_r^-|$. Beyond the ERA front the radiation temperature remains nearly constant $(\approx T_*)$ and almost all the incoming electron heat flux is outwardly radiated ($q_e + S_r \approx 0$).

4.5 DOUBLE ABLATION FRONT THEORY

The resolution of the system of equations (74)-(76) is rather complex, and it makes untractable to deal with the stability analysis. A simplification of the model is then convenient. We will consider an asymptotic regime where electron heat flux and radiation energy flux could compete and in some region ($T_a < T < T_t$) radiation and matter temperatures are in equilibrium, $T_r = T$. It is assumed two asymptotic limits in the order of magnitude of the photon mean free path (l_{mfp}), leading to two different radiative regimes of the matter (see figure 16):

- *Optically thick regime.* This regime covers the inner ablation front and the plateau region and it is characterized by a very large mean opacity of the plasma ($K \sim l_{mfp}^{-1} \gg 1$). In this case, if we look at the radiation transfer equation (63)

$$\nabla \cdot \vec{S}_r \sim K_P \left(T^4 - T_r^4\right), \tag{82}$$

a finite divergence of the radiation energy flux implies that the radiation and matter are almost in equilibrium, $T^4 - T_r^4 \sim K_P^{-1} \ll 1$. Therefore, we will assume that the electron temperature equals the radiation temperature, $T_e = T_r = T$. This results in a radiation energy flux behaving as a thermal conduction heat flow ($S_r \sim \nabla T$).

- *Optically thin regime*. This regime covers the outer ablation front and the near-corona region. It is considered that the mean opacity of the plasma is very small. If we look to the diffusion equation (64)

  $$S_r \sim K_R^{-1} \nabla T_r, \tag{83}$$

  the fact of imposing a finite and non-zero radiation energy flux implies a gradient of the radiation energy density to be practically zero. Therefore, the radiation temperature is assumed to be constant in this region. This constant temperature (T_*) is an unkown of the problem. For simplification, we will consider that T_* is equal to the radiative transition temperature of the ablator material, T_t. With this assumption, the boundary condition (72) that determines the radiant energy flux escaping from the ablation region to the corona is needless. The only boundary conditon to apply is the continuity of S_r at $T = T_t$. It is worth noting that the radiation term in the energy conservation equation (68) becomes a radiative cooling law. The total energy loss per unit time due to the radiation is $Q = \int q \, dV$, where $q = \nabla \cdot \vec{S}_r = 4\sigma K_P \left(T^4 - T_r^4\right)$ is the energy loss per unit volume per unit time and dV is an element of volume of the near-corona region.

We have now all the elements to build up the hydrodynamic model that will be used in this thesis. General hydrodynamic equations in the isobaric approximation, assuming that there is fully ionized plasma in the near-corona region, read

$$\frac{\partial \rho}{\partial t} + \nabla \cdot (\rho \vec{v}) = 0, \tag{84}$$

$$\rho \frac{\partial \vec{v}}{\partial t} + \rho \left(\vec{v} \cdot \nabla\right) \vec{v} = -\nabla p + \rho \vec{g}, \tag{85}$$

$$\nabla \cdot \left(\frac{5}{2} P_0 \vec{v} - \bar{\kappa} T^{5/2} \nabla T + \vec{S}_r \right) \quad = \quad 0, \tag{86}$$

$$\begin{cases} \vec{S}_r = -\bar{\kappa}_R T^{\nu} \nabla T & \text{for } T < T_t \\ \nabla \cdot \vec{S}_r = 4\sigma \bar{K}_P T^{-11/2} \left(T^4 - T_t^4\right) & \text{for } T > T_t \end{cases} \tag{87}$$

where the Rosseland conductivity follows a power law in the temperature with $\bar{\kappa}_R = 16\sigma / \left(3\bar{K}_R\right)$ and $\nu = 3 + q_1$. It is convenient to note that the frame of reference is fixed to the ablation region (to both ablation fronts since the plateau length is considered a constant). Therefore, the unperturbed velocity corresponds to the ablation velocity of the expanding plasma.

Steady one-dimensional profiles (subscript 0) come from the integration of equations

$$v_0/v_t = \rho_t/\rho_0 = \theta_0, \tag{88}$$

$$\begin{cases} \theta_0 - \left(\theta_0^{5/2} + \Delta\theta_0^{\nu}\right)\theta_0' = r_D & \text{for } \theta_0 < 1 \\ \left(\theta_0 - \theta_0^{5/2}\theta_0'\right)' = -\beta_t \theta_0^{-11/2}\left(\theta_0^4 - 1\right) & \text{for } \theta_0 \geq 1 \end{cases} \tag{89}$$

where $\theta_0 = T/T_t$ is the dimensionless temperature, r_D is the ratio between density at the transition temperature and the peak density ($r_D = \rho_t/\rho_a < 1$), ν is the power index of the Rosseland-like radiative conductivity, $\Delta = \kappa_{Rt}/\kappa_t$, $\beta_t = 16\left(\sigma T_t^4\right)\left(\kappa_t T_t\right) / \left(5P_0 v_t\right)^2$ and the prime denotes derivative respect to the spatial coordinate $\eta = y/L_{St}$ normalized with the Spitzer length at the transition temperature, $L_{St} \equiv 2\kappa_t T_t / \left(5P_0 v_t\right)$. Note that all the dimensionless variables are normalized by their values at the transition temperature (subscript t). Observe as well that to obtain the first equation of (89), the energy equation in the optically thick region has been integrated with the boundary condition $\theta_0(-\infty) = r_D$. Equation (89) only requires one boundary condition to be integrated. The object of this boundary condition is to fix the origin of coordinates, which is arbitrary. One can choose the origin of coordinates in any point of temperature, within this thesis we will usually apply $\theta_0(0) = 1$.

To simplify the analysis it is convenient to express equation (89) seeting θ_0 as the independent variable:

$$\begin{cases} z = \left(\theta_0 - r_D\right) / \left(\theta_0^{5/2} + \Delta\theta_0^{\nu}\right) & \text{for } \theta_0 < 1 \\ \frac{dz}{d\theta_0} = \frac{z - \frac{5}{2}\theta_0^{3/2} z^2 + \beta_t \theta_0^{-11/2}\left(\theta_0^4 - 1\right)}{\theta_0^{5/2} z} & \text{for } \theta_0 \geq 1 \end{cases} \tag{90}$$

where $z(\theta_0) = \theta_0'$. Numerical integration is straightforward, we only need to ensure the continuity of z at $\theta_0 = 1$. We can obtain the dimensionless profiles by solving the ordinary differential equation (ODE) $d\theta_0/d\eta = z$ with an arbitrary boundary condition that fixes the origin of coordinates.

The system of equations (84)-(87) provides a wide range of solutions. This variety of flow types can be explained by the presence of three different char-

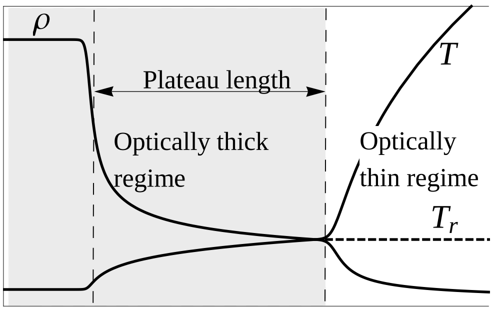

Figure 16: Schematic of the hydrodynamic profiles in the ablation front region.

acteristic lengths in the problem [34]. These characteristic lengths are associated with the different energy transport mechanisms that are considered. In particular, two of them related to the radiation, these are the Rosseland and Planck photon mean free paths, and the last one, the Spitzer length L_S, related to the electron thermal diffusion. In the dimensionless system of equations (89), the characterization of the flow is reduced to four parameters: r_D, ν, Δ and β_t. It is then useful to see the parameters Δ and β_t as the local values, at the transition temperature, of ratios between the characteristic lengths. That is,

$$\Delta = \frac{1}{\mathrm{Bo}} \frac{l_R}{L_S}\bigg|_t, \quad \beta_t = \frac{1}{\mathrm{Bo}} \frac{L_S}{l_P}\bigg|_t. \tag{91}$$

One can estimate the distance between the two fronts by integrating equation (89). There are different possibilities to define the plateau length (d_P) depending on the criteria to situate the ablation fronts. Within this thesis, we will define the plateau length as the distance between the minimum of the density gradient scale length ($|\rho/\left(d\rho/dy\right)|$) at the inner front and the transition temperature ($\theta_0 = 1$), that is estimated as the point where radiation and matter temperatures are equal. Thus, under the assumption of radiation dominated flow at the peak density (ρ_a), we can reduce the energy equation of the inner front (89) to $\theta_0 - \Delta\theta_0^{\nu}\theta_0' \simeq r_D$. The density gradient scale length is defined as $L = |\theta_0/\theta_0'|$ and the point where its minimum takes place at the inner front is determined by setting $L' = 0$, that leads to

$$\theta_0^* = \theta_0|_{L_{\min}^{RA}} = r_D\left(\nu+1\right)/\nu, \tag{92}$$

and the minimum length reads

$$L_{\min}^{RA} = \Delta r_D^{\nu}\left(\nu+1\right)\left(1+\frac{1}{\nu}\right)^{\nu}. \tag{93}$$

The plateau length is then estimated by integrating the energy equation between $\theta_0 = \theta_0^*$ and $\theta_0 = 1$, that leads to

$$d_P = \Delta L_{St} \phi, \tag{94}$$

where ϕ is the definite integral $\int_{\theta_0^*}^{1} \theta_0^{\nu} \left(\theta_0 - r_D\right)^{-1} d\theta_0$. So, if we use the definition of the parameter Δ (91), we see that the plateau length scales up as $d_P \propto l_{Rt} \mathrm{Bo}_t^{-1}$, that is to say, as the radiation effects get stronger in the vicinity of the outer ablation front (i.e. for decreasing values of Bo_t), the distance between two fronts will be longer. Notice as well that for a very large radiation heat power index ($\nu \gg 1$), the inner ablation front gets steeper ($L_{\min}^{RA} \ll 1$) and collapses into a surface interface of a zero thickness. In this case, the point of minimum gradient scale length is obviously situated in the ablation front discontiuity, that is to say, $\theta_0^* \to r_D$, and a simple expression can be found for the plateau length, $d_P \simeq \Delta L_{St} / \left(\nu \left(1 - r_D\right)\right)$.

5

RECAPITULATIF DE LA PARTIE I ET INTRODUCTION À LA PARTIE II (FRENCH VERSION)

L'energie de fusion apparaît comme une alternative aux sources d'énergie conventionnelles. Les premiers efforts de recherche civile sur cette source d'énergie ont commencé il y a plus de 40 ans. Celle-ci repose sur la réaction de fusion de deux éléments légers pour donner un élément plus lourd et la libération d'énergie. En général, le combustible utilisé est un mélange de deutérium et tritium en raison de la haute probabilité que la réaction se produise. Cependant, une énorme quantité d'énergie est demandée pour atteindre les conditions nécessaires au déclenchement de ces réactions. Le critère de Lawson estime que l'ignition aura lieu si le combustible satisfait au moins une valeur de $p\tau_e = 8.3\,\mathrm{atm}\cdot\mathrm{s}$ avec $T = 15\,\mathrm{keV}$, où p est la pression, T la température et τ_e le temps de confinement. Le problème qui se pose est comment confiner le combustible à l'état plasma avec une température si élevée. Deux approches sont envisagées pour contrôler la fusion : soit on maintient le combustible a une pression de quelques atm pendant quelques secondes confiné avec une piège magnétique (fusion par confinement magnétique), soit on atteint des conditions extrêmes de pression (Gatm) pendant un intervalle très court (dixièmes de ns) et le combustible est confiné avec ses propres forces d'inertie (fusion par confinement inertiel). Cette thèse s'inscrit dans le contexte de la fusion par confinement inertiel (FCI).

L'énergie de fusion est une voie prometteuse pour la production d'énergie. On peut énumérer trois importants avantages par rapport à d'autres sources d'énergie :

- l'abondance du combustible (deutérium et tritium),
- le manque de déchets radioactifs à vie longue, et
- la non dépendance vis-à-vis de saisons ou conditions météorologiques.

Néanmoins, elle est toujours une source d'énergie pour l'avenir qui nécessite un gros effort de recherche et développement technologique. Les plus optimistes prévisions parlent de décades avant qu'on puisse utiliser l'énergie de fusion.

LES BASES DE LA FCI

Le concept de la FCI est de brûler quelques milligrammes de combustible thermonucléaire très comprimé dans un intervalle de temps extrêmement court. Les conditions en densité peuvent être atteintes avec l'implosion d'une coquille sphérique qui reçoit un important apport d'énergie au moyen de nombreux faisceaux laser. Dans le schéma de l'attaque directe, les faisceaux laser irradient directement la surface de la cible en la chauffant. Ce fait mène à l'ablation de la couche la plus externe de la cible et génère au même moment, par la conservation de la quantité de mouvement, la pression nécessaire pour provoquer l'implosion violente de la cible. Si l'implosion est suffisamment symétrique, à la fin de la compression le centre de la cible aura atteint les conditions requises pour l'ignition (point chaud central). On peut donc énumérer les différentes étapes de l'attaque directe :

- irradiation,
- implosion de la cible pour l'ablation de la couche externe,
- ignition par point chaud central, et
- déflagration et explosion.

INSTABILITÉ DE RAYLEIGH-TAYLOR

Cette thèse se concentre sur un processus physique qui a lieu pendant la phase de l'implosion de la cible et qui consiste en la croissance instable de perturbations de la surface externe de la cible. Au début de la compression, la surface n'est pas parfaitement lisse mais il existe de petites déformations provenant d'inhomogénéités de l'irradiation laser ou de défauts inhérents de fabrication. Pendant l'implosion de la cible, la couche externe comprimée est continuellement ablatée et génère un plasma de basse densité en expansion. Dans le référentiel du front d'ablation, un plasma de basse densité accélère la matière comprimée vers l'intérieur. C'est une des situations typiques qui favorisent le développement de l'instabilité de Rayleigh-Taylor et, en conséquence, une source potentielle de dégradation de la compression de la cible qui peut même provoquer la rupture de la coquille.

L'évolution de l'interface instable est assez compliquée. Dans le cas classique où il n'y a pas de flux de matière ablatée au travers de l'interface qui sépare les deux fluides, Sharp [36] décrit différents phases du développement de l'instabilité Rayleigh-Taylor :

- Phase 1. Si les perturbations de l'interface sont initialement suffisamment petites, cette première phase du développement de l'instabilité peut être analysée avec la forme linéarisée des équations de la mécanique des fluides. Les perturbations de longueur d'onde λ évoluent donc exponentiellement en temps, $\propto \exp\left(\sqrt{A_T k g t}\right)$, où $k = 2\pi/\lambda$ est le nombre d'onde de la perturbation, g l'accélération, A_T est le nombre d'Atwood définie comme $A_T = (\rho_h - \rho_l)/(\rho_h + \rho_l)$ et ρ_h et ρ_l sont les densités du fluide lourd et légère, respectivement.

- Phase 2. La perturbation croît de façon non-linéaire jusqu'à ce que son amplitude soit de l'ordre de grandeur de la longueur d'onde λ. Le développement de la perturbation est fortement influencé par les effets tridimensionnels et le nombre d'Atwood.

- Phase 3. Cette phase est caractérisée par le développement des structures en aiguilles et bulles.

- Phase 4. On trouve dans cette phase, entre autre, la rupture des aiguilles, ce qui mène au régime turbulent et au mélange chaotique de deux fluides.

Dans cette thèse on s'intéresse à la première phase, la phase linéaire. On vient de voir que dans le cas classique, l'interface est instable pour n'importe quelle longueur d'onde de la perturbation. Cependant le cas ablatif dans le contexte de la FCI est différent, précisément pour le flux de matière ablatée qui traverse l'interface (front d'ablation). L'effet du flux de matière ablatée est stabilisateur et il peut mener à la suppression de l'instabilité pour certaines longueurs d'onde de la perturbation. Bien que cette stabilisation rend l'instabilité de Rayleigh-Taylor ablative moins dramatique que dans le cas classique, elle est toujours dangereuse et peut mener à la rupture de la coquille. Les différents mécanismes de stabilisation sont les suivants :

Force de rappel. L'effet de la pression dynamique

C'est le mécanisme de stabilisation ablative dominant et il est dû à la réaction dans la pression dynamique qui tend à équilibrer la force d'inertie. On peut le voir comme une surpression générée dans les pics de la perturbation et une sous-pression dans les vallées qui relâchent la perturbation.

L'effet « fire polishing »

Cet effet est l'expulsion physique de la perturbation du fait de l'ablation. En effet, le développement instable de la perturbation est toujours localisé dans le front d'ablation, mais celui-ci est continuellement consommé par l'ablation et le « nouveau » front d'ablation est moins perturbé que « l'ancien ».

L'effet de la convection de vorticité

Le processus d'ablation génère de la convection de vorticité à travers le plasma de basse densité qui a un effet stabilisant.

LE DESIGN DE LA CIBLE : LE CHOIX DE L'ABLATEUR

Dans l'approche de l'attaque directe, il y a fondamentalement deux effets qui peuvent empêcher l'assemblage correct du combustible :

- Préchauffage de la cible, généré par des électrons suprathermiques produits par des instabilités de l'interaction laser-plasma, et
- Instabilités hydrodynamiques de la cible en implosion.

Le matériau pour l'ablateur peut influencer les deux effets et, ainsi, son choix est un paramètre important à considérer pour les designs de cible.

Instabilités hydrodynamiques

Les premières expériences d'implosion d'une cible ont été réalisées avec des matériaux hydrogénoïdes (glace de deutérium et tritium, nombre atomique bas) et une fine couche de plastique. L'utilisation de ce type de matériaux est favorisée pour sa densité relativement basse qui leur permet d'atteindre de hautes vitesses d'ablation et un rapport d'aspect en vol peu élevé qui leur confère de bonnes propriétés de stabilité hydrodynamique.

Le choix d'un ablateur non-hydrogénoïdes (donc, de nombre atomique plus élevé) est suspect de détériorer les propriétés de stabilité hydrodynamique de la coquille. En effet, si on veut atteindre de hautes vitesses d'implosion, on doit mincir la coquille parce qu'elle est faite d'un matériau plus lourd. Donc, on se trouve avec une cible de haut ratio d'aspect en vol qui présente des mauvaises propriétés de stabilité hydrodynamique. Cependant, ce raisonnement n'est pas tout à fait vrai et des expériences réalisées par Fujioka et al. [11]] sur l'installation laser GEKKO XII (Osaka, Japon) ont montré que l'utilisation de plastiques brominés réduit la croissance de l'instabilité Rayleigh-Taylor ablative. La cause de cette stabilisation est apparemment due aux effets radiatifs, notamment pour l'augmentation de la vitesse d'ablation et la longueur caractéristique du profil de densité. Lors de simulations réalisées dans cette étude, Fujioka observe l'apparition des structures à double front d'ablation.

Interaction laser-plasma

La région de la couronne (plasma de basse densité) est riche en processus physiques liées à l'interaction laser plasma. En effet, l'absorption des faisceaux laser implique l'apparition des modes collectives d'interaction avec le plasma. Quelques-uns ont une croissance instable avec un effet négatif dans la fusion inertielle qui doit être minimisé. Entre les différentes instabilités paramétriques qui peuvent se développer, on s'intéresse à l'instabilité « two plasmon decay » (TPD). Cette instabilité génère des populations d'électrons chauds qui préchauffent la cible. Ces électrons sont générés par des ondes de plasma en raison de l'interaction des électrons qui se déplacent avec la vitesse de phase de l'onde. Ces électrons peuvent être piégés dans des ondes de plasma de haute amplitude et être accéléré à des vitesses élevées. Les électrons chauds pénétreront alors à l'intérieur de la cible en la préchauffant et, par conséquent, en augmentant son entropie. Ce préchauffage est un obstacle pour atteindre les conditions de compression requises pendant l'implosion de la cible pour atteindre l'ignition.

Des expériences ont été réalisées sur l'installation laser OMEGA (Rochester, USA) pour démontrer qu'avec des implosions de cible réalisées au moyen de faisceaux laser, on peut atteindre des haute taux de compression. Pendant ces campagnes expérimentales, le rôle des électrons chauds dans le préchauffage a été étudié avec les résultats suivants:

- Le préchauffage de la cible dû aux électrons chauds générés par l'instabilité TPD dans la couronne est corrélé avec une augmentation significative de l'entropie de la cible. [39]
- Des ablateurs en plastique réduisent les niveaux de préchauffage comparé à des ablateur en glace de deutérium.[30]
- L'utilisation de la silice comme ablateur réduit significativement le préchauffage par électrons chauds avec des intensités laser de $1 \times 10^{15}\,\mathrm{W/cm^2}$.[40]

Ces études montrent l'intérêt d'utiliser des matériaux de nombre atomique modéré (comme la silice et les plastiques dopés) comme ablateur dans la FCI.

THÉORIE HYDRODYNAMIQUE RADIATIVE POUR LE DOUBLE FRONT D'ABLATION

Le développement d'une structure à double front d'ablation pendant l'implosion de la cible est directement lié à l'importance des effets du flux d'énergie radiative dans la zone d'ablation. Une condition nécessaire pour le développement de ce type de structures exige que le flux d'énergie radiatif soit comparable au flux d'énergie de la matière. Le nombre de Boltzmann mesure le poids relatif de la contribution radiative. Il peut être défini de la façon suivante

$$\mathrm{Bo} = \frac{\frac{5}{2} P_a v}{4\sigma T^4},$$

où σ est la constante de Stefan-Boltzmann. Ainsi, pour un nombre de Boltzmann suffisamment petit le flux d'énergie radiative aura une incidence sur l'hydrodynamique et les équations qui décrivent les profils hydrodynamiques du problème doivent contenir la contribution radiative. En 2009, Sanz et al. [34] ont présenté une telle théorie. La description de la région d'ablation subsonique contient trois contributions d'énergie différentes :

- La contribution du flux d'énergie d'enthalpie. Cette contribution prend en compte les effets de la convection d'énergie interne ainsi que le travail fait par les forces de pression.
- La contribution de la conduction thermique électronique. En effet, une partie de l'énergie laser absorbée dans la région de la couronne est menée vers la couche d'ablation par le flux de chaleur électronique. Il est décrit par la loi de Fourier avec une conductivité qui dépend fortement de la température [41].
- La contribution du flux d'énergie radiative. Les photons énergétiques qui sont émis dans la région de la couronne (pour la transition de couche électronique des atomes ou molécules de l'ablateur) et ils sont absorbés dans des régions plus opaques (le front d'ablation radiative). Cette contribution est décrite avec une approximation de diffusion à deux températures (la température de la matière et la « température » de radiation).

Cette théorie indique qu'en dessous d'une certaine valeur critique du nombre de Boltzmann, Bo^*, (évalué dans le pic de densité), un deuxième minimum dans la longueur caractéristique de la densité apparait dans la région d'ablation. Cela implique la formation d'un deuxième front d'ablation à peu près où la température de la matière et la température radiative sont égales. Le flux d'énergie est pratiquement dominé par le flux radiatif dans la région entre les deux fronts d'ablation. Si l'on diminue le nombre de Boltzmann, une région de densité/température (le plateau) constante se développe entre les deux fronts d'ablation. L'épaisseur de cette région augmente si le nombre de Boltzmann diminue. Autour du deuxième front d'ablation, une couche de transition se développe où le flux radiatif change de signe. Des fronts d'ablation électronique-radiatifs raides se développent avec la condition

$$\beta_t \equiv \frac{16}{25} \frac{\left(\sigma T_t^4 K_{Pt}\right)\left(k_t T_t\right)}{\left(P_t v_t\right)^2} > 1,$$

où k est la conductivité thermique électronique,K_P l'opacité moyenne de Planck, et l'indice « t » fait référence aux conditions dans le deuxième front.

Dans cette thèse, on va utiliser une simplification de la théorie hydrodynamique radiative pour décrire le double front d'ablation (aussi bien pour le fluide de base à l'équilibre que pour le fluide perturbé). Cette simplification suppose deux limites asymptotiques pour l'ordre de grandeur de l'opacité de l'ablateur qui mène à deux régimes radiatifs différents :

- Régime optiquement épais ($T < T_t$). Ce régime s'utilise pour la description du front d'ablation radiatif et la région du plateau. Le flux radiatif se comporte comme un flux de conduction thermique (loi de Fourier).
- Régime optiquement mince ($T > T_t$). Ce régime s'utilise pour la description du front d'ablation électronique-radiatif et la couronne. La température radiative est considérée constante et le flux radiatif est décrit par une loi de refroidissement.

Les équations qui gouvernent ce problème sont alors dans l'approximation isobare

$$\frac{\partial \rho}{\partial t} + \nabla \cdot (\rho \vec{v}) = 0,$$

$$\rho \frac{\partial \vec{v}}{\partial t} + \rho\left(\vec{v} \cdot \nabla\right)\vec{v} = -\nabla p + \rho \vec{g},$$

$$\nabla \cdot \left(\frac{5}{2} P_0 \vec{v} - \bar{\kappa} T^{5/2} \nabla T + \vec{S}_r \right) = 0,$$

$$\begin{cases} \vec{S}_r = -\bar{\kappa}_R T^{\nu} \nabla T & \text{for } T < T_t, \\ \nabla \cdot \vec{S}_r = 4\sigma \bar{K}_P T^{-11/2} \left(T^4 - T_t^4 \right) & \text{for } T > T_t. \end{cases}$$

L'ANALYSE DE STABILITÉ

L'étude de la phase linéaire de l'instabilité de Rayleigh-Taylor ablative dans le contexte de la FCI commença il y a plus de 35 ans. Deux méthodes principalement ont été utilisées pour l'analyse de la stabilité d'un seul front d'ablation: la méthode de discontinuité et la méthode auto-consistante.

Méthode de discontinuité

Ce type de méthode a été utilisé depuis le début (Bodner [5], Baker [2], Manheimer and Colombant [23], Kull and Anisimov [18]). Il est basé sur l'hypothèse d'un front d'ablation d'épaisseur nulle et des écoulements homogènes des deux côtés de cette interface. Le problème ne peut pas être fermé mathématiquement avec les lois de conservation à travers la surface d'ablation, mais il faut incorporer d'information additionnelle, notamment sur la région de la couronne. Le choix de l'équation de fermeture définie la validité physique du modèle, et, au cours des premières années, ce fut un point de controverse majeur.

En 1997, Piriz et al. [27] publie un nouveau modèle de discontinuité avec l'objectif de surmonter toutes les difficultés qui étaient présentes dans les tentatives précédentes. Il y a deux considérations importantes dans le travail de Piriz

1. La reconnaissance que le front d'ablation est un isotherme, ce qui est une correcte condition aux limite du problème, et
2. L'introduction correcte de la longueur caractéristique du mécanisme de déposition de l'énergie qui régit l'ablation.

Le dernier point signifie que la formule de la relation de dispersion est dérivée avec un paramètre inconnu, le rapport entre la densité du fluide léger et du fluide lourd. La détermination de ce paramètre peut se faire avec un modèle simple de la couronne ou avec des simulations unidimensionnelles, c'est-à-dire, on fournit l'information sur la structure de la région de la couronne a posteriori par contraste avec les modèles précédents où cette information est une hypothèse de départ.

Méthode auto-consistante

L'étude de la stabilité d'un écoulement avec un modèle auto-consistant résout chaque quantité hydrodynamique comme une composant d'ordre zéro et une petite perturbation (composant d'ordre un) avec les même équations. On commence par l'analyse des variables d'ordre zéro, qui seront utilisés ultérieurement comme fluide de base. Ensuite, après avoir linéarisé les équations, on obtient les équations auto-consistantes pour les composantes spectrales des perturbations. Les quantités d'ordre zéro apparaissent comme des coefficients dans les équations perturbées. Finalement, la résolution de ces équations mène à la détermination du taux de croissance linéaire de l'instabilité de Rayleigh-Taylor ablative.

Les premières tentatives de résolution de la stabilité d'un seul front d'ablation apparaissent dans les années 1970 (Shiau et al. [37], Henderson et al. [15], Brueckner et al. [7]). Elles résolvent les équations numériquement comme un problème de valeur initial, c'est-à-dire, elles considèrent le problème temporel des perturbations. Ces premières tentatives concluent que le flux de matière ablatée stabilise l'instabilité de Rayleigh-Taylor, mais le mécanisme de stabilisation reste inconnu.

Dans les années 1980 une nouvelle stratégie de résolution fut proposée par Takabe et al. [42, 43]. Celle-là consiste, d'abord, en l'expression des équations linéarisées comme un système d'équations différentielles couplées de premier ordre pour le résoudre numériquement, ensuite, comme un problème aux valeurs propres. La valeur propre est le taux de croissance linéaire de la perturbation. Takabe menait une étude systématique de la relation de dispersion en faisant varier deux paramètres : l'accélération et le rapport entre le pic de densité et la densité au point sonique. Il trouva une formule de raccordement, connue comme la formule de Takabe,

$$\gamma = \alpha\sqrt{kg} - \beta k v_a,$$

où v_a est la vitesse du plasma à travers le front d'ablation, et α et β sont deux paramètres adimensionnés qui prennent les valeurs approximatives

$\alpha = 0.9$ et $\beta = 3.1$.

Toutes ces études numériques ne proportionnent pas une compréhension claire de la phase linéaire de l'instabilité de Rayleigh-Taylor ablative et quelques questions, comme les mécanismes d'ablations restèrent des hypothèses. Cependant, dans les années 1990 plusieurs études auto-consistantes analytiques furent publiées en apportant pour la première fois les lois d'échelle et les mécanismes de stabilisation de l'instabilité (Bychkov et al. [8], Sanz [31, 32], Goncharov et al. [13, 14], Betti et al. [4]). Ces modèles ont en commun quelques hypothèses comme l'écoulement isobarique autour du front d'ablation et la géométrie plane. La résolution analytique n'est possible que dans certains cas limite. Pour cette raison, le fluide de base et le problème perturbé aux valeurs propres est divisé en régions avec des lois d'échelles différentes dont les solutions sont raccordées rigoureusement avec des techniques de raccordement (par exemple l'approximation Wentzel-Kramers-Brillouin, WKB). Trois régions sont identifiées généralement pour un seul front d'ablation, associées avec une longueur caractéristique différente de la fonction propre,

- la région sur-dense,
- le front d'ablation, et
- la région en expansion.

Ces études analytiques ont permis d'identifier les mécanismes de stabilisation qui dépendent du régime d'accélération. Ainsi, pour des valeurs $\mathrm{Fr} \gg 1$ (régime d'accélération faible) les principaux effets stabilisateurs sont dus à l'ablation de matière et à la force de rappel de la pression dynamique. Par contre, pour des valeurs $\mathrm{Fr} \ll 1$ (régime d'accélération fort), les perturbations sont stabilisées avec la convection ablative et le lissage thermique.

Part II

STABILITY OF SINGLE ABLATION FRONTS

This part of the thesis is devoted to the stability analysis of single ablation fronts. A method for the numerical computation of the linear growth rate of the ablative Rayleigh-Taylor instability is presented for the case of an electron-radiative ablation front, and the same procedure is applied afterwards in a radiative ablation front to study its instability. In the latter case, the results are compared with existing linear theories that are widely used by the inertial fusion community. Besides, an analytical development is performed in the case of very steep electron-radiative ablation fronts where radiation transport effects are dominant, leading to a dispersion relation formula that fits considerably well the numerical results.

Veritatis simplex est oratio

6

ELECTRONIC-RADIATIVE ABLATION FRONT

An electronic-radiative ablation (ERA) front does not develop alone in the ICF context, but jointly and behind a primary ablation front (the so-called radiative ablation (RA) front) provided the presence of strongly enough radiation energy transport effects in the ablation region. The development of an ERA front is directly related to

- the laser irradiation conditions, namely the laser intensity, I_L, and
- the ablated material, namely the atomic number, Z.

In particular, an increase of any of these two parameters contributes to the formation of an ERA front and a further increase brings about a clearly-formed double ablation (DA) front structure with both fronts separated by a region of almost constant density (plateau) of thickness d_p. Moreover, contrary to the primary ablation front, an ERA front is not formed immediately after the laser is turned on, but a time interval prior to its appearance (which is inversely proportional to I_L and Z) is necessary [10].

The aim of this chapter is to study a linear stability of a single ERA front. For this purpose, it is necessary to ensure the conditions that allow to isolate the perturbations of this ablation front from the influence of the primary one. This fact strictly implies some constraints on the characteristic lengths of the problem. In particular, we will consider that the plateau length is very large compared to the characteristic length of the ERA front (l_e) and to the wavelength of perturbation (λ), that is to say, $d_p/\lambda \gg 1$ and $d_p/l_e \gg 1$. The fulfillment of these conditions requires the development of a steep ERA front, which is obtained [34] for values

$$\beta_t = \frac{16}{25}\frac{\left(\sigma T_t^4 K_{Pt}\right)\left(\kappa_t T_t\right)}{\left(P_t v_t\right)^2} > 1, \tag{95}$$

where the subscripts t refer to the conditions at the plateau density/temperature (ρ_t, T_t).

Linear stability is studied numerically and analytically with a self-consistent model of the background flow. A sharp boundary model is derived from the dominant order of the self-consistent model. Thus, this chapter is divided as follows. First, a one-dimensional theory for the steady density/temperature profiles around the ERA front is developed from the dynamic equations of a fluid. Second, a numerical method for the calculation of the linear stability is presented. And last, an analytical self-consistent model is developed in the asymptotic limit of very steep ERA fronts ($\beta_t \gg 1$).

6.1 ONE-DIMENSIONAL ISOBARIC MODEL AROUND THE ERA FRONT

We consider a subsonic and steady ablation front resulting from an incoming heat flow from a low density region, an ablated mass flow from a high density region, and a uniform pressure P_t across the ablation front. This description can be considered appropriate inside the ablation region within a layer in the vicinity of the second minimum density gradient scale length. Three energy fluxes are involved within this region:

- the convection of energy, $\propto Pv$, where P is the pressure that this layer is subjected at, and v is the ablation velocity,
- an electronic heat flux, $q_e = -\kappa(T) dT/dy$ and
- a radiation flux, S_r.

It is assumed that in this region the matter is transparent, that is to say, the mean free path of photons is very large, $l_{mfp} \gg 1$. This assumption implies an almost constant radiation temperature, which is considered equal to the temperature in the plateau ($\approx T_t$). Thus, the model chosen for the radiation transport is an optically thin approximation with one spectral-average absorption coefficient, the Planck mean opacity, K_p, and a constant radiation temperature. The radiative energy flux is described then as a *radiative cooling law* that results into energy losses. Equal ion and electron temperatures and the equation of state of an ideal gas with a density $\rho \approx P_t/T$ are assumed.

Let us consider an unbounded plasma slab under a constant acceleration along the longitudinal direction, y. All variables depend only on this spatial coordinate y. In the slab frame of reference, the basic hydrodynamic equations for the temperature (or mass density $\rho_0 \propto T_0^{-1}$) and velocity $\overrightarrow{v_0} = (0, v_0, 0)$ are

$$\rho_0 v_0 = \rho_t v_t, \quad \rho_0 T_0 = \rho_t T_t, \tag{96}$$

$$\frac{d}{dy}\left(\frac{5}{2}\rho_0 v_0 T_0 - \kappa \frac{dT_0}{dy} + S_r\right) = 0, \tag{97}$$

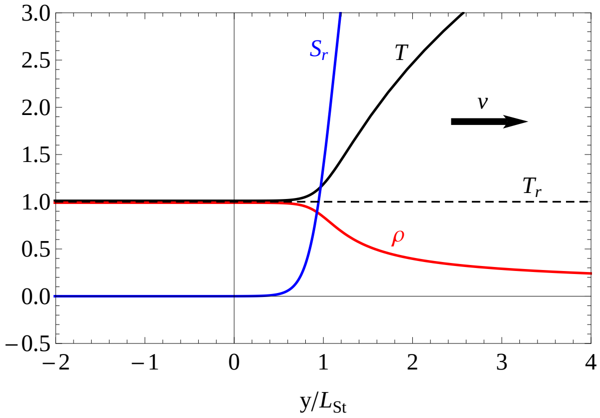

Figure 17: Normalized steady profiles of an ideal ERA front for $\beta_t = 20$ and $q_2 = 11/2$. Radiative energy flux S_r, radiation temperature and matter temperature and density are plotted vs normalized coordinate. The direction of the ablation velocity is represented.

The Spitzer electronic thermal conductivity is written as $\kappa_0 = \kappa_t \left(T_0/T_t\right)^{5/2}$. Notice that in the one-dimensional model the momentum equation is not needed due to the isobaric approximation. This assumption is based on the fact that the flow is highly subsonic and on neglecting the hydrostatic pressure, $\rho g \left|y\right| / P_t \ll 1$, through the relevant ablation layer. For the radiation energy transport we use a diffusion approximation in the spectral average form

$$\frac{dS_r}{dy} = 4\sigma K_P \left(T_0^4 - T_t^4\right). \tag{98}$$

Equation (98) involves the Planck mean volume opacity K_P. This opacity is in general a function depending on the matter temperature and density, but, because of the isobaric approximation, the dependence is reduced to only one hydrodynamic quantity, e.g. the temperature $K_P = K_{Pt} \left(T_0/T_t\right)^{-q_2}$, where K_{Pt} is the opacity at the plateau region. In the case of fully ionized plasma, Zeldovich and Raizer [50] found that the power index of the Planck mean opacity is $q_2 = 11/2$. The system of equations (96)-(98) can be written as a second order ordinary differential equation (ODE) on the temperature, that will be solved with the following boundary conditions

$$\begin{aligned} T_0(y \to -\infty) &= T_t, \\ T_0'(y \to -\infty) &= 0, \end{aligned} \tag{99}$$

that correspond to the plateau region.

6.1.1 *Normalized equations*

Normalized flow variables are obtained with the values of steady profiles at the plateau region and the characteristic length for the electronic thermal diffusion or the *Spitzer length*, $L_{St} = \kappa_t T_t/((5/2)P_t v_t)$,

$$\theta_0 = \frac{T_0}{T_t}, \quad \eta = \frac{y}{L_{St}}. \tag{100}$$

Then, equations (96)-(98) and the boundary conditions (99) can be rewritten in the following simple forms,

$$\frac{v_0}{v_t} = \frac{\rho_t}{\rho_0} = \theta_0 \tag{101}$$

$$\left(\theta_0 - \theta_0^{5/2}\theta_0'\right)' = -\beta_t\theta_0^{-q_2}\left(\theta_0^4 - 1\right) \tag{102}$$

$$\begin{aligned} \theta_0(\eta \to -\infty) &= 1 \\ \theta_0'(\eta \to -\infty) &= 0 \end{aligned} \tag{103}$$

where the prime denotes a derivative with respect to the normalized spatial coordinate η (see example in figure 17). Note that the system of equations is a *translational invariant* with respect to the spatial coordinate η. Thus, in order to simplify the analysis, it is convenient to express equation (102) without the spatial coordinate, setting θ_0 as an independent variable:

$$\underbrace{\theta_0\frac{d\psi}{d\theta_0} + \psi}_{\text{electronic}} = \underbrace{1}_{\text{convective}} + \underbrace{\beta_t\frac{\theta_0^n\left(1 - \theta_0^{-4}\right)}{\psi}}_{\text{radiative}} \tag{104}$$

where $\psi \equiv \theta_0^{3/2}d\theta_0/dy$ and $n = 11/2 - q_2$. The boundary condition for solving this equation is $\psi(\theta_0 \to 1) = 0$, which is equivalent to the boundary conditions (103). It is possible to recover the density/temperature profiles by solving $d\theta_0/dy = \theta_0^{-3/2}\psi$, with a condition that, for example, fixes the origin of coordinates. We will usually impose that at $\eta = 0$ there is the mimimum density gradient scale length, $\min(|d\log\rho/dy|^{-1})$.

The solution of equation (104) depends on two parameters, n and β_t. The parameter n depends on the degree of ionization of the plasma. The main interest of this study lies in the case $n = 0$, which corresponds to a fully ionized plasma [50], since the ERA front and the near-corona are very hot regions and we assume that the plasma is fully ionized there. However, other values of n are physically reasonable for plasmas, especially positive values ($n \leq 1$) that can correspond to partially ionized plasmas. For the sake of completeness, we will consider in the study negative values of n close to zero. The parameter β_t comes naturally into equation (102) from the normalization. This parameter rules the energy equation and causes the existence of different flow types in the problem. It is useful to handle alternative definitions of this parameter that contribute to a more concise physical meaning. For instance, it can be seen as the ratio of the two characteristic lengths of the problem since $\beta_t = \mathrm{Bo}^{-1}(L_S/l_P)\Big|_t$ where Bo_t represents the Boltzmann number at the plateau region and l_{Pt} the Planck photon mean free path. Alternatively, the parameter β_t can also be defined as a ratio among the different energy fluxes present at the ERA front. In particular,

$$\beta_t = \frac{radiative/electronic}{(convective/electronic)^2} \tag{105}$$

The condition $\beta_t \gg 1$ is then equivalent to a situation where practically all the electronic heat flux that drives the ERA front is outwardly radiated by a radiative cooling process.

Some examples of dimensionless density profiles are plotted in figure 18. Observe that increasing values of β_t leads to steeper plasma density/temperature profiles, with the limit case of $\beta_t \gg 1$ where the ablation front can be considered of zero-thickness. The influence of the parameter n is less marked than β_t and its modification slightly changes the minimum density gradient scale length. Nevertheless, the impact of the parameter n in the near-corona region is not negligible.

6.1.2 *Asymptotic behaviours*

The following asymptotic behaviours can be obtained from equation (102)

6.1.2.1 *1. The plateau region. Limit $\theta_0 \to 1$, $\eta \to -\infty$*

We take $\epsilon = \theta_0 - 1$ as a small parameter ($\epsilon \ll 1$) and develop the equation (102) up to $\mathcal{O}(\epsilon^2)$, getting reduced to

$$z\frac{dz}{d\theta_0} - z - 4\beta_t\left(\theta_0 - 1\right) \simeq -\frac{5}{2}\left(z^2 + z\frac{dz}{d\theta_0}\left(\theta_0 - 1\right)\right) - 16\beta_t\left(\theta_0 - 1\right)^2, \tag{106}$$

where it is assumed that $z \equiv \theta_0'$ can be defined as a power series in the small parameter ϵ ($z = \sum_{i=1}^{\infty} a_i \epsilon^i$), so that it automatically fulfills the boundary

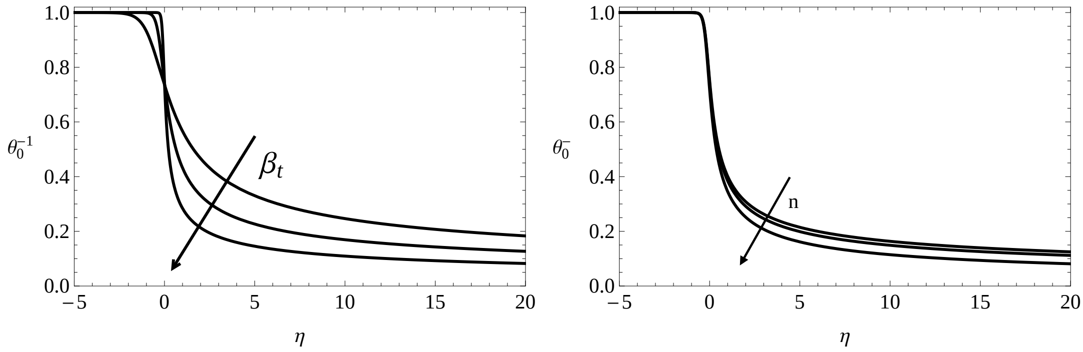

Figure 18: Dimensionless density profile vs dimensionless spatial coordinate. Figure at the left: $n = 0$ and different values of the parameter β_t (1, 5 and 100). Figure at the right: $\beta_t = 20$ and different values of n (-0.5, 0 and 1).

condition $\psi(1) = 0$. Note that the left-hand side of equation (106) is of the order of $\mathcal{O}(\epsilon)$, and the right-hand side $\sim \mathcal{O}\left(\epsilon^2\right)$. This equation is then trivially solved giving the solution $z \simeq a_0\epsilon + a_1\epsilon^2$ where

$$a_0^+ = \frac{1+\sqrt{1+16\beta_t}}{2}, \tag{107}$$

and

$$a_1^+ = -\frac{5\left(a_0^+\right)^2 + 16\beta_t}{3a_0^+ - 1}. \tag{108}$$

The temperature profile is recovered by integrating the equation $z = d\theta_0/dy \simeq a_0^+(\theta_0 - 1)$,

$$\theta_0 \simeq 1 + c_0 e^{a_0^+\eta}, \tag{109}$$

where c_0 is a constant which is determined by fixing the origin of coordinates. This analytic solution is used in the numeric computation as the starter boundary condition.

Notice that for very steep ERA fronts ($\beta_t \gg 1$), the asymptotic solution takes the form $z \simeq 2\sqrt{\beta_t}\epsilon\,(1 - 3\epsilon)$.

6.1.2.2 2. *The near-corona region. Limit* $\theta_0 \gg 1$, $\eta \to +\infty$

The behaviour of the hydrodynamic profiles in this limit depends on the power index n.

- Fully ionized plasmas. $n = 0$

We assume values of β_t of the order of unity. We set $\psi \sim O\left(\sqrt{\beta_t}\right) \sim O(1)$ and, consequently, neglect in this limit terms of the order $\mathcal{O}\left(\theta_0^{-4}\right) \ll 1$, simplifying equation (104) into

$$\psi + \theta_0 \frac{d\psi}{d\theta_0} = 1 + \beta_t \psi^{-1} \tag{110}$$

A first approximation to the solution of equation (110) can be written as $\psi(\theta_0) = \psi_0 + \psi_1(\theta_0)$, where $\psi_0 \sim \mathcal{O}(1)$ is an unknown constant and $|\psi_1| \ll 1$ is a θ_0-dependent function. This leads to the approximate solution

$$\psi \simeq \psi_0 + c_1 \theta_0^{-\left(1+\beta_t \psi_0^{-2}\right)}, \tag{111}$$

where $\psi_0 = \left(1 + \sqrt{1+4\beta_t}\right)/2$, and c_1 is a free parameter that only depends on β_t and can be computed numerically with the expression

$$c_1 \to \left(\psi_N - \psi_0\right) \theta_0^{1+\beta_t \psi_0^{-2}} \Big|_{\theta_0 \to \infty}, \tag{112}$$

where ψ_N is the numerical value calculated from equation (104). It can be shown numerically (see figure 19) that $c_1 \to -\sqrt{\beta_t}$ when $\beta_t \gg 1$.

In the case where radiation effects are dominant ($\beta_t \gg 1$), we have $\psi \sim O\left(\sqrt{\beta_t}\right) \gg 1$ so that we can neglect the energy convection term from equation (110) , that is to say, we assume that the electron heat flux is balanced in a first approximation by the radiation energy transport, $q_e + S_r \approx 0$, and arrive to

$$\psi + \theta_0 \frac{d\psi}{d\theta_0} = \beta_t \psi^{-1}, \tag{113}$$

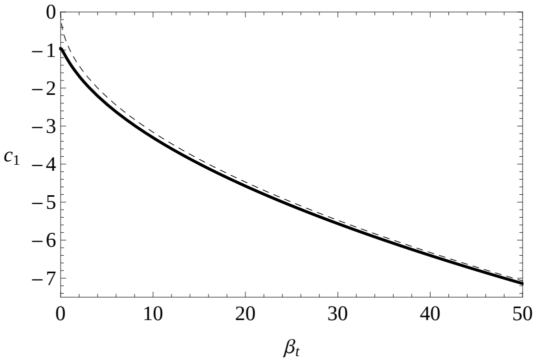

Figure 19: Numerical value of the parameter c_1 vs β_t (solid line). In dashed line the function $-\sqrt{\beta_t}$ is plotted.

which has a formal solution $\psi = \sqrt{\beta_t \left(1 - c_2\theta_0^{-2}\right)}$, where c_2 is a free parameter that numerically is found to be $c_2 \simeq 2$.

- Partially ionized plasma. $0 < n \leq 1$

In this case we set $\psi^2 \sim \mathcal{O}(\beta_t\theta_0^n) \gg 1$ to obtain the dominant order of the solution. With this order of magnitude, the energy equation (104) can be simplified into

$$\psi^2 + \frac{1}{2}\theta_0\frac{d\psi^2}{d\theta_0} = \beta_t\theta_0^n. \tag{114}$$

We look for solutions of the form $\psi^2 = a\theta_0^n$, where a is a parameter to be determined by introducing this solution into equation (114). The solution reads

$$\psi^2 = \frac{2\beta_t}{2+n}\theta_0^n. \tag{115}$$

The *general* energy equation (104) is not completely balanced with this solution, but, instead, terms of the order unity and lower remain unbalanced. A more general solution can be built up as a power series in θ_0. The first two terms read

$$\psi \simeq \sqrt{\frac{2\beta_t}{2+n}}\theta_0^{n/2} + \frac{2}{4+n}. \tag{116}$$

This power expansion is strictly valid until the term $\beta_t\psi^{-1}\theta_0^{n-4}$ becomes of the order of unity, that is to say, for positive values $n < 8$ and $\beta_t \sim \mathcal{O}(1)$.

- Case $-1 \ll n < 0$

The dominant order of ψ goes in this case as $\psi^2 \sim \mathcal{O}(1) \gg \mathcal{O}(\beta_t\theta_0^n)$, where the condition $\theta_0^n \ll \beta_t$ can always be reached sufficiently far from the ablation front. In this way the energy equation (104) at the dominant order is

$$\theta_0 + \theta_0\frac{d\psi}{d\theta_0} = 1, \tag{117}$$

and it admits as a formal solution $\psi = 1 + c_3\theta_0^{-1}$, where c_3 is a free parameter. Nevertheless, if we introduce this solution into the energy equation (104), we notice that the biggest term which is not balanced is of the order $\mathcal{O}(\theta_0^n) \gg \mathcal{O}(\theta_0^{-1})$. The term $c_3\theta_0^{-1}$ is not the following to the dominant one $\psi = 1$, but instead one term proportional to θ_0^n. Thus the first two terms of the solution take the form

$$\psi \simeq 1 + \frac{\beta_t}{1+n}\theta_0^n. \tag{118}$$

In table 4 we show a summary of the different behaviours of the temperature profile in the near-corona region ($\theta_0 \gg 1$).

n	$\psi = \theta_0^{3/2}\theta_0'$
$-1 \ll n < 0$	$\psi \simeq 1 + \frac{\beta_t}{1+n}\theta_0^n$
$n = 0$	$\psi \simeq \psi_0 + c_1\theta_0^{-\left(1+\beta_t\psi_0^{-2}\right)}$ with $\psi_0 = \left(1+\sqrt{1+4\beta_t}\right)/2$
$0 < n \leq 1$	$\psi \simeq \sqrt{\frac{2\beta_t}{2+n}\theta_0^{n/2} + \frac{2}{4+n}}$

Table 4: Asymptotic behaviour of ψ in the limit $\theta_0 \gg 1$ for different values of the power index n.

6.1.3 *Characteristic length of the ERA front*

A quantitative measure of the steepness of ablation front is given with the minimum gradient scale length, which is defined as

$$L_{\min} = \min\left(\left|\frac{d\ln\rho}{dy}\right|^{-1}\right). \tag{119}$$

It can be expressed in a non-dimensional form as $L_{\min}/L_{St} = \min|\theta_0/\theta_0'|$. This characteristic length can be analytically found in the case without radiation transport effects ($\beta_t = 0$). In that case the gradient scale length is defined as $L/L_{St} = \theta_0^{7/2}/(\theta_0 - 1)$ and the point θ_m where the minimum takes place is computed by solving $d(L/L_{St})/d\theta_0 = 0$, that gives $\theta_m = 7/5$ and a characteristic length of $L_0 \equiv L_{\min}(\beta_t = 0) \simeq 8L_{St}$ (see figure 20).

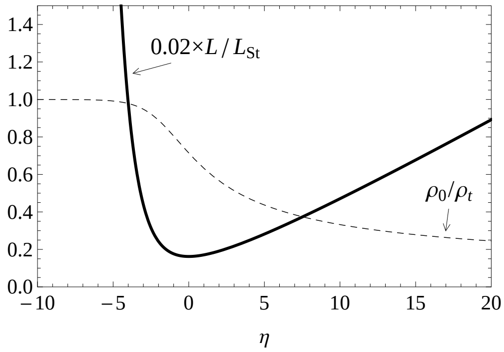

Figure 20: Dimensionless gradient scale length L/L_{St} vs spatial coordinate η (solid line) for $\beta_t = 0$. Density profile on dashed line.

In a general case for $\beta_t \neq 0$, the determination of the minimum gradient scale length shall be performed numerically. The position where it takes place is situated at a temperature of the order of unity, around $\theta_0 \approx 7/5$. In the figure 21 the ratio L_{min}/L_0 is represented as a function of the parameter β_t

and several values of n. The asymptotic behaviour observed numerically for $\beta_t \gg 1$ in the range $-1 < n < 1$ is

$$\frac{L_{min}}{L_0} \simeq 0.58(1-0.1n)\beta_t^{-1/2}, \tag{120}$$

that indicates that an increasing importance of radiation energy transport effects contributes to the steepness of the ERA front.

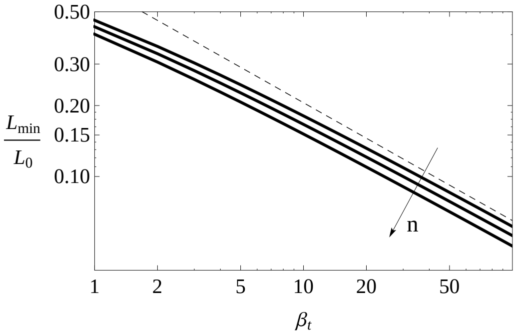

Figure 21: Normalized minimum gradient scale length L_{min}/L_0 vs β_t for three values of the power index n (-1, 0 and 1). Dashed line shows the function $\simeq 0.65\beta_t^{-1/2}$.

6.2 LINEAR STABILITY ANALYSIS. NUMERICAL SOLUTION

6.2.1 *Governing equations*

The equations governing the flow dynamics in the vicinity of the ERA front are the mass and momentum conservation,

$$\frac{\partial \rho}{\partial t} + \nabla \cdot (\rho \vec{v}) = 0, \tag{121}$$

$$\rho \frac{\partial \vec{v}}{\partial t} + \rho \vec{v} \cdot \nabla \vec{v} = -\nabla p + \rho g \vec{e_y}, \tag{122}$$

together with an isobaric approximation ($\rho \sim T^{-1}$) of the energy equation retaining electronic heat conduction and radiation transport

$$\nabla \cdot \left(\frac{5}{2} P_t \vec{v} - \kappa \nabla T \right) = -4\sigma K_P \left(T^4 - T_t^4 \right). \tag{123}$$

It is noted, however, that the pressure gradient cannot be neglected in the momentum equation (122) because the remaining terms are of the same order of smallness. In order to simplify the analysis we consider only perturbations along the x and y coordinates. We look for solutions of perturbed quantities of the form $\exp(\gamma t + ikx)$, where γ is the growth rate and k the wavenumber of the perturbation. We would then proceed with the analysis of the hydrodynamic equations expanding the velocity and other functions as follows $\overrightarrow{v} = \left(v_{1x}\exp(\gamma t + ikx),\, v_0 + v_{1y}\exp(\gamma t + ikx)\right)$, ..., etc, and linearizing them in their first order perturbations (subscript 1). The same normalization as for the zero order solution is used, with the normalized wavenumber $\hat{k} = kL_{St}$ and the normalized growth rate $\hat{\gamma} = \gamma L_{St}/v_t$. Normalized perturbed velocities are denoting by u_{1x}, u_{1y}, temperature by θ_1 and perturbed pressure by p_1.

Thus, the continuity equation may be written as

$$u'_{1y} = \frac{\theta'_0}{\theta_0}u_{1y} - i\hat{k}u_{1x} + \frac{1}{\theta_0}\left(\hat{\gamma} - \theta'_0\right)\theta_1 + \theta'_1, \tag{124}$$

the momentum equation along the main flow as

$$p'_1 = -\frac{1}{\theta_0}\left(\hat{\gamma} + 2\theta'_0\right)u_{1y} + i\hat{k}u_{1x} - \frac{1}{\theta_0^2}\left(\theta_0\hat{\gamma} + Fr_t^{-1} - 2\theta_0\theta'_0\right)\theta_1 - \theta'_1, \tag{125}$$

the momentum equation along the unperturbed front as

$$u'_{1x} = -\frac{\hat{\gamma}}{\theta_0}u_{1x} - i\hat{k}p_1, \tag{126}$$

and the energy equation as

$$\begin{gathered}\left(\theta_0^{5/2}\theta_1\right)'' - \hat{k}^2\theta_0^{5/2}\theta_1 = \\ \tfrac{1}{\theta_0}\left(\hat{\gamma} - \theta'_0 - \beta_t\theta_0^{n-11/2}\left(\left(\tfrac{3}{2} - n\right)\theta_0^4 - \left(\tfrac{11}{2} - n\right)\right)\right)\theta_1 + \tfrac{\theta'_0}{\theta_0}u_{1y} + \theta'_1.\end{gathered} \tag{127}$$

Notice that the perturbed density can be recovered with the expression $\rho_1/\rho_t = -\theta_1/\theta_0^2$. The set of equations can be written in a matrix form

$$\frac{d\mathbf{V}}{d\eta} = \mathbf{A}\,\mathbf{V}, \tag{128}$$

where $\mathbf{V} = \left(u_{1y},\, iku_{1x},\, p_1,\, \theta,\, \theta'_1\right)$ and the matrix $\mathbf{A}$ is a function of the normalized perturbation wavenumber $\hat{k}$, growth rate $\hat{\gamma}$, profiles of the 1D solution θ_0, parameter β_t and the Froude number $\mathrm{Fr}_t = v_t^2/gL_{St}$.

$$\mathbf{A} = \begin{bmatrix} \frac{\theta_0'}{\theta_0} & -1 & 0 & \frac{\hat{\gamma}-\theta_0'}{\theta_0} & 1 \\ 0 & -\frac{\hat{\gamma}}{\theta_0} & \hat{k}^2 & 0 & 0 \\ -\frac{\hat{\gamma}+2\theta_0'}{\theta_0} & 1 & 0 & -\frac{\mathrm{Fr}_t^{-1}+\theta_0\left(\hat{\gamma}-2\theta_0'\right)}{\theta_0^2} & -1 \\ 0 & 0 & 0 & 0 & 1 \\ \frac{\theta_0'}{\theta_0^{7/2}} & 0 & 0 & A_{45} & \frac{1-5\theta_0^{3/2}\theta_0'}{\theta_0^{5/2}} \end{bmatrix}, \tag{129}$$

where

$$A_{45} = \hat{k}^2 + \frac{\hat{\gamma}-\theta_0'}{\theta_0^{7/2}} - \frac{5}{2}\frac{\theta_0''}{\theta_0} - \frac{15}{4}\left(\frac{\theta_0'}{\theta_0}\right)^2 - \beta_t \frac{(3/2-n)\,\theta_0^4 - (11/2-n)}{\theta_0^{9-n}}. \tag{130}$$

If we look for the leading eigenvalues of the matrix $\mathbf{A}$ in the near-corona region ($\theta_0 \gg 1,\ \eta \to +\infty$) for $n = 0$, we substitute the value of derivatives of the temperature ($\theta_0' = \sqrt{\beta_t}\theta_0^{-3/2}$ and $\theta_0'' = -(3/2)\beta_t\theta_0^{-4}$) and expand the matrix $\mathbf{A}$ in powers of θ_0, in the form $\mathbf{A} = \mathbf{A_0} + \theta_0^{-1}\mathbf{A_1} + \theta_0^{-2}\mathbf{A_2} + \theta_0^{-5/2}\mathbf{A_3} + \ldots$ The leading term reads

$$\mathbf{A_0} = \begin{bmatrix} 0 & -1 & 0 & 0 & 1 \\ 0 & 0 & \hat{k}^2 & 0 & 0 \\ 0 & 1 & 0 & 0 & -1 \\ 0 & 0 & 0 & 0 & 1 \\ 0 & 0 & 0 & \hat{k}^2 & 0 \end{bmatrix}. \tag{131}$$

This matrix has five eigenvalues: one single, $\lambda_0 = 0$, and two doubles $\lambda_0 = \pm\hat{k}$. A complication in this analysis arises when computing the associated eigenvectors, since two of them, one for each double eigenvalue, are zero. Therefore, in order to solve mathematical difficulties in the modal analysis related to the appearance of zero eigenvectors, it is convenient to make the following change of variables

$$\begin{aligned} G_1 &= \theta_0 F_1 = u_{1y} - \theta_1, \\ W_1 &= i\hat{k}u_{1x}, \\ Q_1 &= 2u_{1y} + p_1 - \theta_1, \\ T_1 &= \theta_0^{5/2}\theta_1, \\ H_1 &= \left(\theta_0^{5/2}\theta_1\right)' - u_{1y}, \end{aligned} \tag{132}$$

where the new vector $\mathbf{Y} = (G_1, W_1, Q_1, T_1, H_1)$ can be obtained through the matrix relation $\mathbf{V} = \mathbf{CY}$, where the transformation matrix $\mathbf{C}$ is defined as

$$C = \begin{bmatrix} 1 & 0 & 0 & \theta_0^{-5/2} & 0 \\ 0 & 1 & 0 & 0 & 0 \\ -2 & 0 & 1 & -\theta_0^{-5/2} & 0 \\ 0 & 0 & 0 & \theta_0^{-5/2} & 0 \\ \theta_0^{-5/2} & 0 & 0 & \theta_0^{-5} - \frac{5}{2}\theta_0^{-7/2}\theta_0' & \theta_0^{-5/2} \end{bmatrix} \qquad (133)$$

Thus, the fifth order system of differential equations takes the form

$$\frac{d\mathbf{Y}}{d\eta} = \mathbf{M}\,\mathbf{Y}, \qquad (134)$$

where the matrix $\mathbf{M}$ is calculated algebraically, $\mathbf{M} = \mathbf{C}^{-1}\mathbf{A}\mathbf{C} - \mathbf{C}^{-1}\mathbf{C}'$, where $\mathbf{C}' = d\mathbf{C}/d\eta$and reads

$$M = \begin{bmatrix} \frac{\theta_0'}{\theta_0} & -1 & 0 & \frac{\hat{\gamma}}{\theta_0^{7/2}} & 0 \\ -2\hat{k}^2 & \frac{\hat{\gamma}}{\theta_0} & \hat{k}^2 & -\frac{\hat{k}^2}{\theta_0^{5/2}} & 0 \\ -\frac{\hat{\gamma}}{\theta_0} & -1 & 0 & -\frac{\mathrm{Fr}_t^{-1}}{\theta_0^{9/2}} & 0 \\ 1 & 0 & 0 & \frac{1}{\theta_0^{5/2}} & 1 \\ 0 & 1 & 0 & \hat{k}^2 - \beta_t \frac{(3/2-n)\theta_0^4 - (11/2-n)}{\theta_0^{9-n}} & 0 \end{bmatrix} \qquad (135)$$

This change of variable is not arbitrary but it goes in the sense of gaining also physical insight in the problem. Notice that $F_1 = G_1/\theta_0 = (\rho u_y)_1$ represents the perturbed flux of mass, $Q_1 = \left(p + \rho u_y^2\right)_1$ the perturbed flux of momentum and $H_1 = -\,(h + q_e)_1$, where h is the enthalpy and q_e the electron thermal conduction, represents a perturbed flux of energy.

6.2.2 *Modal analysis*

Determination of the eigenmodes for both asymptotic limits, $\theta_0 \to 1$ and $\theta_0 \gg 1$, is crucial in the stability analysis since these modes provide the boundary conditions to be imposed in the matrix system (134), that determines the dispersion relation, $\hat{\gamma} = \hat{\gamma}\left(\hat{k}\right)$.

6.2.2.1 *The plateau region, $\theta_0 \to 1$*

In the first case ($\eta \to -\infty$), the aim is to get to a matricial expansion of the equation (134) around $(\theta_0 - 1)$, which is a singular point. After simple manipulation and taking θ_0 as the independent variable, the equation (134) can be written as $(\theta_0 - 1)(d\mathbf{Y}/d\theta_0) = \mathbf{M}^*\mathbf{Y}$. The matrix $\mathbf{M}^* = ((\theta_0 - 1)/\theta_0')\,\mathbf{M}$, where $\theta_0' = \sum\limits_{i=1}^{\infty} a_i (\theta_0 - 1)^i$ (see subsection (6.1.2.1)) can be developed into series in powers of $(\theta_0 - 1)$ in the way

$$\mathbf{M}^* = \sum_{r=0}^{\infty} \mathbf{M}_r^* (\theta_0 - 1)^r . \tag{136}$$

It leading order,$\mathbf{M}_\mathbf{0}^*$, reads

$$\mathbf{M}_\mathbf{0}^* = \frac{1}{a_0^+} \begin{bmatrix} 0 & -1 & 0 & \hat{\gamma} & 0 \\ -2\hat{k}^2 & -\hat{\gamma} & \hat{k}^2 & -\hat{k}^2 & 0 \\ -\hat{\gamma} & -1 & 0 & -\mathrm{Fr}_\mathrm{t}^{-1} & 0 \\ 1 & 0 & 0 & 1 & 1 \\ 0 & 1 & 0 & \hat{k}^2 + 4\beta & 0 \end{bmatrix}, \tag{137}$$

and it has five distinct eigenvalues $\{\lambda_j\}$,

$$\begin{aligned} &\lambda_1 = \hat{k}/a_0^+, && \lambda_2 = (1+b)/2a_0^+, \\ &\lambda_3 = -\hat{k}/a_0^+, && \lambda_4 = (1-b)/2a_0^+, \\ &\lambda_5 = -\hat{\gamma}/a_0^+, \end{aligned} \tag{138}$$

where $b = \sqrt{1 + 16\beta_t + 4\hat{k}^2 + 4\hat{\gamma}}$. Therefore, the matrix $\mathbf{M}_\mathbf{0}^*$ can be diagonalized through the matrix of the associated eigenvectors $\mathbf{N}$, in the form $\mathbf{B_0} = \mathbf{N^{-1}M_0^*N} = \mathbf{diag}\{\lambda_j\}$. If we apply the change of variable $\mathbf{Y} = \mathbf{NY}^*$, the matricial system is transformed into

$$(\theta_0 - 1)\frac{d\mathbf{Y}^*}{d\theta_0} = \left(\mathbf{diag}\{\lambda_j\} + \sum_{r=1}^{\infty} \mathbf{B}_r (\theta_0 - 1)^r\right)\mathbf{Y}^*. \tag{139}$$

This equation has a fundamental vector solution of the form

$$\bar{\mathbf{y}}^* = (\theta_0 - 1)^\lambda \mathbf{Y}^*, \tag{140}$$

where $\mathbf{Y}^*$ is expanded as $\mathbf{Y}^* = \sum\limits_{r=0}^{\infty} \mathbf{Y}_\mathbf{r}^* (\theta_0 - 1)^r$ and every coefficient $\mathbf{Y}_\mathbf{r}^*$ can be explicitly calculated by algebraic operations with the following recursive method

$$\mathbf{Y}_\mathbf{0}^* = \mathbf{I}, \quad \mathbf{Y}_\mathbf{n,i}^* = -\left(\mathbf{B_0} - (\lambda_i + n)\,\mathbf{I}\right)^{-1} \sum_{j=0}^{n-1} \mathbf{B_{n-j}} \mathbf{Y}_\mathbf{j,i}^*. \tag{141}$$

This procedure is fully described in the book by Wasow [46].

The third, fourth and fifth eigenvalues are negative, so the coefficients in front of their associated eigenmodes have to be set to zero (otherwise these modes will explode at $\theta_0 \rightarrow 1$) to fulfill the boundary condition that perturbations must completely vanish far enough from the ablation front. The associated eigenmodes to the positive eigenvalues (λ_1 and λ_2) take the following form

$$\mathbf{Y}_{\lambda_1} = (\theta_0 - 1)^{\hat{k}/a_0^+} \times \left(\begin{bmatrix} -1 \\ \hat{k} \\ \hat{\gamma}/\hat{k} - 1 \\ 0 \\ 1 \end{bmatrix} + (\theta_0 - 1)\,\mathbf{Y_{11}} + O\left(\theta_0 - 1\right)^2 \right), \quad (142)$$

$$\mathbf{Y}_{\lambda_2} = (\theta_0 - 1)^{(1-b)/2a_0^+} \times \left(\mathbf{Y_{20}} + (\theta_0 - 1)\,\mathbf{Y_{21}} + O\left(\theta_0 - 1\right)^2 \right) \quad (143)$$

where $\mathbf{Y}_{11}$, $\mathbf{Y}_{20}$ and $\mathbf{Y}_{21}$ are lengthy expressions that can be algebraically computed with the recursive method (141). It is worth noting that the perturbed temperature θ_1 does not have any component in the eigenvector associated to the first eigenvalue. For $\beta_t \gg 1$, the eigenvalue $\lambda_1 \approx \hat{k}/2\sqrt{\beta_t}$ corresponds to the mode of slow decay and any mode associated to the eigenvalue $\lambda_2 \approx 1 \gg \lambda_1$ decay much faster (thermal mode). Therefore, *on the cold side of the ERA front (in the plateau region) the perturbed temperature tends to zero much faster than any other perturbed quantity.*

6.2.2.2 *The near-corona region, $\theta_0 \gg 1$*

In this region, the modal solution depends on the particular value of the parameter n. We will present the procedure (based on Sanz [31, 32]) to calculate the eigenmodes that develop in this region for the case $n = 0$, and we will use the same methodology to extend the results to the case $n = 1$.

CASE $n = 0$

We saw in the preceding section that the solution of the steady state takes the form $\psi \simeq \psi_0 + c_1 \theta_0^{-\left(1+\beta_t \psi_0^{-2}\right)}$.Thus, the leading order of the temperature profile is $\theta_0 \simeq \left((5/2)\psi_0 \eta\right)^{2/5} + \ldots$ It is convenient then for further work to set $\zeta \equiv (2/5\psi_0)\,\theta_0^{5/2}$ as the independent variable. The matricial system of equation (134) can be rewritten in the form

$$\frac{d\mathbf{Y}}{d\zeta} = \frac{1}{z\, d\zeta/d\theta_0}\mathbf{M}\mathbf{Y}. \tag{144}$$

The matrix $\mathbf{M}$ can be expressed as a series expansion in powers of θ_0 as $\mathbf{M} = \mathbf{M_0} + \frac{1}{\theta_0}\mathbf{M_1} + \frac{1}{\theta_0^{5/2}}\mathbf{M_2} + \ldots$ where

$$\mathbf{M_0} = \begin{bmatrix} 0 & -1 & 0 & 0 & 0 \\ -2\hat{k}^2 & 0 & \hat{k}^2 & 0 & 0 \\ 0 & -1 & 0 & 0 & 0 \\ 1 & 0 & 0 & 0 & 1 \\ 0 & 1 & 0 & \hat{k}^2 & 0 \end{bmatrix}, \tag{145}$$

$$\mathbf{M_1} = \begin{bmatrix} 0 & 0 & 0 & 0 & 0 \\ 0 & -\hat{\gamma} & 0 & 0 & 0 \\ -\hat{\gamma} & 0 & 0 & 0 & 0 \\ 0 & 0 & 0 & 0 & 0 \\ 0 & 0 & 0 & 0 & 0 \end{bmatrix}, \tag{146}$$

$$\mathbf{M_2} = \begin{bmatrix} \psi_0 & 0 & 0 & 0 & 0 \\ 0 & 0 & 0 & -\hat{k}^2 & 0 \\ 0 & 0 & 0 & 0 & 0 \\ 0 & 0 & 0 & 1 & 0 \\ 0 & 0 & 0 & 0 & 0 \end{bmatrix}. \tag{147}$$

The aim is to expand the complete matrix up to the terms of the order of $\mathcal{O}\left(\zeta^{-1}\right)$. This power expansion reads

$$\begin{aligned} \tfrac{1}{z\, d\zeta/d\theta_0}\mathbf{M} \simeq \mathbf{M_0} + \left(\tfrac{5\psi_0}{2}\zeta\right)^{-2/5}\mathbf{M_1} - \tfrac{c_1}{\psi_0}\left(\tfrac{5\psi_0}{2}\zeta\right)^{-\alpha}\mathbf{M_0} + \\ + \left(\tfrac{5\psi_0}{2}\zeta\right)^{-1}\mathbf{M_2} + \ldots \end{aligned} \tag{148}$$

where $\alpha = 2\left(1 + \beta_t/\psi_0^2\right)/5$. We consider a formal solution of the type

$$\begin{aligned} \mathbf{Y}(\zeta) = \zeta^{\lambda_p} \exp\left(\lambda_0\zeta + \lambda_1\zeta^{3/5} + \lambda_2\zeta^{1-\alpha}\right) \times \\ \times \left(\mathbf{Y_0} + \mathbf{Y_1}\zeta^{-2/5} + \mathbf{Y_2}\zeta^{-\alpha} + \mathbf{Y_3}\zeta^{-1}\right). \end{aligned} \tag{149}$$

Substituting into equation (144) and collecting terms

$$(\mathbf{M_0} - \lambda_0 \mathbf{I})\,\mathbf{Y_0} = 0, \tag{150}$$

$$\left(\left(\frac{2}{5\psi_0}\right)^{2/5} \mathbf{M_1} - \frac{3}{5}\lambda_1 \mathbf{I}\right)\mathbf{Y_0} + (\mathbf{M_0} - \lambda_0 \mathbf{I})\,\mathbf{Y_1} = 0, \tag{151}$$

$$\left(-\frac{c_1}{\psi_0}\left(\frac{2}{5\psi_0}\right)^{\alpha} \mathbf{M_0} - (1-\alpha)\,\lambda_2 \mathbf{I}\right)\mathbf{Y_0} + (\mathbf{M_0} - \lambda_0 \mathbf{I})\,\mathbf{Y_2} = 0, \tag{152}$$

$$\left(\frac{2}{5\psi_0}\mathbf{M_2} - \lambda_p \mathbf{I}\right)\mathbf{Y_0} + (\mathbf{M_0} - \lambda_0 \mathbf{I})\,\mathbf{Y_3} = 0, \tag{153}$$

where **I** is the identity matrix. This set of equations let us compute the eigenvalues $(\lambda_0, \lambda_1, \lambda_2, \lambda_p)$ and the associated eigenvectors $(\mathbf{Y_0}, \mathbf{Y_1}, \mathbf{Y_2}, \mathbf{Y_3})$. The first of the compatibility equations is the usual eigenvalue problem for the matrix $\mathbf{M_0}$. Its solution provides five values for the leading eigenvalue λ_0 with five associated linearly independent eigenvectors$\mathbf{Y_0}$:

- Mode I: This is a simple root called *vorticity mode*, its eigenvalue is $\lambda_0 = 0$ and the associated eigenvector $\mathbf{Y_0^I} = \{-1, 0, -2, 0, 1\}$. This main eigenvalue is insufficient to conclude whether the associated mode is bounded or explodes in the near-corona region ($\eta \to +\infty$). Thus, higher order eigenvalues are needed to allow us to evaluate the behaviour of this mode.

- Modes II-III: This is a double root, that accounts for *incompressible and thermal* effects. Its eigenvalue is $\lambda_0 = \hat{k}$ and the two associated eigenvectors are $\mathbf{Y_0^{II}} = \left\{-1, \hat{k}, -1, 0, 1\right\}$ and $\mathbf{Y_0^{III}} = \left\{\hat{k}, -\hat{k}^2, \hat{k}, 1, 0\right\}$ [1]. These modes are unbounded (positive eigenvalue) for $\eta \to +\infty$, so their amplitudes should be set to zero in order to fulfill the boundary conditions of vanishing perturbations.

- Modes IV-V: This is a double root, that also accounts for *incompressible and thermal* effects. Its eigenvalue is $\lambda_0 = -\hat{k}$ and the two associated eigenvectors are $\mathbf{Y_0^{IV}} = \left\{-1, -\hat{k}, -1, 0, 1\right\}$ and $\mathbf{Y_0^{V}} = \left\{-\hat{k}, -\hat{k^2}, -\hat{k}, 1, 0\right\}$. These modes are bounded (negative eigenvalue) for $\eta \to +\infty$.

---

[1] Note that the fourth element of $\mathbf{Y_0^{II}}$ is zero. This element is related to the perturbed temperature $T_1 \propto \theta_1$ and, at the same time, to the perturbed density ρ_1 ($\rho_1/\rho_t = -\theta_1/\theta_0^2$). In that sense, this root (mode II) is said to account for incompressible effects, $\rho_1 \equiv 0$. This terminology applies, analogously, to mode IV.

Let $\mathbf{N}$ be a nonsingular matrix that diagonalizes $\mathbf{M_0}$ (we have just shown the existence of five independent eigenvectors) and we make $\mathbf{Y} = \mathbf{N}\,\mathbf{Z}$ and write equation (144) as

$$\frac{d\mathbf{Z}}{d\zeta} = \frac{1}{z\,d\zeta/d\theta_0}\mathbf{BZ}, \tag{154}$$

where $\mathbf{B} = \mathbf{N}^{-1}\mathbf{MN}$.

The procedure to compute the higher order eigenvalues depends on whether the root is simple or double. For a single root (in this case the eigenvalue $\lambda_0^I = 0$), left hand multiplying equation (151) by the associated eigenvector $\mathbf{Y_0^I}$, gives the *compatibility equation* that determines λ_1,

$$\mathbf{Z_0^I}\left(\left(\frac{2}{5\psi_0}\right)^{2/5}\mathbf{B_1} - \frac{3}{5}\lambda_1\mathbf{I}\right)\mathbf{Z_0^I} = 0, \tag{155}$$

$$\lambda_1^I = -\frac{5}{3}\left(\frac{2}{5\psi_0}\right)^{2/5}\hat{\gamma}. \tag{156}$$

Observe that λ_1^I is negative for an unstable *ERA* front, i. e. $Re\,(\hat{\gamma}) > 0$. Therefore, this vorticity mode is bounded in the near-corona region if the ablation front is unstable. Once λ_1^I is known, we can calculate the associated eigenvector $\mathbf{Y}_1^I$ directly from the equation (151).

Analogously, the compatibility equations for determining λ_2 and λ_p are derived by pre-multiplying equations (152) and (153) by the eigenvector $\mathbf{Y_0^I}$

$$\mathbf{Z_0^I}\left(-\frac{c_1}{\psi_0}\left(\frac{2}{5\psi_0}\right)^{\alpha}\mathbf{B_0} - (1-\alpha)\,\lambda_2^I\mathbf{I}\right)\mathbf{Z_0^I} = 0, \tag{157}$$

$$\mathbf{Z_0^I}\left(\frac{2}{5\psi_0}\mathbf{B_2} - \lambda_p^I\mathbf{I}\right)\mathbf{Z_0^I} = 0. \tag{158}$$

In this case the eigenvalues take the value

$$\lambda_2 = 0 \quad \text{and} \quad \lambda_p = -\frac{2}{5}. \tag{159}$$

Therefore, the vorticity mode reads

$$\mathbf{Z^I}\,(x) = \zeta^{-2/5}\exp\left(-\frac{5}{3}\left(\frac{2}{5\psi_0}\right)^{2/5}\hat{\gamma}\zeta^{3/5}\right) \times \left(\begin{bmatrix} -1 \\ 0 \\ -2 \\ 0 \\ 1 \end{bmatrix} + \mathcal{O}\left(\zeta^{-2/5}\right)\right). \tag{160}$$

This procedure must be modified at the first step if there are double roots. Let $\lambda_0^{II,III}$ represent one such eigenvalue and $\mathbf{Z}_0^{\mathbf{II}}$, $\mathbf{Z}_0^{\mathbf{III}}$ its two independent eigenvectors. Obviously, $\mathbf{Z}_0^{\mathbf{II,II}} = \mu_{II}\mathbf{Z}_0^{\mathbf{II}} + \mu_{III}\mathbf{Z}_0^{\mathbf{III}}$ satisfies equation (150), with μ_{II} and μ_{III} being arbitrary constants. Left hand multiplying equation (151) by $\mathbf{Z}_0^{\mathbf{II}}$ and $\mathbf{Z}_0^{\mathbf{III}}$ gives

$$\begin{aligned}
\mathbf{Z}_0^{\mathbf{II}}\left(\left(\tfrac{2}{5\psi_0}\right)^{2/5}\mathbf{B_1} - \tfrac{3}{5}\lambda_1\mathbf{I}\right)\left(\mu_{\mathrm{II}}\mathbf{Z}_0^{\mathbf{II}} + \mu_{\mathrm{III}}\mathbf{Z}_0^{\mathbf{III}}\right) &= 0,\\
\mathbf{Z}_0^{\mathbf{III}}\left(\left(\tfrac{2}{5\psi_0}\right)^{2/5}\mathbf{B_1} - \tfrac{3}{5}\lambda_1\mathbf{I}\right)\left(\mu_{\mathrm{II}}\mathbf{Z}_0^{\mathbf{II}} + \mu_{\mathrm{III}}\mathbf{Z}_0^{\mathbf{III}}\right) &= 0.
\end{aligned} \tag{161}$$

The homogeneous system in μ_{II} and μ_{III} has a non-trivial solution only if the corresponding determinant is equal to zero

$$\begin{aligned}
&\left[\mathbf{Z}_0^{\mathbf{II}}\left(\left(\tfrac{2}{5\psi_0}\right)^{2/5}\mathbf{B_1} - \tfrac{3}{5}\lambda_1\mathbf{I}\right)\mathbf{Z}_0^{\mathbf{II}}\right] \times \left[\mathbf{Z}_0^{\mathbf{III}}\left(\left(\tfrac{2}{5\psi_0}\right)^{2/5}\mathbf{B_1} - \tfrac{3}{5}\lambda_1\mathbf{I}\right)\mathbf{Z}_0^{\mathbf{III}}\right]\\
&-\left[\mathbf{Z}_0^{\mathbf{II}}\left(\left(\tfrac{2}{5\psi_0}\right)^{2/5}\mathbf{B_1} - \tfrac{3}{5}\lambda_1\mathbf{I}\right)\mathbf{Z}_0^{\mathbf{III}}\right] \times \left[\mathbf{Z}_0^{\mathbf{III}}\left(\left(\tfrac{2}{5\psi_0}\right)^{2/5}\mathbf{B_1} - \tfrac{3}{5}\lambda_1\mathbf{I}\right)\mathbf{Z}_0^{\mathbf{II}}\right] = 0.
\end{aligned} \tag{162}$$

The same procedure is followed for the determination of λ_2 and λ_p. The compatibility equations read

$$\begin{aligned}
&\left[\mathbf{Z}_0^{\mathbf{II}}\left(-\tfrac{c_1}{\psi_0}\left(\tfrac{2}{5\psi_0}\right)^{\alpha}\mathbf{B_0} - (1-\alpha)\lambda_2\mathbf{I}\right)\mathbf{Z}_0^{\mathbf{II}}\right] \times \left[\mathbf{Z}_0^{\mathbf{III}}\left(-\tfrac{c_1}{\psi_0}\left(\tfrac{2}{5\psi_0}\right)^{\alpha}\mathbf{B_0} - (1-\alpha)\lambda_2\mathbf{I}\right)\mathbf{Z}_0^{\mathbf{III}}\right]\\
&-\left[\mathbf{Z}_0^{\mathbf{II}}\left(-\tfrac{c_1}{\psi_0}\left(\tfrac{2}{5\psi_0}\right)^{\alpha}\mathbf{B_0} - (1-\alpha)\lambda_2\mathbf{I}\right)\mathbf{Z}_0^{\mathbf{III}}\right] \times \left[\mathbf{Z}_0^{\mathbf{III}}\left(-\tfrac{c_1}{\psi_0}\left(\tfrac{2}{5\psi_0}\right)^{\alpha}\mathbf{B_0} - (1-\alpha)\lambda_2\mathbf{I}\right)\mathbf{Z}_0^{\mathbf{II}}\right] = 0.
\end{aligned} \tag{163}$$

$$\begin{aligned}
&\left[\mathbf{Z}_0^{\mathbf{II}}\left(\tfrac{2}{5\psi_0}\mathbf{B_2} - \lambda_p\mathbf{I}\right)\mathbf{Z}_0^{\mathbf{II}}\right] \times \left[\mathbf{Z}_0^{\mathbf{III}}\left(\tfrac{2}{5\psi_0}\mathbf{B_2} - \lambda_p\mathbf{I}\right)\mathbf{Z}_0^{\mathbf{III}}\right]\\
&-\left[\mathbf{Z}_0^{\mathbf{II}}\left(\tfrac{2}{5\psi_0}\mathbf{B_2} - \lambda_p\mathbf{I}\right)\mathbf{Z}_0^{\mathbf{III}}\right] \times \left[\mathbf{Z}_0^{\mathbf{III}}\left(\tfrac{2}{5\psi_0}\mathbf{B_2} - \lambda_p\mathbf{I}\right)\mathbf{Z}_0^{\mathbf{II}}\right] = 0.
\end{aligned} \tag{164}$$

In further work we will be interested on the unbounded modes (II and III). Solving the above equations, the modes II and III can be expressed as

$$\mathbf{Z}^{\mathbf{II,III}}(\zeta) = \zeta^{\lambda_p^{II,III}}\exp\left(\hat{k}\zeta + \lambda_2^{II,III}\zeta^{1-\alpha}\right) \times \left(\mu_{II}\begin{bmatrix}0\\1\\0\\0\\0\end{bmatrix} + \mu_{III}\begin{bmatrix}0\\0\\1\\0\\0\end{bmatrix} + \mathcal{O}\left(\zeta^{-2/5}\right)\right), \tag{165}$$

where

$$\lambda_2^{II,III} = -\frac{c_1\left(\frac{2}{5\psi_0}\right)^{\alpha}}{\psi_0(1-\alpha)}\hat{k}, \tag{166}$$

and

$$\lambda_p^{II,III} = \frac{1 + 2\psi_0 + \sqrt{1 + (2\psi_0)^2}}{10\psi_0}. \tag{167}$$

CASE $n = 1$

The asymptotic behaviour of the steady state in the near-corona region was determined up to the second order term for $n > 0$. However, in order to perform rigorously the modal analysis, that development is insufficient for $n = -2.5$ and we need to consider the next term of the steady state. In particular, we have to consider the terms up to the order $\mathcal{O}\left(\theta_0^{-1}\right)$,

$$\psi \simeq \sqrt{\frac{2}{3}} \left(\beta_t \theta_0\right)^{1/2} + \frac{2}{5} + \frac{3\sqrt{6}}{50} \left(\beta_t \theta_0\right)^{-1/2} + \frac{6}{125} \left(\beta_t \theta_0\right)^{-1}. \tag{168}$$

The independent variable is defined as $\zeta \equiv \sqrt{3/8\beta_t}\theta_0^2$ and the power expansion of the matrix $\mathbf{M}$ is $\mathbf{M} = \mathbf{M_0} + \theta_0^{-1}\mathbf{M_1} + \theta_0^{-2}\mathbf{M_2} + \ldots$ where $\mathbf{M_0}$ and $\mathbf{M_1}$ are the same as in equations (145) and (146), with the matrix $\mathbf{M_2}$ having the following form

$$\mathbf{M_2} = \begin{bmatrix} \sqrt{\frac{2\beta_t}{3}} & 0 & 0 & 0 & 0 \\ 0 & 0 & 0 & 0 & 0 \\ 0 & 0 & 0 & 0 & 0 \\ 0 & 0 & 0 & 0 & 0 \\ 0 & 0 & 0 & 0 & 0 \end{bmatrix}. \tag{169}$$

We proceed to diagnonalize the matrix $\mathbf{M_0}$. The system of equations (144) reads

$$\frac{d\mathbf{Z}}{d\zeta} = \frac{1}{z\, d\zeta/d\theta_0}\mathbf{B}\mathbf{Z}, \tag{170}$$

where

$$\begin{gathered} \tfrac{1}{z\, d\zeta/d\theta_0}\mathbf{B} \simeq \mathbf{B_0} - \zeta^{-1/4}\tfrac{1}{5}\left(\tfrac{2\cdot 3^5}{\beta_t^5}\right)^{1/8}\mathbf{B_0} + \zeta^{-1/2}\left(\tfrac{3}{2^3\beta_t^5}\right)^{1/4}\left(\tfrac{3}{50}\mathbf{B_0} + \beta_t\mathbf{B_1}\right) - \\ -\zeta^{-3/4}\tfrac{1}{5}\left(\tfrac{3^7}{2^5\beta_t^7}\right)^{1/8}\mathbf{B_1} + \zeta^{-1}\tfrac{1}{1000}\left(\tfrac{3}{2\beta_t^5}\right)^{1/2}\left(9\mathbf{B_0} + 10\beta_t(3\mathbf{B_1} + 50\beta_t\mathbf{B_2}\right)\ldots = \\ = \mathbf{B_0} + \zeta^{-1/4}\mathbf{B_1^*} + \zeta^{-1/2}\mathbf{B_2^*} + \zeta^{-3/4}\mathbf{B_2^*} + \zeta^{-1}\mathbf{B_p^*}\ldots \end{gathered} \tag{171}$$

The above expression suggests us to attempt a formal solution of the type

$$\begin{gathered} \mathbf{Z}(\zeta) = \zeta^{\lambda_p}\exp\left(\lambda_0\zeta + \lambda_1\zeta^{3/4} + \lambda_2\zeta^{1/2} + \lambda_3\zeta^{1/4}\right) \times \\ \times\left(\mathbf{Y_0} + \mathbf{Y_1}\zeta^{-1/4} + \mathbf{Y_2}\zeta^{-1/2} + \mathbf{Y_3}\zeta^{-3/4} + \mathbf{Y_4}\zeta^{-1}\right). \end{gathered} \tag{172}$$

The secondary eigenvalues associated to the unbounded eigenvalue $\lambda_0 = \hat{k}$ (double root) are

$$\lambda_1 = -\frac{4}{5}\frac{2^{1/8}}{3^{3/8}}\frac{\hat{k}}{\beta_t^{5/8}}, \tag{173}$$

$$\lambda_2 = \frac{3}{25}\frac{3^{1/4}}{2^{3/4}}\frac{\hat{k}}{\beta_t^{5/4}}, \tag{174}$$

$$\lambda_3 = 0, \tag{175}$$

$$\lambda_p = \frac{1}{2} + \frac{9\sqrt{6}}{2000}\frac{\hat{k}}{\beta_t^{5/2}}. \tag{176}$$

6.2.3 *Numerical dispersion relation*

6.2.3.1 *Computation method*

The preceding modal study will be useful later on in the numerical computation, since we can impose the solution to be a linear combination of bounded eigenmodes in both limits as boundary conditions. Hence, we avoid falling into exploding and non-physical solutions. Moreover, the modal study let us determine *a priori* the nature of the dispersion relation. Since there are the same number of bounded modes at the left of the ablation front that unbounded ones at the right and vice-versa, we can expect the dispersion relation to be discrete.

The method used in the computation, similar to the one used by Kull in his studies of the stability of electronic ablation fronts [17], can be summarized as follows: we integrate the matrix system (134) with a boundary condition at the left which is a linear combination of equations (142)-(143). Let it be $\mathbf{Y}^- = a_1\mathbf{Y}_{\lambda_1} + a_2\mathbf{Y}_{\lambda_2}$ where a_1 and a_2 are still two undefined parameters[2]. Let $\bar{\mathbf{Y}}$ be the solution normalized with the most unbounded mode (Modes II-III) at the right. This solution will tend to a constant vector $\mathbf{c}$ when $\theta_0 \gg 1$ or,

---

[2] Note that if we decide to integrate the system from the right (near-corona region) to the left (compressed ablator region), the boundary condition to be imposed at the right is a linear combination of three bounded modes (Modes I, IV and V). This fact makes that the computation method needs an additional integration at each step (three integrations instead of two) that slows down the computation of the growth rate compared to the procedure expounded in this paragraph.

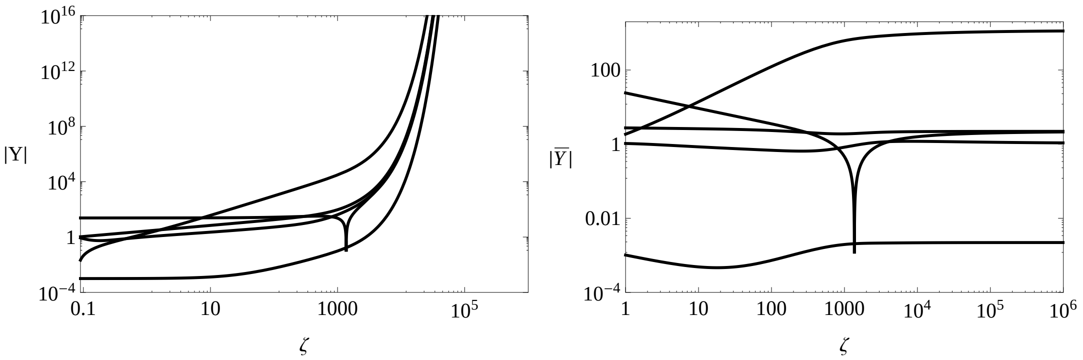

Figure 22: Vector solution of the system of equations (144) in the case $\hat{k} = 0.001$, $\hat{\gamma} = 0.025$, $\beta_t = 20$, $n = 0$ and $\mathrm{Fr_t} = 0.5$, with the initial condition $(a_1, a_2) = (1, 0)$. Left figure corresponds to the absolute value of the vector solution without normalization, and right figure corresponds to the absolute value of the vector solution normalized with the most unbounded mode (equation (165)).

equivalently, $\zeta \gg 1$ (see figure 22). Each component of the vector $\mathbf{c}$ is a linear combination of a_1 and a_2,

$$c_i = f_i\left(a_1, a_2\right) = a_1 f_i\left(1, 0\right) + a_2 f_i\left(0, 1\right), \tag{177}$$

and shall be zero to ensure a bounded solution. We select any two components of the vector solution (components i and j)

$$\begin{aligned} a_1 f_i\left(1, 0\right) + a_2 f_i\left(0, 1\right) = 0, \\ a_1 f_j\left(1, 0\right) + a_2 f_j\left(0, 1\right) = 0, \end{aligned} \tag{178}$$

and we arrive to a homogeneous system of linear equations. In order to have a *non-trivial solution*, that is to say, a solution different from $a_1 = a_2 = 0$, we force the matrix of the system to be *singular* by setting its determinant to zero (see example in figure 23)

$$\det = \begin{vmatrix} f_i\left(1, 0\right) & f_j\left(1, 0\right) \\ f_i\left(0, 1\right) & f_j\left(0, 1\right) \end{vmatrix} = 0. \tag{179}$$

This condition leads to the dispersion relation given the perturbation wavenumber and the parameters β_t, n and $\mathrm{Fr_t}$.

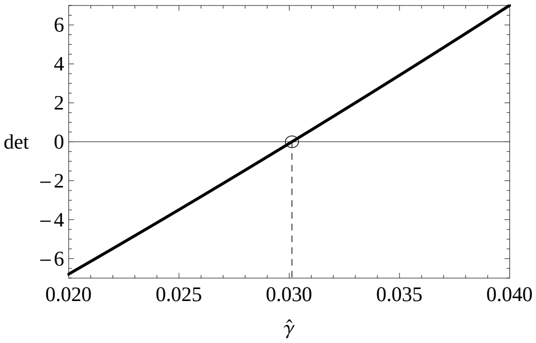

Figure 23: Determinant vs $\hat{\gamma}$ in the case $\hat{k} = 0.001$, $\beta_t = 20$, $n = 0$ and $\mathrm{Fr_t} = 0.5$. The position of the zero of the determinant (marked with a circle) determines the value of the growth rate, in this case $\hat{\gamma} \simeq 0.0301$.

6.2.3.2 *Results*

We present here a parametric study of the dispersion relation in β_t , n, and Fr_t. This can be seen in figures 24-25, where we are plotting the normalized growth rate versus the normalized wavenumber. Observe that all the plots present a classical shape of an ablative RTI dispersion relation. Thus, for long perturbation wavelengths the dispersion relation converges to the classical growth rate $\gamma = \sqrt{kg}$. Besides, stabilization effects due to the ablation process begin to be felt at shorter wavelengths, where a maximum in the growth rate is found. Quite close to this maximum the growth rate tends rapidly to zero at the so-called *cut-off wavelength* $\lambda_{co} = 2\pi/k_{co}$. Any perturbation of wavelength shorter than λ_{co} is stable. In each of the plots 24-25 presented here, we vary one parameter to see its influence in the stability of the ERA front. Obviously, as it is expected for an acceleration-driven instability, the smaller the Froude number is, the more the perturbation is amplified (see figure 25 left). Two other parameters (β_t and n) account for the radiation transport in the ablation front. Large values of β_t and n increase the role of radiation transport. The radiation transport stabilizes the disturbances growth (see figure 24 and 25 right). Indeed, it is noticeable that the effect of increasing β_t (and n) corresponds to decrease of the maximum growth rate and to displacement of the cut-off wavenumber to the left, that is to say, perturbations are stabilized for longer wavelengths.

The asymptotic trends of the cut-off wavenumber can be seen in figures 26 and 27, where the cut-off wavenumber is represented versus the parameter β_t for different values of $\mathrm{Fr_t}$ and n. The cut-off wavenumber seems to follow an asymptotic potential law in β_t with an exponent that varies with the parameter n. Thus, we have that for $n = 0$, the cut-off wavenumber fits a power law of the type $\hat{k}_{co} \propto \beta_t^{-7/6}$ when $\beta_t \gg 1$ and for $n = 1$ it is $\hat{k}_{co} \propto \beta_t^{-7/2}$. These trends will be justified in the next subsection. While changing the value of Froude number, the asymptotes are parallel displaced down with increasing values of $\mathrm{Fr_t}$.

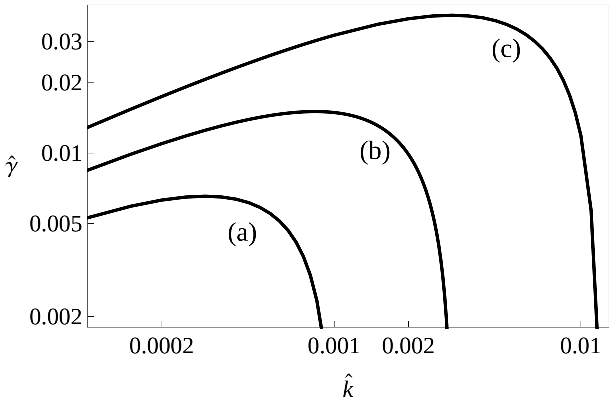

Figure 24: Numerical solution of the dispersion relation of an ERA front for different values of $\mathrm{Fr_t}$ and $\beta_t = 20$ and $n = 0$. (a) $\mathrm{Fr_t} = 2$, (b) $\mathrm{Fr_t} = 1$, and (c) $\mathrm{Fr_t} = 0.5$.

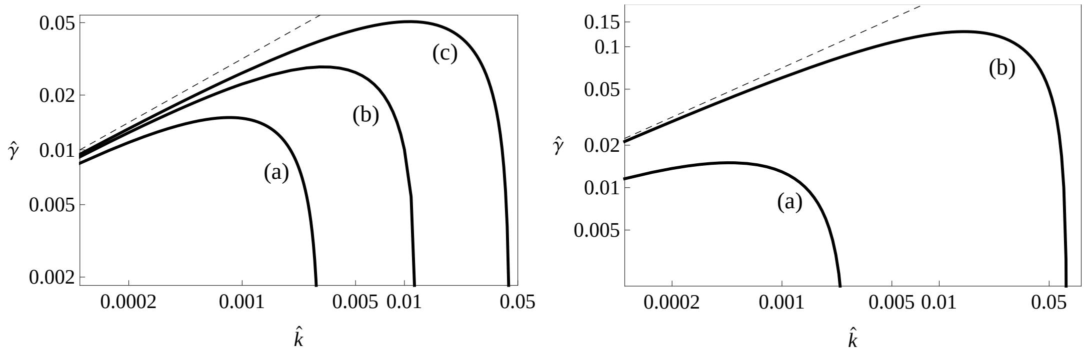

Figure 25: Numerical solution of the dispersion relation of an ERA front. Left figure corresponds to the case with $\mathrm{Fr_t} = 1$ and $n = 0$ and different values of β_t: (a) $\beta_t = 20$, (b) $\beta_t = 5$, and (c) $\beta_t = 1$. Right figure corresponds to the case with $\mathrm{Fr_t} = 0.2$ and $\beta_t = 10$ and different values of n: (a) $n = 1$ and (b) $n = 0$. In both figures, dashed line shows the classical RT dispersion relation $\sqrt{kg}$.

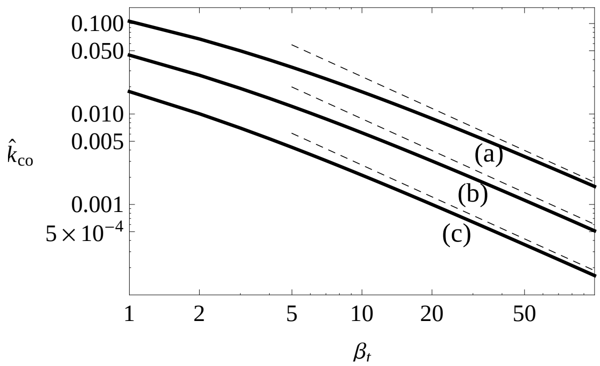

Figure 26: Numerical solution of the cut-off wavenumber of an ERA front (solid line) vs parameter β_t for $n = 0$ and different values of $\mathrm{Fr_t}$: (a) $\mathrm{Fr_t} = 0.5$, (b) $\mathrm{Fr_t} = 1$, and (c) $\mathrm{Fr_t} = 2$. Dashed lines correspond to $\hat{k}_{co} \propto \beta_t^{-7/6}$, showing the tendency of the cut-off wavenumber for $\beta_t \gg 1$.

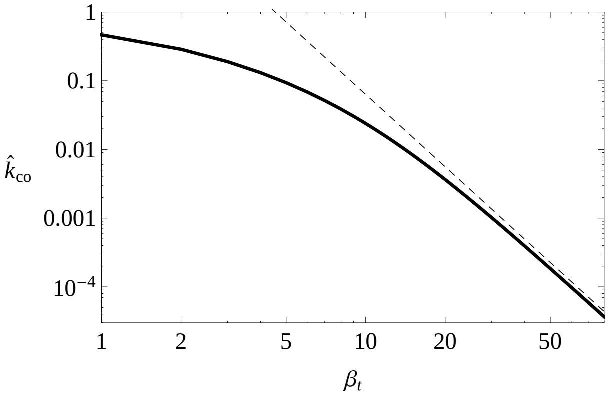

Figure 27: Numerical solution of the cut-off wavenumber of an ERA front (solid line) vs parameter β_t for $n = 1$ and $\mathrm{Fr_t} = 0.1$. Dashed line corresponds to $\hat{k}_{co} \propto \beta_t^{-7/2}$, showing the tendency of the cut-off wavenumber for $\beta_t \gg 1$.

6.3 LINEAR STABILITY ANALYSIS. ANALYTICAL SOLUTION FOR $\beta_t \gg 1$.

From the preceding subsections we can state that as β_t increases the ERA front becomes steeper, that is to say, the gradients in density and temperature profiles are more pronounced, and the cut-off wavenumber decreases. These two facts suggest that the characteristic length of the problem varies with the parameter β_t. In particular, that it increases with β_t. In this way, the Spitzer length, which has been used as the spatial scale, does not correspond to the characteristic length of the problem, since it underestimates it. The procedure to find out the appropriate length scale is conducted through the analysis of the order of magnitude of variables that appear in the governing equations, under the assumption $\beta_t \gg 1$.

6.3.1 *Characteristic length. Order of magnitude of perturbed quantities*

The assumption $\beta_t \gg 1$ implies that the problem is dominated by the radiation transport so that the enthalpy term of the energy equation can be neglected. In this way, the dominant order of the energy equation can be written as $\psi + d\psi/d\theta_0 \simeq \beta_t \theta_0^n \psi^{-1}$, where it is assumed $\beta_t > 1/\theta_0^n$. The order of magnitude of the steady solution is $\psi \equiv \theta_0^{3/2}\theta_0' \sim \mathcal{O}\left(\beta_t^{1/2}\theta_0^{n/2}\right)$. If we now assume that the spatial coordinate goes like the inverse of the wavenumber, i.e. $\hat{k}\eta \sim O(1)$, we can state that

$$\theta_0 \sim \beta_t^{1/(5-n)} \hat{k}^{-2/(5-n)} \overline{\theta}_0, \tag{180}$$

with $\overline{\theta}_0 \sim O(1)$ and keeping the order of magnitude of the wavenumber $\hat{k}$ still unknown. Next, we assume that the perturbed velocities are of the same order of magnitude no matter the direction ($u_{1x} \sim u_{1y}$) and, after balancing terms from the momentum equation, we arrive to $u_{1x} \sim u_{1y} \sim p_1$. In order to relate this estimation to the temperature, it is necessary to turn our attention to the perturbed energy equation. Assuming θ_1 scales up as θ_0 and that the perturbed convective term is as important as the two other perturbed energy fluxes, we balance convection with electron heat flux to, finally, obtain the following relation

$$u_{1y} \sim \hat{k}\theta_0^{7/2}. \tag{181}$$

We complete the estimation analyzing the forces that are present in the perturbed front of amplitude ξ_e. By balancing hydrostatic force ($\sim \rho_0 g \xi_e k^{-2}$) and dynamic pressure ($\sim \rho_0 v_0 v_{1y} k^{-2}\,(k\xi_e)$), we arrive to the relation $\hat{k}^2\theta_0^{7/2} \sim O(1)$. This last relation is obtained under the assumption that the Froude number is of the order of unity that allows us, for simplification, not to consider this parameter in the scaling laws. The order of magnitude of every variable and parameter can then be put as a function of β_t and n. In order to simplify the notation, we use the characteristic length that provides the preceding analysis as the scaling parameter. This characteristic length (called $(k^*)^{-1}$) has the following form

$$(k^*)^{-1} = \beta_t^{7/2(3-2n)}, \tag{182}$$

that corresponds to the scaling law of the cut-off wavenumber found numerically for $n = 0$ and 1 in the preceding section.

Any variable is then divided into two parts: a quantity of the order of unity that contains all the information of the variable except its order of magnitude that is provided by a scaling parameter (a power of the characteristic length $(k^*)^{-1}$). They read as follows

(I) wavenumber, growth rate and spatial coordinate

$$\begin{aligned} &\hat{k} \equiv k^* \overline{k}, \quad \hat{\gamma} \equiv (k^*)^{1/2} \overline{\gamma}, \\ &\eta \equiv \left(k^* \overline{k}\right)^{-1} \overline{\eta}, \end{aligned} \tag{183}$$

(II) quantities of the steady state (obtained from equation 180)

$$\theta_0 \equiv (k^*)^{-4/7} \overline{k}^{-2/(5-n)} \overline{\theta}_0, \tag{184}$$

(III) perturbed quantities (obtained from equations (180) and (181))

$$\begin{aligned} &\theta_1 \equiv (k^*)^{-4/7} \overline{k}^{-2/(5-n)} \overline{\theta}_1, \\ &u_{1y} \equiv (k^*)^{-1} \overline{k}^{-(2+n)/(5-n)} \overline{u}_{1y}, \\ &F_1 \equiv (k^*)^{-3/7} \overline{k}^{-n/(5-n)} \overline{F}_1, \\ &Q_1 \equiv (k^*)^{-1} \overline{k}^{-(2+n)/(5-n)} \overline{Q}_1, \\ &W_1 \equiv \overline{k}^{2-(7/(5-n))} \overline{W}_1, \end{aligned} \tag{185}$$

where the bar over any symbol denotes that the associated quantity is of the order of unity.

6.3.2 *Governing equations*

Since density/temperature profiles become very steep as β_t increases, it is convenient for the analysis to introduce a mathematical definition of the ablation front as the isotherm surface of temperature θ_0^e such that $\theta_0^e - 1 \sim \mathcal{O}(1)$ (around the same place where the minimum density gradient scale length takes place). The exact value of θ_0^e chosen is irrelevant for the asymptotic analysis $\beta_t \gg 1$ and the matching orders considered here. Choosing the origin of coordinates at $\theta_0(0) = \theta_0^e$, the perturbed ablation front surface, $\eta_e \simeq \xi_e \exp(\gamma t + ikx)$, will be obtained from $\xi_e \theta_0'(0) = -\theta_1(0)$. It is convenient for the purpose of this subsection to apply the method of strained coordinates and *strain*, in the hydrodynamic equations, the η spatial coordinate defining it in the form $s = \eta - \eta_e$. An essential reference that deals with the method of strained coordinates is the book by Van Dyke Van-Dyke [45]. The aim of this technique is to remove nonuniformities from perturbation solutions. It is based on the idea that the linearized solution may have the right form, but not quite at the right place. The remedy is to slightly strain the coordinates, by expanding one of them as well as the dependent variables in asymptotic series. Regarding the analysis of ablation fronts, a singularity arises in the limit $\beta_t \gg 1$. In particular, the transition layer collapses into a surface discontinuity. The RT instability is localized within this zero-thickness surface, where the density jump occurs. While imposing conservation laws across the three regions, we must be sure to impose them at the right place, the interface between two adjacent regions. These two interfaces are located, in the asymptotic limit $\beta_t \gg 1$, at the same place because the distance that separates them (the transition layer thickness) has collapsed. For the base flow this place is at $\eta = 0$, and for the perturbed flow at $\eta = \xi_e \exp\left(\gamma t + ikx\right)$, that depends on the time and the transversal coordinate. In the strained frame of reference, however, the interfaces are located at $s = 0$ in the zero and first order of the perturbation. This fact help us to impose the conservation laws at the right place.

Taking into account the change of variable $s = \eta - \eta_e$, partial derivatives are transformed as follows

$$\begin{aligned} \tfrac{\partial}{\partial t} &\to \tfrac{\partial}{\partial t} - \hat{\gamma}\eta_e \tfrac{\partial}{\partial s}, \\ \tfrac{\partial}{\partial \eta} &\to \tfrac{\partial}{\partial s}, \\ \tfrac{\partial}{\partial x} &\to \tfrac{\partial}{\partial x} - i\hat{k}\eta_e \tfrac{\partial}{\partial s}. \end{aligned} \tag{186}$$

We expand the normalized velocity $\vec{u}$, and temperature θ as

$$\begin{aligned} \vec{u} = {} & \tilde{u}_{1x}\left(s\right)\exp(\hat{\gamma}t + i\hat{k}x)\vec{e}_x + \\ & + \Big(\theta_0\left(s\right) + \left(\tilde{u}_{1y}\left(s\right) + \hat{\gamma}\xi_e\right)\exp(\hat{\gamma}t + i\hat{k}x)\Big)\,\vec{e}_y, \\ \theta = {} & \theta_0\left(s\right) + \tilde{\theta}_1\left(s\right)\exp(\hat{\gamma}t + i\hat{k}x). \end{aligned} \tag{187}$$

We also perform the expansion for the density and perturbed pressure in a similar way. Notice that all the tilde variables are the perturbed quantities defined with respect to the moving corrugated ablation surface, which is located at $s = 0$. We will call them hereafter the *strained perturbed quantities*. Thus, the expanded equations that correspond to the vector of state

$$\begin{aligned} &\{\tilde{F}_1, \tilde{W}_1, \tilde{Q}_1, \tilde{T}_1, \tilde{T}_1'\} \equiv \\ &\equiv \left\{\theta_0^{-1}\left(\tilde{u}_{1y} - \tilde{\theta}_1\right), i\hat{k}\tilde{u}_{1x}, 2\tilde{u}_{1y} + \tilde{p}_1 - \tilde{\theta}_1, \theta_0^{5/2}\tilde{\theta}_1, \left(\theta_0^{5/2}\tilde{\theta}_1\right)'\right\} \end{aligned} \tag{188}$$

read

$$\begin{bmatrix} \tilde{F}_1 \\ \tilde{W}_1 \\ \tilde{Q}_1 \\ \tilde{T}_1 \\ \tilde{T}_1' \end{bmatrix}' = \begin{bmatrix} 0 & -\theta_0^{-1} & 0 & \hat{\gamma}\theta_0^{-9/2} & 0 \\ -2\theta_0\hat{k}^2 & -\hat{\gamma}\theta_0^{-1} & -\hat{k}^2 & \hat{k}^2\theta_0^{-5/2} & 0 \\ -\hat{\gamma} & -1 & 0 & -\mathrm{Fr}_\mathrm{t}^{-1}\theta_0^{-9/2} & 0 \\ 0 & 0 & 0 & 0 & 1 \\ \theta_0' & 0 & 0 & h_{45} & \theta_0^{-5/2} \end{bmatrix} \begin{bmatrix} \tilde{F}_1 \\ \tilde{W}_1 \\ \tilde{Q}_1 \\ \tilde{T}_1 \\ \tilde{T}_1' \end{bmatrix} + \mathbf{B} \tag{189}$$

where

$$h_{45} = \hat{k}^2 + \frac{\hat{\gamma}}{\theta_0^{7/2}} - \frac{5}{2}\frac{\theta_0'}{\theta_0^{7/2}} - \beta_t\theta_0^{-5+n}\left(\left(\frac{3}{2} - n\right) - \left(\frac{11}{2} - n\right)\theta_0^{-4}\right)$$

and

$$\mathbf{B} = \left\{0, \hat{k}\left(\theta_0' - \mathrm{Fr}_\mathrm{t}^{-1}\theta_0^{-1}\right), -\frac{\hat{\gamma}^2}{\hat{k}\theta_0}, 0, -\hat{k}\theta_0^{5/2}\theta_0'.\right\}$$

Notice in the above system of equations the factor $\hat{k}\xi_e$ (multiplying the inhomogeneous terms of equations) has been absorbed in all perturbed variables with subscript 1.

6.3.3 *Regions*

In order to proceed with an analytical approach to the problem, it is convenient to divide it into three distinct regions, each of them with a different scaling law (see schematic in figure 28). This assumption is based on the shape of the temperature profile of the order zero, where the temperature is almost constant in the cold region and then it abruptly increases in a thin layer (transition region); behind that layer, a hot region develops. A physically relevant problem consists in considering cold, transition and hot regions separately and connect them by imposing conservation laws in the two interfaces (cold/transition and transition/hot interface) . These matching conditions will give us the dispersion equation.

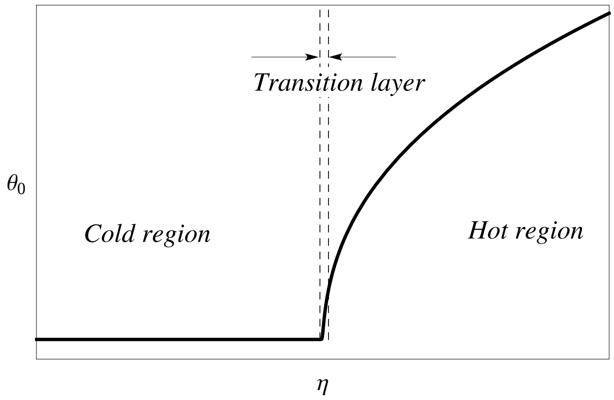

Figure 28: Schematic of the three different regions where the asymptotic problem is considered.

6.3.3.1 *a) Cold region*

The order zero solution states a temperature behaviour of $\theta_0 \simeq 1 + e^{2\sqrt{\beta_t}\eta} \equiv 1 + \delta$, where $\delta \ll 1$, in the limit $s \to -\infty$ and $\beta_t \gg 1$. This fact let us work with the hypothesis $\theta_0 \simeq 1$ and $\theta_0' \simeq 0$ that captures the most important physical aspects. Under that assumption, the system of equations (189) presents two bounded modes in this region ($\propto e^{\lambda_j s}$) with eigenvalues

$$\begin{aligned} \lambda_1^{cold} &= \hat{k}, \\ \lambda_2^{cold} &= \tfrac{1}{2} + \sqrt{4\beta_t + \hat{k}^2 + \hat{\gamma} + \tfrac{1}{4}} \simeq 2\sqrt{\beta_t}. \end{aligned} \tag{190}$$

The first eigenvalue corresponds to an *incompressible mode* (the associated eigenvector $\left\{\hat{k}/\left(\hat{k}-\hat{\gamma}\right), -\hat{k}^2/(\hat{k}-\hat{\gamma}), 1, 0, 0\right\}$ has no component in the perturbed temperature or in its derivative) and the second eigenvalue to a *thermal mode*. As $\lambda_2^{cold} \simeq 2\sqrt{\beta_t} \gg \lambda_1^{cold}$, we can admit that the influence of the perturbed temperature is very small compared to the influence of the rest perturbed quantities which are associated to the incompressible mode. Consequently, we neglect the perturbed temperature from the equations. The resolution of the system (189) is, then, immediate:

$$\begin{aligned} \tilde{F}_1 &= Ae^{\hat{k}s} - \hat{\gamma}/\hat{k}, \\ \tilde{W}_1 &= -A\hat{k}e^{\hat{k}s}, \\ \tilde{Q}_1 &= A\left(1 - \hat{\gamma}/\hat{k}\right)e^{\hat{k}s} + \left(\mathrm{Fr}_t^{-1} - 2\hat{\gamma}\right)/\hat{k}, \end{aligned} \tag{191}$$

where A is a free constant. By approaching this solution to $s \to 0^-$ and eliminating the constant A from the mass and longitudinal momentum conservation equations, we obtain the expression

$$\hat{\gamma}^2 + \hat{k}\left(1 + f_1\right)\hat{\gamma} - \hat{k}\mathrm{Fr}_t^{-1} + \hat{k}^2\left(q_1 - f_1\right) = 0 \tag{192}$$

where $f_1 = \tilde{F}_1\left(0^-\right)$ and $q_1 = \tilde{Q}_1\left(0^-\right)$. Because of their definition, f_1 and q_1 represent the perturbed mass flow rate and momentum, respectively, respect to the perturbed ablation front. Although expression (192) looks like a dispersion relation, it is not yet, since f_1 and q_1 are still unknown. The procedure for determining these constants consists in analyzing the hot and transition layers and, afterwards, matching the solutions of the three layers.

6.3.3.2 *b) Hot region*

The scaling law in this region corresponds to the one that was used to reach the characteristic length of the problem (equations (182)-(185)). In order to simplify the notation, four new parameters are introduced whose definitions are as follows

$$\begin{aligned}
\epsilon_0 &\equiv \left(k^*\right)^{1/14} \bar{k}^{-(3-n)/(5-n)} \bar{\gamma}, \\
\epsilon_1 &\equiv \left(k^*\right)^{3/7} \bar{k}^{n/(5-n)}, \\
\epsilon_2 &\equiv \left(k^*\right)^{4/7} \bar{k}^{-(1-2n)/(5-n)}, \\
\epsilon_3 &\equiv \left(k^*\right)^{16/7} \bar{k}^{8/(5-n)}.
\end{aligned} \tag{193}$$

We will consider these parameters as independent among them and obeying the relation $\epsilon_0 \gg \epsilon_1 \gg \epsilon_2 \gg \epsilon_3$, what is justified by the powers in k^*. In this way, the equation of the steady state takes the form

$$\bar{\theta}_0^{5/2}\bar{\theta}_0'' + \frac{5}{2}\bar{\theta}_0^{3/2}\left(\bar{\theta}'_0\right)^2 - \bar{\theta}_0^{-\frac{3}{2}+n} - \epsilon_1\bar{\theta}'_0 + \epsilon_3\bar{\theta}_0^{-\frac{11}{2}+n} = 0. \tag{194}$$

It admits a solution up to the order $\mathcal{O}(\epsilon_2)$ of the type

$$\bar{\theta}_0 \simeq \bar{\theta}_{00} + \epsilon_1\bar{\theta}_{01}, \tag{195}$$

where

$$\bar{\theta}_{00} = c_0\bar{s}^{2/(5-n)} = \left(\frac{(5-n)}{\sqrt{2(2+n)}}\bar{s}\right)^{2/(5-n)}, \tag{196}$$

$$\bar{\theta}_{01} = \frac{4c_0^{7/2}(5-n)}{4c_0^5(7-n) + c_0^n(5-n)^2(3-2n)}\bar{s}^{(2-n)/(5-n)}. \tag{197}$$

Note that this solution is not valid for $n = -2$ where it is singular. For $n = 0$, it takes a simple form $\bar{\theta}_{00} = \left((5/2)\bar{s}\right)^{2/5}$ and $\bar{\theta}_{01} = (1/5)\left((5/2)\bar{s}\right)^{2/5}$.

While applying the scaling law to the system of hydrodynamic equations (189), one finds

$$\begin{bmatrix} \bar{F}_1 \\ \bar{W}_1 \\ \bar{Q}_1 \\ \bar{T}_1 \\ \bar{T}_1' \end{bmatrix}' = \begin{bmatrix} 0 & -\bar{\theta}_0^{-1} & 0 & \epsilon_1\epsilon_0\bar{\theta}_0^{-9/2} & 0 \\ -2\bar{\theta}_0 & -\epsilon_0\bar{\theta}_0^{-1} & 1 & -\epsilon_1\bar{\theta}_0^{-5/2} & 0 \\ -\epsilon_0 & -1 & 0 & -\epsilon_2\mathrm{Fr}_\mathrm{t}^{-1}\bar{\theta}_0^{-9/2} & 0 \\ 0 & 0 & 0 & 0 & 1 \\ \bar{\theta}_0' & 0 & 0 & h_{45} & \epsilon_1\bar{\theta}_0^{-5/2} \end{bmatrix} \begin{bmatrix} \bar{F}_1 \\ \bar{W}_1 \\ \bar{Q}_1 \\ \bar{T}_1 \\ \bar{T}_1' \end{bmatrix} + \mathbf{B} \tag{198}$$

where

$$h_{45} = 1 - \left(\frac{3}{2} - n\right)\bar{\theta}_0^{-5+n} - \frac{\epsilon_1}{\bar{\theta}_0^{7/2}}\left(\frac{5}{2}\bar{\theta}_0' - \epsilon_0\right) + \epsilon_3\left(\frac{11}{2} - n\right)\bar{\theta}_0^{-9+n}$$

and the nonhomogeneous term is

$$\mathbf{B} = \left\{0, \epsilon_1\bar{\theta}_0' - \epsilon_2\mathrm{Fr}_\mathrm{t}^{-1}\bar{\theta}_0^{-1}, -\epsilon_2\frac{\bar{\gamma}^2}{\bar{k}\bar{\theta}_0}, 0, -\bar{\theta}_0^{5/2}\bar{\theta}_0'\right\}.$$

The above hot region's equations suggest that the perturbed quantities can be expressed in the form

$$\begin{aligned} \bar{V}_1 \simeq \bar{V}_{10}\left(\epsilon_0\right) + \epsilon_1\bar{V}_{11}\left(\epsilon_0\right) + \\ +\epsilon_2\left(\mathrm{Fr}_\mathrm{t}^{-1}\bar{V}_{12g}\left(\epsilon_0\right) + \tfrac{\bar{\gamma}^2}{\bar{k}}\bar{V}_{12\gamma}\left(\epsilon_0\right)\right) + \epsilon_3\bar{V}_{13}\left(\epsilon_0\right), \end{aligned} \tag{199}$$

where the dependence on ϵ_0 is weak. The linearity in $\mathrm{Fr}_\mathrm{t}^{-1}$ and $\bar{\gamma}^2/\bar{k}$ of the terms of the order $\mathcal{O}(\epsilon_2)$ comes from the respective linearity in the above equations. Approaching the transition layer, the flux of mass and momentum are written as

$$\begin{aligned} \bar{f}_1\left(\epsilon_0, \epsilon_1, \epsilon_2, \mathrm{Fr}_\mathrm{t}^{-1}, \bar{\gamma}^2/\bar{k}\right) = \bar{F}_1\left(0^+\right), \\ \bar{q}_1\left(\epsilon_0, \epsilon_1, \epsilon_2, \mathrm{Fr}_\mathrm{t}^{-1}, \bar{\gamma}/\bar{k}\right) = \bar{Q}_1\left(0^+\right), \end{aligned} \tag{200}$$

where 0^+ means that the value of the perturbed quantity is taken when we approach $\bar{s} = 0$ from the right side, i. e. from the hot region towards the transition layer.

The aim of this subsection is to compute order by order these two functions ($\bar{f}_1$ and $\bar{q}_1$). The dominant order is governed in the range $-1 < n < 1$ by the equations

$$\begin{bmatrix} \bar{F}_{10} \\ \bar{W}_{10} \\ \bar{Q}_{10} \\ \bar{T}_{10} \\ \bar{T}'_{10} \end{bmatrix}' = \begin{bmatrix} 0 & -\bar{\theta}_{00}^{-1} & 0 & 0 & 0 \\ -2\bar{\theta}_{00} & -\epsilon_0\bar{\theta}_{00}^{-1} & 1 & 0 & 0 \\ -\epsilon_0 & -1 & 0 & 0 & 0 \\ 0 & 0 & 0 & 0 & 1 \\ \bar{\theta}'_{00} & 0 & 0 & h_{45} & 0 \end{bmatrix} \begin{bmatrix} \bar{F}_{10} \\ \bar{W}_{10} \\ \bar{Q}_{10} \\ \bar{T}_{10} \\ \bar{T}'_{10} \end{bmatrix} + \begin{bmatrix} 0 \\ 0 \\ 0 \\ 0 \\ b_5 \end{bmatrix} \tag{201}$$

where $h_{45} = 1 - \left(\frac{3}{2} - n\right)\bar{\theta}_{00}^{-5+n}$ and $b_5 = -\bar{\theta}_{00}^{5/2}\bar{\theta}'_{00}$. The boundary conditions at $\bar{s} \to 0^+$ needed to integrate the preceding system of equations are

$$\bar{F}_{10} \to \bar{f}_{10} - \frac{5}{8c_0}\bar{q}_{10}\bar{s}^{8/5} + \dots \tag{202}$$

$$\bar{W}_{10} \to \bar{q}_{10}\bar{s} - \frac{10c_0}{7}\bar{f}_{10}\bar{s}^{7/5} + \dots \tag{203}$$

$$\bar{Q}_{10} \to \bar{q}_{10} - \epsilon_0\bar{f}_{10}\bar{s} - \frac{1}{2}\bar{q}_{10}\bar{s}^2 + \frac{25c_0}{42}\bar{f}_{10}\bar{s}^{12/5} + \dots \tag{204}$$

$$\bar{\theta}_{00}^{5/2}\bar{\theta}_{10} \to \begin{cases} \frac{4}{5}\frac{c_0^{6-n}}{3-2n}\bar{f}_{10}\bar{s}^{(7-2n)/5} - \frac{4}{5}\frac{c_0^{17/2-n}}{3-2n}\bar{s}^{(12-2n)/5} & \\ \quad -\frac{c_0^{5-n}}{2(3-2n)}\bar{q}_{10}\bar{s}^{3-2n/5} + \dots & \text{for} \quad n < 0 \\ & \\ \frac{1}{2}\left(\frac{5}{2}\right)^{2/5}\bar{f}_{10}\bar{s}^{7/5} - \frac{5}{18}\left(\frac{5}{2}\right)^{2/5}\bar{s}^{12/5} & \text{for} \quad n = 0 \\ \quad -\frac{25}{624}\bar{q}_{10}\bar{s}^3 + \dots & \\ & \\ \frac{5c_0}{7}\bar{f}_{10}\bar{s}^{7/5} - \frac{5c_0^{7/2}}{42}\bar{s}^{12/5} - \frac{1}{24}\bar{q}_{10}\bar{s}^3 + \dots & \text{for} \quad n > 0 \end{cases} \tag{205}$$

It is remarkable that this computation of $\bar{f}_{10}$ and $\bar{q}_{10}$ is oblivious to information coming from the cold region. Notice as well that the functions $\bar{f}_{10}$ and $\bar{q}_{10}$ (and their following orders) are universal in the sense that they only need to be computed once and then apply to every case permitted by the hypothesis. The procedure to compute the eigenvalues $\bar{f}_{10}$ and $\bar{q}_{10}$ is similar to the one used in the numerical dispersion relation computation. We profit from the linearity of the problem to assume a vector solution of the type $\mathbf{V_1} = \bar{f}_{10}\mathbf{V_1^f} + \bar{q}_{10}\mathbf{V_{1q}^q} + \mathbf{V_1^{inh}}$ that will blow up in the region $\bar{s} \gg 1$ since unstable modes proportional to $\exp(\bar{s})$ develop. The unstable modes do not fulfill

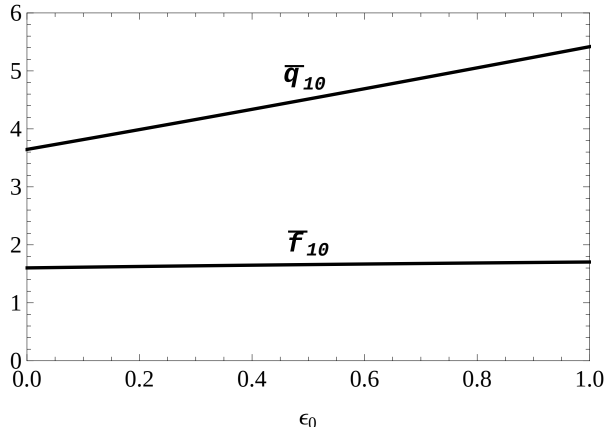

Figure 29: Functions $\bar{f}_{10}$ and $\bar{q}_{10}$ vs ϵ_0 for the case $n = 0$.

the boundary conditions (perturbations do not grow away from the ablation front), so the search for a solution compatible with the boundary conditions will determine the eigenvalues. The difference with respect to the method used in the numerical dispersion relation computation stems from the *inhomogeneity* of the system of equations (201). The nonhomogeneous term comes from the introduction of the strained variables that are attached to a frame of reference moving with the perturbed ablation front. Let $\bar{\mathbf{V}}_1$ be the solution normalized with the most unbounded mode at the right ($\propto \exp(\bar{s})$). This solution will tend to a constant vector $\mathbf{c}$ when $\bar{s} \gg 1$. Each component of the vector $\mathbf{c}$ is a linear combination of $\bar{f}_{10}$ and $\bar{q}_{10}$, and it can be written as,

$$c_i = c_i\left(a_1, a_2\right) = \bar{f}_{10}\left(c_i\left(1,0\right) - c_i\left(0,0\right)\right) + \bar{q}_{10}\left(c_i\left(0,1\right) - c_i\left(0,0\right)\right) + c_i\left(0,0\right), \tag{206}$$

and shall be zero in order to ensure a bounded solution. We select any two components of the vector solution (components i and j)

$$\begin{aligned} \bar{f}_{10}\left(c_i\left(1,0\right) - c_i\left(0,0\right)\right) + \bar{q}_{10}\left(c_i\left(0,1\right) - c_i\left(0,0\right)\right) + c_i\left(0,0\right) = 0, \\ \bar{f}_{10}\left(c_j\left(1,0\right) - c_j\left(0,0\right)\right) + \bar{q}_{10}\left(c_j\left(0,1\right) - c_j\left(0,0\right)\right) + c_j\left(0,0\right) = 0, \end{aligned} \tag{207}$$

and we arrive to a nonhomogeneous system of linear equations. If the matrix of the system is *non-singular*, there is *a single unique solution*, i. e., we can determine the eigenvalues $\bar{f}_{10}$ and $\bar{q}_{10}$ for the given set of parameters (there are two parameters in the dominant order: ϵ_0 and n).

Figure 29 shows the values of $\bar{f}_{10}$ and $\bar{q}_{10}$ for $n = 0$ as a function of the parameter ϵ_0. We can see that $\bar{f}_{10}$ slightly varies with the parameter ϵ_0 and $\bar{q}_{10}$ is almost a constant. Thus, we will model these two functions as $\bar{f}_{10} = const$

and $\bar{q}_{10} = \bar{q}_{10}(0) + \bar{q}'_{10}\epsilon_0$ where $\bar{q}'_{10} = d\bar{q}_{10}/d\epsilon_0$ is the slope of the line. In the case of $n = 0$, they take the values

$$\begin{aligned} \bar{f}_{10} &= 1.60 \\ \bar{q}_{10} &= 3.65 + 1.77\epsilon_0 \end{aligned} \tag{208}$$

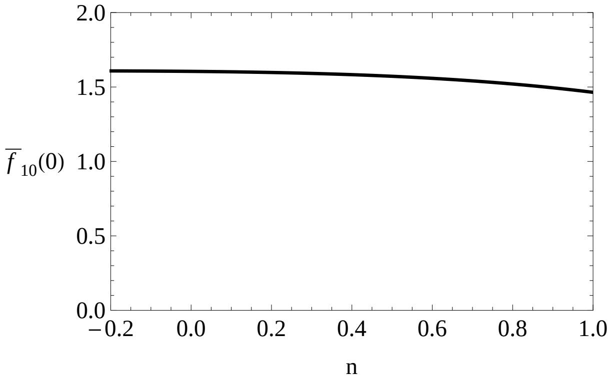

Figure 30: Function $\bar{f}_{10}$ $(\epsilon_0 = 0)$ vs parameter n.

The computations of these two functions for different values of the power index n are represented in figures 30-31. We can see that the perturbed flux of mass and momentum $\bar{f}_{10}$ and $\bar{q}_{10}$ fit a linear behaviour around $n = 0$ that can be expressed by the formulas $\bar{f}_{10} = 1.60 - 0.11n$ and $\bar{q}_{10} = (3.65 - 0.82n) + (1.77 - 0.13n)\epsilon_0$.

The following orders of perturbed fluxes of mass and momentum shall be computed in the same way. Hereafter, the equations corresponding to the order $\mathcal{O}(\epsilon_1)$ and $\mathcal{O}(\epsilon_2)$ are presented in the case $n = 0$. Note that for $n = 0$, there is no term of the order $\mathcal{O}(\epsilon_2)$ that appears in the steady

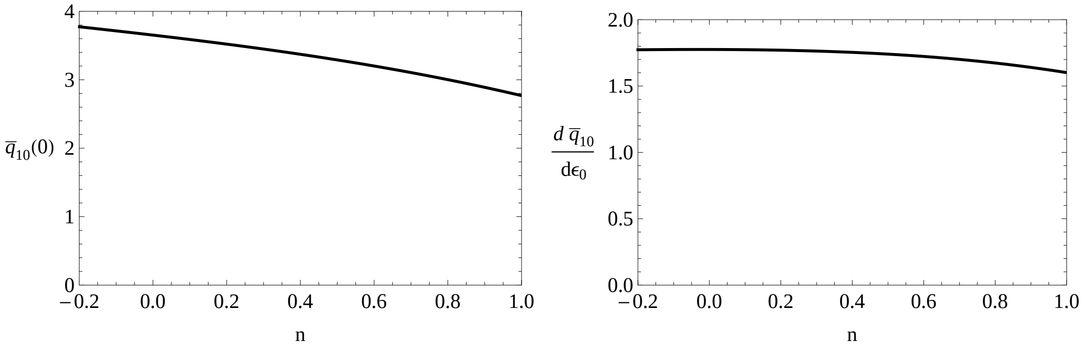

Figure 31: Function $\bar{q}_{10}$ $(\epsilon_0 = 0)$ (left figure) and $\bar{q}'_{10}$ (right figure) vs parameter n.

state solution so that the expansion is described by $\bar{\theta}_0 \simeq \bar{\theta}_{00} + \epsilon_1 \bar{\theta}_{01}$. In contrast, the perturbed variables are expanded in the form $\bar{V}_1 = \bar{V}_{10} + \epsilon_1 \bar{V}_{11} + \epsilon_2 \left(\mathrm{Fr}_t^{-1} \bar{V}_{12g} + (\bar{\gamma}^2/\bar{k}) \bar{V}_{12\gamma} \right)$, including the functions $\bar{f}_1$ and $\bar{q}_1$.

The equations of the order $\mathcal{O}(\epsilon_1)$ are

$$
\begin{gathered}
\bar{F}'_{11} + \tfrac{1}{\bar{\theta}_{00}} \left(\bar{W}_{11} - \bar{W}_{10} \tfrac{\bar{\theta}_{01}}{\bar{\theta}_{00}} \right) - \epsilon_0 \tfrac{\bar{T}_{10}}{\bar{\theta}_{00}^{9/2}} = 0, \\
\bar{W}'_{11} - \bar{Q}_{11} + 2 \left(\bar{F}_{11} \bar{\theta}_{00} + \bar{F}_{10} \bar{\theta}_{01} \right) + \tfrac{\bar{T}_{10}}{\bar{\theta}_{00}^{5/2}} - \bar{\theta}'_{00} + \tfrac{\epsilon_0}{\bar{\theta}_{00}} \left(\bar{W}_{11} - \bar{W}_{10} \tfrac{\bar{\theta}_{01}}{\bar{\theta}_{00}} \right) = 0, \\
\bar{Q}'_{11} + \bar{W}_{11} + \epsilon_0 \bar{F}_{11} = 0, \\
\bar{T}''_{11} - \left(1 - \tfrac{3}{2} \bar{\theta}_{00}^{-5} \right) \bar{T}_{11} - \tfrac{15}{2} \tfrac{\bar{T}_{10}}{\bar{\theta}_{00}^{6}} \bar{\theta}_{01} - \left(\bar{F}_{11} \bar{\theta}'_{00} + \bar{F}_{10} \bar{\theta}'_{01} \right) \\
+ \bar{\theta}_{00}^{5/2} \left(\bar{\theta}'_{01} + \tfrac{5}{2} \tfrac{\bar{\theta}'_{00}}{\bar{\theta}_{00}} \bar{\theta}_{01} \right) + \bar{\theta}_{00}^{-5/2} \left(\bar{T}'_{10} - \tfrac{5}{2} \tfrac{\bar{\theta}'_{00}}{\bar{\theta}_{00}} \bar{T}_{10} \right) - \epsilon_0 \tfrac{\bar{T}_{10}}{\bar{\theta}_{00}^{7/2}} = 0.
\end{gathered}
\tag{209}
$$

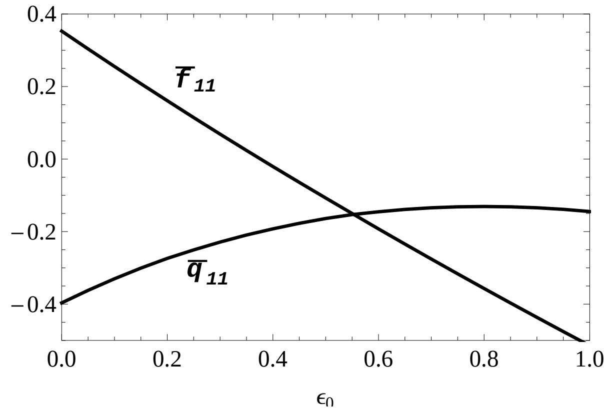

Figure 32: Functions $\bar{f}_{11}$ and $\bar{q}_{11}$ Vs ϵ_0 for the case $n = 0$.

The equations of the order $\mathcal{O}(\epsilon_2)$ are

$$
\begin{aligned}
&\bar{F}'_{12} + \tfrac{\bar{W}_{12}}{\bar{\theta}_{00}} = 0, \\
&\bar{W}'_{12} - \bar{Q}_{12} + 2\bar{F}_{12}\bar{\theta}_{00} + \tfrac{1}{\bar{\theta}_{00}\mathrm{Fr}_t} + \epsilon_0 \tfrac{\bar{W}_{12}}{\bar{\theta}_{00}} = 0, \\
&\bar{Q}'_{12} + \bar{W}_{12} + \tfrac{\bar{T}_{10}}{\bar{\theta}_{00}^{9/2}\mathrm{Fr}_t} + \tfrac{\bar{\gamma}^2}{\bar{k}} \tfrac{1}{\bar{\theta}_{00}} + \epsilon_0 \overline{F}_{12} = 0, \\
&\bar{T}''_{12} - \left(1 - \tfrac{3}{2} \bar{\theta}_{00}^{-5} \right) \bar{T}_{12} - \bar{F}_{12} \bar{\theta}'_{00},
\end{aligned}
\tag{210}
$$

The procedure to compute each order of the solution ($\bar{f}_{11}$, $\bar{q}_{11}$, ...) is the same that the one explained in the dominant order case. Solution of the order $\mathcal{O}(\epsilon_1)$ and $\mathcal{O}(\epsilon_2)$ are presented in figures 32 and 33, respectively.

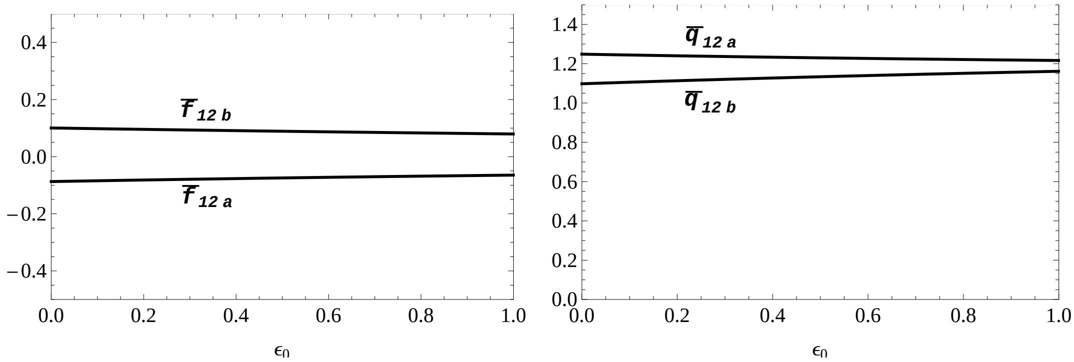

Figure 33: Functions $\bar{f}_{12a}$ and $\bar{f}_{12b}$ (left figure) and $\bar{q}_{12a}$ and $\bar{q}_{12b}$ (right figure) vs ϵ_0 for the case $n = 0$.

6.3.3.3 *c) Transition region*

This is a very thin region with a characteristic length of order $\mathcal{O}(\beta_t^{-1/2})$ which is much smaller than the length of the problem $(k^*)^{-1}$. That is the reason why this region is considered as a discontinuity surface between the hot region and the cold region. The perturbed flux of mass and momentum tend to a constant in the hot region when approaching this transition layer. Besides, the dominant order of these quantities is conserved through the transition layer. Therefore, the scaling laws for $\tilde{F}_1$ and $\tilde{Q}_1$ coincide with the one used in the hot region. Regarding the lateral velocity, we need to scale it differently, since from the hot region's point of view this quantity tends to zero as $\bar{\eta} \to 0^+$. We take the scale from the cold region, i.e. $\tilde{W}_1^{cold} \simeq -\tilde{\gamma} \sim \sqrt{k^*} \sim W_1^t$. Thus, the transition region is scaled as follows

$$\begin{aligned} \eta &\equiv \eta^t/\sqrt{\beta_t}, & \tilde{F}_1 &\equiv (k^*)^{-3/7} F_1^t, \\ \hat{k} &\equiv k^* \bar{k}, & \tilde{Q}_1 &\equiv (k^*)^{-1} Q_1^t, \\ \hat{\gamma} &\equiv (k^*)^{1/2} \bar{\gamma}, & \tilde{W}_1 &\equiv (k^*)^{1/2} W_1^t, \\ \theta_0 &\equiv \theta_0^t, & \tilde{\theta}_1 &\equiv \theta_1^t, \end{aligned} \tag{211}$$

Applying (211) to the mass and momentum flux equations, we get

$$\begin{aligned} (F_1^t)' &= O(k^*) \simeq 0 \\ (Q_1^t)' &= O(k^*) \simeq 0 \end{aligned} \tag{212}$$

6.3.4 *Matching conditions and analytical dispersion relation for $n = 0$*

Using expansion (199) and the fact that until order $\mathcal{O}(\epsilon_2)$ the mass and momentum flux are conserved across the transition layer, we can relate the cold region to the hot region through the following expressions

$$\bar{f}_{10} + \epsilon_1 \bar{f}_{11} + \epsilon_2 \left(\mathrm{Fr}_{\mathrm{t}}^{-1} \bar{f}_{12a} + \frac{\bar{\gamma}^2}{\bar{k}} \bar{f}_{12b} \right) = (k^*)^{3/7} f_1^{cold}, \tag{213}$$

$$\bar{q}_{10} + \epsilon_1 \bar{q}_{11} + \epsilon_2 \left(\mathrm{Fr}_{\mathrm{t}}^{-1} \bar{q}_{12a} + \frac{\bar{\gamma}^2}{\bar{k}} \bar{q}_{12b} \right) = k^* \bar{k}^{2/5} q_1^{cold}, \tag{214}$$

that can be substituted into equation (192) yielding an analytical formula for the dispersion relation for $n = 0$

$$\begin{aligned} \bar{\gamma}^2 + \left(\beta_t^{-1/12} \bar{f}_{10} + \beta_t^{-7/12} \left(1 + \bar{f}_{11}\right) \right) \bar{k} \bar{\gamma} - \\ - A_T \bar{k} Fr_t^{-1} + \bar{k}^{8/5} \left(\bar{q}_{10} \left(1 - \mu_b\right) + \beta_t^{-1/2} \bar{k} \bar{q}_{11} \right) - \beta_t^{-2/3} \bar{k}^2 \bar{f}_{10} = 0, \end{aligned} \tag{215}$$

where the Atwood number is defined as

$$A_T = \frac{1 - \mu_a}{1 + \mu_b} \simeq 1 - \mu_a - \mu_b, \tag{216}$$

and $\mu_a = \beta_t^{-2/3} \bar{k}^{2/5} \bar{q}_{12a}$ and $\mu_b = \beta_t^{-2/3} \bar{k}^{2/5} \bar{q}_{12b}$. In these expressions we only retain terms up to the order $\mathcal{O}\left(\beta_t^{-2/3}\right)$.By considering the terms up to the order $\mathcal{O}\left(\epsilon_0\right) \sim \mathcal{O}\left(\beta_t^{-1/12}\right)$, the dispersion relation gets reduced to

$$\bar{\gamma}^2 + \beta_t^{-1/12} 3.37 \bar{k} \bar{\gamma} - \bar{k} Fr_t^{-1} + 3.65 \bar{k}^{8/5} = 0 \tag{217}$$

where the values from the equation (208) have been introduced. From the expression (217), we can draw some preliminary considerations. The dominant contribution to the stabilization term comes from momentum (term in $\bar{q}_{10}(0) = 3.65$), which represents the rocket effect equilibrating the gravity force. The damping term accounts for the convective stabilization which is a mitigation of the unstable growth affecting the large perturbation wavenumbers. The rocket effect can lead to complete stabilization of the front for wavenumbers k larger than the cutoff, given approximately (at leading order) from equation (217) as

$$k_{co} L_{St} \simeq \beta_t^{-7/6} \left(3.65 \mathrm{Fr}_{\mathrm{t}}\right)^{-5/3}. \tag{218}$$

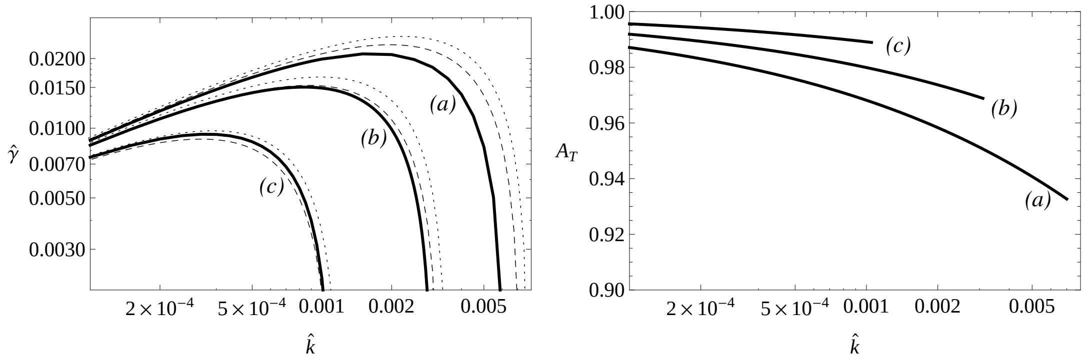

Figure 34: Left figure: Comparison between the numerical (solid line) and analytical (dashed line correspond to equation (215) and dotted line to equation (217)) solutions to the dispersion relation for $\mathrm{Fr_t} = 1$ and different values of parameter β_t: (a) $\beta_t = 10$, (b) $\beta_t = 20$ and (c) $\beta_t = 50$. Right figure shows the corresponding Atwood number (equation 216) to the cases of the left figure.

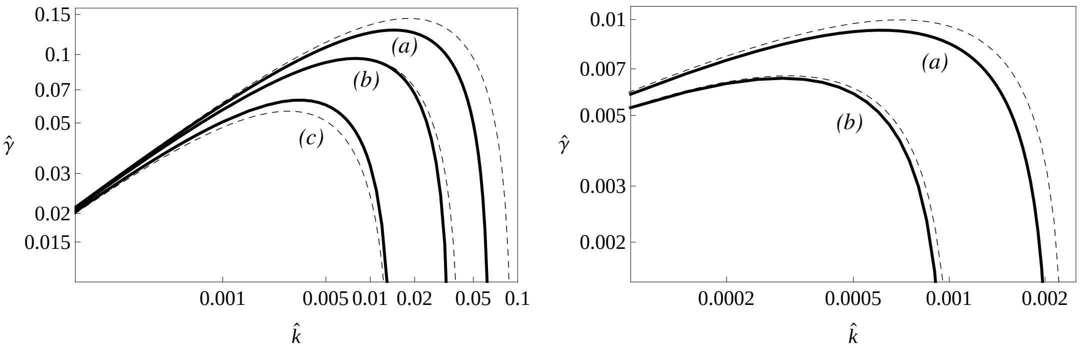

Figure 35: Comparison between the numerical (solid line) and analytical (dashed line, equation (215)) dispersion relation for different values of the parameter β_t: (a) $\beta_t = 10$, (b) $\beta_t = 20$ and (c) $\beta_t = 50$. Left figure corresponds to $\mathrm{Fr_t} = 0.2$ and right figure to $\mathrm{Fr_t} = 2$

Figures 34-35 show comparisons between the analytical and numerical dispersion curves. Figure 34 shows the analytical dispersion relation with two degrees of approximation, the dotted line with terms up to $\mathcal{O}(\beta_t^{-1/12})$ and the dashed line retaining terms up to $\mathcal{O}(\beta_t^{-2/3})$. The second approximation (equation (215)) provides a better agreement with the numerical solution. In a rough approximation of the dispersion relation (217) only the dominant terms of the rocket effect and the convective stabilization are considered. In equation (215) the stabilization mechanisms are described with a higher accuracy and other physical effects as the impact of the Atwood number (see figure 34 left panel) are retained. Moreover, we can note that the analytical approach fits better the numerical results for increasing values of the parameter β_t. This fact is expected since the analytical development is conducted under the hypothesis of $\beta_t \gg 1$. Figure 35 shows some other comparisons between the analytical model and numerical results for different values of the Froude number demonstrating a similar behaviour as described before.

6.4 CHAPTER REVIEW

In this chapter, a self-consistent model for the electron radiative ablation (ERA) front is presented. It is based on an optically thin approximation for the radiation transport model that implies a constant radiation temperature. The strong dependence of radiative effects (measured with the parameter β_t) on the length scale of the hydrodynamic profiles is shown. The dispersion curves are computed numerically demonstrating a remarkable influence of the radiative energy transport in the stabilization of a single ERA front. Both maximum growth rate of the perturbations and the cut-off wavenumber decrease with β_t. Analytical dispersion relation formula is obtained in the limit of very steep ERA front, $\beta_t \gg 1$. The order of magnitude of perturbed quantities is related to powers of a characteristic length $(k^*)^{-1} = \beta_t^{7/6} L_{St}$, which is much larger that the Spitzer length, leading to larger plasma blow-off velocities and larger stabilizing rocket effect. For instance, the cut-off wavenumber scales up as $k_{co} \propto (k^*)^{-1} \mathrm{Fr}_t^{-5/3}$, where Fr_t is the Froude number measured at the transition temperature point. Analytical dispersion relation formula is developed and shows a good agreement to numerical results for $\beta_t = 20$ and a range of Froude numbers $0.2 < \mathrm{Fr}_t < 5$.

7

RADIATIVE ABLATION FRONT

The inner ablation front in a DA front structure is mainly driven by radiation. The physical process of energy deposition for the *radiative* ablation (RA) front is roughly the following: the incident laser beams are absorbed around the critical density point of the plasma. The absorbed laser energy is then converted to thermal electrons which heat up the low-density plasma of the corona region and go towards the target. Due to the shell transitions, the atoms of the high-temperature corona plasma emit energetic photons, which pass through the corona region and the electron-radiative ablation front (which is transparent) and are absorbed in a more opaque region, driving in this way the RA front.

The radiation hydrodynamic theory of DA front structures used within this thesis (see chapter 4) assumes an optically thick regime for the region covering the RA front. In this regime, the radiation energy transport behaves as a thermal conduction term ($\vec{S}_r \propto -\kappa_R \nabla T$) where the conductivity coefficient κ_R depends on the temperature through a power law ($\kappa_R = \bar{\kappa}_R T^\nu$). A simple description can be given considering a radiation-dominated ablation front, where the convection of internal energy ($\propto P\vec{v}$) is practically balanced by the radiation energy transport. In this case, within a thin layer encompassing the RA front, we can write

$$\frac{5}{2}P_0\vec{v} - \bar{\kappa}_R T^\nu \nabla T \approx \text{const}, \tag{219}$$

where P_0 is a constant ablation pressure. This treatement of the energy equation is equivalent to the one employed in the work by Kull and Anisimov [18] for single ablation fronts, and it has been extensively used later on in the analytical and numerical stability analysis of single ablation fronts in the ICF domain (e. g. the series of papers by Betti and Goncharov [3, 4, 28, 13]).

It is convenient to note that in the case of single ablation fronts the heat flow term ($\vec{q} = -\bar{\kappa} T^\nu \nabla T$) accounts for a *generic* thermal conduction, that can include different physical processes like electron or radiation heat conduction. On the contrary, in the RA front (which is a piece of the DA front structure), it only refers to the radiation energy transport since the electron heat conduction is neglected in the radiation-dominated approximation. The mathematical description is, however, the same, and the results can be extrapolated from one case to the other.

Therefore, the object of this chapter is to apply to a radiation-dominated RA front (and, equivalently, to a single ablation front) the mathematical procedure for the computation of the dispersion relation presented in the case of ERA fronts, and compare the results to the analytical stability theory by Betti and Goncharov [3, 4, 28, 13] and to the one by Piriz *et al* [27]. Besides, we will give some comments about the influence of the power index ν on the stabilization mechanisms for single ablation fronts.

7.1 SELF-CONSISTENT NUMERICAL DISPERSION RELATION

General hydrodynamic equations that describe a thin layer covering the RA front where the front is subsonic are (see section 4.5)

$$\begin{gathered} \partial_t \rho + \nabla \cdot (\rho \vec{v}) = 0, \\ \rho \partial_t \vec{v} + \rho \left(\vec{v} \cdot \nabla \right) \vec{v} = -\nabla p + \rho \vec{g}, \\ \nabla \cdot \left(\tfrac{5}{2} P_0 \vec{v} - \bar{\kappa} T^{5/2} \nabla T - \bar{\kappa}_R T^{\nu} \nabla T \right) = 0. \end{gathered} \tag{220}$$

This system of equations is closed with the equation of state of an ideal gas $P = \rho T$. In this chapter we will assume a radiation-dominated regime so that the term of electron heat conduction can be neglected. In this way, the isobaric approximation of the energy equation can be rewritten as the following divergence-free equation

$$\nabla \cdot \left(\frac{5}{2} P_0 \vec{v} - \bar{\kappa}_R T^{\nu} \nabla T \right) \simeq 0. \tag{221}$$

7.1.1 *Steady one-dimensional solution*

We will normalize the set of equations (220)-(221) with the values of the flow variables at the peak density (subscribt a). Thus, the steady one-dimensional profiles come from the integration of the following equations

$$\begin{gathered} v_0 / v_a = \rho_a / \rho_0 = \theta_0, \\ \theta_0 - \theta_0^{\nu} \theta_0' = 1, \end{gathered} \tag{222}$$

where $\theta_0 = T_0 / T_a$ is the dimensionless temperature and the prime denotes derivative with respect to the normalized spatial coordinate $\eta = y / l_c$ with

$l_c \equiv \kappa_{Ra} T_a / (5 P_0 v_a / 2)$ a characteristic length associated to the radiative heat flow. The boundary condition to be imposed is arbitrary, and it only fixes the origin of coordinates of the problem. For convenience we will choose $\eta = 0$ the point θ_0^* where the minimum of the density gradient scale length ($L = \theta_0 / \theta_0'$) takes place. Note that $\theta_0^* = (\nu + 1) / \nu$, and, consequently [17]

$$L_{\text{min}} = \frac{(\nu+1)^{\nu+1}}{\nu^\nu}. \tag{223}$$

This minimum gradient scale length goes to $L_{\text{min}} = 1$ when $\nu \ll 1$ and to $L_{\text{min}} = (1+\nu)\, e$ when $\nu \gg 1$. It is a monotonically increasing function with respect to the parameter ν, that is to say, the radiation-dominated RA front steepens with increasing values of ν.

The asymptotic behaviours of equation (222) are easily found. Thus, we have

$$\begin{aligned} \theta_0 &\to 1 + \exp(\eta) \quad &&\text{for} \quad \eta \to -\infty, \\ \theta_0 &\to (\nu\eta)^{1/\nu} \quad &&\text{for} \quad \eta \to +\infty. \end{aligned}$$

7.1.2 *Perturbed solution*

We look for solutions of perturbed quantities (subscript 1) of the form $\exp(\gamma t + ikx)$. We would then proceed in the same way that in the preceding chapter, with the analysis of hydrodynamic equations (220)-(221) expanding $\overrightarrow{v} = (v_{1x} \exp(\gamma t + ikx), v_0 + v_{1y} \exp(\gamma t + ikx))$, ..., etc, and linearizing them in their first order perturbations. The same normalization as for the steady state solution is applied using the flow variables at the peak density and the characteristic radiative length $l_c \equiv \kappa_{Ra} T_a / (5 P_0 v_a / 2)$. By choosing the variable vector as $\mathbf{Y} = (G_1, W_1, Q_1, T_1, H_1)$, where its components are defined as

$$\begin{aligned} G_1 &= \theta_0 F_1 = u_{1y} - \theta_1, \\ W_1 &= i\hat{k} u_{1x}, \\ Q_1 &= 2u_{1y} + p_1 - \theta_1, \\ T_1 &= \theta_0^\nu \theta_1, \\ H_1 &= (\theta_0^\nu \theta_1)' - u_{1y}, \end{aligned} \tag{224}$$

the matrix of the perturbed problem $\mathbf{Y}' = \mathbf{M}\mathbf{Y}$ becomes

$$\mathbf{M} = \begin{bmatrix} \frac{\theta_0'}{\theta_0} & -1 & 0 & \frac{\hat{\gamma}}{\theta_0^{\nu+1}} & 0 \\ -2\hat{k}^2 & -\frac{\hat{\gamma}}{\theta_0} & \hat{k}^2 & -\frac{\hat{k}^2}{\theta_0^{\nu}} & 0 \\ -\frac{\hat{\gamma}}{\theta_0} & -1 & 0 & -\frac{\mathrm{Fr}_\mathrm{t}^{-1}}{\theta_0^{\nu+2}} & 0 \\ 1 & 0 & 0 & \frac{1}{\theta_0^{\nu}} & 1 \\ 0 & 1 & 0 & \hat{k}^2 & 0 \end{bmatrix}. \tag{225}$$

7.1.2.1 *The cold region ($\theta_0 \to 1$)*

We take θ_0 as an independent variable and develop the perturbed system of equation around the singular point $(\theta_0 - 1)$,

$$(\theta_0 - 1)\frac{d\mathbf{Y}}{d\theta_0} = \mathbf{M}^*\mathbf{Y}. \tag{226}$$

The matrix $\mathbf{M}^* = ((\theta_0 - 1)/\theta_0')\,\mathbf{M}$, where $\theta_0' = \sum\limits_{i=1}^{\infty} a_i (\theta_0 - 1)^i$ and $a_0 = 1$ can be developed into series in powers of $(\theta_0 - 1)$ in the way

$$\mathbf{M}^* = \sum_{r=0}^{\infty} \mathbf{M}_r^* (\theta_0 - 1)^r. \tag{227}$$

The leading order of the matrix of the perturbed system $\mathbf{M}^*$ reads

$$\mathbf{M}_\mathbf{0}^* = \begin{bmatrix} 0 & -1 & 0 & \hat{\gamma} & 0 \\ -2\hat{k}^2 & -\hat{\gamma} & \hat{k}^2 & -\hat{k}^2 & 0 \\ -\hat{\gamma} & -1 & 0 & -\mathrm{Fr}_\mathrm{t}^{-1} & 0 \\ 1 & 0 & 0 & 1 & 1 \\ 0 & 1 & 0 & \hat{k}^2 & 0 \end{bmatrix}, \tag{228}$$

and it has five distinct eigenvalues $\{\lambda_j\}$,

$$\begin{aligned} &\lambda_1 = \hat{k}, \quad && \lambda_2 = \tfrac{1}{2}\left(\sqrt{4\hat{\gamma} + 4\hat{k}^2 + 1} + 1\right), \\ &\lambda_3 = -\hat{k}, && \lambda_4 = -\tfrac{1}{2}\left(\sqrt{4\hat{\gamma} + 4\hat{k}^2 + 1} - 1\right), \\ &\lambda_5 = -\hat{\gamma}, \end{aligned} \tag{229}$$

The first two eigenvalues (positive) are bounded in the cold region. On the contrary, the last three eigenvalues (negative) are unbounded, so we set their corresponding amplitudes to zero in order to fulfill the boundary condition of vanishing perturbation away from the ablation front. The fact of dealing with a linear problem let us express the boundary condition at the left ($\eta \rightarrow -\infty$) for the integration of the perturbed system $\mathbf{Y}' = \mathbf{MY}$ as a linear combination of the two bounded eigenmodes. At the leading order, that is to say, considering terms only up to the order $(\theta_0 - 1)$, the boundary condition reads

$$\mathbf{Y^{left}} = \alpha_1 \left(\theta_0 - 1\right)^{\hat{k}} \mathbf{Y_1^{left}} + \alpha_2 \left(\theta_0 - 1\right)^{\left(\sqrt{4\hat{\gamma}+4\hat{k}^2+1}+1\right)/2} \mathbf{Y_2^{left}}, \tag{230}$$

where

$$\mathbf{Y_1^{left}} = \begin{bmatrix} -1 \\ \hat{k} \\ \frac{\hat{\gamma}}{\hat{k}} - 1 \\ 0 \\ 1 \end{bmatrix} \quad \text{and}$$
$$\mathbf{Y_2^{left}} = \begin{bmatrix} -1 \\ \lambda_2 \\ -1 + \frac{\gamma+\lambda_2+\gamma\lambda_2}{k^2} \\ 0 \\ 1 \end{bmatrix} + \mathrm{Fr_t} \begin{bmatrix} -2\gamma - \lambda_2 - \frac{\gamma(\gamma+\lambda_2+\gamma\lambda_2)}{k^2} \\ k^2 + \gamma + \gamma^2 + \lambda_2 + 2\gamma\lambda_2 \\ -\frac{(k-\gamma)(k+\gamma)(\gamma+\lambda_2)}{k^2} \\ \frac{(k-\lambda_2)(k+\lambda_2)(\gamma+\lambda_2)}{k^2} \\ 0 \end{bmatrix} \tag{231}$$

7.1.2.2 *The hot region ($\theta_0 \gg 1$)*

The leading order of the most unstable mode that develops in the hot region was computed by Sanz [31, 32] and it goes like $\sim \zeta^{\left(3+\sqrt{5}\right)/4\nu} \exp\left(k\zeta\right)$, where $\zeta \equiv \theta_0^\nu/\nu$. We can compute higher orders of eigenvalues following the procedure of Sanz [31, 32] that was described in the preceding chapter.

The equation describing the base flow reads $\theta_0' = \left(\theta_0 - 1\right)/\theta_0^\nu$, that can be approximately integrated for $\theta_0 \gg 1$ given $\eta_\infty \simeq \theta_0^\nu/\nu$. Let us take, for simplicity, $\zeta \equiv \theta_0^\nu/\nu$ as the independent variable. The system of perturbed differential equations expressed in the new variable reads $\mathbf{Y}' = \mathbf{M}^*\mathbf{Y}$ where

$$\mathbf{M}^* = \frac{1}{\left(d\theta_0/dy\right)\left(d\zeta/d\theta_0\right)}\mathbf{M} = \frac{1}{1 - 1/\theta_0}\mathbf{M} = \left(1 + \sum_{i=1}^{\infty} \theta_0^{-i}\right)\mathbf{M} \tag{232}$$

We are only interested in developing this term in series until $\theta_0^{-\nu}$ which is equivalent to ζ^{-1}. As the square matrix $\mathbf{M}$ can be developed in the power series $\mathbf{M} = \mathbf{M_0} + \theta_0^{-1}\mathbf{M_1} + \theta_0^{-\nu}\mathbf{M_2} + \ldots$, the development in series of $\mathbf{M}^*$ can be written as follows

$$\mathbf{M}^* = \sum_{i=0}^{\lfloor \nu \rfloor} \theta_0^{-i}\mathbf{M_0} + \sum_{i=0}^{\lfloor \nu-1 \rfloor} \theta_0^{-i-1}\mathbf{M_1} + \theta_0^{-\nu}\mathbf{M_2} + ..., \tag{233}$$

where $\lfloor \cdot \rfloor$ corresponds to the floor function. Depending on the value of the parameter ν, we will have a different eigenmode solution for $\mathbf{Y}(\zeta)$. In the case where $\nu = 5/2$, the development of the matrix of the perturbed system takes the form $\mathbf{M}^* = \mathbf{M_0} + \theta_0^{-1}\left(\mathbf{M_0} + \mathbf{M_1}\right) + \theta_0^{-2}\left(\mathbf{M_0} + \mathbf{M_1}\right) + \theta_0^{-5/2}\mathbf{M_2}$. We attempt then a formal solution of the type

$$\mathbf{Y}\left(\zeta\right) \propto \zeta^{\lambda_p} \exp\left(\lambda_0 \zeta + \lambda_1 \zeta^{3/5} + \lambda_2 \zeta^{1/5}\right) \ , \tag{234}$$

and solving the compatibility equations for the double eigenvalue $\lambda_0 = +\hat{k}$, we arrive to

$$\begin{aligned} \lambda_1 &= \tfrac{1}{3} 2^{2/5} 5^{3/5} \hat{k} \\ \lambda_2 &= 2^{4/5} 5^{1/5} \hat{k} \\ \lambda_p &= \tfrac{1}{10}\left(3 \pm \sqrt{5}\right) \end{aligned} \tag{235}$$

7.2 COMPARISONS WITH EXISTING STABILITY THEORIES

The most extended stability theory for single ablation fronts is the one developed by Betti and Goncharov [4, 13, 14, 28] in the mid 1990's. This theory deals with single ablation fronts driven by thermal conduction. The power index for thermal conduction ν ($\kappa \sim T^\nu$) is a parameter so that different natures of the thermal conduction can be analyzed (for instance $\nu = 5/2$ for pure electron thermal conduction). This fact let us compare the numerical results obtained in this section for a radiation-dominated RA front with the Betti and Goncharov theory. Such a comparison is not possible, however, with the analytical and numerical analysis of an ERA front (see preceding chapter) since an energy contribution besides thermal conduction is considered there, the radiative cooling law. Existing stability theories only takes into account the effect of thermal conduction in the ablation region, so there are no previous results that permit us compare with the analyisis of an ERA front ($\beta_t \neq 0$) discussed, for the first time, in this thesis.

Betti and Goncharov arrived to an analytic solution of the perturbed problem (a single fifth-order differential equation) in different asymptotic limits depending on the order of magnitude of the Froude number and the normalized wavenumber. For large Froude numbers ($\mathrm{Fr} \gg 1$), the dispersion curve, as we saw in chapter 2 (equation (34)) can be written in the following form

$$\gamma = \sqrt{A_T k g - A_T^2 k^2 V_a V_{bo}} - (1 + A_T) k V_a, \tag{236}$$

where

$$\begin{aligned} A_T &= \tfrac{1-(\rho_{bo}/\rho_a)}{1+(\rho_{bo}/\rho_a)}, \\ \tfrac{\rho_{bo}}{\rho_a} &= \tfrac{V_a}{V_{bo}} = \mu_0 \left(k L_0\right)^{1/\nu}, \\ \mu_0 &= \tfrac{(2/\nu)^{1/\nu}}{\Gamma(1+1/\nu)} + \tfrac{0.12}{\nu^2}, \end{aligned} \tag{237}$$

$\Gamma(x)$ is the gamma function and the subscript "bo" refers to a hydrodynamic quantity of the blow-off region evaluated at a distance $\sim \lambda$ from the ablation front. For small Froude numbers ($\mathrm{Fr} \ll 1$), the resolution of the fifth-order differential equation gets more complicated and the stability analysis can be carried out only in the limits of small and large wavenumbers. They arrived to a series of growth rate formulas depending on the limit considered [14]. They combined that series of growth rate formulas ($\mathrm{Fr} \ll 1$ and $kL_0 \ll 1$, $kL_0 \gg 1$) with equation (236) ($\mathrm{Fr} \gg 1$) into a single expression that reproduces the analytic results in the appropriate limits. Within this thesis, we will refer to this lengthy expression [14, 28] as the Betti and Goncharov (BG) formula. They compared the BG formula with the numerical stability theory by Kull [17] showing a good agreement. Hereafter we present new comparisons between the BG formula and the growth rate obtained with the numerical procedure described in section 6.2.3. Figure 36 shows plots of the normalized growth rate $\hat{\gamma}$ versus the normalized wavenumber $\hat{k}$ for $0.05 < \mathrm{Fr} < 20$ and $\nu = 5/2$. Observe that the asymptotic formula reproduces the numerical growth rates for small as well as large Froude numbers. Moreover, we have represented in figure 37 the neutral curve as a function of the Froude number and for three different values of the parameter ν $(3/2, 5/2 \,\text{and}\, 5)$. The neutral curve represents the frontier between a stable and an unstable ablation front. This is characterized by the *cut-off* wavenumber, and, in this way, any perturbation with a wavenumber enclosed inside the neutral curve will be unstable. We can point out that the BG formula fits remarkably well with respect to the numerical results in the limits $\mathrm{Fr} \ll 1$ and $\mathrm{Fr} \gg 1$, and that it has still an accurate approximation in the intermediate range $\mathrm{Fr} \sim 1$.

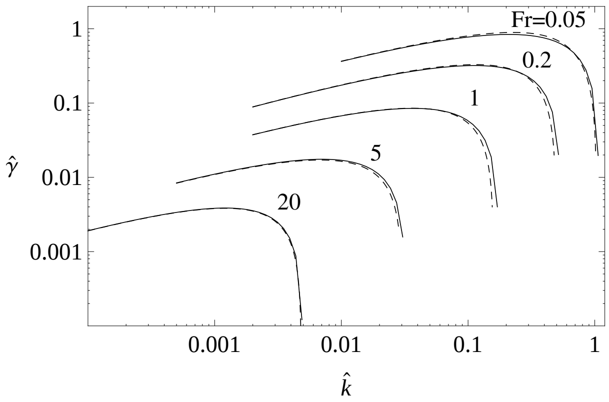

Figure 36: Dispersion relation curves calculated using the numerical procedure described in section 6.2.3 (solid line) and using the asymptotic formula by Betti and Goncharov [13, 28] (dased line) for the range of Froude numbers $0.05 < \mathrm{Fr} < 20$ and $\nu = 5/2$.

7.3 INFLUENCE OF THE POWER INDEX ν ON THE STABILIZATION MECHANISMS

In this paragraph we review the influence of the parameter ν on the stability of a single ablation front driven by thermal conduction [27, 28], and extend, for the first time, the study for values $\nu < 1$ with the results of numerical calculations. The value of the parameter ν reveals the nature of the thermal conduction mechanism. Spitzer and Harm [41] found theoretically the value $\nu = 5/2$ for pure electron thermal conduction. However, other physical processes are present in the problem that can modify the power dependence of the conductivity coefficient with respect to the temperature. It is worth noting that this modification of the parameter ν from the theoretical one comes from the fact of having imposed only one thermal conduction term in the energy equation to describe several physical processes (radiation, electron heat flow...). It is then a rough way of modeling the physics, where one parameter (ν) accounts for the information of the complex energy exchanges in the ablation front region. In the work of Betti and Goncharov [28], they adjusted the parameter ν and the characteristic length L_0 in order to fit the density profiles obtained with one-dimensional simulations. They explored different target configurations, changing the ablator material (DT, CH and Be), the thickness of the ablator (from 10 to 190 μm) and the laser intensity (from 50 to 240 TW/cm^2), and they found for these configurations a range $0.6 < \nu < 2.1$. The smallest values of ν comes from the Be ablator, indicating that radiative materials have smoother density profiles compared to

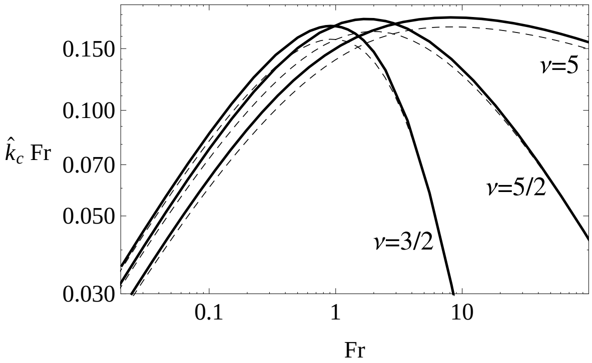

Figure 37: Neutral curve calculated using the numerical procedure described in section 6.2.3 (solid line) and using the asymptotic formula by Betti and Goncharov [13, 28] (dased line). Three cases are presented: $\nu = 3/2,\ 5/2$ and 5.

solid DT targets. These small values of ν are somehow problematic since the analytic stability theory by Betti and Goncharov is built up under the assumption $\nu > 1$. Nevertheless, we will present some comparisons in this paragraph between the BG formula and the numerical results that show that the BG formula still fits pretty well the numerical results even for $\nu \leq 1$. In the case of radiation-dominated RA front, the 1D radiation-hydrodynamic theory (chapter 4) imposes the constraint $\nu > 3$, since $\nu \equiv 3 + q_1$ where q_1 is a positive number. However, as we will see in the next chapters, the adjustment of parameters of the problem (analaguously as in reference [28]) in order to reproduce realistic flow profiles relaxes this constraint over ν. In conclusion, in this paragraph we will consider a wide range of ν values, including $\nu \leq 1$ and $\nu > 1$, to see how this parameter can influence the stabilization mechanisms of a single ablation front.

The first considerations can be extracted from the neutral curve plotted in figure 37. There, depending on the order of magnitude of the Froude number, two asymptotic behaviors are found:

- For Fr $\ll 1$, the role of an increasing value of ν is weakly stabilizing (the cutoff wavenumber gets reduced). Numerical results in this limit fit pretty well with the analytic expression given by Piriz et al. [27]

$$\kappa_c = h(\nu)\,\mathrm{Fr}^{2/3}, \quad h(\nu) \approx 1.5\frac{(2\nu+2)^{(2\nu+2)/3}}{(2\nu+3)^{(2\nu+3)/3}}, \tag{238}$$

where $\kappa_c = \hat{k}_c \mathrm{Fr}$ and the variables are normalized with the characteristic length and the velocity evaluated at the peak density. This expression was developed in the case of a steady ablation front with smooth gradients by means of the WKB approximation, and it shows two interesting facts. First, the asymptotic behaviour of $\hat{k}_c$ is a power law with an exponent independent of ν and, second, $\hat{k}_c$ is a decreasing function although weakly of ν. The scaling of the cut-off wavenumber as $\hat{k}_c \propto \mathrm{Fr}^{-1/3} \gg 1$ was already found by Goncharov et al. [14].

- For $\mathrm{Fr} \gg 1$, the tendency is just the opposite and the cutoff wavenumber increases for higher values of ν. In this case the range of unstable perturbation wavelengths widens for higher ν. A good agreement is found with the analytic theory of Betti *et al.* that predicts a cut-off wavenumber [28, 13]

  $$\kappa_c = \mu(\nu)\, \mathrm{Fr}^{-1/(\nu-1)}, \quad \mu(\nu) \approx \mu_0^{\nu/(\nu-1)}. \tag{239}$$

  Note that in this limit the asymptotic behavior of $\hat{k}_c$ is a power law with an exponent depending on the parameter ν, which strongly destabilizes steep hydrodynamic profiles ($\nu \gg 1$). This exponent dependence breaks up for $\nu = 1$. However, in those equilibria with $\nu \simeq 1$, Betti and Goncharov [28] concluded that they are RT stable for all perturbation wavelenghts provided that $\mathrm{Fr} > 2$. They arrive to this conclusion analyzing the growth rate formula (236). Indeed, if we balance the instability-drive term $A_T k g$ with the dominant stabilizing term $-A_T^2 k^2 V_a V_{bo}$ (the second term in the square root) in order to obtain, at the leading order, zero growth rate, we arrive in the case $\nu = 1$ to

  $$\mathrm{Fr_c} \simeq \mu_0(\nu = 1) = 2.12. \tag{240}$$

  This value represents the *cut-off Froude number*, that is to say, the minimum acceleration needed to drive the instability growth. We present a numerical confirmation in figure 38. There, the neutral curve for $\nu = 1$ obtained with the numerical procedure of the preceding chapter 6.2.3 shows a vertical asymptote at $\mathrm{Fr} \approx 2.1$.

In the region where $\mathrm{Fr} \sim \mathcal{O}(1)$, it is not possible to establish a general behavior since neutral curves get crossed (see figures 37 and 38).

It is also worthy to notice a peculiar feature observed in neutral curves for $\nu < 1$ (see figure 38) that was first reported by Yanez et al. [49]. The neutral curve becomes a *multievaluated function* with two cut-off wavenumbers for the

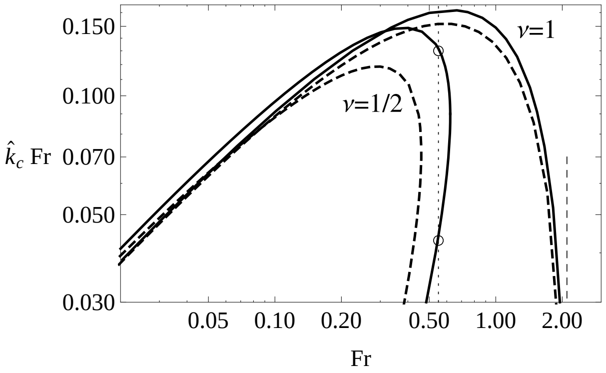

Figure 38: Neutral curve of a single ablation front depending on the Froude number and the conductivity power index ν.

same acceleration-driven condition, a cut-off for small and for long wavenumbers. Equivalent to the case $\nu = 1$, smooth hydrodynamic profiles with $\nu < 1$ present a cut-off Froude number ($\mathrm{Fr_c}$). For larger Fr the ablation front is stable for any perturbation wavelength, in other words, a sufficiently small acceleration will not lead to perturbation growth. From this point of the plot two different branches of the neutral curve develop for decreasing Froude numbers. This yields the appearance of the two different cut-off wavenumbers, staying away from the classical picture of the ablative RT instability. Actually, instead of following the classical trend of unstable growth rate $\gamma = \sqrt{kg}$ for very small wavenumbers, there is a stable region. Thus, the dispersion relation is composed of three regions: two stable regions (for both small and large wavenumbers) and an intermediate unstable region which is delimited by two cut-off wavenumbers. An example of this behavior can be seen in figure 39 where we show the case $\mathrm{Fr} = 0.55$ for two different values of thermal conductivity power index ($\nu = 1/2$ and $5/2$). Although the BG formula was derived under the assumption of $\nu > 1$, we can see in figure 38 that it arrives to reproduce the two branches found numerically in the neutral curve and, consequently, the existence of two cut-off wavenumbers in those equilibria with $\nu < 1$ and $\mathrm{Fr} < \mathrm{Fr_c}$.

The existence of the cut-off for long-wavelength modes is explained by an enhanced restoring force due to the hydrodynamic pressure (rocket effect) for those modes. In a very schematic approach with $kL_0 \ll 1$ (L_0 is a characteristic length of the ablation front), the leading terms of the relation dispersion for a single ablation front (236) are

$$\gamma \simeq \sqrt{k\left(g-(\nu/2)^{1/\nu}\,(kL_0)^{1-1/\nu}\,v_a^2/L_0\right)}-2kv_a, \qquad (241)$$

where v_a is the ablation velocity and it is assumed $A_T \simeq 1$ and $\mu_0 \simeq (2/\nu)^{1/\nu}$. The same dispersion relation formula can be obtained following the sharp-boundary model by Piriz et al. [27] if it is assumed a simple corona model going like $\bar{\rho} = (\nu y/L_0)^{1/\nu}$ where $\bar{\rho}$ is the dimensionless density, and a characteristic length of $y = (2k)^{-1}$.

Two stabilizing mechanisms are present in equation (241). The term inside the square root and proportional to v_a^2 (rocket effect) represents an overpressure or an enhancement of the dynamic pressure occurring in the crests of the corrugated ablation front (an under pressure is occurring in the valleys). This self-regulation of the ablation pressure when the front is perturbed is related to the variation of the local temperature gradient. The second stabilization mechanism (so-called convective stabilization), the term proportional to kv_a, takes its origin in the effects of fire polishing, mass convection and vorticity (see reference [27]).

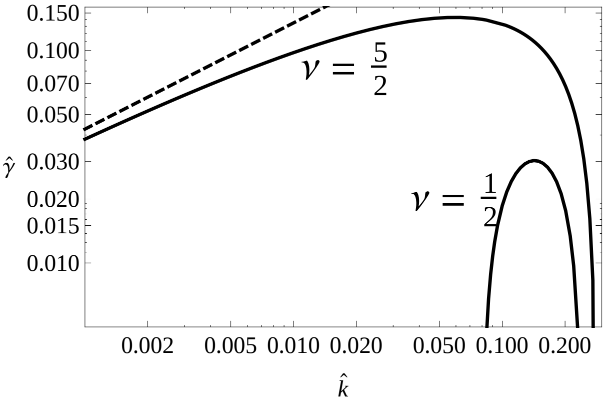

Figure 39: Dispersion relation curves for two different values of the conductivity power index ν and Fr $= 0.55$. Dashed line represents the classical RT growth rate $\gamma = \sqrt{kg}$.

The dependence of the rocket effect term on the wavenumber is defined by the nature of the thermal conduction mechanism. For a general thermal conductivity ($\kappa \sim T^{\nu}$), the rocket effect term is proportional to $k^{1-1/\nu}$

[4, 3, 13, 14, 32, 28]. On one hand, if $\nu > 1$, the rocket effect goes like k^{α} with α a positive number. This stabilizing term is effective for long perturbation wavenumbers and leads to the supression of instability when it is larger than the instability-drive term ($\propto g$), a situation that occurs for wavenumbers larger than the cut-off wavenumber. On the other hand, if $\nu < 1$, the rocket effect goes like k^{α} with α a negative number, and it affects the small perturbation wavenumbers. In this case, the rocket effect can completely suppress the unstable modes associated to small wavenumbers, which explains the smallest cut-off wavenumber that we have found numerically in figures 38 and 39.

7.4 CHAPTER REVIEW

This chapter is focused on the analyis of the radiative ablation (RA) front by means of a numerical stability method based on a self-consistent background flow. A radiation-dominated RA front is assumed with radiation tranport described by the Fourier law and a conductivity strongly dependent on the temperature ($\kappa \propto T^{\nu}$). This flow model is also considered in existing analytical self-consistent theories ([31, 3, 4, 13, 14, 32]) and several comparisons between the dispersion curves obtained with them are presented, verifying in this way the scaling laws of the problem. The Betti and Goncharov (BG) theory fits remarkably well with the numerical results in the limits where the analytical theory can be solved, $\mathrm{Fr} \ll 1$ and $\mathrm{Fr} \gg 1$. In those cases where the Froude number is of order of unity, the fitting formula by BG presents a good agreement with respect to the numerical results. This numerical self-consistent model demonstrates the existence of a new cut-off acting over the long wavelength modes for hydrodynamic profiles where the thermal conductivity power index is less than the unity, $\nu < 1$. The emergence of this cut-off for long-wavelength modes is explained by an enhanced restoring force due to the dynamic pressure (rocket effect) for those modes. Furthermore, those hydrodynamic profiles with $\nu < 1$ are stable in the case of a small acceleration (at least $\mathrm{Fr} > 2$). We can then speak of the existence of a cut-off Froude number.

Part III

STABILITY OF DOUBLE ABLATION FRONTS

This part of the thesis is devoted to the stability analysis of double ablation fronts. Numerical simulations indicate the emergence of such structures in laser-driven implosions of targets with moderate-Z ablators, such as silica or doped plastics. The stability analysis is conducted through two different approaches. In the first chapter, we present a sharp boundary model where the thin front approximation is assumed. This model takes the information concerning the near-corona region from the self-consistent analysis of an electronic-radiative ablation front carried out in the preceding part. The second chapter deals with a numerical self-consistent stability analysis. This model takes into account the finite length of the ablation fronts, and, therefore, it is able to analyze a wider range of double ablation front structures. Physical stabilization mechanisms of double ablation fronts are explained, including those concerning the double-hump shape of the dispersion relation curve. Numerical simulations are performed with the code CHIC, showing a good agreement with the theoretical results.

Ad Finem ubi perveneris, ne velis reverti

8

SHARP BOUNDARY MODEL FOR DOUBLE ABLATION FRONTS

Double ablation fronts develop in an imploding inertial fusion target when the effects in the ablation region of the radiation energy transport are strong enough compared to the material energy transport. We have seen in chapter 4 that the relative importance between radiation and material energy tranports can be measured by the dimensionless Boltzmann number, $\mathrm{Bo} = 5Pv/(8\sigma T^4)$. In this chapter we will consider the case of a *very small Boltzmann number* ($\mathrm{Bo} \ll 1$) in the ablation region. Under this condition, a well-formed DA front develops, that is to say, two ablation fronts are well defined and separated by a plateau in density/temperature. The radiation hydrodynamic theory (Sanz et al. [34]) indicates the following characteristics of the ablation region (see also figure 40):

- The energy flux is practically radiation dominated through all the plateau region. In this way the ratio $\alpha(y) \equiv S_r/(|S_r| + |q_e|)$ that measures locally the importance of radiative enegy flux takes the value $\alpha \approx -1$ in this region.
- In the plateau region, radiation and matter are almost in equilibrium.
- The thickness of the plateau region scales as $d_p \propto l_{Rt}/\mathrm{Bo}_t$, where l_R is the Rosseland mean free path and both quantities are evaluated at the transition temperature point.
- Through the ERA front, the radiative energy flux changes its sign and the value of the fraction $\alpha(y)$ changes very abruptly from $\alpha \approx -1$ in the plateau region to $\alpha \approx 1/2$ in the near-corona region where almost all the incoming electron heat flux is outwardly radiated ($q_e + S_r \approx 0$)

Naming l_{RA} and l_{ERA} to the characteristic lengths of the radiative and electron-radiative ablation fronts, respectively, we assume that these lengths are sufficiently small compared to the thickness of the plateau region (d_P). Thus, the characteristic length of the DA front structure scales as the thickness of the plateau region, and, at this scale length, both ablation fronts can be represented as a zero-thickness surface (see figure 40). In order to apply a sharp boundary model for the stability analyisis of the DA front structure

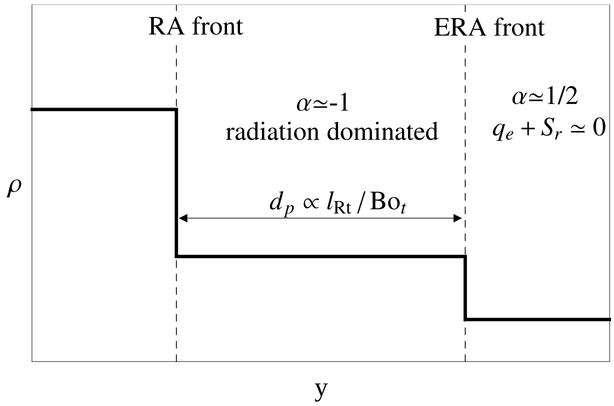

Figure 40: Schematic of a well-formed double ablation front structure.

it is also necessary that the condition $kL_0 \ll 1$, where L_0 is the characteristic length of any of the two ablation fronts (i.e. l_{RA} and l_{ERA}) and k the wavenumber of the perturbation, is fulfilled. This means that both ablation fronts are steep enough compared to the perturbation wavelength so that the zero-thickness representation is a valid approach.

In this chapter we present a sharp boundary model for the stability analyisis of the DA front structure. The inner front has been extensively studied in the past and, in order to better illustrate the coupling between both ablation fronts, we will take the sharp boundary model developed by Piriz et al. [27] as the baseline for the RA front analysis. The information concerning the stability of the ERA front will be provided by the leading order of the analytical self-consistent analyisis performed in the chapter 6. Finally, both ablation fronts are linked through a plateau region of constant density ρ_t and length d_p, where the coupling procedure shall be done by imposing conservation laws.

8.1 RADIATIVE ABLATION FRONT

8.1.1 *Governing hydrodynamic equations*

The study of the inner ablation front is carried out following the sharp boundary model reported in reference 27. This model considers a steady ablation front as a surface of zero thickness placed at $y = 0$, that is displaced in a wave-like form with a perturbation $y = \xi_a \exp(\gamma t + ikx)$. This surface separates two fluids that are initially homogeneous. In our frame of reference, the fluid ahead of the front (left) corresponds to the compressed ablator region of density ρ_a, and the fluid behind the front (right) corresponds to the plateau region of density ρ_t ($r_D = \rho_t/\rho_a < 1$). The hydrodynamic equations that govern this problem are, in the isobaric approximation, the following:

$$\begin{gathered}\partial_t\rho + \nabla\cdot(\rho\vec{v}) = 0,\\ \rho\partial_t\vec{v} + \rho\left(\vec{v}\cdot\nabla\right)\vec{v} = -\nabla p + \rho\vec{g},\\ \nabla\cdot\left(\tfrac{5}{2}P_0\vec{v} - \bar{\kappa}_R T^{\nu}\nabla T\right) = 0.\end{gathered} \tag{242}$$

This system of equations is closed with the equation of state of an ideal gas $P = \rho RT$, where R is the specific gas constant. Note that the radiation dominated regime is supposed for the plateau region so that the term accounting for the electron heat flux is neglected in the energy equation. Besides, the treatement of the compressed ablator region (ahead of the front) is simplified by assuming the effect of thermal transport to be negligible, that is to say, the peak density region is considered *adiabatic* and, consequently, the energy equation is needless for describing the fluid behaviour in that region.

8.1.2 *Perturbation modes*

We proceed by linearizing the system of equations (242). In the compressed ablator region (ρ_a, v_a), we can express the perturbed system of equations in the following matrix form

$$\frac{d}{dy}\begin{bmatrix} v_{1y} \\ w_1 \\ P_1 \end{bmatrix} = \begin{bmatrix} 0 & -1 & 0 \\ 0 & -\frac{\gamma}{v_a} & k^2 \\ -\frac{\gamma}{v_a} & 1 & 0 \end{bmatrix}\begin{bmatrix} v_{1y} \\ w_1 \\ P_1 \end{bmatrix}, \tag{243}$$

where v_a is the ablation velocity ($= r_D v_t$), $w_1 = ikv_{1x}$ and the subscript 1 refers to perturbed quantities. Note that the system is reduced to a square matrix of order 3 because of the adiabatic assumption for this region (see preceding subsection). Then, considering that the possible perturbation modes go like $\propto \exp(\lambda y)$ and solving the eigenvalue problem, we find that ahead of the front (y < 0) there are two incompressible modes (±) and one vorticity mode:

$$\begin{gathered}\lambda_{ai} = \pm k,\\ \lambda_{av} = -\gamma/v_a.\end{gathered} \tag{244}$$

The instability is expected to be localized at the interface, thus the boundary condition to be imposed in this region should be that the perturbations have to vanish at $y \to -\infty$. This boundary condition means that we have to reject those perturbed modes that explode away from the ablation front, that is to say, the perturbed modes with a negative eigenvalue. Summarizing, the income flow ($y < 0$) is assumed to be incompressible (see reference 27) with only one perturbed mode developing inside. The perturbed flow variables are then:

$$\begin{aligned} &v_{1y} = -iv_{1x} = A_1 \exp(ky), \\ &P_1 = -\rho_a \left(\gamma/k + v_a\right) v_{1y}, \\ &\rho_1 = T_1 = 0, \end{aligned} \tag{245}$$

We apply the same procedure to the flow behind the front ($0 < y < d_p$). Particularizing the linearized system of equations (242) in the plateau region (ρ_t, v_t, T_t), we can express it in the matrix form

$$\frac{d}{dy}\begin{bmatrix} v_{1y} \\ w_1 \\ P_1 \\ T_1 \\ dT_1/dy \end{bmatrix} = \begin{bmatrix} 0 & -1 & 0 & \gamma & 1 \\ 0 & -\gamma & k^2 & 0 & 0 \\ -\gamma & 1 & 0 & -\mathrm{Fr}_t^{-1} - \gamma & -1 \\ 0 & 0 & 0 & 0 & 1 \\ 0 & 0 & 0 & k^2 + \frac{\gamma}{\Delta} & \frac{1}{\Delta} \end{bmatrix} \begin{bmatrix} v_{1y} \\ w_1 \\ P_1 \\ T_1 \\ dT_1/dy \end{bmatrix}, \tag{246}$$

where $\Delta = \frac{2}{5}\bar{\kappa}_R T_t^{\nu}/\rho_t v_t$ is a characteristic thermal length. We can then solve the associated eigenvalue problem to obtain five modes that can develop inside the plateau region. There are two incompressible modes (±), two thermal conduction modes (±), and one vorticity mode:

$$\begin{aligned} &\lambda_{ti}^{1,2} = \pm k, \\ &\lambda_{tv}^{3} = -\gamma/v_t, \\ &\lambda_{tT}^{4,5} = \tfrac{1}{2\Delta} \pm \sqrt{k^2 + \tfrac{\gamma}{\Delta v_t} + \tfrac{1}{4\Delta^2}}. \end{aligned} \tag{247}$$

These modes were already reported in the paper by Kull and Anisimov [18]. Piriz et al. [27], however, assumed that the effect of the thermal transport is relatively strong behind the ablation front, and they express this condition in the *isothermal limit* $k\Delta \gg 1$. In that limit the expression of the thermal conduction modes coincide with the incompressible modes ($\lambda_{tT}^{4,5} \simeq \pm k$). Notice that it is possible to relate the characteristic thermal length (Δ) with the plateau length by integrating the zero order energy equation between two fronts. This approximated relation reads $\Delta \approx \nu\,(1 - r_D)\, d_p$.

The plateau region has a finite length (d_P). This fact allows for all five modes to develop inside the plateau region, since none of them will diverge. Thus, behind the front, in region $0 < y < d_p$, we keep the five modes

$$\begin{aligned} v_{1y} &= \textstyle\sum_{i=1}^{5} B_i \exp(\lambda_t^i y) = B_1 \exp(ky) + B_2 \exp(-ky) + B_3 \exp(-\gamma y/v_t) + \\ &\qquad\qquad + B_4 \exp(\lambda_{tT}^4 y) + B_5 \exp(\lambda_{tT}^5 y), \\ v_{1x} &= \textstyle\sum_{i=1}^{5} \frac{ik\left(\lambda_t^i g + \left(\gamma + \lambda_t^i v_t\right)^2\right)}{k^2 g + \lambda_t^i \left(\gamma + \lambda_t^i v_t\right)^2} v_{1y}^i, \\ P_1 &= -\textstyle\sum_{i=1}^{5} \frac{\rho_t \left(\gamma + \lambda_t^i v_t\right)\left(g\lambda_t^i + \left(\gamma + \lambda_t^i v_t\right)^2\right)}{k^2 g + \lambda_t^i \left(\gamma + \lambda_t^i v_t\right)^2} v_{1y}^i, \\ \rho_1 &= -\tfrac{\rho_t}{T_t} T_1 = \textstyle\sum_{i=1}^{5} \frac{\rho_t \left(k^2 - \left(\lambda_t^i\right)^2\right)\left(\gamma + \lambda_t^i v_t\right)}{k^2 g + \lambda_t^i \left(\gamma + \lambda_t^i v_t\right)^2} v_{1y}^i. \end{aligned} \tag{248}$$

It is worth noting that the perturbed temperature and density only have components for the thermal conduction modes. Besides, we find a vorticity mode in the flow inside the plateau ($v_{1y} = B_3 \exp(-\gamma y/v_t)$, $v_{1x} = -(i\gamma/kv_t)v_{1y}^i$, $P_1 = \rho_1 = T_1 = 0$), that is not present ahead of the front. Thus, the corrugated surface front acts as a source of vorticity in this model.

8.1.3 *Conservation laws at the radiative ablation surface*

The perturbed flow in the compressed ablator and plateau regions is described by equations (245) and (248), respectively. The perturbed hydrodynamic quantities depend on six arbitrary constants A_1, B_1, B_2, B_3, B_4 and B_5, that represent the amplitudes of the different modes existing in the flow at both sides of the corrugated ablation surface $y = \xi_a \exp\left(\gamma t + ikx\right)$. Mass, momentum and energy fluxes are conserved through the ablation fronts. This jump conditon at the ablation surface provides the relationships among the amplitudes of the different perturbed modes.

We have to assure first the continuity of mass across the ablation front. Thus, the perturbed flux of mass, $F_1 = \left(\rho v_y\right)_1 = \rho_0 v_{1y} + \rho_1 v_0$, must be conserved. Note that v_{1y} is the velocity with respect to the frame of reference. But, as the ablation front is moving with the time ($\propto \exp\left(\gamma t\right)$), in order to take into account effectively the mass that is crossing it, we should consider the velocity with respect to the ablation front, which is $v_{1y} - \gamma\xi_a$ (see figure 41). Then, the mass conservation law is written as

$$\rho_0 \left(v_{1y} - \gamma\xi_a\right) + \rho_1 v_0 \big|_{-}^{+} = 0, \tag{249}$$

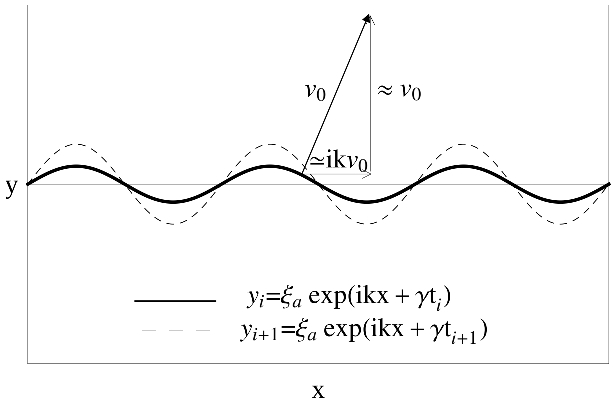

Figure 41: Schematic of the perturbed RA front.

where $\chi|_-^+ = \chi(y = 0^+) - \chi(y = 0^-)$, being χ any hydrodynamic quantity that depends on the longitudinal coordinate y.

The perturbed transverse velocity is also conserved. In this conservation law, we should take into account the perturbed transverse velocity itself and the projection of main stream velocity into the horizontal axis due to the perturbation of the ablation front (see figure 41). The jump condition reads

$$v_{1x} + ik\xi_a v_0|_-^+ = 0, \tag{250}$$

The perturbed dynamic pressure with respect to the moving front frame can be expressed as $Q_1 = \left(P + \rho v_y^2\right)_1 = P_1 + \rho_1 v_0^2 + 2\rho_0 v_0 v_{1y} \left(v_{1y} - \gamma\xi_a\right)$. Besides, the displacement of the front surface (ξ_a) leads to the apparition of the perturbed volume forces (gravity) in the flow crossing the interface. Thus, the jump condition for the momentum conservation reads

$$P_1 + \rho_1 v_0^2 + 2\rho_0 v_0 \left(v_{1y} - \gamma\xi_a\right) + \rho_0 g\xi_a|_-^+ = 0, \tag{251}$$

The perturbed quantity related to the energy that is conserved across the interface accounts for the convection of energy and the thermal conduction, and it is written in the form $H_1 = (5/2)P_0 v_{1y} - \bar{\kappa}_R \left(T_0^\nu T_1\right)'$. Note that the term corresponding to the thermal conduction is not considered ahead of the front because of the adiabatic assumption in the compressed ablator region. After some manipulations and having introduced the definition of the characteristic thermal length (Δ), the energy jump condition reads

$$v_{1y}|_-^+ = \frac{\Delta v_t}{T_t} T_1'(0), \tag{252}$$

The conservation equations across the interface do not close the problem mathematically, and we still have more unknowns than equations. In order to solve this problem, we will use an additional equation together with the above jump conditions, which describes the front surfaces as an isotherm. This physical property of the ablation front surface was originally noted by Bodner [5] and Baker [2] and it was confirmed in a rigorous way in the self-consistent theory by Sanz [31, 32]. The isothermal equation reads

$$T_1\left(0\right)+\xi_a T_0'\left(0\right)=0. \tag{253}$$

The derivative of the steady state temperature (T_0') can be find out from the energy jump condition of the steady state. The quantity that is conserved across the interface is $H_0=(5/2)P_0v_0-\bar{\kappa}_R T_0^{\nu}T_0'$. This condition yields $T_0'=T_t(1-r_D)/\Delta$.

After normalizing all variables and parameters with their respective values at the plateau region, we obtain the dispersion relation formula for the RA front in terms of the density jump r_D and two unknown constants $b_1=B_1/\left(k\xi_a\right)$ and $b_4=B_4/\left(k\xi_a\right)$ by solving equations (249)-(253).

$$\begin{aligned}&\hat{\gamma}^2+4\hat{\gamma}\hat{k}\tfrac{r_D}{1+r_D}\left(1+\tfrac{1-r_D}{4\hat{k}\hat{\Delta}}\right)-A_T\hat{k}Fr_t^{-1}+\hat{k}^2r_D\left(1+\tfrac{1-r_D}{2\hat{k}\hat{\Delta}}\right)\\&-\tfrac{2\hat{k}r_D\left(\hat{\gamma}+\hat{k}v_t\right)}{1+r_D}b_1-\tfrac{2\hat{k}r_D\left(\hat{\gamma}+\hat{k}\right)\left(A_T\hat{k}Fr_t^{-1}-\left(\hat{\gamma}+\hat{k}\right)^2\right)}{(1-r_D)\left(\hat{k}Fr_t^{-1}+\left(\hat{\gamma}+\hat{k}\right)^2\right)}b_4\\&-\tfrac{r_D\left(\hat{\gamma}+\hat{k}\right)\left(\left(\hat{k}Fr_t^{-1}\right)^2(1-r_D)\left(\hat{\gamma}+2\hat{k}\right)-\hat{k}Fr_t^{-1}(2+r_D)\left(\hat{\gamma}+\hat{k}\right)^3-\left(\hat{\gamma}+\hat{k}\right)^4\left(\hat{\gamma}-\hat{k}(2+r_D)\right)\right)}{\hat{k}\hat{\Delta}\left(1-r_D^2\right)\left(\hat{k}Fr_t^{-1}+\left(\hat{\gamma}+\hat{k}\right)^2\right)^2}b_4=0,\end{aligned} \tag{254}$$

where $A_T=\left(1-r_D\right)/\left(1+r_D\right)$ is the Atwood number of the RA front, $\hat{\Delta}\equiv\Delta/L_{St}$ and thermal modes are approximated by $\lambda_{tT}^{4,5}=\pm k+\frac{1}{2k\Delta}\left(k\pm\frac{\gamma}{v_t}\right)$. In the limit case $kd_p\sim k\Delta\rightarrow\infty$, that is to say, considering that there is only one ablation front, the RA front, we would proceed by setting to zero the constants b_1 and b_4 (in order to fulfill the boundary condition of vanishing perturbations at $y\rightarrow+\infty$), and the resulting relation dispersion equation coincides with the one given in reference [27],

$$\hat{\gamma}^2+4\hat{\gamma}\hat{k}\frac{r_D}{1+r_D}-A_T\hat{k}Fr_t^{-1}+\hat{k}^2r_D=0. \tag{255}$$

The constants b_1 and b_4 are related to the outer ablation front, and their expression will be obtained when we apply the jump conditions across the ERA front.

8.2 ABLATION FRONTS COUPLING

The sharp boundary model for the DA front is completed by imposing conservation laws across the outer ablation interface. This procedure can be accomplished using the information from the near-corona region (or hot region) that was computed in the analytical stability study of the ERA front (see chapter 6). Thus, it is possible to relate the unknown constants b_1 and b_4 of equation (254) to the perturbed flux of mass and momentum just behind the ERA front (the functions f_1 and q_1). It is worth to remind that, using the scaling law of the hot region, the only hydrodynamic quantities that are finite when we approach the ERA front are the perturbed flux of mass and momentum, and the rest of them (perturbed transverse velocity, temperature and flux of energy) tend to zero as $y \to d_p^+$. Therefore, the conservation laws across the ERA front that we impose are those of mass and momentum. Besides, we will only consider the leading order of the functions f_1 and q_1, that is to say, we assume $\beta_t \gg 1$. This fact implicitly considers the ERA front as a discontinuity surface, since the characteristic length of the ERA front goes like $\propto \beta_t^{-1/2}$ (see chapter 6), which allows us to match directly the solution of the hot region ($y > d_p$) with the solution of the plateau region ($0 < y < d_p$) given by equation (248) and, moreover, ensures the consistency of the coupled model. The jump conditions at the ERA front read

$$\rho_t \left(v_{1y} - \gamma \xi_e \right) + \rho_1 v_t \Big|_{y \to d_p} = \rho_t v_t \beta_t^{1/2} \bar{f}_{10} k \xi_e, \tag{256}$$

$$P_1 + \rho_1 v_t^2 + 2 \rho_t v_t \left(v_{1y} - \gamma \xi_e \right) + \rho_t g \xi_e \Big|_{y \to d_p} = \rho_t v_t^2 \beta_t^{7/10} \bar{q}_{10} (k L_{St})^{-2/5} k \xi_e, \tag{257}$$

where $\bar{q}_{10} \simeq 3.65 + 1.77 \beta_t^{-1/5} \hat{k}^{-3/5} \hat{\gamma}$ and $\bar{f}_{10} \simeq 1.60$. Observe that we have introduced a new unknown in the above equations. This unknown corresponds to the semi-amplitude of ERA surface distortion at the initial time (ξ_e). An additional equation is then needed. Similar to the treatment of RA front, this additional equation comes from the physical property of the ablation front as an isotherm

$$T_1 \left(d_p \right) + \xi_e T_0' \left(d_p \right) = 0, \tag{258}$$

These three equations jointly with equations (249)-(253) (eight equations for eight unkowns ξ_e, ξ_e, A, B_1,B_2, B_3, B_4 and B_5) determine the dispersion relation for the DA front structure. They can be rewritten in the way

$$\begin{aligned} R_{aa} \xi_a + R_{ae} \xi_e = 0, \\ R_{ea} \xi_a + R_{ee} \xi_e = 0, \end{aligned} \tag{259}$$

where R_{ij} are four lengthy expressions containing $\hat{\gamma}$, $\hat{k}$, $\mathrm{Fr_t}$, r_D, d_P, Δ and β_t and can be found at the end of this chapter. Observe that the procedure of constant elimination could be done in a different way, and hence equation (254) is implicitly already contained in equations (259). The condition of non-trivial solution of the system of equations (259) gives us the double ablation front dispersion relation

$$R_{aa}R_{ee} - R_{ae}R_{ea} = 0. \tag{260}$$

8.2.1 *Effect of the transverse diffusion in the ablation process*

The relaxation by transverse thermal diffusion is an important physical aspect concerning the stability properties of the ablation fronts, and some authors pointed it as the primary cause of the ablative stabilization (Clavin and Masse [9], Masse [24]). In the context of sharp-boundary model, the effects of transverse diffusion is taken into account in the plateau region, namely, by the thermal modes [48]. While the thin front approximation holds, $kL_0 \ll 1$, the thermal modes contain the information about the thermal relaxation in the ablation region. However, as it was noted by Piriz et al. [27], when $kL_0 \approx 1$ or larger, these effects are not properly considered since the jump condition of the energy conservation law at the ablation front neglects it. Thus, the perturbation growth rate obtained with the sharp boundary model is not able to reproduce numerical results in those regimes where $kL_0 \approx 1$. Piriz et al. [27] remarked that this discrepancy can be solved by taking into account the transverse thermal flux in the jump conditons. The transverse thermal flux inside the ablation surface is then assumed to be the most physically significant effect not included in the sharp boundary model statement. In order to modify accordingly the jump condition, we impose that the quantity that is conserved across the front is $H_1 = (5/2)P_0 v_{1y} - \bar{\kappa}_R \left(T_0^\nu T_1\right)' - ik\bar{\kappa}_R T_0^\nu T_1$. After some manipulations and having introduced the definition of the characteristic thermal length (Δ), the energy jump condition reads

$$v_{1y}|_-^+ = \frac{\Delta v_t}{T_t}\phi T_1'(0), \tag{261}$$

where $\phi = 1 + kL_0$. This modification in the jump condition is an approximated approach in order to include the relaxation by the transverse thermal diffusion that occurs inside the ablation front. A comparison between the sharp boundary model with the lateral transport and the numerical calculations for a single ablation front [27] indicates that the lateral transport inside the ablation front is indeed the new physical mechanism arising as kL_0 increases. Note that in the case of DA front this effect is only included in the

RA front, that is to say, it is assumed that the ERA front is steeper than the RA front so that the effects of a kL_0 of the order of unity are weaker in the outer front. In the next chapter we will present several one-dimensional simulations with the CHIC code that supports this assumption, being the steepness of the ERA front more pronounced that the RA front.

8.3 DISPERSION RELATION CURVES FOR DOUBLE ABLATION FRONTS

Equation (260) provides the growth rate $\hat{\gamma}$ of a sinusoidal perturbation of wavenumber $\hat{k}$ developing within the double ablation front region. This DA front which is subject to an acceleration defined by the Froude number $\mathrm{Fr_t}$ is characterized by the ratio between the plateau and peak densities (r_D), the distance between two fronts (d_P) and two parameters containing the information about the importance of radiative transport in the ablation region, Δ and β_t.

In this section we assume for simplicity that the value of the parameter β_t is 20 (such a value was reported in references [34, 10] as an approximation in the case of a SiO_2 ablator), and the value of the thermal conductivity power index ν is 5. This value of ν is large enough so that the relation between the plateu length and the thermal characteristic length, that is to say $\triangle = \nu\,(1 - r_D)\,d_p$, holds. These large values of the parameters β_t and ν guarantee that the thin front approximation is valid and, therefore, the use of a sharp boundary model to analyze the stability of the ablation region is justified. Then, in this first approach, we study the variation of stability properties of the DA front with respect to three parameters: $\mathrm{Fr_t}$, r_D and d_P.

A collection of dispersion curves can be seen in figures 42, 43 and 44. Their shape depends mainly on the plateau length. As the plateau length increases with time (reference [10]), we can say that for the same laser irradation condition and the same ablator material, short plateau regions represent early stages of target acceleration, whereas long plateau regions represent the final stages of accelearation. Regarding the left side of these figures, one can see that the dispersion curve approaches the classical RT growth rate $\sqrt{kg}$ for small wavenumbers as expected. Indeed, in the limit of small wavenumbers, the DA front structure cannot be distinguished and it dissappears into a single ablation interface that separates a dense flow of density ρ_a and a light flow of density $\rho \ll 1$ (i. e. $A_T \approx 1$). The intermediate region of the dispersion curve (between the classical trend and the maximum growth rate) is richer in behaviors, being stronlgy influenced by the value of the plateau length. A

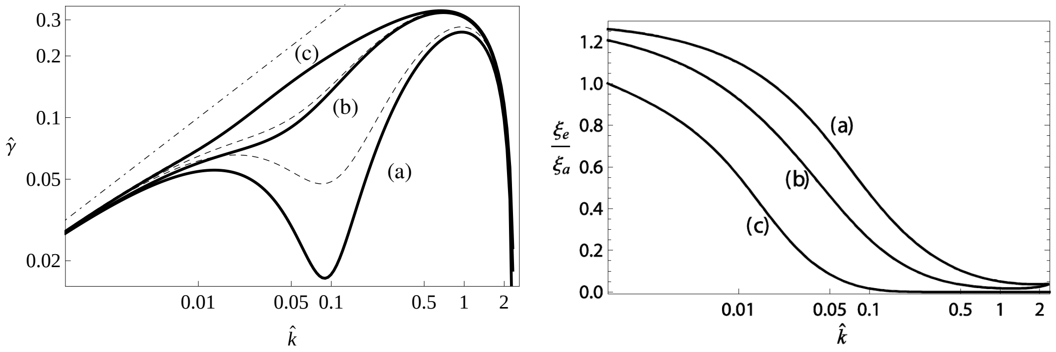

Figure 42: The left panel shows the dispersion relation of DA fronts for the parameters $\beta_t = 20$, $\mathrm{Fr}_t = 1$, $r_D = 0.25$, $\triangle = \nu\,(1 - r_D)\,d_p$ with $\nu = 5$ and different values of the plateau length, (a) $d_p = 2L_{St}$, (b) $d_p = 5L_{St}$ and (c) $d_p = 30L_{St}$. Dashed lines show the growth rate in the limit $\triangle \gg 1$. Dash-dotted line corresponds to the classical RT dispersion relation $\sqrt{kg}$. Right panel shows the ratio of semi-amplitude perturbations of the DA fronts versus the normalized wavenumber for the same parameters that the left panel.

sufficient separation between the ablation fronts ($d_p = 30L_{St}$ as in the case of the plotted figures, or longer) makes the dispersion curve similar to the growth rate of the equivalent single RA front, which is the more unstable among two fronts, except for small wavenumbers where the asymptote is, as we have already mentioned, $\sqrt{kg}$ instead of $\sqrt{A_T kg}$. This feature may indicate a weak influence of coupled modes, that is to say, the perturbed modes (including those that lead to the stabilization) that develop within the inner and outer ablation fronts are damped in the long plateau region and are not strong enough to interact with the perturbed modes of the other front and modify the overall stability behaviour of the DA front structure. Nevertheless, the situation changes when we decrease the plateau length, strengthening the effect of coupled modes. In this case an additional stabilization coming from the interaction between the two ablation fronts (coupled modes) appears, and it is enhanced as a closer distance is taken. At a first sight, it is noticeable the apparition of a local minimum that gives a characterisitic double-hump shape to the dispersion curve. This minimum is more pronounced as d_p decreases, and in some circumstances it can end up with the division of the dispersion curve into two lobes with a stable range of wavenumbers in the middle. For instance, in figure 43 the case corresponding to $d_p = 3L_{St}$ (right panel) shows a suppression of the RT instability for perturbations with wavenumbers between $\hat{k} \simeq 0.033$ and $\hat{k} \simeq 0.126$ and, obviously, after the cut-off ($\hat{k}_{co} \simeq 1.326$). It is also remarkable a slight decrease in the maximum growth rate observed

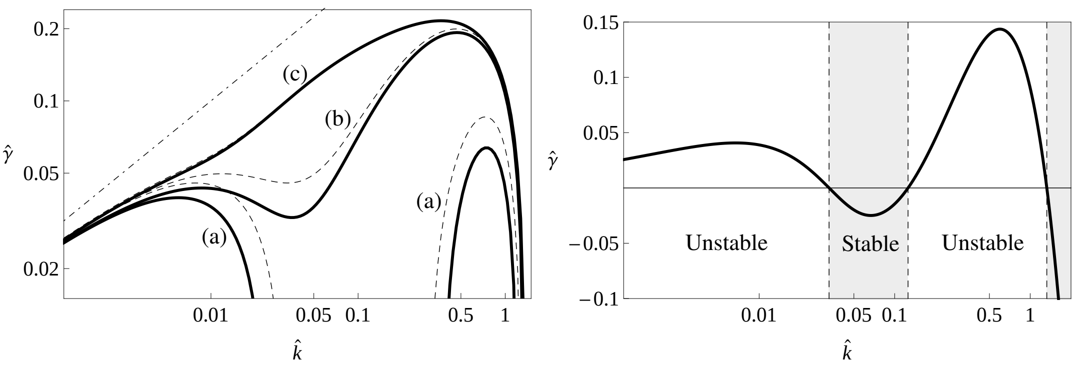

Figure 43: Dispersion relation of the DA fronts for the parameters $\beta_t = 20$, $\mathrm{Fr}_t = 1$, $r_D = 0.35$, $\triangle = \nu\,(1 - r_D)\,d_p$ with $\nu = 5$ and different values of the plateau length: left figure (a) $d_p = 2L_{St}$, (b) $d_p = 5L_{St}$ and (c) $d_p = 30L_{St}$, and right figure $d_p = 3L_{St}$. Dashed lines in the left panel show the growth rate in the limit $\triangle \gg 1$, and the dash-dotted line corresponds to the classical RT dispersion relation $\sqrt{kg}$.

for a wide range of values of the plateau length. A signficant decrease of the maximum growth rate, which would be decisive for the ICF applications, only takes place for the regimes with a very short plateau length (less than $d_p/L_{St} = 5$). In order to conclude this approach to finding the dispersion relations, we point out that the cut-off wavenumber is practically equal to the equivalent single RA front one and it does not vary significantly with d_p.

One can see the effect of the density jump and the Froude number comparing figures 42, 43 and 44. In particular,

- the effect of the density jump refers to the height of the unstable flow column of the RA front. As the inner ablation front is the most unstable, a decrease in the density jump (r_D tending to the unity) stabilizes the DA front structure. Between figures 42 and 43 the only modification in the flow configuration concerns r_D (we pass from $r_D = 0.25$ to $r_D = 0.35$), and we can appreciate in the latter curves a reduction in the maximum growth rate, a smaller cut-off wavenumber and more pronounced effects of the coupled modes stabilization.

- As it is expected in an acceleration-driven instability, the increase of the Froude number (decrease of the acceleration) makes the DA front structure less unstable. Thus, the cut-off wavenumber and the maximum growth rate get reduced as well as the the stabilization due to the coupled modes is enhanced in a regime of smaller acceleration.

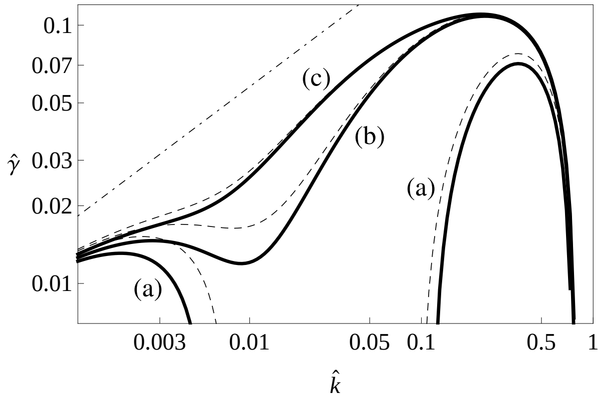

Figure 44: Dispersion relation of the DA fronts for the parameters $\beta_t = 20$, $\mathrm{Fr}_t = 3$, $r_D = 0.25$, $\triangle = \nu\,(1 - r_D)\, d_p$ with $\nu = 5$ and different values of the plateau length, (a) $d_p = 5L_{St}$, (b) $d_p = 15L_{St}$ and (c) $d_p = 30L_{St}$. Dashed lines show the growth rate in the limit $\triangle \gg 1$. Dash-dotted line corresponds to the classical RT dispersion relation $\sqrt{kg}$.

Figure 42 (panel right) shows the ratio between the semi-amplitude ξ of the perturbation for both ablation fronts. This is a way to measure the relative importance of each front in the instability. We can see that for small wavenumbers the weight of both fronts are similar $\xi_e/\xi_a \to 1$, slightly increasing the influence of the ERA front when the separation distance is shorter. As we consider larger wavenumbers, the RA front gets more important, and two effects can be highlighted. First, when the plateau length is long enough, the ratio ξ_e/ξ_a goes practically to zero. That indicates that the role played by the ERA front is very limited in this regime ($d_p \gg 1$), which agrees with the fact that the dispersion relation suits approximately the same curve than for a single RA front. Second, the ratio ξ_e/ξ_a can be very small but it never reaches zero. This fact means that, although a single ERA front would be stable (in our case, $\beta_t = 20$ and $\mathrm{Fr}_t = 1$, the cut-off wavenumber is $\hat{k}_{co}^{ERA} \simeq 0.003$), the coupled ERA front continues to be unstable for any perturbation wavenumber until the global cut-off wavenumber is reached (or in an intermediate stable region, if it is formed).

Figure 45 shows a preliminary comparison of the growth rate obtained in 2D axisymmetric numerical simulations and with the present linear theory. A good agreement is found. Single-mode 2D simulations were carried out with the radiative-hydrodynamic code CHIC [6, 22, 21], considering a spherical shell composed of an external SiO_2 layer of 20 μm, which is irradiated by a laser pulse with a rise time of 900 ps to a maximum intensity of about

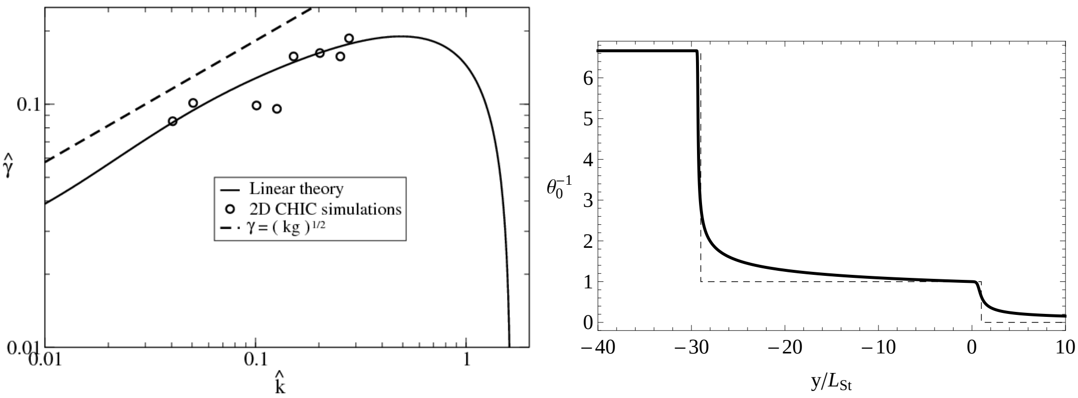

Figure 45: (Panel left) Normalized growth rate obtained with 2D single-mode simulations (circles) and applying the linear theory (solid line) for the parameters $\beta_t = 20$ (SiO_2), $\mathrm{Fr}_t = 3$, $r_D = 0.15$, $\triangle = \nu\,(1 - r_D)\,d_p$ with $\nu = 5$ and plateau length $d_p = 28.5 L_{St}$. Dashed line corresponds to the classical RT dispersion relation $\sqrt{kg}$. (Panel right) Dimensionless density profile according to the radiation hydrodynamic theory of DA fronts (chapter 4) with the above parameters (solid line) or the thin front approximation (dashed line).

500 TW/cm^2. The acceleration of the ablation zone occurs after the shock propagates through an interface cryogenic-DT/SiO$_2$, whose radius is initially 700 μm. Simulations results are taken at the time 1 ns at the ERA front. At that time, the ablation velocity is about 10^6 cm/s, the acceleration 10^{16} cm/s^2 and $L_{St} \approx 3.5 \cdot 10^{-5}$cm, that corresponds to a Froude number equal to 3 and $\beta_t \approx 20$. The density ratio is $r_D \approx 0.15$ and $d_p \approx 28.5\, L_{St}$. The corresponding solution of the linear theory is presented in figure 45, jointly with the simulation results. The simulation results correspond to cases $1 < kd_p < 10$, i.e. the Legendre mode number, n, of the spherical perturbation lies in the range $80 < n < 500$.

8.3.1 *Discussion of results*

The approach to a linear stability theory for a DA front structure that we have developed in this chapter is based on a sharp boundary model for both fronts. This thin front approximation corresponds to an ablator material that exhibits a clear DA front structure, which is mainly governed by the dimensionless parameter $\beta_t \sim T_t^5 K_{Pt} \kappa_t / \left(P_t v_t\right)^2$. Its value can easily be estimated from the plasma conditions at the ERA front: pressure P_t, temperature T_t, velocity v_t, Planck opacity K_{Pt}, and Spitzer thermal conductivity κ_t. Notice that increasing values of β_t leads to steeper electron temperature profiles and larger plasma blow-off velocities, and this is the primary origin of stabilization. The DA front instability growth rate has been obtained numerically and it depends on several physical parameters, $\gamma = v_t L_{St} \hat{\gamma} \left(k L_{St}, \mathrm{Fr_t}, d_p / L_{St}, \rho_t / \rho_a, \beta_t \right)$. The dimensionless growth rate, $\hat{\gamma}$, is plotted in figures 42-44, versus the normalized wave number $\hat{k} = k L_{St}$ for several values of the parameters. By decreasing the value of d_p / L_{st} and/or increasing the values of ρ_t / ρ_a or β_t, the coupling between both fronts is increased. Stabilizing effects appear as a consequence of interaction between the two ablation fronts (modes generated there become coupled), and they are very effective when β_t is large. First there is an increased perturbed mass flow rate at the EA front (right hand side of equation (256)), $\propto \rho_t v_t \sqrt{\beta_t}$, and second we also have an increased perturbed hydrodynamic pressure (rocket effect, right hand side of equation (257)) $\propto \beta_t^{7/10} \rho_t v_t^2 k^{-2/5} L_{St}^{-2/5}$. Notice also that the ablation velocity v_t at the EA front is r_D^{-1} times larger than the ablation velocity at the RA front. This stabilizing effect is consistent with the reduced growth rate found in Fujioka et al. [11] with brominated plastic ablators.

One interesting result of the present stability analysis is the strongly stabilizing effect we find for such ablators and laser irradiation conditions that β_t is large, $r_D \approx 1$ and d_p is relatively small (dispersion curves in panels (a) in figures 42-44). Although r_D and d_p are changing in time during the target implosion, one may shape the laser intensity in order to hold $r_D \approx 1$ and d_p as small as possible. In particular, by introducing a picket laser pulse that increases temperature at RA front (and decreases density ρ_a) one may maintain r_D values closer to unity. In the ideal case where d_p remains relatively small and $T_a \simeq T_t$ we would have almost an electron-radiative single ablation front, early stable.

8.4 CHAPTER REVIEW

In this chapter a sharp boundary model is developed for the stability analysis of double ablation fronts. Because of the thin front approximation, the scope of this model lies in those hydrodynamic structures with steep ablation fronts, which are encountered in one-dimensional simulations when a moderate-Z ablator such as SiO_2 is considered. A dispersion relation formula is obtained by coupling through conservation laws an existing sharp boundary model for the RA front [27] to the leading order of the ERA front solution (obtained in chapter 6). Results show the preponderance of unstable modes associated to the RA front for large plateau lengths and a noticeable influence of coupled modes for short plateau lengths. These coupled modes lead to the appearance of a double-hump shape in the dispersion curves that can even split the dispersion curve into two, forming a new intermediate stable region. A comparison of the dispersion curve given by the analytical model with growth rates obtained in 2D single-mode simulations is presented showing a good agreement for wave numbers $1 < kd_p < 10$.

8.5 ANNEXES

8.5.1 *Expressions for the DA front dispersion relation formula*

Expressions of the coefficients R_{aa}, R_{ee}, R_{ae}, and R_{ea} in the limit $\hat{\Delta} \gg 1$:

$$\begin{aligned} R_{den}R_{aa}r_D = {} & \mathrm{Ch}\left(2\hat{k}d_p\right)\left(\hat{\gamma}^3+\hat{\gamma}^2\hat{k}r_D-\hat{\gamma}\hat{k}^2\left(2-r_D\right)r_D-\hat{\gamma}\hat{k}\mathrm{Fr}_{\mathrm{t}}^{-1}\left(1-r_D\right)-\hat{k}^3r_D\right) \\ & +\mathrm{Sh}\left(2\hat{k}d_p\right)\times\left(\hat{\gamma}^3r_D-\hat{\gamma}^2\hat{k}\left(1-2r_D\right)-\hat{k}^2\left(\hat{\gamma}r_D-\mathrm{Fr}_{\mathrm{t}}^{-1}\left(1-r_D\right)\right)-\hat{k}^3r_D^2\right) \\ & +2\exp(-\hat{\gamma}d_p)\left(1-r_D\right)\hat{k}\left(\mathrm{Ch}\left(\hat{k}d_p\right)\hat{k}\left(\hat{\gamma}+\hat{k}\right)r_D+\mathrm{Sh}\left(\hat{k}d_p\right)\left(\hat{\gamma}^2+\hat{k}\left(\hat{\gamma}r_D-\mathrm{Fr}_{\mathrm{t}}^{-1}\right)\right)\right) \\ & -\left(\hat{\gamma}^3-\hat{\gamma}^2\hat{k}r_D-\hat{\gamma}\hat{k}^2r_D^2-\hat{\gamma}\hat{k}\mathrm{Fr}_{\mathrm{t}}^{-1}\left(1-r_D\right)+\hat{k}^3r_D\left(3-2r_D\right)\right), \end{aligned}$$

$$\begin{aligned} R_{den}R_{ee} = {} & \mathrm{Sh}\left(2\hat{k}d_p\right)\left(\hat{\gamma}^3+\hat{\gamma}^2\bar{f}_{10}\hat{k}-\hat{k}^2\left(\hat{\gamma}-\mathrm{Fr}_{\mathrm{t}}^{-1}\right)-\hat{k}^3\left(\bar{q}_{10}-\bar{f}_{10}\right)\right) \\ & +\hat{\gamma}\hat{k}\mathrm{Ch}\left(2\hat{k}d_p\right)\left(\hat{k}\left(\bar{q}_{10}-2\bar{f}_{10}\right)-\mathrm{Fr}_{\mathrm{t}}^{-1}\right)+\hat{\gamma}\hat{k}\left(2\hat{\gamma}-\hat{k}\left(\bar{q}_{10}-2\bar{f}_{10}-2r_D\right)+\mathrm{Fr}_{\mathrm{t}}^{-1}\right) \\ & -2\hat{k}^2\exp(-\hat{\gamma}d_p)\mathrm{Sh}\left(\hat{k}d_p\right)\left(\hat{\gamma}-\hat{k}\left(\bar{q}_{10}-2\bar{f}_{10}-2r_D\right)+\mathrm{Fr}_{\mathrm{t}}^{-1}\right)-2k^2\mathrm{Ch}\left(\hat{k}d_p\right)e^{-\hat{\gamma}d_p}\left(\hat{k}+\hat{\gamma}r_D\right), \end{aligned}$$

$$\begin{aligned} R_{den}R_{ae} = {} & 2\left(\hat{\gamma}+\hat{k}\right)\hat{k}^2\left(\bar{f}_{10}\mathrm{Sh}\left(\hat{k}d_p\right)+2\mathrm{Ch}\left(\hat{k}d_p\right)-\left(1-r_D\right)\exp(-\hat{\gamma}d_p)-r_D\exp(-\hat{k}d_p)\right) \\ & -2\left(\hat{\gamma}+\hat{k}\right)\hat{\gamma}\hat{k}\left(\bar{f}_{10}\mathrm{Sh}\left(\hat{k}d_p\right)+\mathrm{Ch}\left(\hat{k}d_p\right)\right)-\hat{\gamma}^2\mathrm{Sh}\left(\hat{k}d_p\right), \end{aligned}$$

$$\begin{aligned} R_{den}R_{ea}\exp(\left(\hat{\gamma}-\hat{k}\right)d_p) = {} & -2\hat{\gamma}^3\exp(\left(\hat{\gamma}-\hat{k}\right)d_p)\mathrm{Sh}\left(\hat{k}d_p\right)+2\hat{\gamma}^2\hat{k}\left(\mathrm{Sh}\left(\hat{k}d_p\right)-\exp(\hat{\gamma}d_p)\right) \\ & +\hat{\gamma}\hat{k}^2\left(\left(1-2r_D\right)\exp(\hat{\gamma}d_p)+2\left(r_D\mathrm{Ch}\left(\hat{k}d_p\right)+\mathrm{Sh}\left(\hat{k}d_p\right)\right)-\exp(\left(\hat{\gamma}-2\hat{k}\right)d_p)\right) \\ & +2\hat{k}^3\left(r_D\mathrm{Sh}\left(\hat{k}d_p\right)+\exp(-\hat{k}d_p)\right), \end{aligned}$$

where $R_{den} = \hat{k}\mathrm{Ch}\left(\hat{k}d_p\right) - \hat{\gamma}\mathrm{Sh}\left(\hat{k}d_p\right) - \hat{k}\exp(-\hat{\gamma}d_p)$.

8.5.2 *Simplified dispersion relation formula for the double ablation front structure*

Simplification of the DA front analytic dispersion relation formula of the sharp boundary model presented in [48] is performed under the following assumptions $\Delta \gg 1$ and $r_D \ll 1$.

The dispersion relation will be built up as a fitting between two asymptotic limits, small and large wavelengths compared to the plateau length ($\hat{k}d_p \gg 1$ and $\hat{k}d_p \ll 1$, respectively). The simplified expression reads

$$\hat{\gamma}_{DA} = \hat{\gamma}_P \left(1 - \exp\left(-2\hat{k}d_p\right)\right) + \hat{\gamma}_S \exp\left(-2\hat{k}d_p\right), \tag{262}$$

where $\hat{\gamma}_{DA}$ is the growth rate of the DA structure and $\hat{\gamma}_P$ and $\hat{\gamma}_S$ correspond to the growth rate given by each limit. Normalization is made with the values at the transition temperature of the velocity and the Spitzer length, v_t and $L_{St} \equiv 2\kappa_t T_t/(5P_t v_t)$ respectively.

In the first limit, the general formula is reduced to $R_{D1} \cdot R_{D2} = 0$, where each factor is the dispersion relation of an isolated ablation front (both the inner and outer one). As the RA is much more unstable, the dispersion relation that dominates is the one associated to the first front (so, $R_{D1} = 0$). This is equivalent to the growth rate proposed by Piriz [27] (here named as $\hat{\gamma}_P$),

$$\hat{\gamma}^2 + \frac{4}{1+r_D}\hat{k}r_D\hat{\gamma} - \frac{1-r_D}{1+r_D}\hat{k}\mathrm{Fr}_\mathrm{t}^{-1} + \hat{k}^2 r_D = 0. \tag{263}$$

In the second limit, the general formula is decomposed in a series of powers of d_p. We keep zero and first order terms. The growth rate $\hat{\gamma}_S$ is obtained by solving the cubic equation:

$$\begin{aligned}\hat{\gamma}^2 + \bar{f}_{10}^{+}\hat{k}r_D\hat{\gamma} - \hat{k}\bar{\mathrm{Fr}}_\mathrm{t}^{-1} + C_0\hat{k}d_p\left(\hat{\gamma}^2 + C_1\hat{k}r_D\hat{\gamma} - \hat{k}\left(C_{21}\bar{\mathrm{Fr}}_\mathrm{t}^{-1} + C_{22}\mathrm{Fr}_\mathrm{t}^{-1}\right)\right) +\\ + \tfrac{4}{3}\hat{\gamma}d_p\left(\hat{\gamma}^2 + \tfrac{\bar{f}_{10}^{+}}{4}\hat{k}r_D\hat{\gamma} - \hat{k}\bar{\mathrm{Fr}}_\mathrm{t}^{-1}\right) = 0,\end{aligned} \tag{264}$$

where $C_0 = 2 + \bar{f}_{10} + r_D\bar{q}'_{10}$, $C_1 = \left(2\bar{f}_{10}^{+} + r_D\left(\bar{q}'_{10} - 1\right)\right)/C_0$, $C_{21} = (2 + r_D)/C_0$, $C_{22} = \bar{f}_{10}(1 - r_D)/C_0$, $\bar{\mathrm{Fr}}_\mathrm{t}^{-1} = \mathrm{Fr}_\mathrm{t}^{-1} - \bar{q}_{10}$, $\bar{f}_{10}^{+} = \bar{f}_{10} + \bar{q}'_{10} - 1$, $\bar{f}_{10} = 1.60\sqrt{\beta_t}$, $\bar{q}_{10} = 3.65\hat{k}^{3/5}r_D\beta_t^{7/10}$ and $\bar{q}'_{10} = 1.80\sqrt{\beta_t}$.

It is worth noting the presence of the factor $\bar{\mathrm{Fr}}_\mathrm{t}^{-1} = \mathrm{Fr}_\mathrm{t}^{-1} - \bar{q}_{10}$ in the last expression. This reduced Froude number shows a stabilizing influence of the perturbed momentum flux. This overpressure generated on the rippled ablation surface inhibits or even completely suppresses the growth. Another important factor that we highlight is $\bar{f}_{10}^{+} = \bar{f}_{10} + \bar{q}'_{10} - 1$, which corresponds to the so-called ablative stabilization. It takes an approximate value of $\bar{f}_{10}^{+} = 3.4\sqrt{\beta_t}$ for large β_t.

9

NUMERICAL SELF-CONSISTENT MODEL FOR DOUBLE ABLATION FRONTS

THE development of a DA front structure during the implosion of an ICF target is intrinsically related to the important role inside the ablation region played by the radiative transport in the overall energy balance. This structure emerges from absorption of the radiation energy and electron heat fluxes at two different locations, driving and supporting, in this way, two ablation fronts. In the radiation hydrodynamic theory (chapter 4), the emergence of a DA front structure, that is to say, the appearance of a second jump in the density profile, is characterized by a critical value Bo^* of the dimensionless Boltzmann number ($\mathrm{Bo} = 5Pv/8\sigma T^4$). As the Boltzmann number decreases, that physically can correspond to increase either the laser intensity I_L or the atomic number Z of the ablator, the two ablation fronts steepen and a plateau in temperature/density develops between them.

According to numerical simulations, the typical hydrodynamic profiles that are formed in the acceleration stage of the foil depend on the atomic number Z. They are shown schematically in figure 46. The ablation region passes from being composed of one steep ablation front for very low-Z ablators (e.g. DT) to a smooth one for low-Z ablators (e.g. CH) with increasing importance of radiation field. Next, this smooth front breaks up into two ablation fronts for low/moderate-Z ablators (e.g. doped CH) due to different locations of absorption of the radiation energy and electron heat fluxes. Finally, both ablation fronts get steeper and a plateau density region develops between them for moderate-Z ablators, such as SiO_2. The stability analysis of the two first cases (single ablation front) can be performed with several self-consistent theories existing in the literature [4, 28, 13, 31, 32] or with the sharp boundary models [27] if the approximation $kL_0 \ll 1$ holds, where k is the wavenumber of the perturbation and L_0 the characteristic length of the ablation front. The latter case where the DA front structure is clearly formed fullfills the assumptions $kL_0 \ll 1$ for both fronts and $L_0/d_p \ll 1$, where d_p is the plateau length. Thus, its stability properties can be analyzed with the sharp boundary model for DA fronts presented in the preceding chapter. The remaining case (the third one) is no longer a single ablation front neither a well-formed DA front structure. The density gradient scale length has two minimums, i. e.

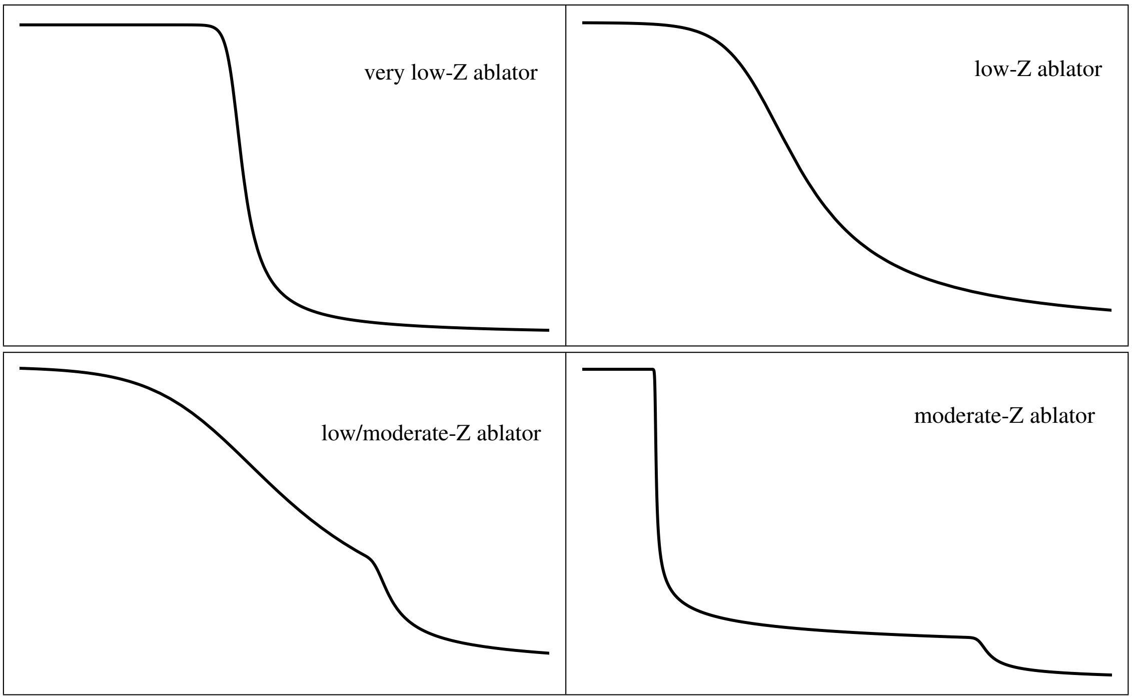

Figure 46: Schematic of density profiles of the ablation region depending on the atomic number of the ablator foil.

two ablation fronts are present, but there is no clear plateau separating both fronts. In contrast, the magnitude of the characteristic length of the inner ablation front is of the order of the plateau length[1] so that the inner ablation front covers the plateau region. In this case, both, the single ablation front theories and the sharp boundary model for DA fronts, are supposed to fail in giving trustworthy stability behaviours of the ablation region since none of them are able to reproduce the equilibrium hydrodynamic profiles of smooth DA fronts. We should turn then to self-consistent models that incorporate more accurate equilibrium profiles in the stabilitly analysis. The object of this chapter is to present a numerical self-consistent model for DA front structure.

---

[1] It is worth noting the definition of the plateau length. In the thin front approximation it is unambiguously the distance between the two fronts. However, when the characteristic length of the ablation fronts is finite, we have to be more rigorous with the definition. In this case, the plateau length is the distance between the minimum density gradient scale length of the inner ablation front and the point of transition temperature.

9.1 BASE FLOW

In the present model, we use a simplification of an existing 1D hydrodynamic radiation theory as the background flow [34]. We briefly described this model hereafter (an extensive description is given in chapter 4), This model is suitable to describe a thin layer encompassing the ablation region, where the flow is subsonic. Thus, within this layer, the variations of the mean pressure respect to the spatial coordinate are negligible, leading to a uniform pressure that will be called hereafter P_0, the ablation pressure. Besides, it lets us neglect the kinetic energy compared to the enthalpy term in the energy balance. We have then a subsonic and steady ablation region resulting from an incoming heat flow, an ablated mass flow, and a uniform pressure P_0. Two energy transport mechanisms are taken into account: the electronic heat flux and radiation. In order to perform the simplification in the base flow model that allows us to deal with the stability analysis, two asymptotic limits in the order of magnitude of the photon mean free path (l_{mfp}) are assumed leading to two different radiative regimes of the matter:

- *Optically thin regime*. This regime covers the outer ablation front and the close corona region. It is considered that the mean opacity of plasma ($K \sim l_{mfp}^{-1}$) is very small. This implies that the gradient of the radiation energy density is practically zero, and, therefore, the radiation temperature is constant and equal to a transition temperature T_t. Thus, the radiation term in the energy conservation equation corresponds to a radiative cooling law.

- *Optically thick regime*. This regime covers the inner ablation front and the plateau region and it is characterized by a very large mean opacity of plasma. In this case, a finite divergence of the radiation energy flux implies that radiation and matter are almost in equilibrium, and therefore, the electron temperature equals to the radiation temperature, $T_e = T_{rad} = T$. This results in a radiation energy flux behaving as a thermal conduction heat flow ($\vec{S}_r \sim \nabla T$).

This simplification lays on the existence of some characteristic opacity transition temperature of the material, T_t, where the dependence of the isobaric mean opacity with the temperature changes abruptly [34]. Governing hydrodynamic equations in the moving front frame are

$$\begin{aligned} \partial_t \rho + \nabla \cdot (\rho \vec{v}) &= 0, \\ \rho \partial_t \vec{v} + \rho \left(\vec{v} \cdot \nabla \right) \vec{v} &= -\nabla p + \rho \vec{g}, \\ \nabla \cdot \left(\tfrac{5}{2} P_0 \vec{v} - \kappa \nabla T + \vec{S}_r \right) &= 0, \end{aligned} \tag{265}$$

where the radiation energy transport is defined as

$$\begin{cases} \vec{S}_r = -\kappa_R \nabla T & \text{for} \quad T < T_t, \\ \nabla \cdot \vec{S}_r = 4\sigma K_P \left(T^4 - T_t^4 \right) & \text{for} \quad T \geq T_t, \end{cases} \tag{266}$$

and $\kappa_R = \bar{\kappa}_R T^{\nu}$ and $\kappa = \bar{\kappa} T^{5/2}$ are the Rosseland and Spitzer conductivities. Equations (265)-(266) involve two different-spectral average absorption coefficients, the Planck mean opacity $K_P \sim l_P^{-1}$ and the Rosseland mean opacity $K_R = 16\sigma T^3 / 3\kappa_R \sim l_R^{-1}$, that are functions that depend only on the matter temperature for an isobaric flow. In particular, the Planck mean opacity can be described as $K_P = \bar{K}_P T^{-11/2}$ in the case of a fully ionized plasma [50].

9.1.1 *One-dimensional solution*

Stationary one-dimensional profiles come from integration of the following equations

$$\begin{aligned} v_0 / v_t = \rho_t / \rho_0 = \theta_0, & \\ \left(\theta_0 - \left(\theta_0^{5/2} + \Delta \theta_0^{\nu} \right) \theta_0' \right)' = 0 & \qquad \text{for} \quad \theta_0 < 1, \\ \left(\theta_0 - \theta_0^{5/2} \theta_0' \right)' = -\beta_t \theta_0^{-11/2} \left(\theta_0^4 - 1 \right) & \qquad \text{for} \quad \theta_0 \geq 1, \end{aligned} \tag{267}$$

with the boundary condition

$$\theta_0' = \frac{\theta_0 - r_D}{r_D^{5/2} + \Delta r_D^{\nu}} \quad \text{when} \quad \theta_0 \to r_D \tag{268}$$

where $\theta_0 = T_0 / T_t$ is the dimensionless temperature, r_D is the ratio between density at the transition temperature and the peak density ($r_D \equiv \rho_t / \rho_a < 1$), ν is the power index of the Rosseland-like radiative conductivity, $\Delta = \bar{\kappa}_{Rt} / \bar{\kappa}_t$, $\beta_t = 16 \left(\sigma T_t^4 K_{Pt} \right) \left(\kappa_t T_t \right) / \left(5 P_0 v_t \right)^2$ and the prime denotes derivative respect to the spatial coordinate $\eta = y / L_{St}$ normalized with the Spitzer length at the transition temperature, $L_{St} \equiv 2\kappa_t T_t / \left(5 P_0 v_t \right)$.

The system of equations (267) provides a wide range of solutions. This variety of flow types can be explained by the presence of three different characteristic lengths in the problem [34]. These characteristic lengths are associated with the different energy mechanisms that are considered. In particular, two of them related to the radiation, these are the Rosseland and Planck photon mean free paths, and the last one, the Spitzer length L_S, related to the electron thermal diffusion. In the dimensionless system of equations (267), the characterization of flow is reduced to four parameters: r_D, ν, Δ and β_t. It is then useful to see the parameters Δ and β_t as the local values, at the transition temperature, of the ratios between the characteristic lengths. That is,

$$\Delta = \frac{1}{\mathrm{Bo}} \frac{l_R}{L_S}\bigg|_t, \quad \beta_t = \frac{1}{\mathrm{Bo}} \frac{L_S}{l_P}\bigg|_t. \tag{269}$$

9.1.2 *Matching theoretical base flow profiles to numerical simulation ones*

The hydrodynamic stability analysis is rather sensitive to the shape of the density/temperature profiles. Actually, it is necessary to ensure that the linearization is performed around the right equilibrium profiles, that is to say, perturbed quantities shall be imposed over a base flow that can be found in the nature. In the model described above, there are four free parameters (r_D, ν, Δ and β_t) but not every combination of them is allowed. We will adjust these parameters in order to get a trustworthy background flow. These realistic equilibrium profiles are assumed to come from one-dimensional simulations. For this purpose we use a Lagrangian hydrodynamic code, CHIC [6, 22, 21], developed at CELIA. This code includes the ion and electron heat conduction, the thermal coupling of electrons and ions and a multi-group diffusion model for the radiation transport with LTE opacities. Among different options, the following ones were retained to perform the simulations:

(i) flux-limited Spitzer electron heat conduction;

(ii) SESAME and QEOS equation of state;

(iii) the Thomas-Fermi ionization model.

The first information that we can extract from the simulation profiles of the acceleration stage is the parameter r_D. We locate the point where radiation and matter temperature are equal, which is an estimate of transition temperature. Finding the density at this point, we can directly obtain the paramter r_D as the ratio between the density at that point (ρ_t) and the peak density (ρ_a). The parameters that describe the inner ablation front (ν and Δ) are not independent, but, instead, the plateau length (simulation output) imposes a constraint between them. In sharp boundary models, the plateau length is unambiguously defined as the distance between the two surface discontinuities. However, the difinition is more ambiguous if the ablation fronts have finite characteristic lengths. So, we define the plateau length (d_p) as the distance

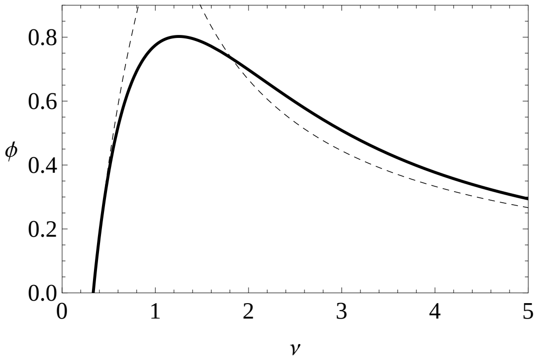

Figure 47: Function ϕ vs the thermal power index ν for the case $r_D = 0.25$ (solide line). Dashed lines corresponds to the approximation to ϕ in the asymptotic cases $\nu \ll 1$ and $\nu \gg 1$.

between the minimum of the density gradient scale length at the RA front and the transition temperature. We can relate this distance with the parameters ν and Δ in the following way. Under the assumption of radiation-dominated flow at the peak density (ρ_a), we can integrate once the energy equation of the inner ablation front and arrive to $\theta_0 - \Delta\theta_0^\nu\theta_0' \simeq r_D$. It is possible to determine straightaway the point of the profile, θ_0^*, where the characteristic length $L_{\min}^{RA}$ takes place by setting $\left(\theta_0/\theta_0'\right)' = 0$. This leads to $\theta_0^* = r_D\left(\nu+1\right)/\nu$. Then, integrating for a second time the energy equation between $\theta_0 = \theta_0^*$ and $\theta_0 = 1$, i.e. all along the plateau region, enables us to relate the plateau length to the parameter Δ. This relation reads

$$\Delta\left(\nu, r_D\right) = \frac{d_p}{L_{St}}\phi^{-1}, \tag{270}$$

where ϕ is the definite integral

$$\phi = \int_{\theta_0^*}^{1} \theta_0^\nu \left(\theta_0 - r_D\right)^{-1} d\theta_0. \tag{271}$$

Simple expressions can be found depending on asymptotic values of ν. Actually, in the case where $\nu \gg 1$ we arrive to $\Delta \simeq \nu\left(1 - r_D\right) d_p/L_{St}$ and for $\nu \ll 1$, $\Delta \simeq \ln^{-1}\left(\nu\left(1-r_D\right)/r_D\right) d_p/L_{St}$ (see figure 47). The former case ($\nu \gg 1$) implies a very thin RA front and, therefore, the corresponding expression of Δ is used in the sharp boundary model for DA fronts (see previous chapter). The fitting procedure is reduced then to determining one parameter for each ablation front (ν and β_t for the inner and outer one, respectively).

Two methods are described hereafter: an error minimization method and a gradient method.

- In the *error minimization method*, similarly to the Betti *et al.* procedure for single ablation fronts [28], we define an integrated quadratic error function that, for the inner ablation fronts, reads
$$\mathrm{err}\left(\nu\right)=\int_{\eta_{\max}}^{\eta_t}\left(\bar{\rho}_s\left(\eta\right)-\bar{\rho}_0\left(\eta\right)\right)^2 d\eta, \tag{272}$$
where $\bar{\rho}_s\left(\eta\right)$ is the unperturbed density profile obtained with the simulations (normalized with the maximum density) and $\bar{\rho}_0\left(\eta\right)=1/\theta_0$ is dimensionless density profile given by equations (267). Note that the domain of integration is from the peak density to the transition temperature. The minimization of $\mathrm{err}\left(\nu\right)$ is obtained by setting to zero the derivative respect to ν,
$$\frac{d\mathrm{err}\left(\nu\right)}{d\nu}=0. \tag{273}$$
This procedure can be applied analogously to the outer ablation front for the determination of β_t, apart from the fitting region that goes from the transition temperature to an arbitrary minimum density point (e. g., $\bar{\rho}_0\left(\eta_{\min}\right)=0.05$), defining the extent of the ablation front.

- The *gradient method* does not need the complete simulated profiles, but, instead, two characteristic lengths computed from the 1D simulations output. They are the minimum gradient scale length ($|d\log\rho/dy|^{-1}$) of the ablation fronts, $L^{RA}_{\min}$ and $L^{ERA}_{\min}$ for the inner and outer front, respectively. This method, although less accurate than the first one, gives a good estimate of the parameters for smooth ablation fronts. It provides simple algebraic expressions by relating the parameters to the characteristic lengths. First expression is given by introducing the value of θ_0^* in the definition of $L^{RA}_{\min}$. It reads
$$L^{RA}_{\min}/L_{St}=\Delta\frac{\left(\nu+1\right)^{\nu+1}}{\nu^{\nu}}r_D^{\nu}. \tag{274}$$
For the second expression, we need a change of variables. Re-writing the optically thin energy equation with the temperature as an independent variable, we obtain
$$z\left(1-5\theta_0^{3/2}z/2-\theta_0^{5/2}dz/d\theta_0\right)\simeq-\beta_t\theta_0^{-3/2}, \tag{275}$$
where $z\equiv\theta_0'$ is a θ_0-dependent function. Searching the minimum of the density gradient scale length ($L^{ERA}\equiv\theta_0/z$) implies $z'=z/\theta_0$ and, therefore, the characteristic length can be written as
$$L^{ERA}_{\min}/L_{St}=\frac{7\left(\theta_0^{**}\right)^{5/2}}{1+\sqrt{1+14\beta_t}}\simeq 4.68\beta_t^{-1/2}, \tag{276}$$

	$CHSi_{9\%}$	$CHSi_{5.5\%}$	$CHBr_{4.2\%}$	$CHBr_{3.3\%}$	$CHBr_{2\%}$	SiO_2
$< r_D >$	0.25	0.24	0.27	0.25	0.24	0.13
$< \nu >$	1.33	1.29	1.12	1.08	1.02	4.3
$< \Delta/L_{St} >$	3.9	3.7	3.0	2.55	2.23	37.1
$< \beta_t >$	4.5	3.2	12.2	9.7	6.3	18.0

Table 5: Parameters of the 1D analytical model that reproduce simulated hydro-profiles at time t≈1.8 ns for different ablator materials. Parameters are computed with the error minimization method.

where θ_0^{**} is the temperature at the point of minimum density gradient scale length in the outer ablation front ($\theta_0^{**} \approx (5/2)^{2/5}$).

Resolution of equations (270)-(276) gives us a set of parameters that provide realistic interpolation of the hydrodynamic profiles. Table 5 presents some results of 1D CHIC simulations with the corresponding parameters calculated with the error minimization method. We use several low/moderate-Z ablators (doped plastics with different dopants and concentrations) that are expected to develop a smooth DA front structure, and a moderate-Z ablator (SiO_2). The initial density for the doped plastic layers is obtained from the formula

$$\rho_D = \rho_U \frac{\sum_i A_i F_i}{(\sum_i A_i F_i)_U}, \tag{277}$$

where ρ_D and ρ_U are the density of doped and undoped material respectively, A_i is the mass number and F_i is the atom fraction for each element [16]. In our case that expression gets reduced to

$$\rho_D = \rho_{CH} \frac{A_{CH} F_{CH} + A_{dop} F_{dop}}{A_{CH} F_{CH}} = \rho_{CH} \frac{1}{1-x}, \tag{278}$$

where x is the mass fraction of the dopant. We consider a 25 μm thick ablator in planar geometry that is irradiated by a 3 ns constant laser pulse of 100 TW/cm^2. A practically constant acceleration is observed from $t \approx 1.5$ ns, and values of the analytical parameters are given for the hydro-profiles at $t \approx 1.8$ ns.

A relevant feature of the density/temperature profiles is given by the ratio $L_{\min}^{RA}/d_p$ (see table 6). We can classify the ablator materials, for which the DA front appear, into two groups as we have noted in the introduction of this chapter [34, 10]: weakly radiant fronts where the ratio is of the order of unity

	ρ_i(g/cc)	$< r_D >$	$< L^{RA}_{\text{min}}/L_{St} >$	$< L^{ERA}_{\text{min}}/L_{St} >$	$< d_p/L_{St} >$
$\text{CHSi}_{9\%}$	1.50	0.27	4.83	1.94	5.24
$\text{CHBr}_{4.2\%}$	1.62	0.21	4.70	1.24	4.56
SiO_2	2.2	0.12	3.50	1.04	13.23

Table 6: Initial density, mean minimum density gradient scale length of the radiative and the electron-radiative ablation fronts in the interval 1.5 ns < t < 2.5 ns for different ablator materials.

(low/moderate-Z ablators), and strongly radiant ones where $L^{RA}_{\text{min}}/d_p \ll 1$ (moderate-Z ablators). The glass ablators belong to the latter case. In the acceleration stage, the hydrodynamic profiles show two steep ablation fronts clearly separated by a plateau region. Sharp boundary models are then suitable to analyze the stability of the fluid structure. In contrast, doped plastic ablators present profiles where the plateau region is not distinguished from the inner ablation front (their characteristic lengths are of the same order). In this case, a density/temperature profile composed of layers of homogeneous flows separated by discontinuity surfaces is no longer a proper representation of the problem, and sharp boundary models are expected to fail in giving an accurate expression for the Rayleigh-Taylor growth rate. This supports the necessity of having a self-consistent model for stability studies. Figure 48 shows two comparisons between profiles computed from the theory and those of the simulations. In both cases we use doped plastic as the ablator material (one with the bromine dopant and the other with the silicon one), and a remarkable agreement is found.

We focus now our attention on the value of the parameter ν. The Rosseland thermal conductivity is defined as $\kappa_R = 16\sigma T^3/3K_R = \bar{\kappa}_R T^\nu$. The dependence on the temperature comes from two factors: explicitly from the cubic factor and implicitly from the Rosseland mean opacity. For an ionized material, the opacity is a decreasing function of the temperature, that is to say, it becomes more transparent as the temperature increases. A simple model describing the opacity was proposed in reference [34] and it consists of a piecewise continuous power law of temperature in the way (see chapter 4)

$$K_R = \begin{cases} \bar{K}_R(T/T_a)^{-q_1} & \text{for} \quad T < T_t \\ \bar{K}_R(T_t/T_a)^{-q_1}(T/T_t)^{-q_2} & \text{for} \quad T \geq T_t \end{cases} \tag{279}$$

where $\bar{K}_R$ is the Rosseland mean opacity at the peak density ρ_a and temperature T_a, and $0 < q_1 < q_2$. Thus, we expect to have $\nu > 3$, which is not

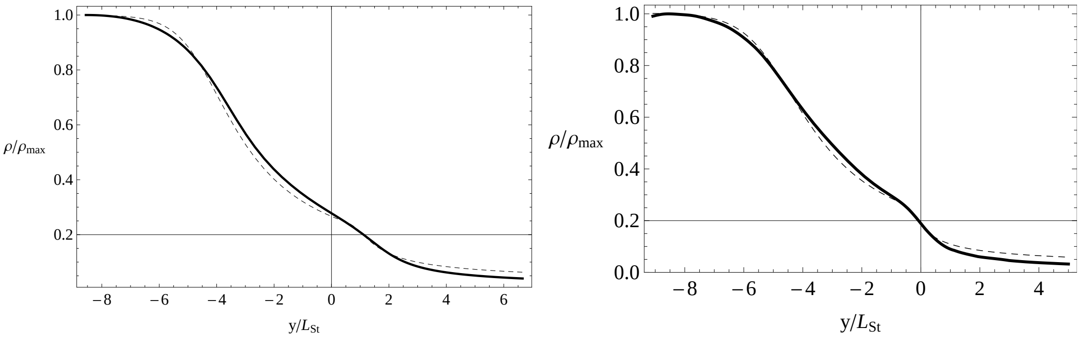

Figure 48: Dimensionless density profile taken from CHIC simulations (solid line) at time $t \approx 1.8$ ns, compared to the density profile computed from the model (dashed line). Left panel corresponds to CHSi$_{9\%}$ as ablator material, and the parameters of the model are $r_D = 0.25$, $\beta_t = 4.5$, $\nu = 1.33$ and $\Delta/L_{St} = 3.9$. Right panel corresponds to CHBr$_{4.2\%}$ as ablator material, and the parameters of the model are $r_D = 0.27$, $\beta_t = 12.2$, $\nu = 1.12$ and $\Delta/L_{St} = 3.0$.

the case (see the table 5). A possible explanation of this difference between the one-dimensional radiation hydrodynamic model and results derived from the simulations can be noticed in figure 49. We can see that immediately beyond the transition temperature (approximately the point where the matter and radiation temperatures are equal) the matter becomes transparent as a consequence of sharp increase of the electron temperature. This yields to a radiation temperature that remains constant, that is the main property of the optically thin regime. On the contrary, the assumption of an optically thick regime for $T < T_t$ is not fully satisfied since radiation and electron temperatures do not stay the same. Nevertheless, the adjustment of parameters from simulations output let us partially recover some of the missing physics regarding the radiative ablation front, included in the low values of power index ν.

Another source of discrepancy between the one-dimensional theory and the simulations comes from the assumption of a diffusion grey model for the radiation energy flux S_r [1]. That model assumes a Planckian spectrum $U_v(\vec{r}, t) \approx U_{Pv}(T_{rad}(\vec{r}, t))$ for the radiation field, that enables to calculate the mean opacities as spectral averages of the absorption coefficient κ (see chapter 4). In particular, the Planck mean opacity reads

$$K_P U_P(T) \equiv K_P 4\sigma T^4/c = \int_0^\infty \kappa_v U_{Pv}(T)\, dv, \tag{280}$$

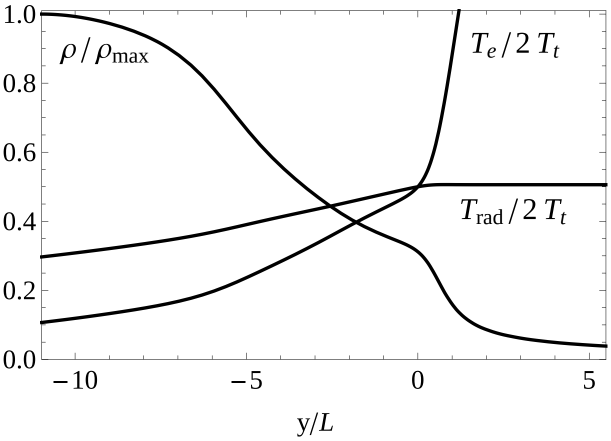

Figure 49: Dimensionless profiles of density, electron temperature and radiation temperature taken from CHIC simulations with ablator material CHBr4.2% at time $t = 2.0$ ns.

and the Rosseland mean opacity

$$K_R^{-1} dU_P/dT \equiv K_R^{-1} 16\sigma T^3/c = \int_0^\infty \kappa_v^{-1}\left(dU_{Pv}/dT\right) dv, \qquad (281)$$

where v is the frequency and κ_v the absorption coefficient per frequency. However, it is known that whereas the spectral radiant energy density follows approximately a Planckian distribution in a layer around the outer ablation front, it does not close to the peak density [34]. This causes an overestimate of the radiation heating ($\propto \nabla \cdot \vec{S}_r$) in a layer around the inner ablation front, and, consequently, the analytical model fails in an accurate representation of the hydrodynamic profiles.

As it is commented above, a similar procedure for determining accurate hydrodynamic profiles was already carried out in reference [28] for single ablation fronts. There, an error minimization method led to obtain the effective power index for thermal conduction ν and the characteristic length of the ablation front L_0 by fitting the analytic density profiles to the 1D simulation results. In particular, they start from the one-temperature diffusive transport model that describes the density profile of a subsonic ablation front. The density profile is given by the following first-order differential equation

$$\frac{d\bar{\rho}_0}{dy} = -\frac{\bar{\rho}_0^{\nu+1}(1-\bar{\rho}_0)}{L_0}, \qquad (282)$$

where the spatial coordinate y is left in its dimensional form. Note that the power index ν used in equation (282) refers to a general thermal conduction (including electron and radiation effects) and not to a specific Rosseland-like radiative conduction as treated in the DA front theory. Replacing $\bar{\rho}_0$ (the theoretical density profile) with $\bar{\rho}_s$ (simulated density profile) in equation (282) leads to an error. The minimization of this error yields the parameters ν and L_0 that better fit the simulated hydrodynamic profiles. For convenience, they minimize the integrated quadratic error (δ) defined as

$$\delta(\nu, L_0) \equiv \int_{\bar{\rho}_{min}}^{\bar{\rho}_{max}} \left[(\nu+1)\ln\bar{\rho}_s - \ln L_0 - \ln\left(-\frac{d\bar{\rho}_s}{dy}\frac{1}{1-\bar{\rho}_s} \right) \right]^2 d\bar{\rho}_s, \qquad (283)$$

where $\bar{\rho}_{max}$ and $\bar{\rho}_{min}$ are the maximum and minimum values of the density in the ablation region, respectively. The procedure to obtain the fitting parameters ν and L_0 is, then, setting to zero the partial derivatives with respect them,

$$\frac{\partial\delta}{\partial\nu} = \frac{\partial\delta}{\partial L_0} = 0. \qquad (284)$$

In the case of solid DT targets (very low-Z ablator) within a range of foil thickness of 100-190 μm and laser intenstity 50-100 TW/cm^2, steep density profiles ($L_0 \approx 0.03\mu$m) were found with a value $\nu \approx 2$, close to the Spitzer value, that indicate a predominance of electron heat flux over a low level of radiation transport for this material. However, the use of a higher Z target material like CH (low-Z ablator) within a range of foil thickness of 10-25 μm and laser intensity 50-240 TW/cm^2 provided smoother density profiles ($L_0 \approx 0.3\,\mu$m) and a lower value of the thermal conductivity power index, $\nu \approx 0.9$. This fact shows that the radiation transport becomes non-negligible in the case of plastic ablators, although the single temperature model still holds. The information concerning the radiation transport effects is somehow contained in the low values of ν. However, this one-temperature diffusive transport model breaks down for low/moderate-Z ablators with emergence of the second ablation front, making necessary to turn to a DA front theory for its stability analysis.

9.2 PERTURBED FLOW

In the frame of a self-consistent analysis, the perturbed problem is governed by the same equations used in the study of the background flow, that is to say, in our case, the mass, momentum and energy conservation around the ablation region (265)-(266). The stability analysis is restricted to a two-dimensional domain for simplification, so we only consider flow perturbations along the x and y spatial coordinates. We look then for solutions of perturbed quantities in the wavelike form $\exp\left(\gamma t + ikx\right)$. Any hydrodynamic quantity is expanded to the first order perturbation, for instance $\vec{v}\left(x,y,t\right) = \left(v_{1x}(y)\exp\left(\gamma t + ikx\right), v_0(y) + v_{1y}(y)\exp\left(\gamma t + ikx\right)\right)$, and the set of equations (265)-(266) is linearized around the zero order flow. This leads to an eigenvalue problem that can be expressed in a matrix form as

$$\mathbf{V}' = \begin{cases} \mathbf{A}^{\mathbf{RA}}\mathbf{V} & \text{for} \quad r_D < \theta_0 < 1, \\ \mathbf{A}^{\mathbf{ERA}}\mathbf{V} & \text{for} \quad \theta_0 > 1, \end{cases} \tag{285}$$

where $\mathbf{V} = (u_{1y}, i\hat{k}u_{1x}, p_1, \theta_1, \theta_1')$ is the vector of the first order hydrodynamic quantities normalized by their base flow value at the transition temperature (T_t, ρ_t, v_t, ...), and the fifth order square matrix,

$$\mathbf{A}^{\mathbf{RA}} = \begin{bmatrix} \frac{\theta_0'}{\theta_0} & -1 & 0 & \frac{\hat{\gamma}-\theta_0'}{\theta_0} & 1 \\ 0 & -\frac{\hat{\gamma}}{\theta_0} & \hat{k}^2 & 0 & 0 \\ -\frac{\hat{\gamma}+2\theta_0'}{\theta_0} & 1 & 0 & -\frac{\mathrm{Fr_t}^{-1}+\theta_0(\hat{\gamma}-2\theta_0')}{\theta_0^2} & -1 \\ 0 & 0 & 0 & 0 & 1 \\ \frac{\theta_0'}{\theta_0 R(\theta_0)} & 0 & 0 & \hat{k}^2 + \frac{\hat{\gamma}-\theta'_0}{\theta_0 R(\theta_0)} - \frac{R''(\theta_0)}{R(\theta_0)} & \frac{1-2R'(\theta_0)}{R(\theta_0)} \end{bmatrix}, \tag{286}$$

where $R(\theta_0) = \Delta\theta_0^{\nu} + \theta_0^{5/2}$, and

$$\mathbf{A}^{\mathbf{ERA}} = \begin{bmatrix} \frac{\theta_0'}{\theta_0} & -1 & 0 & \frac{\hat{\gamma}-\theta_0'}{\theta_0} & 1 \\ 0 & -\frac{\hat{\gamma}}{\theta_0} & \hat{k}^2 & 0 & 0 \\ -\frac{\hat{\gamma}+2\theta_0'}{\theta_0} & 1 & 0 & -\frac{\mathrm{Fr_t}^{-1}+\theta_0(\hat{\gamma}-2\theta_0')}{\theta_0^2} & -1 \\ 0 & 0 & 0 & 0 & 1 \\ \frac{\theta_0'}{\theta_0^{7/2}} & 0 & 0 & h_{45} & \frac{1-2\left(\theta_0^{5/2}\right)'}{\theta_0^{5/2}} \end{bmatrix}, \tag{287}$$

where

$$h_{45} = \hat{k}^2 + \frac{\hat{\gamma} - \theta'_0}{\theta_0^{7/2}} - \frac{\left(\theta_0^{5/2}\right)''}{\theta_0^{5/2}} - \beta_t \frac{3\theta_0^4 - 11}{2\theta_0^9} \tag{288}$$

for the inner and outer ablation front regions, respectively, depend on the base flow (θ_0, r_D, β_t, ν, Δ). The prime denotes a derivative respect to the independent variable θ_0. Here, the Froude number, $\mathrm{Fr_t}$, is defined as $\mathrm{Fr_t} = v_t^2/gL_{St}$, and $\hat{k} = kL_{St}$ and $\hat{\gamma} = \gamma L_{St}/v_t$, are the normalized wavenumber and growth rate, respectively. Notice that normalized perturbed velocities are denoted by u_{1x}, u_{1y}, the temperature by θ_1 and the perturbed pressure by

p_1. It is convenient to make a change of variables [48] prior to the stability computation in order to avoid the appearance of zero eigenvectors in the modal analysis and also to increase our physical insight in the problem. Thus, the perturbed quantities read

$$\begin{aligned}
&G_1 = \theta_0 F_1 = u_{1y} - \theta_1, \\
&W_1 = i\hat{k} u_{1x}, \\
&Q_1 = 2u_{1y} + p_1 - \theta_1, \\
&T_1^{RA} = \left(\Delta\theta_0^{\nu} + \theta_0^{5/2}\right)\theta_1, \quad T_1^{ERA} = \theta_0^{5/2}\theta_1, \\
&H_1^{RA} = \left(T_1^{RA}\right)' - u_{1y}, \qquad H_1^{ERA} = \left(T_1^{ERA}\right)' - u_{1y},
\end{aligned} \tag{289}$$

which leaves the unknown vector as $\mathbf{Y} = (G_1, W_1, Q_1, T_1, H_1)$, and the matrices of the fifth order system of differential equations are renamed to $\mathbf{M^{RA}}$ and $\mathbf{M^{ERA}}$. The eigenvalue problem reads

$$\mathbf{Y}' = \begin{cases} \mathbf{M^{RA}}\mathbf{Y} & \text{for} \quad r_D < \theta_0 < 1, \\ \mathbf{M^{ERA}}\mathbf{Y} & \text{for} \quad \theta_0 > 1, \end{cases} \tag{290}$$

$$\mathbf{M^{RA}} = \begin{bmatrix} \frac{\theta_0'}{\theta_0} & -1 & 0 & \frac{\hat{\gamma}}{\theta_0 R(\theta_0)} & 0 \\ -2\hat{k}^2 & -\frac{\hat{\gamma}}{\theta_0} & \hat{k}^2 & -\frac{\hat{k}^2}{R(\theta_0)} & 0 \\ -\frac{\hat{\gamma}}{\theta_0} & -1 & 0 & -\frac{\mathrm{Fr}_\mathrm{t}^{-1}}{\theta_0^2 R(\theta_0)} & 0 \\ 1 & 0 & 0 & \frac{1}{R(\theta_0)} & 1 \\ 0 & 1 & 0 & \hat{k}^2 & 0 \end{bmatrix}, \tag{291}$$

$$\mathbf{M^{RA}} = \begin{bmatrix} \frac{\theta_0'}{\theta_0} & -1 & 0 & \frac{\hat{\gamma}}{\theta_0^{7/2}} & 0 \\ -2\hat{k}^2 & -\frac{\hat{\gamma}}{\theta_0} & \hat{k}^2 & -\frac{\hat{k}^2}{\theta_0^{5/2}} & 0 \\ -\frac{\hat{\gamma}}{\theta_0} & -1 & 0 & -\frac{\mathrm{Fr}_\mathrm{t}^{-1}}{\theta_0^{9/2}} & 0 \\ 1 & 0 & 0 & \frac{1}{\theta_0^{5/2}} & 1 \\ 0 & 1 & 0 & \hat{k}^2 - \beta_t \frac{3\theta_0^4 - 11}{2\theta_0^9} & 0 \end{bmatrix}, \tag{292}$$

It is worth noting the physical meaning of F_1, Q_1 and H_1 that represent the local perturbed flux of mass, momentum and energy respectively. In the above system of equations, for a given base flow and a given acceleration of the foil, the only remaining free parameters are the perturbation wavenumber and its growth in time. Our goal is to establish a relation between them, this is to find. the dispersion relation. The statement of the linear problem is completed with the boundary conditions that provide the necessary information to close the perturbed problem, and, therefore, to determine the dispersion relation.

The fulfillment of the boundary conditions impose constraints on the perturbations; in particular, we can state that unstable disturbances in the flow shall be localized within the double ablation front region. In other words, perturbation shall vanish down- and upstream. This is equivalent to set $Y_i \to 0$ in both limits $\theta_0 \to r_D$ (or $\eta \to -\infty$, peak density) and $\theta_0 \to +\infty$ ($\eta \to +\infty$, near-corona region). In that way, the boundary condition at the peak density determines the starting point of the integration (a linearly stable mode), whereas the boundary condition at near-corona region leads to the dispersion relation $\hat{\gamma} = \hat{\gamma}\left(\hat{k}, \text{base flow, acceleration}\right)$. Mathematically we need to carry out a modal analysis of the matrices $\mathbf{M}^{\mathbf{RA/ERA}}$ to be able to discriminate stable and unstable eigenmodes to properly state the boundary conditions.

At the peak density ($\rho_a = 1/r_D$), we perform a matrix expansion around the singular point $(\theta_0 - r_D)$ in order to determine the five independent eigenmodes of $\mathbf{M}^{\mathbf{RA}}$ [48]. Notice that the asymptotic behavior of the temperature is $\theta_0 \simeq r_D + c_0 \exp(a\eta)$, where c_0 is an arbitrary constant depending on the origin of coordinates and $a = \left(r_D^{5/2} + \Delta r_D^{\nu}\right)^{-1} > 0$. Therefore, the leading order of the eigenmodes goes like $(\theta_0 - r_D)^{\lambda} \sim \exp(\lambda a \eta)$, where λ is the associated eigenvalue. In order to satisfy the boundary condition, we are only interested in having bounded modes developing at the peak density, what, in this case, means a positive eigenvalue (since $\eta \to -\infty$). In particular, there are two of them

$$\begin{aligned} \lambda_1^{left} &= \tfrac{\hat{k}}{a}, \\ \lambda_2^{left} &= \tfrac{1}{2}\left(1 + \sqrt{1 + \left(\tfrac{2\hat{k}}{a}\right)^2 + 4\tfrac{\hat{\gamma}}{ar_D}}\right), \end{aligned} \tag{293}$$

and we discard the three unbounded eigenmodes.

The linearity of the problem allows us to write the starting point of the integration as a linear combination of the two stable modes in the way

$$\mathbf{Y^{left}} = \alpha_1 (\theta_0 - r_D)^{\lambda_1^{left}} \mathbf{Y_1^{left}} + \alpha_2 (\theta_0 - r_D)^{\lambda_2^{left}} \mathbf{Y_2^{left}} \tag{294}$$

where α_1 and α_2 are two undefined parameters and $\mathbf{Y_1^{left}}$ and $\mathbf{Y_2^{left}}$ are the eigenmodes vectors for λ_1^{left} and λ_2^{left}, respectively.

Analogously, at the near-corona region, the boundary condition is composed of a linear combination of three bounded eigenmodes ($\lambda < 0$). However, in this case, the computation procedure (described in the next section) is only concerned with the fastest growing unbounded eigenmode, so we focus on this mode that, at leading order and for an arbitrary value of β_t reads (see chapter (6)),

$$\mathbf{Y^{right}}(\zeta) = \zeta^{\lambda_p^{right}} \exp\left(\lambda_0^{right}\zeta + \lambda_1^{right}\zeta^{3/5} + \lambda_2^{right}\zeta^{1-\alpha}\right)\mathbf{Y_0^{right}}, \qquad (295)$$

where $\zeta \equiv (2/5\psi_0)\theta_0^{5/2}$, $\alpha = 2(1+\beta_t/\psi_0^2)/5$ and $\psi_0 = (1+\sqrt{1+4\beta_t})/2$. The fastest growing unbounded eigenmode corresponds to the main eigenvalue $\lambda_0^{right} = \hat{k}$. The corresponding secondary eigenvalues are

$$\begin{aligned} \lambda_1^{right} &= 0, \\ \lambda_2^{right} &= (2/5)^{\alpha} c_1 / \left((1-\alpha)\,\psi_0^{1+\alpha}\right), \\ \lambda_p^{right} &= \left(1 + \left(1+\sqrt{1+4\psi_0^2}\right) / \left(2\psi_0\right)\right)/5, \end{aligned}$$

where c_1 is numerically computed through the expression

$$c_1 = \left(\theta_0^{3/2}\theta_0' - \psi_0\right)\theta_0^{5\alpha/2}\Big|_{\eta\to\infty}. \qquad (296)$$

A simple expression for the fastest growing unbounded eigenmode is found in the asymptotic limit $\beta_t \gg 1$,

$$Y^{right}(\zeta) \propto \zeta^{2/5} \exp\left(\hat{k}\zeta - 2(5/2)^{1/5}\beta_t^{-2/5}\zeta^{1/5}\right), \qquad (297)$$

where $\zeta \approx 2\theta_0^{5/2}/\left(5\beta_t^{1/2}\right)$.

9.2.1 *Growth rate calculation*

The method used in the computation of the dispersion relation is similar to the one used by Kull in electronic ablation fronts [17], and it is fully described in the chapter 6. As a reminder, we first need to define the base flow with the set of parameters (r_D, β_t, ν and Δ), the acceleration at which the foil is subjected to, and the wavelength of the perturbation. Next, we integrate the matrix system (290) forwards from the boundary condition $\mathbf{Y}^{\mathbf{left}}$ to a distance of several perturbation wavelengths. The solution generally explodes since the unbounded modes at the near-corona region develop; this means that the boundary condition is not satisfied in that region. The way to impose vanishing perturbations away from the ablation fronts is the following: we normalize the vector solution by the fastest growing unbounded mode (297). Thus, the solution will tend to a constant vector $\mathbf{C}$ when $\theta_0 \gg 1$. Actually, $Y^{right}\mathbf{C}$ represents the exploding mode. Its amplitude shall be set to zero in order to ensure a bounded solution. Linearity of the problem enables us to express each component of the vector $\mathbf{C}$ as a linear combination of α_1 and α_2 (the free parameters of the boundary condition at the peak density (294)), let it be, $\mathbf{C} = \mathbf{f}(\alpha_1, \alpha_2) = \alpha_1 \mathbf{f}(1,0) + \alpha_2 \mathbf{f}(0,1)$. In order to have a non-trivial solution, we select any two components i, j of the vector solution and force the following determinant to be zero

$$\begin{vmatrix} f_i(1,0) & f_j(1,0) \\ f_i(0,1) & f_j(0,1) \end{vmatrix} = 0, \tag{298}$$

that yields the growth rate of the perturbation.

9.2.2 *Comparisons with the sharp boundary model and 2D CHIC simulations*

As a test of the numerical self-consistent theory, we compare the numerical dispersion relation with the analytic sharp boundary model for DA fronts [48]. The latter has been developed from the thin ablation front assumption, so we expect an agreement of the results as the characteristic scale lengths of both fronts get shorter. We also use in the comparison a simplified dispersion relation formula derived from the analytic theory (see chapter 9).

Figure 50 shows such a comparison. We apply the numerical method to several cases varying the characteristic scale length of the RA front. In order to make comparable the different background flows, we keep constant the plateau length (in this case $d_p \approx 12 L_{St}$) and the density ratio, $r_d = 0.25$. Thus, the characteristic length L_{min}^{RA} is controlled by a pair of parameters ν and Δ. The different cases considered in this comparison are

(A) $L_{\text{min}}^{RA}/L_{St} \simeq 2 \cdot 10^{-3}$, where the RA front can be assimilated to a surface discontinuity,

(B) $L_{\text{min}}^{RA}/L_{St} \simeq 0.6$,

(C) $L_{\text{min}}^{RA}/L_{St} \simeq 5$, and

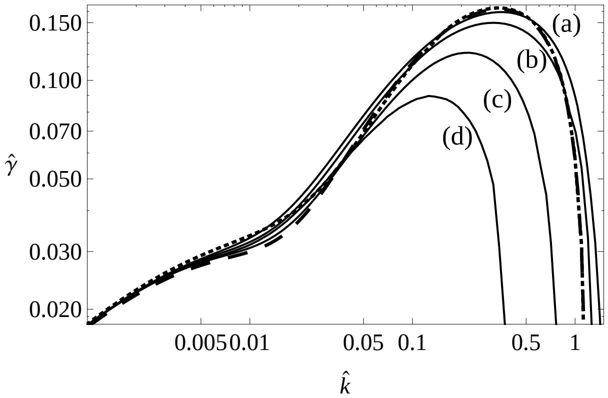

Figure 50: Dispersion relation curves obtained from the numerical method (solid line) for the parameters $r_D = 0.25$, $\beta_t = 20$, $\mathrm{Fr_t} = 2$ and (a) $\nu = 10$ and $\Delta = 87$, (b) $\nu = 5$ and $\Delta = 41$, (c) $\nu = 5/2$ and $\Delta = 20$ and (d) $\nu = 6/5$ and $\Delta = 15$. Dashed line corresponds to the solution of the analytic formula with $d_p = 12$ and dotted line plots the asymptotic limit of the analytic formula .

(D) $L_{\min}^{RA}/L_{St} \simeq 13$, where the RA front is smooth and completely covers the plateau region.

The finite characteristic length of the ablation fronts shall not influence perturbation modes of a very large wavelength ($kL_{\min}^{RA} \ll 1$) since these modes cannot distinguish the details of the hydrodynamic profiles, but, on the contrary, it shall have a decisive impact in those perturbed modes such that $kL_{\min}^{RA}$ is of the order of unity or larger. Thus, as it is expected, results in the very large wavelength range are very close no matter what the characteristic length of the inner front is (it is still too short compared to the wavelength). However, as the wavelength of the perturbation becomes comparable to $L_{\min}^{RA}$, the self-consistent growth rate differs in each case and the sharp boundary model can only reproduce the results of the case (a), which is the case where the thin front approximation is still valid. In particular, important target design parameters such as the maximum growth rate and its associated wavelength are in excellent agreement with the case (a), and the sharp boundary model can be used as an accurate estimate. Moreover, the simplified dispersion formula also provides a remarkable agreement. The situation changes when the density is smoothly varying in the RA front and the perturbation wavelength is of the order of the minimum gradient scale length ($kL_{\min}^{RA} \sim \mathcal{O}(1)$). In this case, perturbed modes are affected by the profile gradient that yields to the mitigation of the unstable term for short wavelengths. In the classical theory, this is captured by the asymptotic formula

$$\gamma_{cl} = \sqrt{\frac{A_T k g}{1 + A_T k L_{\min}}}, \tag{299}$$

where $A_T = (\rho_h - \rho_l) / (\rho_h + \rho_l)$ is the Atwood number, and ρ_h and ρ_l are the density of the heavy and the light fluid, respectively. An analogous mitigation for short wavelength modes is observed in the ablation region stability of figure 50, where the cut-off wavenumber decreases as the characteristic length of the RA front increases. Furthermore, the maximum growth rate is reduced by a factor of 2 from the configuration of case (a) to the one of case (d).

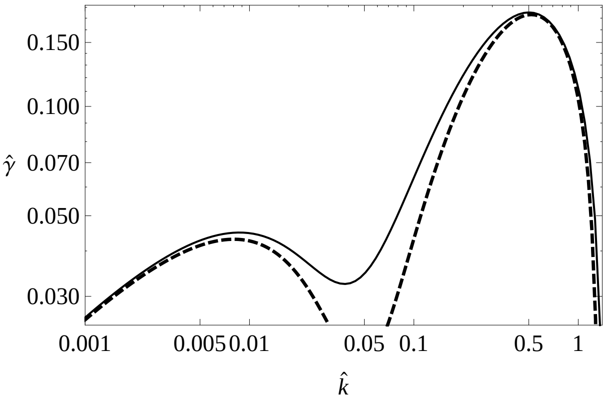

Figure 51: Dispersion relation curves obtained from the numerical method (solid line) for the parameters $r_D = 0.35$, $\beta_t = 20$, $\mathrm{Fr_t} = 1$, $\nu = 10$ and $\Delta = 20$. Dashed line corresponds to the analytic solution according to the formula (260) with $d_p \approx 3$.

A peculiar feature of the dispersion relation that was observed in the preceden chapter with the sharp boundary model is the appearance of a double-hump shape for short plateau configurations [48]. Figure 51 shows that such a shape of the dispersion relation is also found in the self-consistent analysis. Before stating the physical mechanism that leads to this double-hump shape, we summarize the results obtained from the analysis of a single electronic-radiative ablation front when its radiative component is sufficiently strong, i.e for values of β_t well above unity (see chapter 6). The expression at the leading order of the growth rate for a single ERA front reads

$$\gamma \approx \sqrt{k\left(g - q_0\left(kL_{St}\right)^{3/5}\beta_t^{7/10}v_t^2/L_{St}\right)} - f_0\sqrt{\beta_t}kv_t, \tag{300}$$

where $f_0 \simeq 1.70$ and $q_0 \simeq 3.65$. As in a single ablation front driven by thermal conduction, the ablative Rayleigh-Taylor instability in ERA fronts is mitigated by the rocket effect and the so-called convective stabilization. The rocket effect, which is usually the dominant one, is proportional to $k^{3/5}$ since a pure electron thermal conduction is assumed ($\nu = 5/2$). Regarding the convective stabilization term it is proportional to the wavenumber, affecting, then, the large perturbation wavenumbers. It is worth noting the stabilizing effect of radiation, which is consistent with the increased perturbed mass rate ($\propto \sqrt{\beta_t}\rho_t v_t$) and dynamic pressure ($\propto \beta_t^{7/10}\rho_t v_t^2$) at the ERA front. Thus, the double-hump shape, which was related to enhancement of the mode coupling in reference [48], can be explained as follows: let k_c^{ERA} be the cutoff wavenumber of the ERA front, then, any disturbance of wavelength $\delta = 2\pi/k_c^{ERA}$ or shorter is completely stabilized in the vicinity of the ERA front by the rocket effect mechanism. Perturbed modes (including those associated to the dynamic pressure that leads to the stabilization) are assumed to involve a region within a distance of $y^* \sim \delta$. Thus, the stabilizing rocket effect, which is self-generated by the ERA front, is felt up to a distance of δ and, if the condition $d_p/\delta < 1$ is fulfilled, the perturbed dynamic pressure that stabilizes the ERA front will not be completely damped within the plateau region. This relaxation process will affect the RA front in the form of an additional stabilization. Since the cut-off wavelength goes like $\delta \sim \beta_t^{7/5}\mathrm{Fr}_t^{5/3}$, this additional stabilization due to mode coupling is enhanced with a higher Froude number, a higher β_t (optically thicker plateau region) or a shorter plateau length. All these dependencies are consistent with the results presented in the precedent chapter.

Figures 52 and 53 show three comparisons of the growth rates obtained with 2D planar simulations and with the linear theory for different ablator materials and laser intensities. Single-mode 2D simulations were carried out with the radiative-hydrodynamic code CHIC, considering a 25 μm layer of ablator irradiated by a laser pulse with a maximum intensity of 100 TW/cm^2 for the cases of doped plastics (CHBr and CHSi), and a 20 μm layer of SiO_2 subjected to a directed laser pulse with a maximum intensity of 200 TW/cm^2. Simulation results are averaged over a 1 ns time duration ($1.5 \leq t \leq 2.5$), when the target is already accelerated. Characteristic values for normaliza-

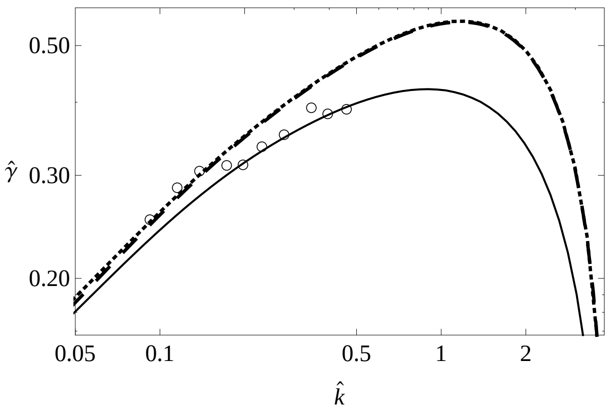

Figure 52: Normalized growth rate for SiO_2 foil obtained with 2D single-mode simulations (circles) and with the linear theories, both, analytical sharp boundary model (dashed line) and numerical self-consistent model (solid line). Dotted line corresponds to the simplified formula derived from the SBM dispersion curve (see chapter 9). Parameters used are $r_D = 0.22$, $\nu = 4.7$, $\Delta/L_{St} = 45$, $d_p/L_{St} = 14$, $\beta_t = 21$ and $\mathrm{Fr_t} = 0.7$.

tion are taken around the outer ablation front, in the point where radiative and electron temperatures are equal. An exponential regression in time is performed on the peak-to-valley perturbation depth in order to obtain an estimate of the linear growth rate (circles in the figures). The range of perturbation wavelengths explored covers almost a decade from $\lambda_{\mathrm{min}} = 20\,\mu\mathrm{m}$ to $\lambda_{\mathrm{max}} = 150\,\mu\mathrm{m}$. Good agreement is found between the numerical self-consistent model and the 2D planar simulations. In the glass ablator case (figure 52), both, sharp-boundary and self-consistent models, give a reasonable approximation. However, it is worth noting the cases of doped plastic (figure 53), where growth rates from simulations are in better agreement with the self-consistent model. This fact points out that there are some physics missing in the sharp boundary model, especially when the plateau length is of the order of the characteristic length of the RA front, L_0. Obviously, the effect of the Atwood number with a finite L_0 (that can be of the order of the plateau length) is not considered in the sharp boundary model since it is assumed a discontinuity front ($kL_0 \ll 1$). Another physical aspect concerns the effect of transverse diffusion in the ablation process (reference [9, 33], see discussion in chapter 9). The resulting dispersion relation including the effect of transverse diffusion in the RA front provides a better agreement with the numerical self-consistent method in terms of the cut-off wavenumber and the maximum growth rate as it is shown in figure 53.

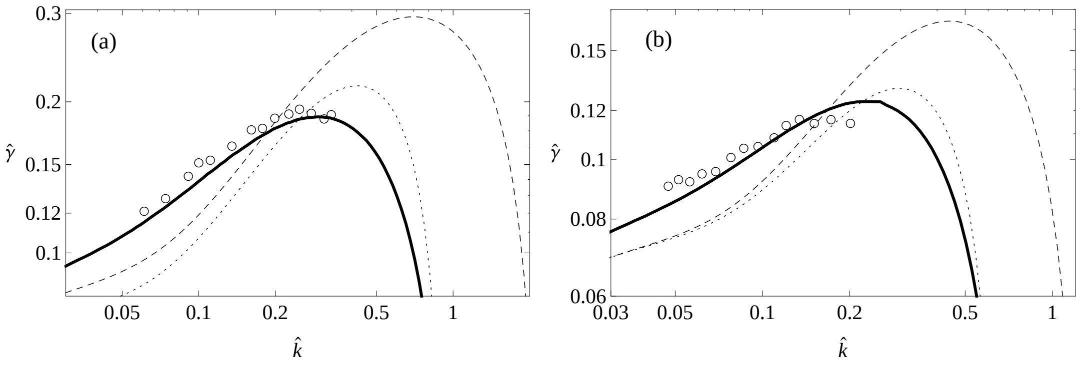

Figure 53: Normalized growth rate obtained with 2D single-mode simulations (circles) and with the linear theories, both, analytical sharp boundary model (dashed line) and numerical self-consistent model (solid line). Dotted line corresponds to the sharp boundary model including the effects of transverse diffusion. (a) $\mathrm{CHBr}_{4\%}$ ablator foil, parameters used are $r_D = 0.26$, $\nu = 1.12, \Delta/L_{St} = 5.2$, $d_p/L_{St} = 4.0$, $\beta_t = 12.2$ and $\mathrm{Fr_t} = 0.99$. (b) $\mathrm{CHSi}_{9\%}$ ablator foil, parameters used are $r_D = 0.27$, $\nu = 1.33, \Delta/L_{St} = 6.7$, $d_p/L_{St} = 5.2$, $\beta_t = 4.5$ and $\mathrm{Fr_t} = 1.58$.

9.3 APPLICATIONS

9.3.1 *Stability analysis of low-Z ablators irradiated by high laser intensity*

The development of a DA front structure is directly related to the atomic number of the ablator and the laser irradiation conditions. Radiative effects are enhanced with higher laser intensities and with a material of higher atomic number, bringing about, in this way, the emergence of a second ablation front. In this subsection, we aim to analyze a hydrodynamic structure that stays in the frontier between a single ablation front and a DA front. For that purpose, several one-dimensional simulations have been carried out with the code CHIC. We have used a 30 μm thick foil of a plastic ablator as a baseline and we have applied different laser intensities (I_L) to it. In figure 54 we present the density profile for the case corresponding to $I_L = 400\,\mathrm{TW/cm^2}$ when the foil is subject to a nearly constant acceleration ($t \simeq 1.25$ ns). The corresponding density gradient scale length presents a clear minimum and an inflection point displaced to the left of that minimum. The latter indicates that the absorption of radiation energy and electron heat fluxes do not occur at the same location, but they begin to be separated in space. In case we increase the laser intensity or we change the ablator material to a higher atomic number one, this effect would be more marked and we could then speak of a DA front structure. Figure 54 represents then a case of transition between a single ablation front and a DA front.

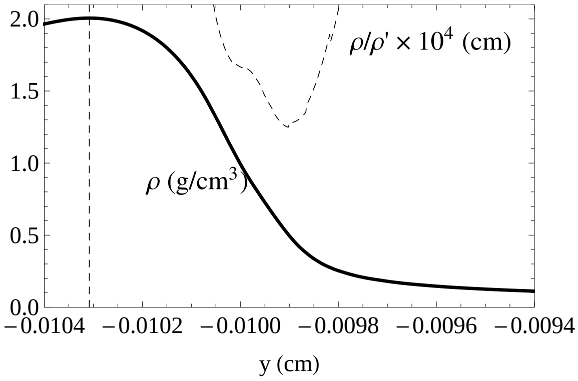

Figure 54: Simulated density profile (solid line) at the time $t = 1.25$ ns. Dashed line corresponds to the density gradient scale length.

Under these circumstances, we intend to apply both, the Betti and Goncharov theory for single ablation fronts and the numerical theory described in this chapter, to analyse the stability of this hydrodynamic structure. Note that the density profile in figure 54 is in the limit of both stability theories, and it is an appropriate example to compare them.

The Betti and Goncharov procedure to compute the analytic parameters consists in the minimization of two error functions, one coming from the energy equation (that describes the density profile) and the other one from the momentum equation (that describes the pressure profile) [28]. These error functions are then minimized with respect to the parameters. In particular, the minimization of the error related to the density profile is obtained by setting to zero the partial derivatives with respect to the thermal power index ν and the characteristic length L_0, and the error related to the pressure profile is minimized with respect to the dimensionless ablation velocity Π_a and the Froude number Fr. Estimates of the parameters are computed with the following expressions

$$\nu = \frac{c_1 a_1 - c_2 b_1}{a_1^2 - a_2 b_1} - 1, \quad L_0 = \exp\left(\frac{a_2 c_1 - a_1 c_2}{a_1^2 - a_2 b_1}\right), \tag{301}$$

$$\mathrm{Fr} = \frac{a_3 b_4 + b_3^2}{b_3 c_3 + a_3 c_4} \frac{1}{L_0}, \quad \Pi_a^2 = \frac{a_3 b_4 + b_3^2}{c_3 b_4 + c_4 b_3} \tag{302}$$

where

$$a_1 = \|\bar{\rho}\,(\ln\bar{\rho}-1)\|\,, \quad a_2 = \left\|\bar{\rho}\,(\ln\bar{\rho}-1)^2+\bar{\rho}\right\|, \quad a_3 = \int_{y(\bar{\rho}_{min})}^{y(\bar{\rho}_{max})}\left(\frac{d\Pi_s}{dy}\right)^2 dy, \tag{303}$$

$$b_1 = \|\bar{\rho}\|\,, \quad b_3 = -\int_{y(\bar{\rho}_{min})}^{y(\bar{\rho}_{max})}\bar{\rho}_s\frac{d\Pi_s}{dy}dy, \quad b_4 = -\int_{y(\bar{\rho}_{min})}^{y(\bar{\rho}_{max})}\bar{\rho}_s^2 dy, \tag{304}$$

$$c_1 = \int_{y(\bar{\rho}_{min})}^{y(\bar{\rho}_{max})}\ln\left(-\frac{d\bar{\rho}_s}{dy}\frac{1}{1-\bar{\rho}_s}\right)\frac{d\bar{\rho}_s}{dy}dy, \tag{305}$$

$$c_2 = \int_{y(\bar{\rho}_{min})}^{y(\bar{\rho}_{max})}\ln\bar{\rho}_s\ln\left(-\frac{d\bar{\rho}_s}{dy}\frac{1}{1-\bar{\rho}_s}\right)\frac{d\bar{\rho}_s}{dy}dy, \tag{306}$$

$$c_3 = \int_{y(\bar{\rho}_{min})}^{y(\bar{\rho}_{max})}\frac{1}{\bar{\rho}_s^2}\frac{d\Pi_s}{dy}\frac{d\bar{\rho}_s}{dy}dy, \quad c_4 = \ln\frac{\bar{\rho}_{max}}{\bar{\rho}_{min}}\;, \tag{307}$$

$\bar{\rho}_{max}$ and $\bar{\rho}_{min}$ are the minimum and the maximum values of the dimensionless density of the fitting region defining the extent of ablation front ($\bar{\rho}_{max} = 0.99$ and $\bar{\rho}_{min} = 0.05$ are taken in this study), $\bar{\rho}_s$ and Π_s are the simulated dimensionless density and pressure profiles and $\|H(\bar{\rho})\| = H(\bar{\rho}_{max}) - H(\bar{\rho}_{min})$. Using the peak density ρ_a and the pressure at the location of the peak density p_a, the acceleration and ablation velocity can be determined as follows

$$V_a = \Pi_a\sqrt{\frac{p_a}{\rho_a}}, \quad g = \frac{V_a^2}{L_0}\frac{1}{\mathrm{Fr}}\;. \tag{308}$$

Substituting the simulated density and pressure profiles (see figure 55) into the above expressions, we obtain the following parameters

$$\begin{aligned} \nu &= 1.68, \\ L_0 &= 0.49\,\mu\text{m}, \\ \mathrm{Fr} &= 0.15, \\ V_a &= 2.89\,\mu\text{m/ns}. \end{aligned}$$

The estimate of parameters for the DA front stability theory are obtained following the error minimization method described at the beginning of this chapter, using the simulated density profile shown in figure 55 ($t \simeq 1.25$ ns). The parameters are the following

$$\begin{aligned} r_D &= 0.35, \\ \Delta &= 2.14, \\ \nu &= 1.09, \\ \beta_t &= 2.5. \end{aligned} \tag{309}$$

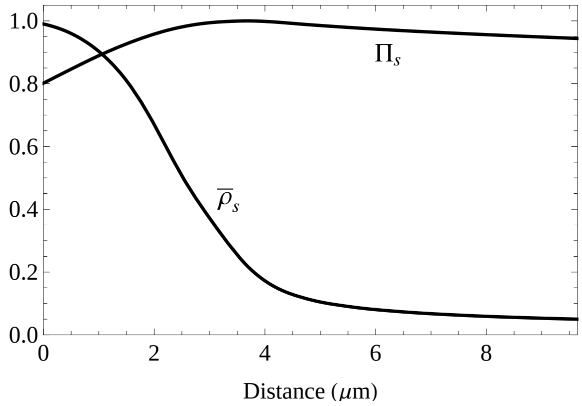

Figure 55: Simulated dimensionless density and pressure profiles.

	γ_{max} (ns^{-1})	$k_{\gamma max}$ (μm^{-1})	k_{co} (μm^{-1})
BG	2.7	0.28	1.29
DAF	2.3	0.55	1.69

Table 7: Maximum growth rate and cut-off wavenumber obtained with the formula by Betti and Goncharov and the DA front stability model for a CH ablator foil.

The Froude number for the DA front model is estimated as an average of the outputs provided by the CHIC simulation over the time interval $1\,\text{ns} < t < 1.5\,\text{ns}$. During this time interval the plastic foil is already accelerated. We obtain an estimate of $\mathrm{Fr_t} \simeq 1.23$.

The dispersion relation curves obtained with both models are plotted in figure 56. Although their orders of magnitude are quite similar, it is worth noticing several features that differ. Results from the DA front stability model present around $k = 0.2\,\mu\text{m}^{-1}$ a sign of stabilization due to the mode coupling that prevents reaching the maximum growth rate that the single ablation front model predicts. Instead of that, the maximum growth rate estimated with the DA front model is smaller and affects perturbations with higher wavenumbers. This displacement in wavenumbers is also observed for the cut-off wavenumber, broadening, in this way, the range of unstable wavelengths (values are specified in table 7). Single-mode 2D simulations were carried out with the code CHIC considering the same background flow. The evolution of perturbations with a wavelength within the range $25\,\mu\text{m} < \lambda < 140\,\mu\text{m}$ has been analyzed. Results are plotted jointly with the theoretical results in figure 56. A good agreement between simulation results and theory is found.

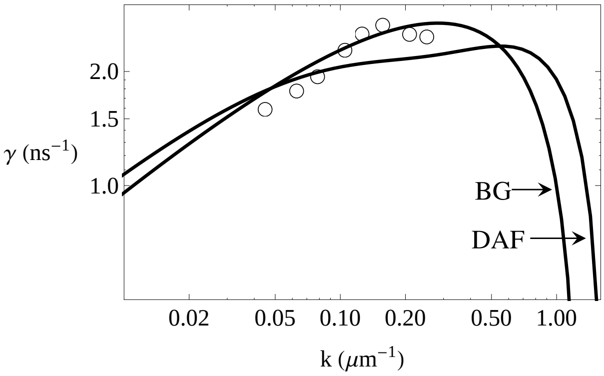

Figure 56: Dispersion curves obtained with the formula by Betti and Goncharov and with the DA front stability model (solid lines). Circles correspond to two-dimensional simulation results.

9.3.2 *Comparison between different ablators*

The aim of this paragraph is to provide a realistic comparison of the stability properties among different ablator materials. The ablator materials analyzed are the plastic (CH), two types of doped plastics ($CHSi_{5.5\%}$ and $CHSi_{9\%}$) and the silice (SiO_2). In order to make the results comparable, the laser intensity remains the same for all cases of study ($I_L = 400\,TW/cm^2$) and the foil thickness varies in order to maintain the same foil areal mass. Since the ablation pressure on the target is roughly determined by the laser intensity [2] ($P_a \propto I_L^{2/3}$), we expect to reach similar accelerations for the different ablators. Initial values of the density and foil thickness used in the one-dimensional simulations carried out with the code CHIC are listed in table 8. The irradiated foils reach an almost constant acceleration during the time interval $1\,ns < t < 1.5\,ns$. Simulation outputs are averaged within this interval and used later on as input data for the theoretical model. Density profiles at $t \simeq 1.25$ ns are plotted in figure 57. Notice that the peak density for the different ablators is located around the same position, indicating that the different foils have been subject roughly to the same acceleration during the initial interval $t < 1.5\,ns$. The thickness of ablation region strongly changes depending on the ablator material and, therefore, on the importance of the radiative transport effects. Defining the ablation region thickness as a distance between the point of maximum density (ρ_a) and an arbitrary point in the near-corona

---

[2] An approximate scaling law reads $P_a \approx 83\,\text{Mbar}\left(\frac{I_{15}}{\lambda_L/0.35}\right)^{2/3}$ where I_{15} is the laser intensity expressed in units of $10^{15}W/cm^2$ and λ_L is the laser wavelength expressed in microns.

	initial density (g/cm^3)	initial thickness (μm)	average acceleration ($\mu m/ns^2$)
CH	1.05	30.0	160.5
$CHSi_{5.5\%}$	1.31	24.0	154.1
$CHSi_{9\%}$	1.50	21.0	152.7
SiO_2	2.20	14.3	155.8

Table 8: Initial density and thickness of the ablator foil, and the average acceleration reached during the interval $1\,\text{ns} < t < 1.5\,\text{ns}$.

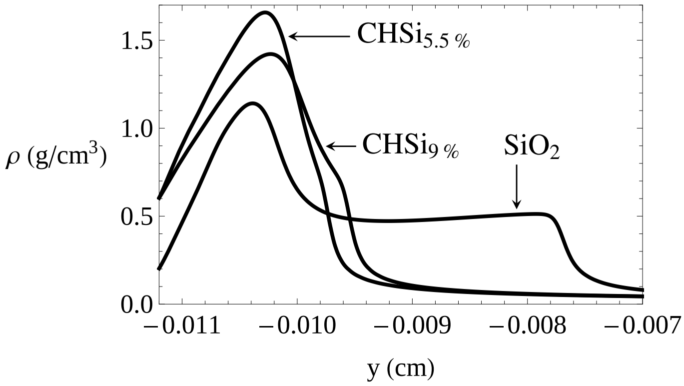

Figure 57: Simulated density profiles of three different ablator foils at the time step $t = 1.25$ ns

region (in this case the point of density $\rho_a/50$), we pass from a thickness of 38 μm in the case of plastic, to a thickness of 50/60 μm for the doped plastic and, finally, to 90 μm for the glass ablator. This feature of the DA front profiles was already reported by Smalyuk et al. [40] where one-dimensional simulations carried out with the code LILAC and using spherical targets subject to a peak laser intensity of 870 TW/cm^2 demonstrated that the glass-ablator target is approximately five times thicker that the all-DT target near the end of acceleration phase.

We have applied the error minimization method to the density profiles of figure 57 in order to estimate the parameters for the theoretical profiles. The value of these parameters are listed in table 9. These values jointly with the average Froude number are necessary to conduct the numerical stability analysis. Figure 58 shows the dispersion curves corresponding to the doped plastic and glass ablators. The maximum growth rate for the cases of moderate-Z ablators decreases considerably compared to the plastic ablator analyzed in

	r_D	Δ	ν	β_t	Fr_t
$\mathrm{CHSi}_{5.5\%}$	0.40	3.80	2.20	4.52	0.96
$\mathrm{CHSi}_{9\%}$	0.48	7.48	4.40	6.18	0.84
SiO_2	0.43	50.50	8.50	19.12	0.50

Table 9: Parameters used in determination of the dispersion curves.

the preceding section (values are listed in table 10). This fact leads to an outstanting improvement in the response of this ablators to the RT instability.

The $\mathrm{CHSi}_{5.5\%}$ case (panel (a) in figure 58) presents a reduction of 35% in the cut-off wavenumber and a reduction of 30% in the maximum growth rate compared to the case of plastic without dopants. This improvement is more obvious if we compare the growth of a perturbation of wavelength $2\pi/k_{\gamma max}$. Taking into account that the semi-amplitude of the perturbation, ξ, evolves in an exponential way, the growth reduction in the case of $\mathrm{CHSi}_{5.5\%}$ compared to CH during a time interval of 1 ns is ∼50%.

The stability properties of the foil get improved if we increase the concentration of dopants in the plastic. Thus, in the case of $\mathrm{CHSi}_{9\%}$ (panel (b) of figure 58), the reduction of the perturbation growth compared to CH during a time interval of 1 ns reaches ∼70%. There are two facts that contribute to this stabilization. First, the height of the unstable liquid column of the RA front decreases (see the values of the parameter r_D in table 9). Having the ERA front largely stabilized by the radiative effects, the RA front is the most propitious region to the development of the RT instability (see chapter 9). Thus, any improvement in the RA front stability brings a reduction of the maximum growth rate of DA front structure. Second, a higher concentration of moderate-Z dopants in the plastic enhances the radiative effects in the ablation region. In particular, the ERA front gets strongly stabilized and because of the short distance between both fronts that this structure presents, the couple mode stabilization is enhanced. We can see this effect in the apparition of a double-hump shape structure in the dispersion curve.

The case of SiO_2 does not present a clear improvement in the target stability properties compared to the $\mathrm{CHSi}_{9\%}$ ablator. Although it is worth noting the decrease of the cut-off wavenumber (reducing, in this way, the range of unstable perturbation wavelengths), the maximum growth rate is larger than in the case of $\mathrm{CHSi}_{9\%}$. The increase of radiative transport effects do not corre-

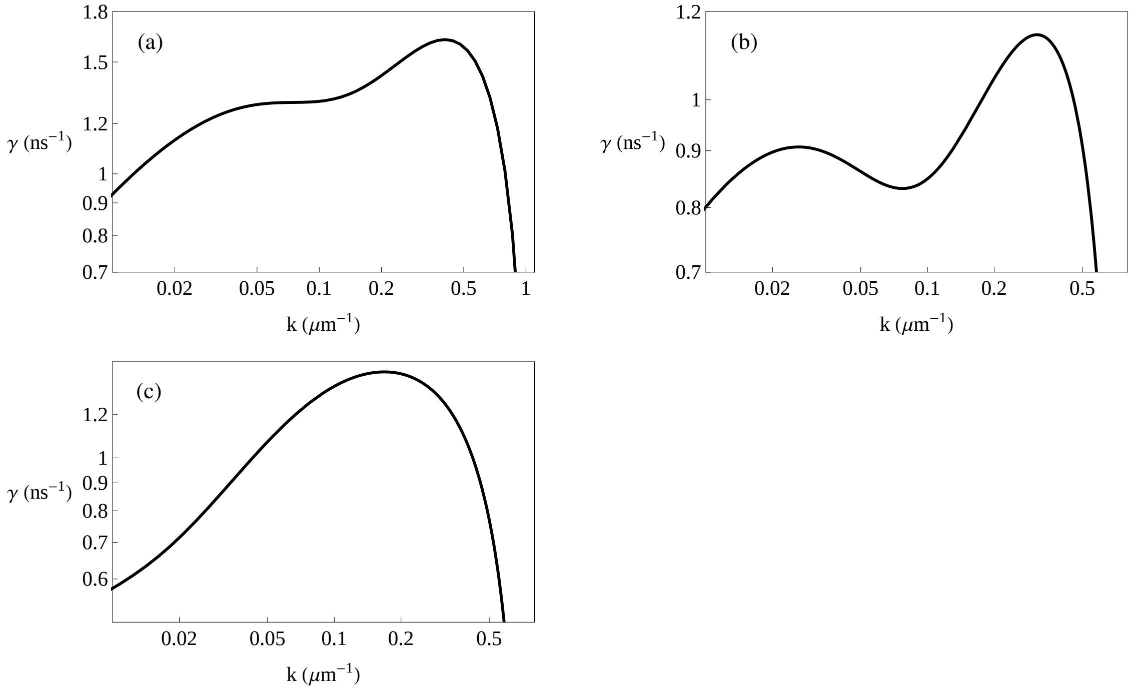

Figure 58: Dispersion curves obtained with the DA front stability model for different ablator materials. Panel (a) corresponds to the $CHSi_{5.5\%}$ ablator, panel (b) to the $CHSi_{9\%}$ ablator and panel (c) to the SiO_2 ablator.

spond immediately to an improvement on stability properties of the ablation region. In the present case, we note that the large plateau length (tens of microns) prevents the couple mode stabilization. Thus, the highly stabilizing modes of the ERA front are mitigated within the plateau region and they do not affect the RA front. In the unstable wavelength domain, the RA front of the SiO_2 behaves as if it is isolated from the rest of the ablation region (in particular, from the ERA front).

9.4 CHAPTER REVIEW

A self-consistent numerical method is developed in this chapter in order to perform the stability analysis of double ablation front structures in a wider range of cases. In contrast to the model described in the preceding chapter, ablation fronts with a finite characteristic length are considered here. This fact enables to analyze the stability of smooth hydrodynamic profiles, like those developed with doped plastics, that cannot be achieved by means of a sharp boundary model. A fitting method is introduced to match theoret-

	γ_{max} (ns^{-1})	$k_{\gamma max}$ (μm^{-1})	k_{co} (μm^{-1})
CH	2.33	0.55	1.69
$CHSi_{5.5\%}$	1.63	0.41	1.09
$CHSi_{9\%}$	1.14	0.31	0.78
SiO_2	1.44	0.17	0.72

Table 10: Maximum growth rate and cut-off wavenumber obtained with the DA front stability model for different ablator materials.

ical hydrodynamic profiles to those coming from one-dimensional simulations. This method uses either an error minimization procedure or takes into account the minimum density gradient scale length of both ablation fronts and the plateau length (outputs of the one-dimensional simulations) in order to estimate the analytic parameters of the profiles. Comparison between the radiation hydrodynamic theory and simulations is given showing good agreement in reproducing the density/temperature profiles. Dispersion relation is obtained numerically in the stability analysis by imposing that the perturbations are localized within the ablation region. Comparisons between the self-consistent model and the sharp boundary one are given. It is shown that the sharp boundary model is in agreement with the self-consistent results when the characteristic lengths of both ablation fronts are sufficiently short compared to the Spitzer and the plateau length. On the contrary, if the ablation fronts are smooth, results from the two models differ, and the self-consistent dispersion relation shows an additional stabilization for short wavelengths, as it is expected. In line with sharp boundary model results, a double-hump shape is also observed in the dispersion curves for some hydrodynamic profiles characterized by a short plateau length. This stabilization for intermediate perturbation wavelengths is due to coupled modes; in particular, it is presumed that for a sufficiently small plateau length, the relaxation process due to the perturbed dynamic pressure generated at the outer ablation front affects the inner one for perturbation wavelengths covering the plateau region and leads to the mitigation and even to the stabilization of these modes. Some comparisons of the dispersion curve given by the self-consistent model with growth rates obtained in 2D single-mode simulations are presented showing good agreement.

10

CONCLUSIONS

This thesis is devoted to the stability analysis of double ablation (DA) fronts. Such hydrodynamic structures became to be of interest for the inertial confinement fusion (ICF) applications in the last decade. Experiments performed on high power laser facilities served as a basis for an alternative scheme that permits improving target compression. These experiments demonstrated, on one hand, a significant reduction of target preheat [40] and, on the other hand, a sign of improvement of the shell stability properties [11], if a moderate-Z material is used as ablator. The use of these ablators changes significantly the target hydrodynamics inducing a DA front structure due to the increasing importance of the role played by the radiation energy flux inside the ablation region.

This thesis is dedicated to a detailed theoretical analysis of stability of double ablation fronts. Linear stability theories are valuable for, at least, two reasons. First, they provide a deep understanding of the physics underlying the instability process and contribute to the explanation of stabilization mechanisms. Second, these theories become a helpful tool for ICF target designers since different target and laser configurations (including parametric studies) can be tested with a quick estimate of the perturbation growth rate. These preliminary studies provide then a first estimate that need to be refined afterwards with time-expensive numerical simulations. There was up to now no linear stability theory suitable to analyze DA fronts. Existing theories consider only a single ablation front driven by thermal conduction, which is modeled by an empirical power dependence of the heat conductivity on the temperature. This model explains reasonable well the laser-driven implosions of low-Z ablator (DT or CH) targets. However, the flows demonstrating a second ablation front with moderate-Z materials stay out of the scope of those theories. This thesis provides for the first time a complete stability theory of double ablation fronts where both electron and radiation energy transport are considered on the same physical grounds.

A prior requirement before undertaking the analysis of DA fronts is the rigorous study of each front independently. Part II of this thesis is devoted to this excercise.

The stability analysis of an electronic-radiative ablation (ERA) front is tackled for the first time. Two approaches are presented:

- a general numerical self-consistent method that permits to analyze profiles no matter what their characteristic length is, and
- an analytical self-consistent approach for steep ablation fronts, where the radiative energy contribution (measured with the parameter β_t) is dominant.

The enhancement of stabilization observed in the numerical results of an ERA front as the radiation contribution increases is explained by the analytical approach. We demonstrate that both stabilization mechanisms, the rocket effect and the convective stabilization (represented by the functions q_{10}, and $f_{10} + dq_{10}/d\epsilon_0$, respectively, see section 6.3) are enhanced with increasing radiation effects.

The stability of a radiative ablation front is analyzed with the same numerical self-consistent method. This ablation front is driven by the radiative energy conduction with the nonlinear thermal conductivity ($\propto T^{\nu}\nabla T$) so that the phenomenological theory by Betti and Goncharov [28] is applicable. Comparisons show an excellent agreement within the range of validity of this theory. Furthermore, we present novel results for smooth profiles ($\nu < 1$). We demonstrate that the dependence of the rocket effet stabilization on the wavenumber depends on the nature of thermal conduction mechanism. These ablation fronts with $\nu < 1$ present a peculiar behaviour described for the first time in this thesis:

- Above a critical value of the Froude number, $\mathrm{Fr_c}$, these profiles are completely stabilized for all perturbation wavelenghts.
- Below $\mathrm{Fr_c}$, these profiles present two cut-off wavenumbers: one for long-wavelength modes stabilized by the rocket effect, and one for short-wavelength (the usual one) stabilized by the convective stabilization.

Part III of this thesis is devoted to the stability analysis of DA fronts. Two approaches are developed: an analytical sharp-boundary model and a numerical self-consistent model. With these models, we generalize previous theories to much broader range of profiles, which are practically important in the ICF studies now. The theory developed in this thesis let us estimate the perturbation growth rate in moderate-Z ablators, such as doped plastics and the silice. Its validity is demostrated by comparison with numerical simulations. A relevant feature described in this thesis is the stabilization due to mode coupling between two fronts. We claim that in certain cases where the separation between fronts is sufficiently small, stabilizing modes associated to the rocket effect at the ERA front are not completely damped within the plateau region and can influence the RA front stabilizing the whole structure. This feature is manifesting itself in the double-hump shape of the dispersion curves.

The analytical and numerical stability theories presented in this thesis provide for the first time the scaling laws of the ablative Rayleigh-Taylor instability for DA fronts. It also contributes to the understanding of the physical stabilization mechanisms involved in these hydrodynamic structures. Furthermore, this theory provides an unique tool to ICF target designers that allows to evaluate stability of implosion calculated in a spherical symmetric geometry. A fitting method is developed that allows to extract the model parameters from the one-dimensional simulated hydrodynamic profiles. This method is demonstrated to be robust and trustworthy. Therefore, one can easy and quickly estimate the perturbation growth rate of any target design. This permits to analyze in a reasonable time the stability of different target configurations, without the systematic use of time-expensive two-dimensional numerical simulations.

PERSPECTIVES

The theory developed in this thesis for the stability analysis of DA fronts assumes a steady and isobaric background flow inside the ablation region and a planar geometry. This description is then appropriate for a thin layer encompassing the ablation region. However, it neglects effects occuring at a distance of several times the ablation region thickness, such as inverse bremsstrahlung absorption in the low-density corona plasma. Further work might consider this physical process and study the target stability in the energy transport zone between the critical surface (where the laser is absorbed) and the ablation region. In certain cases where the radiative flow dominates and creates a well-formed DA front, the plateau can be an order of magnitude thicker than the ablation fronts (see the silice simulated profile in chapter 9). In these cases, the description of the background flow can be improved by removing the isobaric assumption.

ICF target implosions are strongly unsteady. Although the linear phase of the ablative RT instability lasts for a short period of time, extensions from this thesis work might include also spherical and unsteady effects. Moreover, actual ICF target designs comprise the ablator overcoating a DT ice layer. Thus, including multilayer shell targets could be thought interesting for further work, considering the mode coupling at the density jumps and feeding in the perturbations at the inner fuel surface that is unstable at the end of implosion process.

CONCLUSIONS

Ce travail de thèse s'inscrit dans le contexte de la fusion par confinement inertiel (FCI) et il a permis de développer, pour la première fois, une théorie linéaire permettant d'analyser la stabilité des structures à double front d'ablation. Cela concerne la détermination du taux de croissance de perturbations dues à l'instabilité de Rayleigh-Taylor aux fronts d'ablation lors de l'implosion de la cible. Dans un premier temps on a commencé par l'étude rigoureuse de la stabilité linéaire de chaque front indépendamment (part II), ce qui nous permet de traiter dans un second temps l'analyse de stabilité de la structure hydrodynamique complète (part III).

Le chapitre 6 est dédié au développement d'un modèle auto-consistant pour le front d'ablation électronique-radiatif. Le modèle est basé sur une approximation de front optiquement mince pour le transfert radiatif qui implique une température radiative constante. Il existe une forte dépendance des effets radiatifs (lesquels sont mesurés avec le paramètre β_t) sur la longueur caractéristique des profils hydrodynamique. En effet, une augmentation du paramètre β_t se traduit par un profil plus raide. Les courbes de la relation de dispersion sont calculées numériquement et elles mettent en évidence une influence notable du transfert d'énergie radiative dans la stabilisation du front ERA. Le taux de croissance maximum des perturbations comme le nombre d'onde de coupure (cut-off) diminuent avec le paramètre β_t. Une formule analytique pour la relation de dispersion est obtenue pour le cas limite de fronts ERA très raide, $\beta_t \gg 1$. L'ordre de grandeur des quantités perturbées est lié à la longueur caractéristique $(k^*)^{-1} = \beta_t^{7/6} L_{St}$, qui est beaucoup plus grande que la longueur de Spitzer. Cela a pour conséquence une augmentation de la vitesse du plasma en expansion et de la stabilisation du front due à l'effet fusée. Par exemple, le nombre d'onde de coupure est proportionnel à $k_{co} \propto (k^*)^{-1} \mathrm{Fr}_t^{-5/3}$, où Fr_t est le nombre de Froude mesuré au point où le plasma se trouve à la température de transition. Une formule analytique pour la relation de dispersion des structures à double front d'ablation est développée et elle est cohérente avec des résultats numériques pour $\beta_t = 20$ et pour un domaine de nombres de Froude $0.2 < \mathrm{Fr}_t < 5$.

Dans le chapitre 7 la stabilité du front d'ablation radiatif (RA) est analysée avec une méthode numérique basée sur un écoulement non-perturbé auto-consistant. Un front RA dominé par la contribution radiative est considéré avec le transfert d'énergie radiative décrit par la loi de Fourier et une conductivité qui dépend fortement de la température ($\kappa \propto T^{\nu}$). Ce modèle d'écoulement est déjà considéré dans des théories analytiques auto-consistant ([31, 3, 4, 13, 14, 32]), et plusieurs comparaisons entre les courbes de dispersion obtenues avec ces théories et le modèle numérique sont présentées. Cela nous permet de valider les lois d'échelles du problème. La théorie de Betti et Goncharov (BG) présente un excellent accord avec les résultats numériques dans les limites asymptotiques où la théorie analytique peut être résolue, $\mathrm{Fr} \ll 1$ et $\mathrm{Fr} \gg 1$. Dans les cas où le nombre de Froude est de l'ordre de l'unité, la formule de raccordement de BG présente aussi un bon accord avec les résultats numériques. Ce modèle numérique auto-consistant montre l'existence d'un nouveau « cut-off » qui affecte les modes de grande longueur d'onde pour des profils hydrodynamiques où l'exposant de la conductivité thermique est plus petit que l'unité, $\nu < 1$. L'apparition de ce cut-off pour les modes de grande longueur d'onde est expliqué par une augmentation de la force stabilisante due à la pression dynamique (effet fusée) pour ces modes. De plus, si des profils hydrodynamiques avec $\nu < 1$ sont soumis à une faible accélération (au moins $\mathrm{Fr} > 2$), ils sont complétement stabilisés. On peut alors parler de l'existence d'un nombre de Froude de coupure.

Un modèle de discontinuité pour l'analyse de la stabilité de double front d'ablation est présenté dans le chapitre 9. En raison de l'approximation de front mince, la validité de ce modèle est réduite aux structures hydrodynamiques avec des fronts d'ablation suffisamment raides. Ces structures sont rencontrées dans des simulations de cibles avec des ablateurs de nombre atomique modéré, comme la silice. Une formule pour la relation de dispersion est obtenue par le couplage au travers des lois de conservation entre un modèle de discontinuité déjà existant pour le front RA ([27]) et l'ordre dominant de la solution du front ERA (obtenu dans le chapitre 6). Les résultats indiquent la prééminence des modes instables associés au front RA pour des grandes longueurs de plateau, et une remarquable influence des modes couplés pour des petites longueurs de plateau. Les modes couplés mènent l'apparition d'une forme à double bosse dans les courbes de dispersion qui peuvent même diviser la courbe de dispersion en deux avec une nouvelle zone de stabilité au milieu. Une comparaison de la courbe de dispersion obtenue avec le model analytique et le taux de croissance qui donne des simulations bidimensionnelles montre un bon accord pour des nombres d'onde comprises entre $1 < kd_p < 10$.

Finalement, le chapitre 9 est dédié au développement d'une méthode numérique auto-consistante qui permet d'analyser la stabilité des structures à double front d'ablation sans la contrainte d'épaisseur de front nul. Ainsi, contrairement au modèle décrit dans le chapitre précédent, des fronts d'ablation avec une longueur caractéristique finie y sont considérés. Cela nous permet d'analyser la stabilité de profils hydrodynamiques doux comme ceux qui se développent dans des ablateurs de plastiques dopés et qui ne peuvent pas être traité avec le modèle discontinu. Une méthode de raccordement est proposée pour rapprocher les profils hydrodynamiques théoriques des profils obtenus avec des simulations unidimensionnelles. Cette méthode utilise soit une procédure de minimisation de l'erreur, soit la longueur minimum du gradient de densité de chaque front pour estimer les paramètres analytiques des profils de densité/température. Des comparaisons entre la théorie d'hydrodynamique radiative et les simulations réalisées montrent un bon accord dans la reproduction de profils hydrodynamiques réalistes. La relation de dispersion est obtenue numériquement à partir de l'étude du problème perturbé si on impose la condition limite qui établit que les perturbations doivent être localisées dans la région d'ablation. Des comparaisons entre le modèle auto-consistant et le modèle de discontinuité sont montrées. Les résultats du modèle de discontinuité sont en accord avec ceux du modèle auto-consistant lorsque la longueur caractéristique de chaque front d'ablation est suffisamment petite comparée à la longueur de Spitzer et à l'épaisseur du plateau. Cependant, si les fronts d'ablation ne sont pas raides, les résultats des deux modèles sont différents, et la relation de dispersion auto-consistante montre une stabilisation additionnelle pour des petites longueurs d'onde, comme attendu. En accord avec les résultats du modèle de discontinuité, une forme à double bosse est aussi repérée dans les courbes de dispersion pour des profils hydrodynamiques caractérisés par des petites longueurs de plateau. Cette stabilisation pour les longueurs d'onde intermédiaires est due aux modes couplés ; en particulier, on présume que pour des longueurs de plateau suffisamment petites, le processus de relaxation dû à la pression dynamique perturbé qui est généré dans le front d'ablation externe influe sur le front interne pour des longueurs d'onde de l'ordre de l'épaisseur du plateau. Cela mène à la stabilisation des modes instables et même à la complète suppression de ces modes. Des comparaisons de la courbe de dispersion obtenue avec le modèle auto-consistant et le taux de croissance donné par les simulations bidimensionnelles montrent un bon accord.

BIBLIOGRAPHY

[1] S. Atzeni and J. Meyer-Ter-Vehn. *The Physics of Inertial Fusion*. Oxford University Press, 2004. (Cited in pages xxii, 6, and 160.)

[2] L. Baker. Stability of ablation and combustion fronts. *Phys. Fluids*, 21: 295, 1978. (Cited in pages 22, 68, and 139.)

[3] R. Betti, V. Goncharov, R. L. McCrory, and C. P. Verdon. Self-consistent cutoff wave number of the ablative Rayleigh-Taylor instability. *Phys. Plasmas*, 2:3844, 1995. (Cited in pages 26, 29, 115, 116, 127, and 186.)

[4] R. Betti, V. N. Goncharov, R. L. McCrory, P. Sorotokin, and C. P. Verdon. Self-consistent stability analysis of ablation fronts in inertial confinement fusion. *Phys. Plasmas*, 3:2122, 1996. (Cited in pages 26, 29, 70, 115, 116, 120, 127, 151, and 186.)

[5] S. Bodner. Rayleigh-Taylor Instability and Laser-Pellet Fusion. *Phys. Rev. Lett.*, 33:761, 1974. (Cited in pages 21, 23, 68, and 139.)

[6] J. Breil and P. H. Maire. A cell-centered diffusion scheme on two-dimensional unstructured meshes. *J. Comput. Phys.*, 224:785, 2007. (Cited in pages 145 and 155.)

[7] K. A. Brueckner, S. Jorna, and R. Janda. Hydrodynamic stability of a lasaer-driven plasma. *Phys. Fluids*, 17:1554, 1974. (Cited in pages 21 and 69.)

[8] V. V. Bychkov, S. M. Golberg, and M. A. Liberman. Self-consistent model of the Rayleigh-Taylor instability in ablatively accelerated laser plasma. *Phys. Plasmas*, 1:2976, 1994. (Cited in pages 24, 29, and 70.)

[9] P. Clavin and L. Masse. Instabilities of ablation fronts in inertial confinement fusion: A comparison with flames. *Phys. Plasmas*, 11:69, 2004. (Cited in pages 27, 28, 141, and 171.)

[10] V. Drean, M. Olazabal-Loumé, J. Sanz, and V. T. Tikhonchuk. Dynamics and stability of radiation-driven double ablation front structures. *Phys. Plasmas*, 17:122701, 2010. (Cited in pages xi, 75, 142, and 158.)

[11] Shinsuke Fujioka, Atsushi Sunahara, Katsunobu Nishihara, Naofumi Ohnishi, Tomoyuki Johzaki, Hiroyuki Shiraga, Keisuke Shigemori, Mitsuo Nakai, Tadashi Ikegawa, Masakatsu Murakami, Keiji Nagai, Takayoshi Norimatsu, Hiroshi Azechi, and Tatsuhiko Yamanaka. Suppression of the Rayleigh-Taylor instability due to self-radiation in a multiablation target. *Phys. Rev. Lett.*, 92:195001, 2004. (Cited in pages xi, xiv, xvii, xix, 34, 35, 65, 147, and 181.)

[12] Shinsuke Fujioka, Atsushi Sunahara, Naofumi Ohnishi, Yohei Tamari, Katsunobu Nishihara, Hiroshi Azechi, Hiroyuki Shiraga, Mitsuo Nakai, Keisuke Shigemori, Tatsuhiro Sakaiya, Motohiro Tanaka, Kazuto Otani, Kazuki Okuno, Takeshi Watari, Takeshi Yamada, Masakatsu Murakami, Keiji Nagai, Takayoshi Norimatsu, Yasukazu Izawa, Shinya Nozaki, and Yen wei Chen. Suppression of Rayleigh-Taylor instability due to radiative ablation in brominated plastic targets. *Phys. Plasmas*, 11:2814, 2004. (Cited in pages xi, xiv, xvii, xix, xxii, xxiii, xxviii, 35, 36, 37, and 38.)

[13] V. N. Goncharov, R. Betti, R. L. McCrory, P. Sorotokin, and C. P. Verdon. Self-consistent stability analysis of ablation fronts with large Froude numbers. *Phys. Plasmas*, 3:1402, 1996. (Cited in pages xxv, 26, 28, 29, 70, 115, 116, 120, 122, 123, 124, 127, 151, and 186.)

[14] V. N. Goncharov, R. Betti, R. L. McCrory, and C. P. Verdon. Self-consistent stability analysis of ablation fronts with small Froude numbers. *Phys. Plasmas*, 3:4665, 1996. (Cited in pages 26, 70, 120, 121, 124, 127, and 186.)

[15] D. B. Henderson, R. L. McCrory, and R. L. Morse. Ablation stability of laser-driven implosions. *Phys. Rev. Lett.*, 33:205, 1974. (Cited in pages 21 and 69.)

[16] D. G. Hicks, B. K. Spears, D. G. Braun, R. E. Olson, C. M. Sorce, P. M. Celliers, G. W. Collins, and O. L. Landen. Convergent ablator performance measurements. *Phys. Plasmas*, 17:102703, 2010. (Cited in page 158.)

[17] H. J. Kull. Incompressible description of Rayleigh-Taylor instabilities in laser-ablated plasmas. *Phys. Fluids B*, 1:170, 1989. (Cited in pages 23, 28, 95, 117, 121, and 166.)

[18] H. J. Kull and S. I. Anisimov. Ablative stabilization in the incompressible Rayleigh-Taylor instability. *Phys. Fluids*, 29:2067, 1986. (Cited in pages 22, 68, 115, and 136.)

[19] J. D. Lawson. Some criteria for a power producing thermonuclear reactor. *Proceedings of the Physical Society (London)*, 70:6–10, 1957. (Cited in page 6.)

[20] J. D. Lindl. Development of the indirect-drive approach to inertial confinement fusion and the target physics basis for ignition and gain. *Phys. Plasmas*, 2:3933, 1995. (Cited in pages x, xiii, xvi, and 9.)

[21] P. H. Maire. A high-order cell-centered Lagrangian scheme for two-dimensional compressible fluid flows on unstructured meshes. *J. Comput. Phys.*, 228:2391, 2009. (Cited in pages 145 and 155.)

[22] P. H. Maire, R. Abgrall, J. Breil, and J. Ovadia. A cell-centered Lagrangian scheme for two-dimensional compressible flow problems. *SIAM J. Sci. Comput.*, 29:1781, 2007. (Cited in pages 145 and 155.)

[23] W. M. Manheimer and D. G. Colombant. Slab model for Rayleigh-Taylor stabilization by vortex shedding, compressibility, thermal conduction, and ablation. *Phys. Fluids*, 27:983, 1984. (Cited in pages 22 and 68.)

[24] L. Masse. Stabilization effect of anisotropic thermal diffusion on the ablative Rayleigh-Taylor instability. *Phys. Rev. Lett.*, 98:245001, 2007. (Cited in pages 27, 29, and 141.)

[25] P. W. McKenty, V. N. Goncharov, R. P. J.Town, S. Skupsky, R. Betti, and R. L. McCrory. Analysis of a direct-drive ignition capsule designed for the National Ignition Facility. *Phys. Plasmas*, 8:2315, 2001. (Cited in pages x, xiii, xvi, and 34.)

[26] E. Ott and D. A. Russell. Diffuse-Boundary Rayleigh-Taylor Instability. *Phys. Rev. Lett.*, 41:1048, 1978. (Cited in page 17.)

[27] A. R. Piriz, J. Sanz, and L. F. Iba nez. Rayleigh-Taylor instability of steady ablation fronts: The discontinuity model revisited. *Phys. Plasmas*, 4:1117, 1997. (Cited in pages 27, 28, 29, 68, 116, 122, 123, 126, 134, 136, 139, 141, 147, 150, 151, and 186.)

[28] R. L. McCrory R. Betti, V. N. Goncharov and C. P. Verdon. Growth rate of the ablative Rayleigh-Taylor instability in inertial confinement fusion. *Phys. Plasmas*, 5:1446, 1998. (Cited in pages xxv, 27, 36, 115, 116, 120, 121, 122, 123, 124, 127, 151, 157, 161, 173, and 182.)

[29] Lord Rayleigh. Investigation of the character of the equilibrium of an incompressible heavy fluid of variable density. *Proc. Lond. Math. Soc.*, 14: 170, 1883. (Cited in page 9.)

[30] T. C. Sangster, V. N. Goncharov, P. B. Radha, V. A. Smalyuk, R. Betti, R. S. Craxton, J. A. Delettrez, D. H. Edgell, V. Yu. Glebov, D. R. Harding, D. Jacobs-Perkins, J. P. Knauer, F. J. Marshall, R. L. McCrory, P. W. McKenty, D. D. Meyerhofer, S. P. Regan, W. Seka, R. W. Short, S. Skupsky, J. M. Soures, C. Stoeckl, B. Yaakobi, D. Shvarts, J. A. Frenje, C. K. Li, R. D. Petrasso, and F. H. Séguin. High-areal density fuel assembly in direct-drive cryogenic implosions. *Phys. Rev. Lett.*, 100:185006, 2008. (Cited in pages x, xiii, xvi, xxiii, 42, 43, and 65.)

[31] J. Sanz. Self-consistent analytical model of the Rayleigh-Taylor instability in inertial confinement fusion. *Phys. Rev. Lett.*, 73:2700, 1994. (Cited in pages 25, 26, 28, 29, 70, 89, 119, 127, 139, 151, and 186.)

[32] J. Sanz. Self-consistent analytical model of the Rayleigh-Taylor instability in inertial confinement fusion. *Phys. Rev. E*, 53:4026, 1996. (Cited in pages 29, 70, 89, 119, 127, 139, 151, and 186.)

[33] J. Sanz, L. Masse, and P. Clavin. The linear Darrieus-Landau and Rayleigh-Taylor instabilities in inertial confinement fusion revisited. *Phys. Plasmas*, 13:102702, 2006. (Cited in pages 27, 29, and 171.)

[34] J. Sanz, R. Betti, V. A. Smalyuk, M. Olazabal-Loumé, V. Drean, V. Tikhonchuk, X. Ribeyre, and J. Feugeas. Radiation hydrodynamic theory of double ablation fronts in direct-drive inertial confinement fusion. *Phys. Plasmas*, 16:082704, 2009. (Cited in pages xi, xiv, xvii, xxiii, 45, 52, 53, 54, 58, 66, 75, 133, 142, 153, 154, 158, 159, and 161.)

[35] A. J. Schmitt, D. G. Colombant, A. L. Velikovich, S. T. Zalesak, J. H. Gardner, D. E. Fyfe, and N. Meztler. Large-scale high-resolution simulations of high gain direct-drive inertial confinement fusion targets. *Phys. Plasmas*, 11:2716, 2004. (Cited in pages x, xiii, xvi, and 34.)

[36] D. E. Sharp. An overview of Rayleigh-Taylor instability. *Physica*, 12D:3, 1984. (Cited in pages 9, 10, and 62.)

[37] J. N. Shiau, E. B. Goldman, , and C. I. Weng. Linear stability analysis of laser-driven spherical implosions. *Phys. Rev. Lett.*, 32:352, 1974. (Cited in pages 21 and 69.)

[38] V. A. Smalyuk, S. X. Hu, V. N. Goncharov, D. D. Meyerhofer, T. C. Sangster, D. Shvarts, C. Stoeckl, B. Yaakobi, J. A. Frenje, and R. D. Petrasso. Rayleigh-Taylor growth stabilization in direct-drive plastic targets at laser intensities of 1 x 10^{15} w/cm^2. *Phys. Rev. Lett.*, 101:025002, 2008. (Cited in pages x, xiii, and xvi.)

[39] V. A. Smalyuk, D. Shvarts, R. Betti, J. A. Delettrez, D. H. Edgell, V. Yu. Glebov, V. N. Goncharov, R. L. McCrory, D. D. Meyerhofer, PB. Radha, S. P. Regan, T. C. Sangster, W. Seka, S. Skupsky, C. Stoeckl, B. Yaakobi, J. A. Frenje, C. K. Li, R. D. Petrasso, and F. H. Séguin. Role of hot-electron preheating in the compression of direct-drive imploding targets with cryogenic d_2 ablators. *Phys. Rev. Lett.*, 100:185005, 2008. (Cited in pages 42 and 65.)

[40] V. A. Smalyuk, R. Betti, J. A. Delettrez, V. Yu. Glebov, D. D. Meyerhofer, P. B. Radha, S. P. Regan, T. C. Sangster, J. Sanz, W. Seka, C. Stoeckl, B. Yaakobi, J. A. Frenje, C. K. Li, R. D. Petrasso, and F. H. Séguin. Implosion experiments using glass ablators for direct-drive inertial confinement fusion. *Phys. Rev. Lett.*, 104:165002, 2010. (Cited in pages x, xiii, xvi, xxiii, 43, 44, 65, 177, and 181.)

[41] L. Spitzer and R. Harm. Transport phenomena in a completely ionized gas. *Phys. Rev.*, 89:977, 1953. (Cited in pages xxviii, 46, 66, and 122.)

[42] H. Takabe, L. Montierth, and R. L. Morse. Self-consistent eigenvalue analysis of Rayleigh-Taylor instability in an ablating plasma. *Phys. Fluids*, 26:2299, 1983. (Cited in pages 22 and 69.)

[43] H. Takabe, K. Mima, L. Montierth, and R. L. Morse. Self-consistent growth rate of the Rayleigh-Taylor instability in an ablatively accelerating plasma. *Phys. Fluids*, 28:3676, 1985. (Cited in pages 22, 23, 32, and 69.)

[44] G. I. Taylor. The instability of liquid surfaces when accelerated in a direction perpendicular to their planes. *Proc. R. Soc. London A*, 201:192, 1950. (Cited in page 9.)

[45] M. Van-Dyke. *Perturbation methods in fluid mechanics*. The Parabolic Press, Standford, California, 1975. (Cited in page 102.)

[46] R. W. Wasow. *Asymptotic expansions for ordinary differential equations*. Huntington, New York, 1976. (Cited in page 89.)

[47] B. Yaakobi, O. V. Gotchev, R. Betti, and C. Stoeckl. Study of fast-electron transport in laser-illuminated spherical targets. *Phys. Plasmas*, 16:102703, 2009. (Cited in page 44.)

[48] C. Yanez, J. Sanz, M. Olazabal-Loumé, and L. F. Ibanez. Linear stability analysis of double ablation fronts in direct-drive inertial confinement fusion. *Phys. Plasmas*, 18:052701, 2011. (Cited in pages 141, 149, 164, 165, 167, 169, and 170.)

[49] C. Yanez, J. Sanz, and M. Olazabal-Loumé. Self-consistent numerial dispersion relation of the ablative Rayleigh-Taylor instability of double ablation fronts in inertial confinement fusion. *Phys. Plasmas*, 19:062705, 2012. (Cited in page 124.)

[50] Y. B. Zeldovich and Y. P. Raizer. *Physics of Shock Waves and High-Temperature Hydrodynamic Phenomena*. Academic, New York, 1966. (Cited in pages 51, 52, 77, 78, and 154.)

[51] C. D. Zhou and R. Betti. Hydrodynamic relations for direct-drive fast-ignition and conventional inertial confinement fusion implosions. *Phys. Plasmas*, 14:072703, 2007. (Cited in pages 31, 32, and 41.)